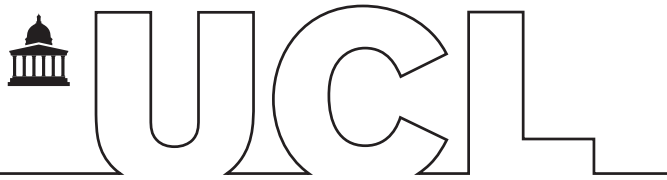

Interaction of XUV and X-ray pulses with diatomic molecules

Miles Elliott Mountney

A dissertation submitted in partial fulfillment

of the requirements for the degree of

Doctor of Philosophy

of

University College London.

Department of Physics and Astronomy

University College London

November 2024

I, Miles Elliott Mountney, confirm that the work presented in this thesis is my own. Where information has been derived from other sources, I confirm that this has been indicated in the work.

Abstract

In this thesis, we study theoretically the angular distributions of electron escape and the process of molecular dissociation during the interaction between diatomic molecules and intense laser pulses in the ultraviolet and X-ray range. We start by demonstrating theoretically a one-to-one mapping between the direction of electron ionization and the phase delay between a linearly-polarized vacuum ultraviolet and a circularly-polarized infrared laser pulse for the N_2 molecule. We compute the dipole matrix element to transition from an initial bound state to the continuum using quantum mechanical techniques. Following the release of the electron in the infrared pulse, we evolve classical trajectories. Neglecting the Coulomb potential and accounting for quantum interference, we compute the distribution of the direction and magnitude of the final electron momentum. We then streak single-photon ionization processes, driven by an X-ray pulse, in open-shell molecules. We obtain continuum molecular wavefunctions while accounting for the singlet or triplet total spin symmetry of the molecular ion. After ionization, we streak the electron dynamics using a circular infrared pulse. For a high intensity infrared pulse, we achieve control of the angle of escape of the ionizing electron. For a low intensity infrared pulse, we obtain final electron momenta distributions on the plane of the infrared pulse and compare them to the angular patterns of electron escape solely due to the X-ray pulse. Finally, we study the interaction between molecular oxygen, O_2, and an extreme ultraviolet pulse. We compute potential energy curves of O_2 up to O_2^{2+}. We find the dissociation limits of these states and the atomic fragments to which they dissociate. We use the Velocity Verlet algorithm to account for the nuclear dynamics. Using Monte Carlo simulations which monitor the nuclear motion and

electronic structure of the molecule, we obtain kinetic energy release distributions of the atomic fragments of O_2.

Impact Statement

The development of theoretical techniques to model the electronic motion of diatomic molecules quantum-mechanically is rare, due to the complexity that arises from the lack of symmetry in molecular orbitals. In this thesis we do so, and apply these techniques to various relevant interactions between diatomic molecules and laser pulses in the ultraviolet (UV) and X-ray range.

In recent years, the experimental advances in developing ultraviolet (UV) and X-ray pulses from free electron lasers (FEL) make studies of inner-shell ionization of atoms and molecules timely. An interesting feature of the interaction of intense laser pulses with matter is that they allow for the removal of an inner-shell electron, leading to processes such as sequential single-photon ionization and Auger-Meitner decay. To effectively study the electron dynamics in the time-domain, recent experiments use attosecond spectroscopy with co-timed UV and infrared (IR) pulses. Known as attosecond streaking, with this procedure it is possible to time-resolve the photoemission process in atomic and molecular targets.

Most studies analyzing the interaction between diatomic molecules and laser pulses utilize closed-shell molecules, due to the difficulty that arises dealing with different spin-states when studying open-shell molecules. Here, we use nitric oxide, NO, to demonstrate the angular streaking technique to study the time-dependent photoemission in open-shell molecular systems. This work provided the theoretical basis for an experiment at SLAC measuring photoionization delay times [1], a subject which is currently a frontier of ultrafast science due to the recent development of attosecond-duration light pulses.

Setups involving UV and IR pulses can also be used to achieve control of elec-

tron current. Recently, utilizing IR laser technology allowed for high-velocity electrons to be arranged in almost any geometric form in semiconductors, including ring currents, relevant for generating solenoidal magnetic fields. These high-velocity electrons, which generate high magnetic fields, were produced using coherent control. Coherent control is a powerful tool with applications in a wide range of areas such as quantum optics, attosecond metrology, optoelectronics and laser cooling. In response to this, using nitrogen, N_2, we theoretically demonstrate that control of electron currents is possible using a combination of vacuum ultraviolet (VUV) and IR pulses.

Finally, due to the high photon energy of UV and X-ray radiation, phenomena such as multi-electron ionization and molecular dissociation are possible. As a result of these experiments, one obtains the distributions of the kinetic energy release (KER) of the atomic fragments resulting from molecular dissociation. As a result of the multiple ionization sequences leading to a dissociation pathway, the kinetic energy spectra as a function of photon energy for a certain dissociation pathway is diverse. Identifying the ionization sequences leading to molecular dissociation is crucial for understanding experimental results in physical, chemical and biological processes taking place when molecules interact with intense laser pulses. In order to do this, one must model both electronic and nuclear motion of the molecule. Using a hybrid quantum-classical technique we have developed, we produce KER distributions of O_2 when an extreme ultraviolet (XUV) pulse is applied to the molecule.

Acknowledgements

Firstly, I would like to express my gratitude to the EPSRC for funding and to the dedicated support staff at UCL, whose contributions made this PhD possible. I'd also like to thank my co-authors and collaborators for their contributions to the research presented in this dissertation.

My thanks also goes to all the members of our research group. In particular, I'd like to thank Antonis Hadjipittas, Georgios Katsoulis, and Matthew Peters for their guidance and thought-provoking discussions. My PhD would not have been possible without the mentorship and expertise of my supervisor, Professor Agapi Emmanouilidou. Your unwavering commitment to excellence has been a constant source of inspiration, and I will carry your work ethic with me throughout my career.

On a personal note, I would like to express my deepest appreciation to those who supported me along the way. To my partner, Kelly Johnson—your love and encouragement were invaluable during the most challenging times, and I am endlessly grateful to have you in my life. Lastly, a special thank you to my mum, Penelope Mountney. You have been my greatest supporter and mentor throughout my entire academic journey, through every high and low. I would not be the person I am today without you.

List of Publications

This dissertation is based on the following publications.

[1] T. Driver, M. Mountney, J. Wang, L. Ortmann, A. Al-Haddad, N. Berrah, C. Bostedt, E. G. Champenois, L. F. DiMauro, J. Duris, D. Garratt, J. M. Glownia, Z. Guo, D. Haxton, E. Isele, I. Ivanov, J. Ji, A. Kamalov, S. Li, M.-F. Lin, J. P. Marangos, R. Obaid, J. T. O'Neal, P. Rosenberger, N. H. Shivaram, A. L. Wang, P. Walter, T. J. A. Wolf, H. J. Wörner, Z. Zhang, P. H. Bucksbaum, M. F. Kling, A. S. Landsman, R. R. Lucchese, A. Emmanouilidou, A. Marinelli and J. P. Cryan. Attosecond Delays in X-ray Molecular Ionization. *Nature*, **632**, 762–767 (2024).

[2] M. Mountney, G. P. Katsoulis, S. H. Møller, K. Jana, P. B. Corkum and A. Emmanouilidou. Mapping the direction of electron ionization to phase delay between VUV and IR laser pulses. *Physical Review A*, **106**, 043106 (2022).

[3] M. Mountney, T. C. Driver, A. Marinelli, M. F. Kling, J. P. Cryan and A. Emmanouilidou. Streaking single-electron ionization in open-shell molecules driven by X-ray pulses. *Physical Review A*, **107**, 063111 (2023).

[4] M. Mountney, Z. Wang, F. Trost, H. Lindenblatt, A. Magunia, R. Moshammer, T. Pfeifer and A. Emmanouilidou. Formation of singly ionized oxygen atoms from O_2 driven by XUV pulses: a toolkit for the break-up of FEL-driven diatomics. arXiv, (2024).

Contents

List of Figures

List of Tables

List of Abbreviations

CASSCF Complete active space self-consistent field

CI Configuration interaction

FEL Free-electron laser

FWHM Full width at half maximum

GTO Gaussian-type orbital

HF Hartree-Fock

IR Infrared

KER Kinetic-energy release

MCSCF Multi-configuration self-consistent field

MF Molecular-fixed

MRCI Multireference configuration interaction

PEC Potential-energy curve

SCE Single-center expansion

SFA Strong-field approximation

UV Ultraviolet

VUV Vacuum ultraviolet

XFEL X-ray free-electron laser

XUV Extreme ultraviolet

Chapter 1

Introduction

The development of sub-femtosecond ultraviolet (UV) and X-ray pulses, either from free-electron lasers (FEL) [5] or from high-harmonic generation [6], has revolutionized our ability to study electron dynamics in the time-domain. For example, using attosecond spectroscopy with co-timed UV and infrared (IR) pulses, it is possible to time-resolve the photoemission process in atomic [7], molecular [8], and solid-state targets [9, 10]. This technique is known as attosecond streaking [11]. These streaking experiments are typically performed with IR pulses of low intensity. A low-intensity IR pulse can be used to image electron dynamics and is also of relevance to time delays in single-electron ionization [12–14]. At low intensities the ponderomotive energy, due to the IR pulse, is lower than the kinetic energy of the electron when released in the continuum by an XUV pulse. However, as we will demonstrate in this thesis, at higher intensities the properties of the IR field dominate the final electron momentum, following ejection from an XUV pulse, resulting in the control of electron motion by the IR field. [2]. Recently, there has been substantial effort to extend the streaking methodology to X-ray free-electron laser (XFEL) sources, which provide a source of high intensity X-ray pulses, for the purpose of characterizing the temporal structure of the X-ray pulse [15–18]. This includes the development of angular streaking, which employs a circularly-polarized IR laser field [19–22]. Similar to studies using table-top sources, XFEL streaking has been extended to study the time-dependent emission pattern of core-excited and core-ionized systems undergoing the Auger-Meitner-Meitner decay process

[22, 23], providing insight into electron coherence and entanglement.

One of the interesting features of the interaction of X-ray pulses with matter is that they allow for the removal of an inner-shell electron that subsequently leads to a cascade of multi-electron processes. Namely, it can lead to sequential single-photon ionization processes, as well as Auger-Meitner processes. The latter involve the creation of an inner-shell hole by single-photon ionization, and the subsequent filling of this hole by a valence electron. During this transition of the electron, energy is released, which is taken up by another valence-shell electron, leading to the ionization of the latter electron. Studying the interplay of single-photon ionization and Auger-Meitner processes in molecules is a challenging task due to the many electrons involved in these interactions.

To study the interplay of photoionization and Auger-Meitner processes in molecules and to compute ion yields, we need to compute accurate singe-photon ionization cross sections and Auger-Meitner rates. In order to do so, we need to compute accurate continuum wavefunctions. The latter is a complicated task due to the fact that one has to account for the interplay of electronic and nuclear motion. As a result, the continuum molecular orbitals employed in other studies, which are used to compute single-photon ionization cross sections and Auger-Meitner rates, are expressed as a combination of atomic continuum wavefunctions [24–28]. Such an approximation is only accurate for very high photon energies. In contrast, in our studies we employ accurate continuum molecular wavefunctions [29].

Here, we also formulate the partial single-photon ionization cross section as a function of the polar and azimuthal angles of ejection of the photo-electron. The polar angle is the angle between the ejected electron and the axis of polarization of the XUV pulse. We describe the ionization of an inner-shell electron due to the XUV pulse using state-of-the-art quantum mechanical methods and computational tools. We aslo describe the steering and/or control that the IR pulse imposes on the ejected electron using classical propagation. We account for interference effects by computing the classical action for each trajectory. This hybrid quantum and classical treatment of ionization processes in the presence of XUV+IR pulses

is a powerful tool for theoretical studies that will complement current and future experiments. In this thesis, we demonstrate our hybrid formalism in the context of the diatomic molecules N_2 and NO.

In chapter 3, we theoretically demonstrate that control of electron currents generated at roughly 100 nm is possible. As in the attosecond streak camera [30], we achieve control by varying the phase delay between a linearly-polarized VUV pulse and a streaking circularly-polarized IR pulse. Generating large and controllable THz magnetic fields is of fundamental importance. For instance, such fields control the direction of magnetization in magnetic devices and, when a maximum speed of magnetic switching is reached, they control the onset of magnetic disorder [31]. Thus, THz magnetic fields have a wide range of applications in optoelectronic devices used for information processing. Such fields can currently be produced by the Stanford Linear Accelerator (SLAC) electron beam. However, while important, these fields are a relatively low-tech application of a state-of-the-art accelerator. Devising optical techniques for generating THz magnetic fields with sufficient spatial and temporal precision to be useful for small devices is a frontier of ultrafast science. Recently, utilizing visible and infrared (IR) laser technology allowed for high-velocity electrons to be arranged in almost any geometric form in semiconductors [32–35]. Such forms include a line current, as in SLAC, and a ring current, relevant for generating solenoidal magnetic fields. These high-velocity electrons, which generate high magnetic fields, were produced using coherent control. Coherent control is a powerful tool with applications in a wide range of areas such as quantum optics and metrology [36–38], attosecond metrology [39, 40], optoelectronics [41] and laser cooling [42, 43].

In chapter 4, we demonstrate the extension of the angular-streaking technique [19, 22, 44, 45] to study the time-dependent photoemission in open-shell molecular systems. Most studies of imaging or controlling single-electron ionization instigated by FEL pulses involve closed-shell molecules [29, 46–48], as they are easier to study compared to open-shell molecules. Indeed, following ionization, for closed-shell molecules, the final molecular ion is in a doublet spin state. For open-

shell molecules, the final molecular ion is in a singlet or triplet spin state, that is, the total spin of the open-shell orbital and the orbital where the electron ionizes from is zero or one [49]. We focus only on single-photon ionization processes in diatomic molecules involving an inner-shell electron. The transition of an electron from a bound molecular state to a continuum molecular state takes place due to an intense, ultra-short extreme ultraviolet (XUV) pulse. We choose a laser pulse of this form to ensure that ionization occurs on the attosecond time-scale. Once the electron transitions to the continuum, we employ a weak infrared (IR) circular laser pulse in order to steer (not ionize) the escaping electron. Our goal is to understand the two-dimensional momentum patterns obtained from the interaction of the molecule with the XUV+IR pulse. The reason is that such studies are relevant to state-of-the-art experiments concerning the interaction of molecules with XUV+IR pulses currently taking place, for instance, at SLAC in Stanford [22]. One goal of these experiments is to use the IR pulses in order to time the delay in the ionization of electrons from different inner-shell molecular orbitals.

Experiments have also utilised FELs, such as FLASH in Hamburg [50, 51], to produce intense XUV pulses. The high photon energy of XUV radiation results in phenomena such as multi-electron ionization and dissociation in molecules. A large number of ionization sequences can contribute to a certain dissociation pathway in strongly-driven molecules. This results in a plethora of features in the sum of the kinetic energies of the atomic fragments, i.e. the kinetic energy release (KER), as a function of photon energy of the atomic fragments resulting from molecular dissociation [52, 53]. Hence, using advanced theoretical models to identify the ionization sequences leading to molecular dissociation is crucial for understanding experimental results in physical, chemical and biological processes taking place when molecules interact with XUV pulses [54–58].

In chapter 5, we formulate a hybrid quantum-classical theoretical model to address the interaction of molecules with intense pulses of high photon energy. We focus on the formation of two O^+ atomic fragments in coincidence resulting from the interaction of O_2 with an XUV pulse with photon energy ranging from 20 eV to

42 eV. We demonstrate that the theoretically obtained kinetic-energy release spectra as a function of the photon energy for the $O^+ + O^+$ dissociation pathway are in very good agreement with experimental results.

Chapter 2

Theory of the interaction of molecules with free-electron lasers

2.1 Electronic Structure of Molecules

2.1.1 Born-Oppenheimer approximation

The time-independent Hamiltonian of a molecular system [59] is given by

$$\hat{H} = -\sum_{\alpha} \frac{1}{2m_\alpha} \nabla_\alpha^2 - \sum_i \frac{1}{2} \nabla_i^2 - \sum_\alpha \sum_i \frac{Z_\alpha}{r_{i\alpha}} + \sum_\alpha \sum_{\beta>\alpha} \frac{Z_\alpha Z_\beta}{r_{\alpha\beta}} + \sum_j \sum_{i>j} \frac{1}{r_{ij}}, \tag{2.1}$$

where i and j refer to the electrons, α and β refer to the nuclei, m_α is the mass of nuclei α, Z_α the atomic number (charge) of nuclei α, r_{ij} the distance between electrons i and j, $r_{i\alpha}$ the distance between electron i and nucleus α and $r_{\alpha\beta}$ the internuclear distance between nuclei α and β. We assume the nuclei and electrons to be point masses and use atomic units. In Eq. (2.1), the first term is the kinetic energy operator of the nuclei and the second term is the kinetic energy operator of the electrons. The third, fourth and fifth terms in Eq. (2.1) are the electron-nucleus, nucleus-nucleus and electron-electron potential energies, respectively. The wave functions ψ and energies E of a molecule can be found by solving the Schrödinger equation, given by

$$\hat{H}\psi(\mathbf{r}_i, \mathbf{r}_\alpha) = E\psi(\mathbf{r}_i, \mathbf{r}_\alpha), \tag{2.2}$$

where $\mathbf{r}_i, \mathbf{r}_\alpha$ are the electronic and nuclear coordinates, respectively. Since the nuclei are far heavier than the electrons ($m_\alpha >> m_e$ where m_e is the mass of an electron), the electrons move much faster than the nuclei. The Born-Oppenheimer approximation [60] uses this fact by regarding the nuclei as fixed during the motion of the electrons. Using this approximation allows us to omit the kinetic energy operator of the nuclei. Furthermore, since the nuclei are fixed in space, the nucleus-nucleus potential energy will be a constant. It can be proven that the omission of a constant term from the Hamiltonian does not affect the wave functions. Hence, we obtain the following Schrödinger equation for electronic motion

$$\hat{H}_{el}\psi_{el}(\mathbf{r}_i;\mathbf{r}_\alpha) = E_{el}\psi_{el}(\mathbf{r}_i;\mathbf{r}_\alpha), \tag{2.3}$$

where $E_{el} = E_{el}(\mathbf{r}_\alpha)$ is the purely electronic energy and

$$\hat{H}_{el} = -\sum_i \frac{1}{2}\nabla_i^2 - \sum_\alpha \sum_i \frac{Z_\alpha}{r_{i\alpha}} + \sum_j \sum_{i>j} \frac{1}{r_{ij}}. \tag{2.4}$$

Note that the electronic wavefunctions ψ_{el} only depend parametrically on the nuclear coordinates, and we solve the electronic Schrödinger equation for each possible nuclear configuration with internuclear distance $r_{\alpha\beta}$. The total energy of the system under the Born-Oppenheimer approximation is

$$U = E_{el} + \sum_\alpha \sum_{\beta>\alpha} \frac{Z_\alpha Z_\beta}{r_{\alpha\beta}}. \tag{2.5}$$

In order to solve the electronic Schrödinger equation, we will utilise the variational principle and the Hartree-Fock (HF) method.

2.1.2 Hartree-Fock method

We will use the Hartree-Fock (HF) method to solve the electronic Schrödinger equation in Eq. (2.3). The HF method is a particular case of the Variational method where we assume that the N-electron wave function is represented by a Slater determinant, Φ, of spin-orbitals. The following derivation is taken from Ref. [61]. We begin by assuming an N-electron atom or molecule in its ground state, with the

non-relativistic electronic Hamiltonian from Eq. (2.3). We separate the Hamiltonian into two terms

$$\hat{H}_{el} = \hat{H}_1 + \hat{H}_2, \tag{2.6}$$

where

$$\begin{aligned} \hat{H}_1 &= \sum_{i=1}^{N} \hat{h}_i, \quad \hat{h}_i = -\frac{1}{2}\nabla r_i^2 - \sum_{\alpha}^{nuc.} \frac{Z_\alpha}{r_{i\alpha}}, \quad r_{i\alpha} = |r_i - R_\alpha| \\ \hat{H}_2 &= \sum_{i<j=1}^{N} \frac{1}{r_{ij}}, \quad r_{ij} = \left|r_i - r_j\right|. \end{aligned} \tag{2.7}$$

By the variational method [61] we know the ground state energy E_0 satisfies

$$E_0 \leq E[\Phi] = \langle \Phi | \hat{H} | \Phi \rangle, \tag{2.8}$$

where Φ is our normalised trial function. The HF method supposes that this trial function is a Slater determinant, i.e.

$$\Phi(q_1, \ldots, q_N) = \frac{1}{\sqrt{N!}} \begin{vmatrix} \phi_1(q_1) & \phi_2(q_1) & \ldots & \phi_N(q_1) \\ \vdots & \vdots & \vdots & \vdots \\ \phi_1(q_N) & \phi_2(q_N) & \ldots & \phi_N(q_N) \end{vmatrix}, \tag{2.9}$$

where the $\phi_i(q)$ are spin-orbitals. A spin-orbital is a one-particle wavefunction taking both the position and spin of a particle as its parameters, represented by q. The subscripts $i = 1, 2, \ldots, N$ represent N sets of the four quantum numbers (the Principal quantum number n, the Azimuthal/ Orbital angular momentum quantum number l, the Magnetic quantum number m_l and the Spin quantum number s). The spin-orbitals are orthonormal

$$\left\langle \phi_j \middle| \phi_i \right\rangle = \int \phi_j^*(q) \phi_i(q) dq = \delta_{ij}. \tag{2.10}$$

We can rewrite the Slater determinant as

$$\begin{aligned}\Phi(q_1,\ldots,q_N) &= \frac{1}{\sqrt{N!}}\sum_P (-1)^P \hat{P}\phi_1(q_1)\ldots\phi_N(q_N) \\ &= \sqrt{N!}\hat{A}\Phi_H,\end{aligned} \tag{2.11}$$

where $\hat{P}$ permutes the spin and position coordinates of a pair of electrons, the symbol $(-1)^P$ is equal to 1 when $\hat{P}$ is an even permutation and -1 when $\hat{P}$ is an odd permutation, and the sum is over all permutations $\hat{P}$. The Hartree wave function, Φ_H, is simply the product of the spin-orbitals

$$\Phi_H(q_1,\ldots,q_N) = \phi_1(q_1)\ldots\phi_N(q_N). \tag{2.12}$$

The antisymmetrisation operator, $\hat{A}$, is equal to

$$\hat{A} = \frac{1}{N!}\sum_P (-1)^P \hat{P}. \tag{2.13}$$

It can be shown that the operator $\hat{A}$ is a projection operator and Hermitian. Furthermore, the Hamiltonians $\hat{H}_1$ and $\hat{H}_2$ are invariant under permutations of the electron coordinates. Namely,

$$\begin{aligned}\hat{A}^2 &= \hat{A} \\ [\hat{H}_1,\hat{A}] &= [\hat{H}_2,\hat{A}] = 0.\end{aligned} \tag{2.14}$$

In order to utilise the variational principle, let us calculate the expectation values of $\hat{H}_1$ and $\hat{H}_2$. Using the properties above, we have

$$\begin{aligned}\langle\Phi|\hat{H}_1|\Phi\rangle &= N!\langle\Phi_H|\hat{A}\hat{H}_1\hat{A}|\Phi_H\rangle \\ &= N!\langle\Phi_H|\hat{H}_1\hat{A}^2|\Phi_H\rangle \\ &= N!\langle\Phi_H|\hat{H}_1\hat{A}|\Phi_H\rangle.\end{aligned} \tag{2.15}$$

Hence, using the definition of $\hat{A}$, the fact that $\hat{H}_1$ is the sum of one-body operators and the orthonormality of the spin-orbitals, we have the following

$$\begin{aligned}\langle\Phi|\hat{H}_1|\Phi\rangle &= \sum_{i=1}^{N}\sum_{P}(-1)^P\langle\Phi_H|\hat{h}_i\hat{P}|\Phi_H\rangle \\ &= \sum_{i=1}^{N}\langle\Phi_H|\hat{h}_i|\Phi_H\rangle \\ &= \sum_{i=1}^{N}\langle\phi_i(q_i)|\hat{h}_i|\phi_i(q_i)\rangle\,.\end{aligned} \tag{2.16}$$

Similarly to Eq. (2.15), for $\langle\Phi|\hat{H}_2|\Phi\rangle$ we have

$$\langle\Phi|\hat{H}_2|\Phi\rangle = N!\,\langle\Phi_H|\hat{H}_2\hat{A}|\Phi_H\rangle\,. \tag{2.17}$$

If $\hat{P}_{ij}$ is an operator which switches the coordinates of electrons i and j, then we have the following

$$\begin{aligned}\langle\Phi|\hat{H}_2|\Phi\rangle &= \sum_{i<j}^{N}\sum_{P}(-1)^P\langle\Phi_H|\frac{1}{r_{ij}}\hat{P}|\Phi_H\rangle \\ &= \sum_{i<j}^{N}\langle\Phi_H|\frac{1}{r_{ij}}(1-\hat{P}_{ij})|\Phi_H\rangle \\ &= \sum_{i<j}^{N}[\big\langle\phi_i(q_i)\phi_j(q_j)\big|\frac{1}{r_{ij}}\big|\phi_i(q_i)\phi_j(q_j)\big\rangle \\ &- \big\langle\phi_i(q_i)\phi_j(q_j)\big|\frac{1}{r_{ij}}\big|\phi_j(q_i)\phi_i(q_j)\big\rangle] \\ &= \frac{1}{2}\sum_{i=1}^{N}\sum_{j=1}^{N}[\big\langle\phi_i(q_i)\phi_j(q_j)\big|\frac{1}{r_{ij}}\big|\phi_i(q_i)\phi_j(q_j)\big\rangle \\ &- \big\langle\phi_i(q_i)\phi_j(q_j)\big|\frac{1}{r_{ij}}\big|\phi_j(q_i)\phi_i(q_j)\big\rangle].\end{aligned} \tag{2.18}$$

Using the variational principle [61] for Φ, we have

$$\delta\langle\Phi|\hat{H}|\Phi\rangle - \sum_i E_i\delta\langle\phi_i|\phi_i\rangle = 0. \tag{2.19}$$

Now we can substitute our equations for $\langle\Phi|\hat{H}_1|\Phi\rangle$ and $\langle\Phi|\hat{H}_2|\Phi\rangle$ into this and apply the chain rule

$$\begin{aligned}
&\sum_{i=1}^{N}\Bigg(\langle\delta\phi_i(q_i)|\hat{h}_i|\phi_i(q_i)\rangle+\langle\phi_i(q_i)|\hat{h}_i|\delta\phi_i(q_i)\rangle\\
&+\frac{1}{2}\sum_{j=1}^{N}[\langle\delta\phi_i(q_i)\phi_j(q_j)|\frac{1}{r_{ij}}|\phi_i(q_i)\phi_j(q_j)\rangle+\langle\phi_i(q_i)\delta\phi_j(q_j)|\frac{1}{r_{ij}}|\phi_i(q_i)\phi_j(q_j)\rangle\\
&+\langle\phi_i(q_i)\phi_j(q_j)|\frac{1}{r_{ij}}|\delta\phi_i(q_i)\phi_j(q_j)\rangle+\langle\phi_i(q_i)\phi_j(q_j)|\frac{1}{r_{ij}}|\phi_i(q_i)\delta\phi_j(q_j)\rangle]\\
&-\frac{1}{2}\sum_{j=1}^{N}[\langle\delta\phi_i(q_i)\phi_j(q_j)|\frac{1}{r_{ij}}|\phi_j(q_i)\phi_i(q_j)\rangle+\langle\phi_i(q_i)\delta\phi_j(q_j)|\frac{1}{r_{ij}}|\phi_j(q_i)\phi_i(q_j)\rangle\\
&+\langle\phi_i(q_i)\phi_j(q_j)|\frac{1}{r_{ij}}|\delta\phi_j(q_i)\phi_i(q_j)\rangle+\langle\phi_i(q_i)\phi_j(q_j)|\frac{1}{r_{ij}}|\phi_j(q_i)\delta\phi_i(q_j)\rangle]\\
&-E_i\langle\delta\phi_i(q_i)|\phi_i(q_i)\rangle-E_i\langle\phi_i(q_i)|\delta\phi_i(q_i)\rangle\Bigg)\\
&=0.
\end{aligned}\tag{2.20}$$

One can show Eq. (2.20) can be simplified to

$$\begin{aligned}
&\sum_{i=1}^{N}\Bigg(\langle\delta\phi_i(q_i)|\hat{h}_i|\phi_i(q_i)\rangle+\sum_{j=1}^{N}\langle\delta\phi_i(q_i)\phi_j(q_j)|\frac{1}{r_{ij}}|\phi_i(q_i)\phi_j(q_j)\rangle\\
&-\sum_{j=1}^{N}\langle\delta\phi_i(q_i)\phi_j(q_j)|\frac{1}{r_{ij}}|\phi_j(q_i)\phi_i(q_j)\rangle-E_i\langle\delta\phi_i(q_i)|\phi_i(q_i)\rangle\Bigg)\\
&=0.
\end{aligned}\tag{2.21}$$

Following the procedure outlined in the variational method in Ref. [61], for electron i we have the following integro-differential equation

$$\begin{aligned}
&\Big[-\frac{1}{2}\nabla r_i^2-\sum_{\alpha}\frac{Z_\alpha}{r_{i\alpha}}\Big]\phi_i(q_i)+\Big[\sum_j\int\phi_j^*(q_j)\frac{1}{r_{ij}}\phi_j(q_j)dq_j\Big]\phi_i(q_i)\\
&-\sum_j\Big[\int\phi_j^*(q_j)\frac{1}{r_{ij}}\phi_i(q_j)dq_j\Big]\phi_j(q_i)=E_i\phi_i(q_i),
\end{aligned}\tag{2.22}$$

where $i, j = 1, \ldots, N$. These are the **Hartree-Fock Equations**. The spin-orbitals can be rewritten in terms of their spatial and spin components

$$\phi_i(q_i) = \phi_i(\mathbf{r}_i)\chi_{\frac{1}{2},m_s^i}, \tag{2.23}$$

where the spin functions are orthonormal, i.e. $\left\langle \chi_{\frac{1}{2},m_s^i} \middle| \chi_{\frac{1}{2},m_s^j} \right\rangle = \delta_{m_s^i,m_s^j}$. We can then translate the HF equations to space wavefunctions and obtain the following form

$$\begin{aligned} &-\frac{1}{2}\nabla r_i^2 \phi_i(\mathbf{r}_i) - \sum_{\alpha}^{nuc.} \frac{Z_\alpha}{r_{i\alpha}}\phi_i(\mathbf{r}_i) + \sum_j \int \phi_j^*(\mathbf{r}_j)\frac{1}{r_{ij}}\phi_j(\mathbf{r}_j)d\mathbf{r}_j\phi_i(\mathbf{r}_i) \\ &-\sum_j \int \phi_j^*(\mathbf{r}_j)\frac{1}{r_{ij}}\phi_i(\mathbf{r}_j)d\mathbf{r}_j\phi_j(\mathbf{r}_i) = E_i\phi_i(\mathbf{r}_i). \end{aligned} \tag{2.24}$$

We will use the HF equations to calculate the continuum wavefunctions of electrons which have escaped to the continuum via photoionization or Auger-Meitner decay. When solving for continuum electrons, we will solve the HF equations in terms of orbitals, rather than spin-orbitals. To do this we will take spin symmetries into account through the use of direct and exchange coefficients, labelled a_i and b_i, respectively. The HF equations then take the following form

$$\begin{aligned} &-\frac{1}{2}\nabla r_i^2 \phi_i(\mathbf{r}_i) - \sum_{\alpha}^{nuc.} \frac{Z_\alpha}{r_{i\alpha}}\phi_i(\mathbf{r}_i) + \sum_j^{orb.} a_j \int \phi_j^*(\mathbf{r}_j)\frac{1}{r_{ij}}\phi_j(\mathbf{r}_j)d\mathbf{r}_j\phi_i(\mathbf{r}_i) \\ &-\sum_j^{orb.} b_j \int \phi_j^*(\mathbf{r}_j)\frac{1}{r_{ij}}\phi_i(\mathbf{r}_j)d\mathbf{r}_j\phi_j(\mathbf{r}_i) = E_i\phi_i(\mathbf{r}_i), \end{aligned} \tag{2.25}$$

where $\phi_i(\mathbf{r})$ now refers to an orbital wavefunction. The direct coefficients a_i are simply the occupancy of the orbital i in the final state of the molecule. However, the values of the exchange coefficients b_i are not immediately obvious. In later sections we explain how to derive them depending on the transition and spin state we are dealing with.

2.1.3 CASSCF method

We will also utilise more accurate techniques to calculate atomic energies and potential energy curves (PECs). While the HF method only uses a single Slater de-

terminant, the multi-configuration self-consistent field (MCSCF) method [62] uses a linear combination of Slater determinants in order to account for electron excitations. In the MCSCF method, virtual orbitals are included in the active space. If all possible electronic configurations within the active space are included in the calculation, this is known as the complete active space self-consistent field (CASSCF) [63]. The coefficients of the Slater determinants and the active space orbitals are optimized to obtain the total electronic wavefunction with the lowest possible energy. Note that when performing CASSCF calculations, we initially perform a HF calculation of the ground state, which is used as an input to the CASSCF method.

2.1.4 MRCI method

In some cases, we can also utilise a further, more accurate technique called the multireference configuration interaction (MRCI) method [64–66]. While the CASSCF method includes all possible excitations only among active orbitals, the MRCI method allows single and double excitations from all active orbitals to all orbitals. This improves the description of the electron-electron repulsion [67]. When performing MRCI calculations, we first perform a CASSCF calculation to be used as an input to the MRCI method.

2.1.5 Single-center expansion

In order to simplify our calculations, we utilise the single-center expansion (SCE) method. In the SCE method, multi-centered molecular orbitals, $\phi_i(\mathbf{r})$, and continuum wavefunctions with energy ε, $\phi_\varepsilon(\mathbf{r})$, are expressed as an expansion over spherical harmonics $Y_{lm}(\theta,\phi)$

$$\begin{aligned}\phi_i(\mathbf{r}) &= \sum_{lm} \frac{P_{i,lm}(r)Y_{lm}(\theta,\phi)}{r} \\ \phi_\varepsilon(\mathbf{r}) &= \sum_{lm} \frac{P_{\varepsilon,lm}(r)Y_{lm}(\theta,\phi)}{r},\end{aligned} \tag{2.26}$$

where l and m are the angular momentum and magnetic quantum numbers, respectively. Spherical harmonics are analytical functions which form an orthonormal basis for the set of functions defined on the surface of a sphere. Projecting the angular

part of the wavefunction using analytic functions means we are only left to solve for the function $P_{lm}(r)$ with one spatial variable, namely r. Thus, we have simplified our system by reducing it from a multi-centred problem in three dimensions to a single-centered problem in one dimension. The $P_{lm}(r)$ are known as single-center coefficients (SCC). Let us multiply both sides of the molecular orbital expression in Eq. (2.26) by $Y^*_{l'm'}(\theta,\phi)$ and integrate over the solid angle $d\Omega = \sin\theta d\theta d\phi$

$$\int d\Omega Y^*_{l'm'}(\theta,\phi)\phi_i(\mathbf{r}) = \sum_{lm} \frac{P_{i,lm}(r)}{r} \int d\Omega Y^*_{l'm'}(\theta,\phi) Y_{lm}(\theta,\phi). \tag{2.27}$$

Using the orthonormality of spherical harmonics [68], this is equal to

$$\int d\Omega Y^*_{l'm'}(\theta,\phi)\phi_i(\mathbf{r}) = \sum_{lm} \frac{P_{i,lm}(r)}{r} \delta_{ll'}\delta_{mm'}. \tag{2.28}$$

Finally, if we sum over the Kronecker delta functions we are left with

$$P_{i,l'm'}(r) = r \int d\Omega Y^*_{l'm'}(\theta,\phi)\phi_i(\mathbf{r}). \tag{2.29}$$

Note that the SCE is an infinite sum over l and m. However, when either of these quantum numbers is conserved, this quantum number is a good quantum number and the summation collapses to a single value. In the case of atoms, both l and m are good quantum numbers. In the case of diatomic molecules, only m is a good quantum number. In this work, where we deal exclusively with diatomic molecules, we will use a single value of m and truncate the infinite sum over l to a suitable l_{max} where a sufficient level of convergence is reached.

2.2 Bound orbitals

2.2.1 Electron configuration of molecules

Molecular orbitals, formed by the linear combination of atomic orbitals, can be classified as either bonding or antibonding orbitals. A bonding orbital is a molecular orbital where the constructive interference of atomic orbitals increases electron density between nuclei, stabilizing the molecule and lowering its energy. Typically,

bonding orbitals are elongated along the internuclear axis. An antibonding orbital results from destructive interference, reducing electron density between the nuclei, destabilizing the molecule, and raising its energy. Antibonding orbitals are characterized by regions of higher electron density away from the internuclear region. Often an antibonding molecular orbital is designated by the superscript $*$.

If the orbital wavefunction satisfies $\psi(-r) = \psi(r)$, the function is classified as gerade or even parity, and the orbital designation is given a subscript g. If $\psi(-r) = -\psi(r)$, the function is classified as ungerade or odd parity, and the orbital designation is given a subscript u. Note that this parity classification only applies to homonuclear molecules, since they have inversion symmetry with respect to the centre of mass. For heteronuclear molecules, there is no inversion symmetry. For homonuclear diatomic molecules, the most likely order in which the molecular orbitals are filled is

$$1\sigma_g < 1\sigma_u < 2\sigma_g < 2\sigma_u < 3\sigma_g \sim 1\pi_u < 1\pi_g < 3\sigma_u, \tag{2.30}$$

where the relative order of the $3\sigma_g$ and $1\pi_u$ orbitals depend on which other molecular orbitals are occupied. For heteronuclear molecules the most likely order is

$$1\sigma < 2\sigma < 3\sigma < 4\sigma < 5\sigma \sim 1\pi < 2\pi < 6\sigma. \tag{2.31}$$

Note that we have only given the order of the first eight molecular orbitals, as these are the orbitals that are relevant to the molecules considered in this thesis. The representation of a molecular state can be given using spectroscopic notation. States of a molecule written in spectroscopic notation are of the following form

$$^{2S+1}\Lambda_{g/u}^{(+/-)}, \tag{2.32}$$

where $2S+1$ is the spin multiplicity, Λ is the projection of the orbital angular momentum along the internuclear axis and g/u the symmetry or parity with respect to inversion through a centre of symmetry. For Σ states only, we have an extra charac-

teristic: the reflection symmetry along an arbitrary plane containing the internuclear axis. The choice of symmetry planes is arbitrary. When an orbital is symmetric, it is labelled +. When an orbital is antisymmetric, it is labelled -. The spectroscopic notation of Σ states is then given as follows

$$^{2S+1}\Sigma^{(+/-)}_{g/u}. \tag{2.33}$$

Note that occasionally a letter or number will prefix a state's spectroscopic notation. This will indicate the energy of a state which possesses the same symmetry and multiplicity as other states. For example, an "X" will indicate that a state is the ground state of that ion.

2.2.2 Gaussian-type orbitals

We calculate the bound orbital wavefunctions used in our calculations using the quantum-chemistry package MOLPRO [69]. MOLPRO outputs these wavefunctions in the form of Gaussian-type orbitals (GTOs), centered around each atom of the molecule. In Cartesian coordinates, primitive Gaussians can be written in the following form

$$G^n(x,y,z;l_x,l_y,l_z,\alpha_n) = N^n_{l_x l_y l_z} d (x-x_c)^{l_x}(y-y_c)^{l_y}(z-z_c)^{l_z} e^{-\alpha_n[(x-x_c)^2+(y-y_c)^2+(z-z_c)^2]}, \tag{2.34}$$

where (x_c, y_c, z_c) is the position of atom n and $N^n_{l_x l_y l_z}$ is a normalization constant given by

$$N^n_{l_x l_y l_z} = \left(\frac{2\alpha_n}{\pi}\right)^{\frac{3}{4}} \left[\frac{(8\alpha_n)^{l_x+l_y+l_z} l!m!n!}{(2l_x)!(2l_y)!(2l_z)!}\right]^{\frac{1}{2}}. \tag{2.35}$$

The coefficients d and α_n are primitive and exponent coefficients, respectively. The values l_x, l_y and l_z represent the three components of the angular momentum. The sum of these values tells us the type of orbital, i.e. $l_x + l_y + l_z = 0$ for an s atomic orbital, $l_x + l_y + l_z = 1$ for a p atomic orbital, $l_x + l_y + l_z = 2$ for a d atomic orbital and so on. There is one possible primitive Gaussian such that $l_x + l_y + l_z = 0$, three primitive Gaussians such that $l_x + l_y + l_z = 1$ and so on. A linear combination of primitive Gaussians with the same symmetry forms a contracted Gaussian of the

form

$$\chi_j^n(x,y,z) = \sum_{l_x+l_y+l_z=k} w_{jk}^n G^n(x,y,z,l_x,l_y,l_z,\alpha_n), \tag{2.36}$$

where k is the symmetry of the orbital and w_{jk}^n are known as the contraction coefficients. A basis of contracted Gaussians are placed on each nuclei making up the component atoms of the molecule,

$$\psi_i^n(x,y,z) = \sum_j c_{ij}^n \chi_j^n(x,y,z), \tag{2.37}$$

where c_{ij}^n are the orbital coefficients for atom n. Finally, the total wavefunction of the molecular orbital i is the sum of these atomic orbital wavefunctions

$$\phi_i(x,y,z) = \sum_n^{nuc.} \psi_i^n(x,y,z). \tag{2.38}$$

When using MOLPRO, one must specify the basis set to be used in the calculations. The basis set determines the primitive, exponent and contraction coefficients. MOLPRO then produces the orbital coefficients using a method such as HF or CASSCF.

2.3 Continuum orbitals

From the HF equation in Eq. (2.25), to find the wavefunction of an electron which has escaped to the continuum we solve the following equation

$$\begin{aligned} &-\frac{1}{2}\nabla^2\phi_\varepsilon(\mathbf{r}) - \sum_\alpha^{nuc.} \frac{Z_\alpha}{|\mathbf{r}-\mathbf{R}_\alpha|}\phi_\varepsilon(\mathbf{r}) + \sum_i^{orb.} a_i \int d\mathbf{r}' \frac{\phi_i^*(\mathbf{r}')\phi_i(\mathbf{r}')}{|\mathbf{r}-\mathbf{r}'|}\phi_\varepsilon(\mathbf{r}) \\ &- \sum_i^{orb.} b_i \int d\mathbf{r}' \frac{\phi_i^*(\mathbf{r}')\phi_\varepsilon(\mathbf{r}')}{|\mathbf{r}-\mathbf{r}'|}\phi_i(\mathbf{r}) = \varepsilon\phi_\varepsilon(\mathbf{r}). \end{aligned} \tag{2.39}$$

The first term in Eq. (2.39) is the kinetic energy of the continuum electron, the second is the electron-nuclei interaction, the third describes the coulomb potential the continuum electron feels from the bound electrons and the fourth is the exchange

interaction. Substituting the SCEs from Eq. (2.26) into Eq. (2.39) gives

$$
\begin{aligned}
&-\frac{1}{2}\nabla^2\Big(\sum_{l'm'}\frac{P_{\varepsilon,l'm'}(r)}{r}Y_{l'm'}(\theta,\phi)\Big)-\sum_{\alpha}^{nuc.}\frac{Z_\alpha}{|\mathbf{r}-\mathbf{R}_\alpha|}\Big(\sum_{l'm'}\frac{P_{\varepsilon,l'm'}(r)}{r}Y_{l'm'}(\theta,\phi)\Big)\\
&+\sum_{i}^{orb.}a_i\int d\mathbf{r}'\frac{\phi_i^*(\mathbf{r}')\phi_i(\mathbf{r}')}{|\mathbf{r}-\mathbf{r}'|}\Big(\sum_{l'm'}\frac{P_{\varepsilon,l'm'}(r)}{r}Y_{l'm'}(\theta,\phi)\Big)\\
&-\sum_{i}^{orb.}b_i\int d\mathbf{r}'\frac{\phi_i^*(\mathbf{r}')\phi_\varepsilon(\mathbf{r}')}{|\mathbf{r}-\mathbf{r}'|}\Big(\sum_{l_3m_3}\frac{P_{i,l_3m_3}(r)}{r}Y_{l_3m_3}(\theta,\phi)\Big)=\varepsilon\phi_\varepsilon(\mathbf{r}).
\end{aligned}
\tag{2.40}
$$

Using the following definition of the Laplacian and properties of spherical harmonics

$$
\begin{aligned}
\nabla^2 f(r)&=\frac{1}{r^2}\frac{\partial}{\partial r}\Big(r^2\frac{\partial f}{\partial r}\Big)\\
r^2\nabla^2 Y_{lm}&=-l(l+1)Y_{lm},
\end{aligned}
\tag{2.41}
$$

the kinetic energy term becomes

$$
\begin{aligned}
&-\frac{1}{2}\nabla^2\Big(\sum_{l'm'}\frac{P_{\varepsilon,l'm'}(r)}{r}Y_{l'm'}(\theta,\phi)\Big)\\
&=-\frac{1}{2}\sum_{l'm'}\left[\nabla^2\left(\frac{P_{\varepsilon,l'm'}(r)}{r}\right)Y_{l'm'}(\theta,\phi)+\frac{P_{\varepsilon,l'm'}(r)}{r}\nabla^2 Y_{l'm'}(\theta,\phi)\right]\\
&=-\frac{1}{2}\sum_{l'm'}\left[\frac{1}{r^2}\frac{d}{dr}\Big(-P_{\varepsilon,l'm'}(r)+r\frac{d}{dr}P_{\varepsilon,l'm'}(r)\Big)Y_{l'm'}(\theta,\phi)-\frac{1}{r^3}l'(l'+1)P_{\varepsilon,l'm'}(r)Y_{l'm'}(\theta,\phi)\right]\\
&=-\frac{1}{2}\sum_{l'm'}\left[\Big(-\frac{1}{r^2}\frac{d}{dr}P_{\varepsilon,l'm'}(r)+\frac{1}{r^2}\frac{d}{dr}P_{\varepsilon,l'm'}(r)+\frac{1}{r}\frac{d^2}{dr^2}P_{\varepsilon,l'm'}(r)\Big)Y_{l'm'}(\theta,\phi)\right.\\
&\left.-\frac{1}{r^3}l'(l'+1)P_{\varepsilon,l'm'}(r)Y_{l'm'}(\theta,\phi)\right]\\
&=\frac{1}{r}\sum_{l'm'}\left[-\frac{1}{2}\frac{d^2}{dr^2}+\frac{l'(l'+1)}{2r^2}\right]P_{\varepsilon,l'm'}(r)Y_{l'm'}(\theta,\phi).
\end{aligned}
\tag{2.42}
$$

We multiply by r to obtain the following

$$\sum_{l'm'}\Bigg[\Big(-\frac{1}{2}\frac{d^2}{dr^2}+\frac{l'(l'+1)}{2r^2}-\varepsilon+\sum_{\alpha}^{nuc.}\frac{-Z_\alpha}{|\mathbf{r}-\mathbf{R}_\alpha|} \\ +\sum_{i}^{orb.}a_i\int d\mathbf{r}'\frac{\phi_i^*(\mathbf{r}')\phi_i(\mathbf{r}')}{|\mathbf{r}-\mathbf{r}'|}\Big)P_{\varepsilon,l'm'}(r)Y_{l'm'}(\theta,\phi) \\ -\sum_{i}^{orb.}b_i\int d\mathbf{r}'\frac{\phi_i^*(\mathbf{r}')\phi_\varepsilon(\mathbf{r}')}{|\mathbf{r}-\mathbf{r}'|}\sum_{l_3m_3}P_{i,l_3m_3}(r)Y_{l_3m_3}(\theta,\phi)\Bigg]=0. \tag{2.43}$$

Spherical harmonics are orthonormal, i.e.

$$\int Y_{lm}^*(\theta,\phi)Y_{l'm'}(\theta,\phi)d\Omega=\delta_{ll'}\delta_{mm'}, \tag{2.44}$$

where $d\Omega=\sin\theta d\theta d\phi$. Multiplying Eq. (2.43) by the complex-conjugate spherical harmonic, $Y_{lm}^*(\theta,\phi)$, and integrating over the solid angle gives

$$\int Y_{lm}^*(\theta,\phi)\sum_{l'm'}\Bigg[\Big(-\frac{1}{2}\frac{d^2}{dr^2}+\frac{l'(l'+1)}{2r^2}-\varepsilon+\sum_{\alpha}^{nuc.}\frac{-Z_\alpha}{|\mathbf{r}-\mathbf{R}_\alpha|} \\ +\sum_{i}^{orb.}a_i\int d\mathbf{r}'\frac{\phi_i^*(\mathbf{r}')\phi_i(\mathbf{r}')}{|\mathbf{r}-\mathbf{r}'|}\Big)P_{\varepsilon,l'm'}(r)Y_{l'm'}(\theta,\phi) \\ -\sum_{i}^{orb.}b_i\int d\mathbf{r}'\frac{\phi_i^*(\mathbf{r}')\phi_\varepsilon(\mathbf{r}')}{|\mathbf{r}-\mathbf{r}'|}\sum_{l_3m_3}P_{i,l_3m_3}(r)Y_{l_3m_3}(\theta,\phi)\Bigg]d\Omega=0. \tag{2.45}$$

For convenience from here onwards we map $b_i\rightarrow -b_i$ so that the exchange term is positive. Using Eq. (2.44) and abbreviating each term gives

$$\sum_{l'm'}\Bigg[\Big(-\frac{d^2}{dr^2}+\frac{l'(l'+1)}{r^2}-2\varepsilon\Big)\delta_{ll'}\delta_{mm'}+2V_{lm,l'm'}^{ne}(r)+2J_{lm,l'm'}^{ee}(r)\Bigg]P_{\varepsilon,l'm'}(r) \\ +2X_{lm}[\bar{P}_\varepsilon](r)=0. \tag{2.46}$$

We will look separately at each of these abbreviated terms. We introduce two formulas which are used in the derivations that follow. Firstly, the Laplace multipole

expansion [68] (see Appendix A) is given by

$$\frac{1}{|\mathbf{r}-\mathbf{r}'|} = \sum_{kq} \frac{4\pi}{2k+1} \frac{r_<^k}{r_>^{k+1}} Y_{kq}(\theta,\phi) Y_{kq}^*(\theta',\phi'), \tag{2.47}$$

where $r_< = \min(r,r')$ and $r_> = \max(r,r')$. The other equation we require is the Wigner-3j representation of the integral of a triple product of spherical harmonics [68] (see Appendix B)

$$\begin{aligned}\int Y_{lm}(\theta,\phi) Y_{kq}(\theta,\phi) Y_{l'm'}(\theta,\phi) d\Omega = \sqrt{\frac{(2l+1)(2k+1)(2l'+1)}{4\pi}} \\ \times \begin{pmatrix} l & k & l' \\ 0 & 0 & 0 \end{pmatrix} \begin{pmatrix} l & k & l' \\ m & q & m' \end{pmatrix}.\end{aligned} \tag{2.48}$$

2.3.1 Electron-nuclei interaction

The fourth term in Eq. (2.46) is

$$V^{ne}_{lm,l'm'}(r) = \int Y_{lm}^*(\theta,\phi) \sum_{\alpha}^{nuc.} \frac{-Z_\alpha}{|\mathbf{r}-\mathbf{R}_\alpha|} Y_{l'm'}(\theta,\phi) d\Omega, \tag{2.49}$$

which describes the Coulombic interaction between the nuclei and continuum electron. Substituting Eq. (2.47) into this gives

$$\begin{aligned} V^{ne}_{lm,l'm'}(r) &= \int Y_{lm}^*(\theta,\phi) \sum_{\alpha}^{nuc.} -Z_\alpha \Big(\sum_{kq} \frac{4\pi}{2k+1} \frac{r_<^k}{r_>^{k+1}} Y_{kq}(\theta,\phi) Y_{kq}^*(\theta_\alpha,\phi_\alpha) \Big) Y_{l'm'}(\theta,\phi) d\Omega \\ &= \sum_{\alpha}^{nuc.} -Z_\alpha \sum_{kq} \frac{4\pi}{2k+1} \frac{r_<^k}{r_>^{k+1}} Y_{kq}^*(\theta_\alpha,\phi_\alpha) \int Y_{lm}^*(\theta,\phi) Y_{kq}(\theta,\phi) Y_{l'm'}(\theta,\phi) d\Omega. \end{aligned} \tag{2.50}$$

Then using Eq. (2.48) and the property of spherical harmonics that $Y^*_{lm}(\theta,\phi) = (-1)^m Y_{l-m}(\theta,\phi)$ we have

$$\begin{aligned} V^{ne}_{lm,l'm'}(r) &= \sum_{\alpha}^{nuc.} -Z_\alpha (-1)^m \sqrt{(2l+1)(2l'+1)} \\ &\times \sum_{kq} \sqrt{\frac{(2k+1)}{4\pi}} \begin{pmatrix} l & k & l' \\ 0 & 0 & 0 \end{pmatrix} \begin{pmatrix} l & k & l' \\ -m & q & m' \end{pmatrix} \frac{4\pi}{2k+1} \frac{r^k_<}{r^{k+1}_>} Y^*_{kq}(\theta_\alpha,\phi_\alpha) \\ &= \sum_{\alpha}^{nuc.} -Z_\alpha (-1)^m \sqrt{(2l+1)(2l'+1)} \sum_{kq} \begin{pmatrix} l & k & l' \\ 0 & 0 & 0 \end{pmatrix} \begin{pmatrix} l & k & l' \\ -m & q & m' \end{pmatrix} \\ &\times \sqrt{\frac{4\pi}{2k+1}} \frac{r^k_<}{r^{k+1}_>} Y^*_{kq}(\theta_\alpha,\phi_\alpha). \end{aligned} \tag{2.51}$$

Note that for diatomic molecules, since the projection of the angular momentum is a good quantum number, we have that $m' = m$. Hence, from the second Wigner-3j symbol, $q = m - m' = 0$. For a homonuclear molecule, given $q = 0$ we have for one nucleus $\sqrt{\frac{4\pi}{2k+1}} Y^*_{k0}(0,0) = 1$ and for the other nucleus $\sqrt{\frac{4\pi}{2k+1}} Y^*_{k0}(\pi,0) = (-1)^k$. Hence, the sum of these two terms in Eq. (2.51) is zero unless k is even. That is, k takes only even values.

2.3.2 Direct interaction

The fifth term in Eq. (2.46) is

$$J^{ee}_{lm,l'm'}(r) = \int Y^*_{lm}(\theta,\phi) \sum_i^{orb.} a_i \int d\mathbf{r}' \frac{\phi^*_i(\mathbf{r}')\phi_i(\mathbf{r}')}{|\mathbf{r}-\mathbf{r}'|} Y_{l'm'}(\theta,\phi) d\Omega. \tag{2.52}$$

Again using Eq. (2.46) and expanding the orbitals by Eq. (2.26) gives

$$
\begin{aligned}
J^{ee}_{lm,l'm'}(r) &= \int Y^*_{lm}(\theta,\phi)\sum_i^{orb.} a_i \\
&\times \int d\mathbf{r}'\Big(\sum_{l_2m_2}\frac{P^*_{i,l_2m_2}(r')Y^*_{l_2m_2}(\theta',\phi')}{r'}\Big)\Big(\sum_{l_3m_3}\frac{P_{i,l_3m_3}(r')Y_{l_3m_3}(\theta',\phi')}{r'}\Big) \\
&\times \Big(\sum_{kq}\frac{4\pi}{2k+1}\frac{r^k_<}{r^{k+1}_>}Y_{kq}(\theta,\phi)Y^*_{kq}(\theta',\phi')\Big)Y_{l'm'}(\theta,\phi)d\Omega \\
&= \int Y^*_{lm}(\theta,\phi)\sum_i^{orb.} a_i \int_0^{2\pi}\int_0^{\pi}\int_0^{\infty}\Big(\sum_{l_2m_2}\frac{P^*_{i,l_2m_2}(r')Y^*_{l_2m_2}(\theta',\phi')}{r'}\Big) \\
&\times \Big(\sum_{l_3m_3}\frac{P_{i,l_3m_3}(r')Y_{l_3m_3}(\theta',\phi')}{r'}\Big)(r')^2\sin\theta' dr' d\theta' d\phi' \\
&\times \Big(\sum_{kq}\frac{4\pi}{2k+1}\frac{r^k_<}{r^{k+1}_>}Y_{kq}(\theta,\phi)Y^*_{kq}(\theta',\phi')\Big)Y_{l'm'}(\theta,\phi)d\Omega \\
&= \sum_i^{orb.} a_i \sum_{l_2m_2}\sum_{l_3m_3}\sum_{kq}\frac{4\pi}{2k+1}\int Y^*_{l_2m_2}(\theta',\phi')Y_{kq}(\theta',\phi')Y_{l_3m_3}(\theta',\phi')d\Omega' \\
&\times \int Y^*_{lm}(\theta,\phi)Y^*_{kq}(\theta,\phi)Y_{l'm'}(\theta,\phi)d\Omega\int_0^{\infty}\frac{r^k_<}{r^{k+1}_>}P^*_{i,l_2m_2}(r')P_{i,l_3m_3}(r')dr',
\end{aligned}
\tag{2.53}
$$

where $d\Omega' = \sin\theta' d\theta' \phi'$ and we have utilised a property of the addition theorem of spherical harmonics, namely

$$
\sum_{kq} Y_{kq}(\theta,\phi)Y^*_{kq}(\theta',\phi') = \sum_{kq} Y^*_{kq}(\theta,\phi)Y_{kq}(\theta',\phi'). \tag{2.54}
$$

Again, using Eq. (2.48) and the following property of spherical harmonics

$$
Y^*_{lm}(\theta,\phi) = (-1)^m Y_{l-m}(\theta,\phi), \tag{2.55}
$$

we have the following

$$
\begin{aligned}
J^{ee}_{lm,l'm'}(r) &= \sum_i^{orb.} a_i \sum_{l_2m_2} \sum_{l_3m_3} \sum_{kq} \frac{4\pi}{2k+1}(-1)^{m+m_2+q} \\
&\times \sqrt{\frac{(2l_2+1)(2k+1)(2l_3+1)}{4\pi}} \begin{pmatrix} l_2 & k & l_3 \\ 0 & 0 & 0 \end{pmatrix} \begin{pmatrix} l_2 & k & l_3 \\ -m_2 & q & m_3 \end{pmatrix} \\
&\times \sqrt{\frac{(2l+1)(2k+1)(2l'+1)}{4\pi}} \begin{pmatrix} l & k & l' \\ 0 & 0 & 0 \end{pmatrix} \begin{pmatrix} l & k & l' \\ -m & -q & m' \end{pmatrix} \\
&\times \int_0^\infty \frac{r_<^k}{r_>^{k+1}} P^*_{i,l_2m_2}(r') P_{i,l_3m_3}(r') dr' \\
&= \sum_i^{orb.} a_i \sum_{l_2m_2} \sum_{l_3m_3} \sum_{kq} (-1)^{m+m_2+q} \sqrt{(2l+1)(2l'+1)(2l_2+1)(2l_3+1)} \\
&\times \begin{pmatrix} l_2 & k & l_3 \\ 0 & 0 & 0 \end{pmatrix} \begin{pmatrix} l_2 & k & l_3 \\ -m_2 & q & m_3 \end{pmatrix} \begin{pmatrix} l & k & l' \\ 0 & 0 & 0 \end{pmatrix} \begin{pmatrix} l & k & l' \\ -m & -q & m' \end{pmatrix} \\
&\times \int_0^\infty \frac{r_<^k}{r_>^{k+1}} P^*_{i,l_2m_2}(r') P_{i,l_3m_3}(r') dr'.
\end{aligned}
\tag{2.56}
$$

Wigner-3j symbols have the following symmetry relations

$$
\begin{aligned}
\begin{pmatrix} l & k & l' \\ m & q & m' \end{pmatrix} &= (-1)^{(l+k+l')} \begin{pmatrix} l & k & l' \\ -m & -q & -m' \end{pmatrix} \\
\begin{pmatrix} l & k & l' \\ m & q & m' \end{pmatrix} &= (-1)^{(l+k+l')} \begin{pmatrix} k & l & l' \\ q & m & m' \end{pmatrix}.
\end{aligned}
\tag{2.57}
$$

So the direct interaction becomes

$$J^{ee}_{lm,l'm'}(r) = \sum_{i}^{orb.} a_i \sum_{l_2m_2} \sum_{l_3m_3} \sum_{kq} (-1)^{m'+m_2} \sqrt{(2l+1)(2l'+1)(2l_2+1)(2l_3+1)} \\ \times \begin{pmatrix} l_2 & k & l_3 \\ 0 & 0 & 0 \end{pmatrix} \begin{pmatrix} l_2 & k & l_3 \\ -m_2 & q & m_3 \end{pmatrix} \begin{pmatrix} l' & k & l \\ 0 & 0 & 0 \end{pmatrix} \begin{pmatrix} l' & k & l \\ -m' & q & m \end{pmatrix} \\ \times \int_0^\infty \frac{r_<^k}{r_>^{k+1}} P^*_{i,l_2m_2}(r') P_{i,l_3m_3}(r') dr', \tag{2.58}$$

where we have used the fact that $-m' + q + m = 0$ (the sum of the bottom row of a Wigner-3j must equal zero). Similarly to the electron-nuclei interaction, since the projection of the angular momentum is a good quantum number, we have that $m' = m$, $m_2 = m_3$ and $q = m_2 - m_3 = 0$. In addition, the Wigner-3j $\begin{pmatrix} l_2 & k & l_3 \\ 0 & 0 & 0 \end{pmatrix}$ in Eq. (2.58) is non-zero only when $l_2 + k + l_3$ is even. Also, l_2 and l_3 are quantum numbers corresponding to a certain bound orbital. However, for homonuclear molecules there is inversion symmetry and hence the l_2 and l_3 are either even or odd. As a result, k is even.

2.3.3 Exchange interaction

The final term in Eq. (2.46) is

$$X_{lm}[\bar{P}_\varepsilon](r) = \int Y^*_{lm}(\theta,\phi) \sum_{l'm'} \sum_{i}^{orb.} b_i \int d\mathbf{r}' \frac{\phi_i^*(\mathbf{r}')\phi_\varepsilon(\mathbf{r}')}{|\mathbf{r}-\mathbf{r}'|} \sum_{l_3m_3} P_{i,l_3m_3}(r) Y_{l_3m_3}(\theta,\phi) d\Omega. \tag{2.59}$$

This term describes a quantum mechanical effect which occurs between indistinguishable particles of the same spin. Again using Eq. (2.47) and expanding the

orbitals we have

$$
\begin{aligned}
X_{lm}[\bar{P}_\varepsilon](r) = & \sum_{l'm'}\sum_{i}^{orb.} b_i \sum_{l_2m_2,l_3m_3,kq} \int Y^*_{lm}(\theta,\phi) \\
& \times \int d\mathbf{r}' \frac{4\pi}{2k+1}\frac{r^k_<}{r^{k+1}_>} Y_{kq}(\theta,\phi) Y^*_{kq}(\theta',\phi') \\
& \times \left(\frac{P^*_{i,l_2m_2}(r')Y^*_{l_2m_2}(\theta',\phi')}{r'}\right)\left(\frac{P_{\varepsilon,l'm'}(r')Y_{l'm'}(\theta',\phi')}{r'}\right) \\
& \times P_{i,l_3m_3}(r) Y_{l_3m_3}(\theta,\phi) d\Omega \\
= & \sum_{l'm'}\sum_{i}^{orb.} b_i \sum_{l_2m_2,l_3m_3,kq} \frac{4\pi}{2k+1} \int Y^*_{lm}(\theta,\phi) Y_{kq}(\theta,\phi) Y_{l_3m_3}(\theta,\phi) d\Omega \\
& \times \int Y^*_{l_2m_2}(\theta',\phi') Y^*_{kq}(\theta',\phi') Y_{l'm'}(\theta',\phi') d\Omega' \\
& \times \int_0^\infty \frac{r^k_<}{r^{k+1}_>} P^*_{i,l_2m_2}(r') P_{\varepsilon,l'm'}(r') dr' P_{i,l_3m_3}(r) \\
= & \sum_{l'm'}\sum_{i}^{orb.} b_i \sum_{l_2m_2,l_3m_3,kq} \frac{4\pi}{2k+1} \int Y^*_{lm}(\theta,\phi) Y^*_{kq}(\theta,\phi) Y_{l_3m_3}(\theta,\phi) d\Omega \\
& \times \int Y^*_{l_2m_2}(\theta',\phi') Y_{kq}(\theta',\phi') Y_{l'm'}(\theta',\phi') d\Omega' \\
& \times \int_0^\infty \frac{r^k_<}{r^{k+1}_>} P^*_{i,l_2m_2}(r') P_{\varepsilon,l'm'}(r') dr' P_{i,l_3m_3}(r),
\end{aligned}
\tag{2.60}
$$

where $d\Omega' = \sin\theta' d\theta' \phi'$ and again we have used the addition theorem of spherical harmonics. Then using the same techniques as for the direct interaction (properties of spherical harmonics and Wigner-3j symbols) we have

$$
\begin{aligned}
X_{lm}[\bar{P}_\varepsilon](r) = = & \sum_{l'm'}\sum_{i}^{orb.} b_i \sum_{l_2m_2}\sum_{l_3m_3}\sum_{kq} (-1)^{m_2+m_3} \sqrt{(2l+1)(2l'+1)(2l_2+1)(2l_3+1)} \\
& \times \begin{pmatrix} l_2 & k & l' \\ 0 & 0 & 0 \end{pmatrix} \begin{pmatrix} l_2 & k & l' \\ -m_2 & q & m' \end{pmatrix} \begin{pmatrix} l_3 & k & l \\ 0 & 0 & 0 \end{pmatrix} \begin{pmatrix} l_3 & k & l \\ -m_3 & q & m \end{pmatrix} \\
& \times \int_0^\infty \frac{r^k_<}{r^{k+1}_>} P^*_{i,l_2m_2}(r') P_{\varepsilon,l'm'}(r') dr' P_{i,l_3m_3}(r).
\end{aligned}
\tag{2.61}
$$

From the Wigner-3j symbols in Eq. (2.61), $q = m_2 - m' = m_3 - m$. For diatomic molecules, the projection of the angular momentum is a good quantum number and

hence $m' = m$ and $m_2 = m_3$. From the Wigner-3j symbol $\begin{pmatrix} l_3 & k & l \\ 0 & 0 & 0 \end{pmatrix}$ in Eq. (2.61), we see that this is non-zero if $l_3 + k + l$ is even. Since l_3 and l are quantum numbers of the bound and continuum orbital, $l + l_3$ can be even or odd. Hence, k can be even or odd.

2.3.4 Matrix form of the differential equation

Firstly, we rearrange Eq. (2.46)

$$\begin{aligned} \frac{d^2 P_{\varepsilon,lm}(r)}{dr^2} = \sum_{l'm'} \Bigg[\Big(\frac{l'(l'+1)}{2r^2} - 2\varepsilon \Big) \delta_{ll'} \delta_{mm'} \\ + 2V^{ne}_{lm,l'm'}(r) + 2J^{ee}_{lm,l'm'}(r) \Bigg] P_{\varepsilon,l'm'}(r) + 2X_{lm}[\bar{P}_\varepsilon](r). \end{aligned} \tag{2.62}$$

We define the solution vector $\bar{P} = \{P_{lm}\}$. The exchange vector, $\bar{X}$, is defined as

$$\bar{X} = \{X_{lm}\} = 2X_{lm}[\bar{P}_\varepsilon](r), \tag{2.63}$$

and the matrix, $\hat{M}$, as

$$\hat{M} = \{M_{lm,l'm'}\} = \Big(\frac{l'(l'+1)}{2r^2} - 2\varepsilon \Big) \delta_{ll'} \delta_{mm'} + 2V^{ne}_{lm,l'm'}(r) + 2J^{ee}_{lm,l'm'}(r). \tag{2.64}$$

Then, Eq. (2.62) can be simplified to the following second order differential equation

$$\frac{d^2 \bar{P}}{dr^2} = \hat{M}\bar{P} + \bar{X}. \tag{2.65}$$

2.3.5 Asymptotics and normalization

In order to solve the HF equations, we need to understand the boundary conditions. The constraints on our integro-differential matrix equation are the following boundary conditions

$$P_{\varepsilon,lm}(r \to 0) \to 0, \tag{2.66}$$

for all l, m. Furthermore, the continuum radial functions should satisfy the normalization condition

$$\begin{aligned}\left\langle P_{\varepsilon_1}^{LM} \middle| P_{\varepsilon_2}^{LM} \right\rangle &= \int_0^\infty dr \sum_{lm} P_{\varepsilon_1,lm}^{*LM}(r) P_{\varepsilon_2,lm}^{LM}(r) \\ &= \delta(\varepsilon_1 - \varepsilon_2).\end{aligned} \tag{2.67}$$

We add the additional superscript LM to discern the different energy degenerate solutions. One can show that the continuum radial functions satisfy the following asymptotic condition [70]

$$P_{\varepsilon,lm}^{LM}(r \to \infty) \to \mathcal{F}_L(r;k)\delta_{l,L}\delta_{m,M} + \mathcal{G}_L(r;k)R_{lm,LM}, \tag{2.68}$$

where $k = \sqrt{2\varepsilon}$ and $\mathcal{F}_L(r;k)$, $\mathcal{G}_L(r;k)$ are energy normalized regular and irregular Coulomb functions, respectively, see Refs. [71, 72]. The regular Coulomb function corresponds to the solution of a point charge. The irregular Coulomb function corresponds to the distortion of the solution from that of a single point charge. The latter is present in a molecule since there is no spherical symmetry. The elements of the hermitian reaction matrix, $R_{l'm',L'M'}$, reflect the deviation from the solution corresponding to a single point charge. Substituting the asymptotic form in Eq. (2.68) into the inner product of the solution vector and using orthogonality of the Coulomb functions, we have

$$\begin{aligned}\left\langle P_{\varepsilon_1}^{LM} \middle| P_{\varepsilon_2}^{L'M'} \right\rangle &= \int_0^\infty dr \sum_{lm} P_{\varepsilon_1,lm}^{*LM}(r) P_{\varepsilon_2,lm}^{L'M'}(r) \\ &= \int_0^\infty dr \sum_{lm} (\mathcal{F}_{L'}^*(r;k_1)\delta_{l,L}\delta_{m,M} + \mathcal{G}_L^*(r;k_1)R_{lm,LM}) \\ &\times (\mathcal{F}_{L'}(r;k_2)\delta_{l,L'}\delta_{m,M'} + \mathcal{G}_L(r;k_2)R_{lm,L'M'}) \\ &= \delta(\varepsilon_1 - \varepsilon_2)\left(\delta_{L'}^L \delta_{M'}^M + \sum_{lm} R_{lm}^{LM} R_{lm}^{L'M'}\right).\end{aligned} \tag{2.69}$$

The energy normalized solutions, $\mathcal{P}^{LM}_{\varepsilon,lm}(r)$, can be obtained from the unnormalized radial functions $P^{LM}_{\varepsilon,lm}(r)$ using the following transformations

$$P^{L''M''}_{\varepsilon,lm}(r) = \cos\phi_{L''M''} \sum_{L'M'} U_{L'M',L''M''} P^{L'M'}_{\varepsilon,lm}(r) \tag{2.70}$$

$$\mathcal{P}^{LM}_{\varepsilon,lm}(r) = \sum_{L''M''} e^{-i\phi_{L''M''}} U_{LM,L''M''} P^{L''M''}_{\varepsilon,lm}(r), \tag{2.71}$$

where the phaseshifts ϕ_{LM} and matrix $U_{LM,L'M'}$ are found by solving the eigenvalue problem

$$\sum_{L'M'} R_{lm,L'M'} U_{L'M',LM} = \tan\phi_{LM} U_{lm,LM}. \tag{2.72}$$

In order to illustrate that the eigenvalues of the reaction matrix $\hat{R}$ have the form of $\tan\phi_{LM}$, we obtain the eigenvalues of $\hat{R}$ for the much simpler atomic case. This is is significantly simpler than a molecule because the L channels do not mix. In the atomic case, the asymptotic form of the wavefunction that satisfies the incoming wave boundary conditions is of the form [73]

$$\Psi_{lm}(\mathbf{r}';k) \to (\frac{1}{\pi k})^{\frac{1}{2}} \frac{1}{2ir} \times [e^{ix_l} - S^*_l(k) e^{-ix_l}] Y_{lm}(\hat{r}'), \tag{2.73}$$

where

$$x_l = kr - \frac{1}{2} l\pi - \frac{Z}{k}\log(2kr) + \sigma_l \tag{2.74}$$

$$\sigma_l = \arg\Gamma(l+1-\frac{Z}{k}). \tag{2.75}$$

and Z is the net charge on the ion core. The scattering amplitude, S_l, can be related to the scattering phaseshift, ϕ_l, by $S_l = \exp(2i\phi_l)$. Expanding Eq. (2.73) and substituting for S_l, one can easily show

$$e^{ix_l} - S^*_l(k) e^{-ix_l} = i(1+S^*_l)(\sin x_l - i\frac{1-S^*_l}{1+S^*_l}\cos x_l) \to \sin x_l + \tan\phi_l \cos x_l. \tag{2.76}$$

Now, we relate $\sin x_l$ and $\cos x_l$ with the Coulomb functions $\mathcal{F}_l$ and $\mathcal{G}_l$. We do so using Ref. [71], where we find that when $r \to \infty$ we have

$$G_l(r;k) + iF_l(r;k) \to \exp(x_l). \tag{2.77}$$

From the above it is clear that the asymptotic form of $\mathcal{F}_l$ coincides with $\sin x_l$ and the asymptotic form of $\mathcal{G}_l$ coincides with $\cos x_l$. Hence, the eigenvalues of the reaction matrix $\hat{R}$ are indeed $\tan\phi_l$ for the atom case.

2.3.6 Grid points

The integro-differential matrix equation in Eq. (2.65) becomes singular at $r = 0$ (the centrifugal term becomes singular) and at the positions of the nuclei (the electrostatic attraction of the nuclei becomes singular). These singularities are dealt with by increasing the density of grid points at these positions and lowering the density of grid points where the effective potential is small. We do this by mapping the grid r to the grid ρ, where

$$\rho(r) = \alpha r + \beta ln(r) + \sum_{i}^{nuc.} \arctan\frac{R_i - r}{\gamma_i}, \tag{2.78}$$

for positive constants α, β and γ_i. The new renormalized solution is

$$F_{lm}(\rho) = \sqrt{\frac{d\rho(r)}{dr}} P_{lm}(r) = \sqrt{\rho'} P_{lm}(r). \tag{2.79}$$

The double differential of the renormalized solution is

$$\begin{aligned}
\frac{d^2F_{lm}(\rho)}{d\rho^2} &= \frac{d}{d\rho}\left(\frac{dF_{lm}(\rho)}{dr}\frac{dr}{d\rho}\right) \\
&= \frac{d}{d\rho}\left[\frac{d}{dr}\left(\sqrt{\rho'}P_{lm}(r)\right)\frac{1}{\rho'}\right] \\
&= \frac{1}{\rho'}\frac{d}{dr}\left[\frac{1}{2}\frac{1}{(\rho')^{\frac{3}{2}}}\rho''P_{lm}(r)+\frac{1}{\sqrt{\rho'}}\frac{d}{dr}P_{lm}(r)\right] \\
&= \frac{1}{\rho'}\left[-\frac{3}{4}\frac{1}{(\rho')^{\frac{5}{2}}}(\rho'')^2P_{lm}(r)+\frac{1}{2}\frac{1}{(\rho')^{\frac{3}{2}}}\rho'''P_{lm}(r)\right. \\
&\left.+\frac{1}{2}\frac{1}{(\rho')^{\frac{3}{2}}}\rho''\frac{d}{dr}P_{lm}(r)-\frac{1}{2}\frac{1}{(\rho')^{\frac{3}{2}}}\rho''\frac{d}{dr}P_{lm}(r)+\frac{1}{\sqrt{\rho'}}\frac{d^2}{dr^2}P_{lm}(r)\right] \\
&= \frac{1}{(\rho')^2}\left[\frac{1}{2}\frac{\rho'''}{\rho'}-\frac{3}{4}\frac{(\rho'')^2}{(\rho')^2}\right]F_{lm}(\rho)+\frac{1}{(\rho')^{\frac{3}{2}}}\frac{d^2}{dr^2}P_{lm}(r).
\end{aligned} \tag{2.80}$$

Hence, the differential equation becomes

$$\begin{aligned}
\frac{d^2F_{\varepsilon,lm}(\rho)}{d\rho^2} = \frac{1}{(\rho')^2}\sum_{l'm'}\Bigg[&\left(\frac{l'(l'+1)}{r(\rho)^2}-2\varepsilon\right)\delta_{ll'}\delta_{mm'}+2V^{ne}_{lm,l'm'}(r(\rho)) \\
&+2J^{ee}_{lm,l'm'}(r(\rho))+\left(\frac{1}{2}\frac{\rho'''}{\rho'}-\frac{3}{4}\frac{(\rho'')^2}{(\rho')^2}\right)\delta_{ll'}\delta_{mm'}\Bigg]F_{\varepsilon,l'm'}(\rho) \\
&+\frac{1}{(\rho')^2}2X_{lm}[\bar{F}_\varepsilon](\rho).
\end{aligned} \tag{2.81}$$

This is equivalent to the following in matrix form

$$\frac{d^2\bar{F}}{dr^2} = \frac{1}{(\rho')^2}\left[\hat{M}^\rho\bar{F}+\bar{X}^\rho\right], \tag{2.82}$$

where

$$\begin{aligned}
\bar{F} &= \{F_{lm}\} \\
\hat{M}^{\rho} &= \{M^{\rho}_{lm,l'm'}\} \\
&= \left(\frac{l'(l'+1)}{2r(\rho)^2} - 2\varepsilon\right)\delta_{ll'}\delta_{mm'} + 2V^{ne}_{lm,l'm'}(r(\rho)) + 2J^{ee}_{lm,l'm'}(r(\rho)) \\
&+ \left(\frac{1}{2}\frac{\rho'''}{\rho'} - \frac{3}{4}\frac{(\rho'')^2}{(\rho')^2}\right)\delta_{ll'}\delta_{mm'} \\
\bar{X}^{\rho} &= \{X^{\rho}_{lm}\} \\
&= 2X_{lm}[\bar{F}_{\varepsilon}](\rho).
\end{aligned} \tag{2.83}$$

2.3.7 Coupling differential equations

While it is possible to solve Eq. (2.82) for $\bar{F}$, we would encounter a few key issues. Since the system of equations we wish to solve contains terms which depend on the solution, the method in which we solve for $\bar{F}$ will be iterative. This is computationally intensive since one must recompute integrals which depend on the solution, i.e. the continuum wavefunction, at every iteration.

In this section, we couple two separate second order differential equations together, resulting in a single system of second order differential equations. This new system of equations does not contain any terms which depend on the solution. Hence, the solution can be found non-iteratively. This method was developed by Demekhin et al., see Ref. [74]. We begin by defining the function

$$\begin{aligned}
Y_k(P_1,P_2) &= r\int \frac{r^k_<}{r^{k+1}_>} P_1^*(r')P_2(r')dr' \\
&= r\int_0^r \frac{(r')^k}{r^{k+1}} P_1^*(r')P_2(r')dr' + r\int_r^{\infty} \frac{r^k}{(r')^{k+1}} P_1^*(r')P_2(r')dr'.
\end{aligned} \tag{2.84}$$

We find that the first and second derivatives of $Y_k(P_1,P_2)$ are

$$\begin{aligned}
\frac{d}{dr}Y_k(P_1,P_2) &= -k\int_0^r \frac{(r')^k}{r^{k+1}}P_1^*(r')P_2(r')dr' \\
&\quad + P_1^*(r)P_2(r) \\
&\quad + (k+1)\int_r^\infty \frac{r^k}{(r')^{k+1}}P_1^*(r')P_2(r')dr' \\
&\quad - P_1^*(r)P_2(r) \\
&= -k\int_0^r \frac{(r')^k}{r^{k+1}}P_1^*(r')P_2(r')dr' \\
&\quad + (k+1)\int_r^\infty \frac{r^k}{(r')^{k+1}}P_1^*(r')P_2(r')dr' \qquad (2.85) \\
,\frac{d^2}{dr^2}Y_k(P_1,P_2) &= k(k+1)\int_0^r \frac{(r')^k}{r^{k+2}}P_1^*(r')P_2(r')dr' \\
&\quad - \frac{k}{r}P_1^*(r)P_2(r) \\
&\quad + k(k+1)\int_r^\infty \frac{r^{k-1}}{(r')^{k+1}}P_1^*(r')P_2(r')dr' \\
&\quad - \frac{(k+1)}{r}P_1^*(r)P_2(r) \\
&= \frac{k(k+1)}{r^2}Y_k(P_1,P_2) - \frac{(2k+1)}{r}P_1^*(r)P_2(r).
\end{aligned}$$

Hence, this function satisfies the following second order differential equation

$$\frac{d^2}{dr^2}Y_k(P_1,P_2) = \frac{k(k+1)}{r^2}Y_k(P_1,P_2) - \frac{(2k+1)}{r}P_1^*(r)P_2(r). \qquad (2.86)$$

The exchange interaction can now be re-written as

$$\begin{aligned}
X_{lm}[\bar{P}_\varepsilon](r) &= \sum_{l'm'}\sum_{i}^{orb.} b_i \sum_{l_2m_2}\sum_{l_3m_3}\sum_{kq}(-1)^{m_2+m_3}\sqrt{(2l+1)(2l'+1)(2l_2+1)(2l_3+1)} \\
&\quad \times \begin{pmatrix} l_2 & k & l' \\ 0 & 0 & 0 \end{pmatrix}\begin{pmatrix} l_2 & k & l' \\ -m_2 & q & m' \end{pmatrix}\begin{pmatrix} l_3 & k & l \\ 0 & 0 & 0 \end{pmatrix}\begin{pmatrix} l_3 & k & l \\ -m_3 & q & m \end{pmatrix} \\
&\quad \times \frac{Y_k(P_{i,l_2m_2},P_{\varepsilon,l'm'})}{r}P_{i,l_3m_3}(r),
\end{aligned} \qquad (2.87)$$

or as

$$\begin{aligned} X_{lm}[\bar{P}_\varepsilon](r) = \sum_i^{orb.} b_i \sum_{l_3 m_3} \sum_{kq} (-1)^{m_3} \sqrt{(2l+1)(2l_3+1)} \\ \times \begin{pmatrix} l_3 & k & l \\ 0 & 0 & 0 \end{pmatrix} \begin{pmatrix} l_3 & k & l \\ -m_3 & q & m \end{pmatrix} \\ \times \frac{Y_{kq}(\bar{P}_i, \bar{P}_\varepsilon)}{r} P_{i,l_3 m_3}(r), \end{aligned} \tag{2.88}$$

where

$$\begin{aligned} Y_{kq}(\bar{P}_i, \bar{P}_\varepsilon) = \sum_{l'm'} \sum_{l_2 m_2} (-1)^{m_2} \sqrt{(2l'+1)(2l_2+1)} \\ \times \begin{pmatrix} l_2 & k & l' \\ 0 & 0 & 0 \end{pmatrix} \begin{pmatrix} l_2 & k & l' \\ -m_2 & q & m' \end{pmatrix} Y_k(P_{i,l_2 m_2}, P_{\varepsilon,l'm'}). \end{aligned} \tag{2.89}$$

Using Eq. (2.85), Y_{kq} satisfies the following second order differential equation

$$\begin{aligned} \frac{d^2}{dr^2} Y_{kq}(\bar{P}_i, \bar{P}_\varepsilon) = \frac{k(k+1)}{r^2} Y_{kq}(\bar{P}_i, \bar{P}_\varepsilon) \\ - \frac{(2k+1)}{r} \sum_{l'm'} \sum_{l_2 m_2} (-1)^{m_2} \sqrt{(2l'+1)(2l_2+1)} \\ \times \begin{pmatrix} l_2 & k & l' \\ 0 & 0 & 0 \end{pmatrix} \begin{pmatrix} l_2 & k & l' \\ -m_2 & q & m' \end{pmatrix} P^*_{i,l_2 m_2}(r) P_{\varepsilon,l'm'}(r). \end{aligned} \tag{2.90}$$

We couple the original second order differential in Eq. (2.65) to the second order differential equation for $Y_{kq}(\bar{P}_i, \bar{P}_\varepsilon)$ in the following matrix equation

$$\frac{d^2 \bar{P}}{dr^2} = \hat{M} \bar{P}, \tag{2.91}$$

where the solution vector, $\bar{P}$, is now defined as

$$\bar{P} = \begin{pmatrix} \{P_{lm}\} \\ \{Y_{kq}(\bar{P}_i, \bar{P}_\varepsilon)\} \end{pmatrix}. \tag{2.92}$$

and the block matrix is given by the following

$$\hat{M} = \begin{pmatrix} \{M_{lm,l'm'}\} & \{M_{lm,i'k'q'}\} \\ \{M_{ikq,l'm'}\} & \{M_{ikq,i'k'q'}\} \end{pmatrix}. \tag{2.93}$$

The top-left components of $\hat{M}$ correspond to the non-exchange terms from the HF equations

$$\{M_{lm,l'm'}\} = \left(\frac{l'(l'+1)}{r^2} - 2\varepsilon \right) \delta_{ll'}\delta_{mm'} + 2V^{ne}_{lm,l'm'}(r) + 2J^{ee}_{lm,l'm'}(r). \tag{2.94}$$

The top-right components of $\hat{M}$ correspond to the multiplicative factors of $Y_{kq}(\bar{P}_i, \bar{P}_\varepsilon)$ from the exchange interaction

$$\begin{aligned} \{M_{lm,i'k'q'}\} = \frac{2b_{i'}}{r} \sum_{l_3 m_3} (-1)^{m_3} \sqrt{(2l+1)(2l_3+1)} \\ \times \begin{pmatrix} l_3 & k' & l \\ 0 & 0 & 0 \end{pmatrix} \begin{pmatrix} l_3 & k' & l \\ -m_3 & q' & m \end{pmatrix} P_{i',l_3 m_3}(r). \end{aligned} \tag{2.95}$$

The bottom-left components of $\hat{M}$ correspond to the multiplicative factors of $P_{\varepsilon,l'm'}$

$$\begin{aligned} \{M_{ikq,l'm'}\} = -\frac{(2k+1)}{r} \sum_{l_2 m_2} (-1)^{m_2} \sqrt{(2l'+1)(2l_2+1)} \\ \times \begin{pmatrix} l_2 & k & l' \\ 0 & 0 & 0 \end{pmatrix} \begin{pmatrix} l_2 & k & l' \\ -m_2 & q & m' \end{pmatrix} P^*_{i,l_2 m_2}(r). \end{aligned} \tag{2.96}$$

Finally, the bottom-right components of $\hat{M}$ correspond to the multiplicative factors of $Y_{kq}(\bar{P}_i, \bar{P}_\varepsilon)$ from the second order differential equation for $Y_{kq}(\bar{P}_i, \bar{P}_\varepsilon)$

$$\{M_{ikq,i'k'q'}\} = \frac{k(k+1)}{r^2} \delta_{kk'}\delta_{ii'}\delta_{qq'}. \tag{2.97}$$

As in Section 2.3.6, we need to transform the grid from r to ρ. We do so as follows

$$Y_{kq}(\bar{P}_i, \bar{F}_\varepsilon) = \sqrt{\rho'} Y_{kq}(\bar{P}_i, \bar{P}_\varepsilon). \tag{2.98}$$

Using the second order differential equation for Y_{kq}, and the calculation for $\frac{d^2F_lm(\rho)}{d\rho^2}$ from Eq. (2.80), we have

$$\begin{aligned}
\frac{d^2Y_{kq}(\bar{P}_i,\bar{F}_\varepsilon)}{d\rho^2} &= \frac{1}{(\rho')^2}\left[\frac{1}{2}\frac{\rho'''}{\rho'}-\frac{3}{4}\frac{(\rho'')^2}{(\rho')^2}\right]Y_{kq}(\bar{P}_i,\bar{F}_\varepsilon)+\frac{1}{(\rho')^{\frac{3}{2}}}\frac{d^2}{dr^2}Y_{kq}(\bar{P}_i,\bar{P}_\varepsilon)\\
&= \frac{1}{(\rho')^2}\left[\frac{1}{2}\frac{\rho'''}{\rho'}-\frac{3}{4}\frac{(\rho'')^2}{(\rho')^2}\right]Y_{kq}(\bar{P}_i,\bar{F}_\varepsilon)+\frac{1}{(\rho')^{\frac{3}{2}}}\left[\frac{k(k+1)}{r^2}Y_{kq}(\bar{P}_i,\bar{P}_\varepsilon)\right.\\
&-\frac{(2k+1)}{r(\rho)}\sum_{l'm'}\sum_{l_2m_2}(-1)^{m_2}\sqrt{(2l'+1)(2l_2+1)}\\
&\times\begin{pmatrix}l_2 & k & l'\\ 0 & 0 & 0\end{pmatrix}\begin{pmatrix}l_2 & k & l'\\ -m_2 & q & m'\end{pmatrix}P^*_{i,l_2m_2}(r(\rho))P_{\varepsilon,l'm'}(r(\rho))\Bigg]\\
&= \frac{1}{(\rho')^2}\left[Y_{kq}(\bar{P}_i,\bar{F}_\varepsilon)\left(\frac{k(k+1)}{r^2(\rho)}+\frac{1}{2}\frac{\rho'''}{\rho'}-\frac{3}{4}\frac{(\rho'')^2}{(\rho')^2}\right)\right.\\
&-\frac{(2k+1)}{r(\rho)}\sum_{l'm'}\sum_{l_2m_2}(-1)^{m_2}\sqrt{(2l'+1)(2l_2+1)}\\
&\times\left.\begin{pmatrix}l_2 & k & l'\\ 0 & 0 & 0\end{pmatrix}\begin{pmatrix}l_2 & k & l'\\ -m_2 & q & m'\end{pmatrix}P^*_{i,l_2m_2}(r(\rho))F_{\varepsilon,l'm'}(\rho)\right].
\end{aligned}\tag{2.99}$$

We can write the matrix equation on the ρ grid as

$$\frac{d^2\bar{F}}{d\rho^2}=\hat{M}^\rho\bar{F},\tag{2.100}$$

where

$$\bar{F}=\begin{pmatrix}\{F_{lm}\}\\ \{Y_{kq}(\bar{P}_i,\bar{F}_\varepsilon)\}\end{pmatrix},\tag{2.101}$$

$$\hat{M}^\rho=\begin{pmatrix}\{M^\rho_{lm,l'm'}\} & \{M^\rho_{lm,i'k'q'}\}\\ \{M^\rho_{ikq,l'm'}\} & \{M^\rho_{ikq,i'k'q'}\}\end{pmatrix},\tag{2.102}$$

with block matrix elements as follows

$$\{M^{\rho}_{lm,l'm'}\} = \frac{1}{(\rho')^2}\left[\left(\frac{l'(l'+1)}{r(\rho)^2} - 2\varepsilon\right)\delta_{ll'}\delta_{mm'} + 2V^{ne}_{lm,l'm'}(r(\rho)) + 2J^{ee}_{lm,l'm'}(r(\rho)) + \left(\frac{1}{2}\frac{\rho'''}{\rho'} - \frac{3}{4}\frac{(\rho'')^2}{(\rho')^2}\right)\delta_{ll'}\delta_{mm'}\right], \tag{2.103}$$

$$\{M^{\rho}_{lm,i'k'q'}\} = \frac{1}{(\rho')^2}\frac{2b_{i'}}{r(\rho)}\sum_{l_3m_3}(-1)^{m_3}\sqrt{(2l+1)(2l_3+1)} \times \begin{pmatrix} l_3 & k' & l \\ 0 & 0 & 0 \end{pmatrix}\begin{pmatrix} l_3 & k' & l \\ -m_3 & q' & m \end{pmatrix} P_{i',l_3m_3}(r(\rho)), \tag{2.104}$$

$$\{M^{\rho}_{ikq,l'm'}\} = -\frac{1}{(\rho')^2}\frac{(2k+1)}{r(\rho)}\sum_{l_2m_2}(-1)^{m_2}\sqrt{(2l'+1)(2l_2+1)} \times \begin{pmatrix} l_2 & k & l' \\ 0 & 0 & 0 \end{pmatrix}\begin{pmatrix} l_2 & k & l' \\ -m_2 & q & m' \end{pmatrix} P^{*}_{i,l_2m_2}(r(\rho)), \tag{2.105}$$

$$\{M^{\rho}_{ikq,i'k'q'}\} = \frac{1}{(\rho')^2}\left[\frac{k(k+1)}{r(\rho)^2} + \frac{1}{2}\frac{\rho'''}{\rho'} - \frac{3}{4}\frac{(\rho'')^2}{(\rho')^2}\right]\delta_{kk'}\delta_{ii'}\delta_{qq'}. \tag{2.106}$$

2.3.8 Numerov method and the Thomas Algorithm

The Numerov method solves differential equations of the form

$$y''(r) = g(r)y(r). \tag{2.107}$$

It relates $y_n = y(nh), g_n = g(nh), n = 1,\ldots,N$ and the radial step size h for a grid size N as follows [75]

$$\left(1 - \frac{h^2}{12}g_{n+1}\right)y_{n+1} - 2\left(1 + \frac{5h^2}{12}g_n\right)y_n + \left(1 - \frac{h^2}{12}g_{n-1}\right)y_{n-1} = 0. \tag{2.108}$$

Comparing Eq. (2.100) with the general form of differential equations applicable to the Numerov method, we have

$$\hat{a}_{n+1}\bar{F}_{n+1} - \hat{b}_n\bar{F}_n + \hat{a}_{n-1}\bar{F}_{n-1} = 0, \tag{2.109}$$

where

$$\hat{a}_n = \mathbb{1} - \frac{h^2}{12}\hat{M}_n^\rho, \tag{2.110}$$

$$\hat{b}_n = 2\left(\mathbb{1} + \frac{5h^2}{12}\hat{M}_n^\rho\right). \tag{2.111}$$

The identity matrix, $\mathbb{1}$, is of size $N_{lm}+N_{ikq}$, where N_{lm} is the number of l,m combinations and N_{ikq} is the number of bound orbitals multiplied by the number of k,q combinations. This can be written as the following system of linear equations with a block tridiagonal matrix

$$\begin{pmatrix} -\hat{b}_1 & \hat{a}_2 & & & & \\ \hat{a}_1 & -\hat{b}_2 & \hat{a}_3 & & & \\ & & \ddots & & & \\ & & \hat{a}_{n-1} & -\hat{b}_n & \hat{a}_{n+1} & \\ & & & & \ddots & \end{pmatrix} \begin{pmatrix} \bar{F}_1 \\ \bar{F}_2 \\ \vdots \\ \vdots \\ \vdots \end{pmatrix} = \begin{pmatrix} 0 \\ 0 \\ \vdots \\ \vdots \\ 0 \end{pmatrix}. \tag{2.112}$$

This can be solved using the Tridiagonal Matrix Algorithm, otherwise known as the Thomas Algorithm [76]. This consists of 2 steps:

1) Forward Sweep First, we define a matrix $\hat{V}_n$ in terms of it's relation between two sequential values of our solution vector

$$\bar{F}_n = \hat{V}_n \bar{F}_{n+1}. \tag{2.113}$$

Since $\bar{F}$ is an $N_{lm}+N_{ikq}$ dimensional vector, $\hat{V}$ is a $(N_{lm}+N_{ikq})\times(N_{lm}+N_{ikq})$ matrix. Substituting Eq. (2.113) into the Numerov solution we have

$$\hat{a}_{n-1}\hat{V}_{n-1}\bar{F}_n - \hat{b}_n\bar{F}_n + \hat{a}_{n+1}\bar{F}_{n+1} = 0. \tag{2.114}$$

Rearranging gives

$$\bar{F}_n = (\hat{b}_n - \hat{a}_{n-1}\hat{V}_{n-1})^{-1}\hat{a}_{n+1}\bar{F}_{n+1}. \tag{2.115}$$

Hence, we have

$$\hat{V}_n = (\hat{b}_n - \hat{a}_{n-1}\hat{V}_{n-1})^{-1}\hat{a}_{n+1}. \tag{2.116}$$

Using this we can outwards sweep from $n = 1$ to find $\hat{V}_n$ for all points in the grid. To do this however, we require the value of $\hat{V}_1$. The inner boundary conditions are given by

$$\hat{V}_1 = \hat{V}_2 = \hat{V}, \tag{2.117}$$

where

$$\hat{V} = (\hat{b}_2 - \hat{a}_1\hat{V})^{-1}\hat{a}_3. \tag{2.118}$$

We start with $\hat{V} = 0$. Then, we solve Eq. (2.118) recursively until it converges to a value for $\hat{V}$.

2) Backward Sweep Once every $\hat{V}_n$ is known for every n, $\bar{F}_n$ is then found by back substitution from N to 0 using Eq. (2.113). In order to sweep backwards from $\bar{F}_N$, we need to find the asymptotic values of $\bar{F}$. For P_{lm}, substituting the asymptotic boundary conditions from Eq. (2.68) for the edge cases $n = N-1, N$ gives

$$(P_{lm}^{LM})_{N-1} = (\mathcal{F}_l)_{N-1}\delta_{lL}\delta_{mM} + (\mathcal{G}_l)_{N-1}R_{lm}^{LM}, \tag{2.119}$$

which is equivalent to

$$\frac{1}{\sqrt{\rho'_{N-1}}}(F_{lm}^{LM})_{N-1} = (\mathcal{F}_l)_{N-1}\delta_{lL}\delta_{mM} + (\mathcal{G}_l)_{N-1}R_{lm}^{LM}. \tag{2.120}$$

Similarly,

$$\frac{1}{\sqrt{\rho'_N}}(F_{lm}^{LM})_N = (\mathcal{F}_l)_N\delta_{lL}\delta_{mM} + (\mathcal{G}_l)_N R_{lm}^{LM}. \tag{2.121}$$

The asymptotic boundary conditions for $Y_{kq}(\bar{P}_i, \bar{P}_\varepsilon)$ are

$$Y_{kq}(\bar{P}_i, \bar{P}_\varepsilon) = B_{ikq}r^{-k} \text{ as } r \to \infty, \tag{2.122}$$

for some constant B_{ikq}. So combining this with the P_{lm} conditions, the boundary conditions for the solution vector $\bar{P}$ for a given L, M channel is

$$\bar{P} = \begin{pmatrix} \{\delta_{lL}\delta_{mM}\mathcal{F}_l(r) + \mathcal{G}_l(r)R_{lm}^{LM}\} \\ \{B_{ikq}r^{-k}\} \end{pmatrix} \text{ as } r \to \infty. \tag{2.123}$$

Considering all L,M channels simultaneously, we use a solution vector of matrices

$$\bar{P} = \begin{pmatrix} \hat{\mathcal{F}}(r) + \hat{\mathcal{G}}(r)\hat{R} \\ \hat{r}(r)\hat{B} \end{pmatrix} \text{ as } r \to \infty, \tag{2.124}$$

where $\hat{\mathcal{F}}(r)$ and $\hat{\mathcal{G}}(r)$ are diagonal matrices with elements $\mathcal{F}_l(r)$ and $\mathcal{G}_l(r)$, respectively, $\hat{B} = \{B_{ikq,LM}\}$ is a matrix of constants B_{ikq} for each L,M channel and $\hat{r}$ is a diagonal matrix with elements r^{-k}. Hence, we have the following relation between $\bar{F}_N$ and $\bar{F}_{N-1}$

$$\begin{aligned} \sqrt{\rho'_{N-1}} \begin{pmatrix} \hat{\mathcal{F}}_{N-1}(r) + \hat{\mathcal{G}}_{N-1}(r)\hat{R} \\ \hat{r}_{N-1}\hat{B} \end{pmatrix} &= \begin{pmatrix} \{V_{lm}, V_{l'm'}\}_{N-1} & \{V_{lm}, V_{i'k'q'}\}_{N-1} \\ \{V_{ikq}, V_{l'm'}\}_{N-1} & \{V_{ikq}, V_{i'k'q'}\}_{N-1} \end{pmatrix} \\ &\quad \times \sqrt{\rho'_N} \begin{pmatrix} \hat{\mathcal{F}}_N(r) + \hat{\mathcal{G}}_N(r)\hat{R} \\ \hat{r}_N\hat{B} \end{pmatrix}. \end{aligned} \tag{2.125}$$

Expanding this gives us the following simultaneous equations

$$\begin{aligned} \sqrt{\rho'_{N-1}}\left(\hat{\mathcal{F}}_{N-1}(r) + \hat{\mathcal{G}}_{N-1}(r)\hat{R}\right) &= \sqrt{\rho'_N}\Big(\{V_{lm}, V_{l'm'}\}_{N-1}(\hat{\mathcal{F}}_N(r) \\ &\quad + \hat{\mathcal{G}}_N(r)\hat{R}) + \{V_{lm}, V_{i'k'q'}\}_{N-1}\hat{r}_N\hat{B}\Big) \\ \sqrt{\rho'_{N-1}}\hat{r}_{N-1}\hat{B} &= \sqrt{\rho'_N}\Big(\{V_{ikq}, V_{l'm'}\}_{N-1}(\hat{\mathcal{F}}_N(r) \\ &\quad + \hat{\mathcal{G}}_N(r)\hat{R}) + \{V_{ikq}, V_{i'k'q'}\}_{N-1}\hat{r}_N\hat{B}\Big). \end{aligned} \tag{2.126}$$

Rearranging these simultaneous equations gives

$$\begin{aligned} \hat{R} = &\left(\sqrt{\rho'_{N-1}}\hat{\mathcal{G}}_{N-1} - \sqrt{\rho'_N}\{V_{lm}, V_{l'm'}\}_{N-1}\hat{\mathcal{G}}_N\right)^{-1} \\ &\times \left(\sqrt{\rho'_N}\{V_{lm}, V_{i'k'q'}\}_{N-1}\hat{r}_N\hat{B} + \sqrt{\rho'_N}\{V_{lm}, V_{l'm'}\}_{N-1}\hat{\mathcal{F}}_N - \sqrt{\rho'_{N-1}}\hat{\mathcal{F}}_{N-1}\right), \end{aligned} \tag{2.127}$$

$$\begin{aligned}\hat{B} = &\left(\sqrt{\rho'_{N-1}}\hat{r}_{N-1} - \sqrt{\rho'_N}\{V_{ikq}, V_{i'k'q'}\}_{N-1}\hat{r}_N\right)^{-1} \\ &\times \left(\sqrt{\rho'_N}\{V_{ikq}, V_{l'm'}\}_{N-1}\left(\hat{\mathcal{F}}_N + \hat{\mathcal{G}}_N\hat{R}\right)\right).\end{aligned} \tag{2.128}$$

By substituting the formula for $\hat{B}$ into the formula for $\hat{R}$, we obtain the following formula for $\hat{R}$

$$\begin{aligned}\hat{R} = &\left[\sqrt{\frac{\rho'_{N-1}}{\rho'_N}}\hat{\mathcal{G}}_{N-1} - \{V_{lm}, V_{l'm'}\}_{N-1}\hat{\mathcal{G}}_N\right. \\ &- \{V_{lm}, V_{i'k'q'}\}_{N-1}\hat{r}_N\left(\sqrt{\frac{\rho'_{N-1}}{\rho'_N}}\hat{r}_{N-1} - \{V_{ikq}, V_{i'k'q'}\}_{N-1}\hat{r}_N\right)^{-1} \\ &\left.\times \{V_{ikq}, V_{l'm'}\}_{N-1}\hat{\mathcal{G}}_N\right]^{-1} \\ &\times \left[\{V_{lm}, V_{l'm'}\}_{N-1}\hat{\mathcal{F}}_N - \sqrt{\frac{\rho'_{N-1}}{\rho'_N}}\hat{\mathcal{F}}_{N-1}\right. \\ &+ \{V_{lm}, V_{i'k'q'}\}_{N-1}\hat{r}_N\left(\sqrt{\frac{\rho'_{N-1}}{\rho'_N}}\hat{r}_{N-1} - \{V_{ikq}, V_{i'k'q'}\}_{N-1}\hat{r}_N\right)^{-1} \\ &\left.\times \{V_{ikq}, V_{l'm'}\}_{N-1}\hat{\mathcal{F}}_N\right].\end{aligned} \tag{2.129}$$

Similarly, by substituting the formula for $\hat{R}$ into the formula for $\hat{B}$, we obtain the following formula for $\hat{B}$

$$\begin{aligned}\hat{B} = &\left[\sqrt{\frac{\rho'_{N-1}}{\rho'_N}}\hat{r}_{N-1} - \{V_{ikq}, V_{i'k'q'}\}_{N-1}\hat{r}_N\right.\\
&- \{V_{ikq}, V_{l'm'}\}_{N-1}\hat{\mathcal{G}}_N\left(\sqrt{\frac{\rho'_{N-1}}{\rho'_N}}\hat{\mathcal{G}}_{N-1} - \{V_{lm}, V_{l'm'}\}_{N-1}\hat{\mathcal{G}}_N\right)^{-1}\\
&\left.\times\{V_{lm}, V_{i'k'q'}\}_{N-1}\hat{r}_N\right]^{-1}\\
&\times\left[\{V_{ikq}, V_{l'm'}\}_{N-1}\hat{\mathcal{F}}_N\right.\\
&+ \{V_{ikq}, V_{l'm'}\}_{N-1}\hat{\mathcal{G}}_N\left(\sqrt{\frac{\rho'_{N-1}}{\rho'_N}}\hat{\mathcal{G}}_{N-1} - \{V_{lm}, V_{l'm'}\}_{N-1}\hat{\mathcal{G}}_N\right)^{-1}\\
&\left.\times\left(\{V_{lm}, V_{l'm'}\}_{N-1}\hat{\mathcal{F}}_N - \sqrt{\frac{\rho'_{N-1}}{\rho'_N}}\hat{\mathcal{F}}_{N-1}\right)\right].\end{aligned} \tag{2.130}$$

To summarize, we use this equation above to find $\hat{B}$, then we substitute this into Eq. (2.127) to find $\hat{R}$. After finding $\hat{B}$ and $\hat{R}$, we can then find $\bar{F}_N$

$$\bar{F}_N = \sqrt{\rho'}\begin{pmatrix}\hat{\mathcal{F}}_N + \hat{\mathcal{G}}_N\hat{R}\\ \hat{r}_N\hat{B}\end{pmatrix}. \tag{2.131}$$

Then, we can find $\bar{F}_n, n = 0,\ldots,N$ by back substitution from $n = N$ to $n = 0$ using Eq. (2.113). Next, we transform the $\{F_{lm}\}$ components of $\bar{F}_n$ into $\{P_{lm}\}$ using Eq. (2.79). Finally, we normalise P_{lm} using Eqs. (2.70) and (2.71).

2.3.9 Direct and Exchange coefficients

Next, we describe how to obtain the coefficients a_i and b_i in Eq. (2.25). After applying the variational principle to the electron-electron interaction terms in the HF method ($\hat{H}_2$ in Section 2.1.2), we have

$$\sum_i^{\text{orb.}} a_i J_i\left|\phi_\varepsilon\right\rangle - \sum_i^{\text{orb.}} b_i K_i\left|\phi_\varepsilon\right\rangle = \varepsilon^{ee}\left|\phi_\varepsilon\right\rangle, \tag{2.132}$$

where

$$\begin{aligned} J_i\,|\phi_\varepsilon\rangle &= \langle\phi_i|\,\frac{1}{r_{12}}\,|\phi_i\rangle\,|\phi_\varepsilon\rangle\,, \\ K_i\,|\phi_\varepsilon\rangle &= \langle\phi_i|\,\frac{1}{r_{12}}\,|\phi_\varepsilon\rangle\,|\phi_i\rangle\,. \end{aligned} \tag{2.133}$$

If an orbital isn't occupied, then the coefficients a_i and b_i are zero as there are no electrons for the electron-electron interaction. In order to determine the a_i and b_i coefficients for occupied orbitals, it is sufficient to find them for four limiting cases. Below we will present the full derivation for only the first limiting case, since the method for computing the coefficients of the other limiting cases is analogous.

2.3.9.1 First limiting case

For the first limiting case we have a two-electron system, with both electrons initially occupying a single orbital i and one of these electrons finally being emitted to the continuum. Spin is conserved and it is equal to zero in the initial and final states. Therefore, a two-electron wavefunction must be constructed that is anti-symmetric in spin and anti-symmetric under exchange of electrons. The wavefunction is given by the sum of the following two Slater determinants

$$\Phi(q_1,q_2) = \frac{1}{\sqrt{2}}\left(\frac{1}{\sqrt{2!}}\begin{vmatrix}\phi_i^{\uparrow}(q_1) & \phi_\varepsilon^{\downarrow}(q_1)\\ \phi_i^{\uparrow}(q_2) & \phi_\varepsilon^{\downarrow}(q_2)\end{vmatrix} - \frac{1}{\sqrt{2!}}\begin{vmatrix}\phi_i^{\downarrow}(q_1) & \phi_\varepsilon^{\uparrow}(q_1)\\ \phi_i^{\downarrow}(q_2) & \phi_\varepsilon^{\uparrow}(q_2)\end{vmatrix}\right). \tag{2.134}$$

Expanding this gives

$$\Phi(q_1,q_2) = \frac{1}{2}(\phi_i^{\uparrow}(q_1)\phi_\varepsilon^{\downarrow}(q_2) - \phi_\varepsilon^{\downarrow}(q_1)\phi_i^{\uparrow}(q_2) - \phi_i^{\downarrow}(q_1)\phi_\varepsilon^{\uparrow}(q_2) + \phi_\varepsilon^{\uparrow}(q_1)\phi_i^{\downarrow}(q_2)). \tag{2.135}$$

In Dirac notation this is equivalent to

$$|\Phi\rangle = \frac{1}{2}\left(\left|\phi_i^{\uparrow}\phi_\varepsilon^{\downarrow}\right\rangle - \left|\phi_\varepsilon^{\downarrow}\phi_i^{\uparrow}\right\rangle - \left|\phi_i^{\downarrow}\phi_\varepsilon^{\uparrow}\right\rangle + \left|\phi_\varepsilon^{\uparrow}\phi_i^{\downarrow}\right\rangle\right). \tag{2.136}$$

Evaluating the mean value of $\frac{1}{r_{12}}$ gives

$$\begin{aligned}
\langle\Phi|\frac{1}{r_{12}}|\Phi\rangle &= \frac{1}{4}\Big(\Big\langle\phi_i^{\uparrow}\phi_\varepsilon^{\downarrow}\Big| - \Big\langle\phi_\varepsilon^{\downarrow}\phi_i^{\uparrow}\Big| - \Big\langle\phi_i^{\downarrow}\phi_\varepsilon^{\uparrow}\Big| + \Big\langle\phi_\varepsilon^{\uparrow}\phi_i^{\downarrow}\Big|\Big) \\
&\times \frac{1}{r_{12}}\Big(\Big|\phi_i^{\uparrow}\phi_\varepsilon^{\downarrow}\Big\rangle - \Big|\phi_\varepsilon^{\downarrow}\phi_i^{\uparrow}\Big\rangle - \Big|\phi_i^{\downarrow}\phi_\varepsilon^{\uparrow}\Big\rangle + \Big|\phi_\varepsilon^{\uparrow}\phi_i^{\downarrow}\Big\rangle\Big) \\
&= \frac{1}{4}\Big(\Big\langle\phi_i^{\uparrow}\phi_\varepsilon^{\downarrow}\Big|\frac{1}{r_{12}}\Big|\phi_i^{\uparrow}\phi_\varepsilon^{\downarrow}\Big\rangle - \Big\langle\phi_i^{\uparrow}\phi_\varepsilon^{\downarrow}\Big|\frac{1}{r_{12}}\Big|\phi_\varepsilon^{\downarrow}\phi_i^{\uparrow}\Big\rangle - \Big\langle\phi_i^{\uparrow}\phi_\varepsilon^{\downarrow}\Big|\frac{1}{r_{12}}\Big|\phi_i^{\downarrow}\phi_\varepsilon^{\uparrow}\Big\rangle \\
&+ \Big\langle\phi_i^{\uparrow}\phi_\varepsilon^{\downarrow}\Big|\frac{1}{r_{12}}\Big|\phi_\varepsilon^{\uparrow}\phi_i^{\downarrow}\Big\rangle - \Big\langle\phi_\varepsilon^{\downarrow}\phi_i^{\uparrow}\Big|\frac{1}{r_{12}}\Big|\phi_i^{\uparrow}\phi_\varepsilon^{\downarrow}\Big\rangle + \Big\langle\phi_\varepsilon^{\downarrow}\phi_i^{\uparrow}\Big|\frac{1}{r_{12}}\Big|\phi_\varepsilon^{\downarrow}\phi_i^{\uparrow}\Big\rangle \\
&+ \Big\langle\phi_\varepsilon^{\downarrow}\phi_i^{\uparrow}\Big|\frac{1}{r_{12}}\Big|\phi_i^{\downarrow}\phi_\varepsilon^{\uparrow}\Big\rangle - \Big\langle\phi_\varepsilon^{\downarrow}\phi_i^{\uparrow}\Big|\frac{1}{r_{12}}\Big|\phi_\varepsilon^{\uparrow}\phi_i^{\downarrow}\Big\rangle - \Big\langle\phi_i^{\downarrow}\phi_\varepsilon^{\uparrow}\Big|\frac{1}{r_{12}}\Big|\phi_i^{\uparrow}\phi_\varepsilon^{\downarrow}\Big\rangle \\
&+ \Big\langle\phi_i^{\downarrow}\phi_\varepsilon^{\uparrow}\Big|\frac{1}{r_{12}}\Big|\phi_\varepsilon^{\downarrow}\phi_i^{\uparrow}\Big\rangle + \Big\langle\phi_i^{\downarrow}\phi_\varepsilon^{\uparrow}\Big|\frac{1}{r_{12}}\Big|\phi_i^{\downarrow}\phi_\varepsilon^{\uparrow}\Big\rangle - \Big\langle\phi_i^{\downarrow}\phi_\varepsilon^{\uparrow}\Big|\frac{1}{r_{12}}\Big|\phi_\varepsilon^{\uparrow}\phi_i^{\downarrow}\Big\rangle \\
&+ \Big\langle\phi_\varepsilon^{\uparrow}\phi_i^{\downarrow}\Big|\frac{1}{r_{12}}\Big|\phi_i^{\uparrow}\phi_\varepsilon^{\downarrow}\Big\rangle - \Big\langle\phi_\varepsilon^{\uparrow}\phi_i^{\downarrow}\Big|\frac{1}{r_{12}}\Big|\phi_\varepsilon^{\downarrow}\phi_i^{\uparrow}\Big\rangle - \Big\langle\phi_\varepsilon^{\uparrow}\phi_i^{\downarrow}\Big|\frac{1}{r_{12}}\Big|\phi_i^{\downarrow}\phi_\varepsilon^{\uparrow}\Big\rangle \\
&+ \Big\langle\phi_\varepsilon^{\uparrow}\phi_i^{\downarrow}\Big|\frac{1}{r_{12}}\Big|\phi_\varepsilon^{\uparrow}\phi_i^{\downarrow}\Big\rangle\Big).
\end{aligned} \tag{2.137}$$

Using spin orthogonality, Eq. (2.137) takes the form

$$\begin{aligned}
\langle\Phi|\frac{1}{r_{12}}|\Phi\rangle = \frac{1}{4}\Big(&\langle\phi_i\phi_\varepsilon|\frac{1}{r_{12}}|\phi_i\phi_\varepsilon\rangle + \langle\phi_i\phi_\varepsilon|\frac{1}{r_{12}}|\phi_\varepsilon\phi_i\rangle \\
&+ \langle\phi_\varepsilon\phi_i|\frac{1}{r_{12}}|\phi_\varepsilon\phi_i\rangle + \langle\phi_\varepsilon\phi_i|\frac{1}{r_{12}}|\phi_i\phi_\varepsilon\rangle \\
&+ \langle\phi_i\phi_\varepsilon|\frac{1}{r_{12}}|\phi_\varepsilon\phi_i\rangle + \langle\phi_i\phi_\varepsilon|\frac{1}{r_{12}}|\phi_i\phi_\varepsilon\rangle \\
&+ \langle\phi_\varepsilon\phi_i|\frac{1}{r_{12}}|\phi_i\phi_\varepsilon\rangle + \langle\phi_\varepsilon\phi_i|\frac{1}{r_{12}}|\phi_\varepsilon\phi_i\rangle\Big),
\end{aligned} \tag{2.138}$$

where we now have spatial orbitals. Now using $\langle\phi_\varepsilon\phi_i|\frac{1}{r_{12}}|\phi_\varepsilon\phi_i\rangle = \langle\phi_i\phi_\varepsilon|\frac{1}{r_{12}}|\phi_i\phi_\varepsilon\rangle$, we have that

$$\varepsilon^{ee} = \langle\Phi|\frac{1}{r_{12}}|\Phi\rangle = \langle\phi_i\phi_\varepsilon|\frac{1}{r_{12}}|\phi_i\phi_\varepsilon\rangle + \langle\phi_i\phi_\varepsilon|\frac{1}{r_{12}}|\phi_\varepsilon\phi_i\rangle\,. \tag{2.139}$$

Using the variational principle for the continuum orbital

$$\begin{aligned}\frac{\partial}{\partial \langle\phi_\varepsilon|}\left(\langle\phi_i\phi_\varepsilon|\frac{1}{r_{12}}|\phi_i\phi_\varepsilon\rangle+\langle\phi_i\phi_\varepsilon|\frac{1}{r_{12}}|\phi_\varepsilon\phi_i\rangle\right)&=\frac{\partial}{\partial\langle\phi_\varepsilon|}(\varepsilon^{ee}\langle\phi_\varepsilon|\phi_\varepsilon\rangle)\\ \iff \langle\phi_i|\frac{1}{r_{12}}|\phi_i\rangle|\phi_\varepsilon\rangle+\langle\phi_i|\frac{1}{r_{12}}|\phi_\varepsilon\rangle|\phi_i\rangle&=\varepsilon^{ee}|\phi_\varepsilon\rangle.\end{aligned} \tag{2.140}$$

So using our definitions for J_i and K_i we have

$$J_i\phi_\varepsilon+K_i\phi_\varepsilon=\varepsilon^{ee}\phi_\varepsilon. \tag{2.141}$$

Hence, in this case we see that $a_i=1$ and $b_i=-1$. This Slater determinant can also be used in the case involving two orbitals i and j. Initially, one electron is in orbital i, while the other is in orbital j, forming a singlet spin state. Then, the electron from orbital j is emitted to the continuum. If instead the electrons from orbitals i and j form a triplet state, the wavefunction can be expressed in terms of the following

$$\Phi(q_1,q_2)=\frac{1}{\sqrt{2}}\left(\frac{1}{\sqrt{2!}}\begin{vmatrix}\phi_i^{\uparrow}(q_1) & \phi_\varepsilon^{\downarrow}(q_1)\\ \phi_i^{\uparrow}(q_2) & \phi_\varepsilon^{\downarrow}(q_2)\end{vmatrix}+\frac{1}{\sqrt{2!}}\begin{vmatrix}\phi_i^{\downarrow}(q_1) & \phi_\varepsilon^{\uparrow}(q_1)\\ \phi_i^{\downarrow}(q_2) & \phi_\varepsilon^{\uparrow}(q_2)\end{vmatrix}\right). \tag{2.142}$$

In this case we find that $a_i=1$ and $b_i=1$.

2.3.9.2 Second limiting case

The next limiting case involves two orbitals i and j and three electrons. Initially, one electron is in orbital i and the other two in orbital j. In the final state one electron from orbital j is emitted to the continuum. A three-electron wavefunction must be constructed which is anti-symmetric in spin regarding the continuum electron and the electron in the j orbital and anti-symmetric under exchange of electrons. The wavefunction for this system can be expressed in terms of the following two Slater

Determinants

$$\Phi(q_1,q_2,q_3) = \frac{1}{\sqrt{2}}\left(\frac{1}{\sqrt{3!}}\begin{vmatrix}\phi_i^{\uparrow}(q_1) & \phi_j^{\downarrow}(q_1) & \phi_\varepsilon^{\uparrow}(q_1)\\ \phi_i^{\uparrow}(q_2) & \phi_j^{\downarrow}(q_2) & \phi_\varepsilon^{\uparrow}(q_2)\\ \phi_i^{\uparrow}(q_3) & \phi_j^{\downarrow}(q_3) & \phi_\varepsilon^{\uparrow}(q_3)\end{vmatrix} - \frac{1}{\sqrt{3!}}\begin{vmatrix}\phi_i^{\uparrow}(q_1) & \phi_j^{\uparrow}(q_1) & \phi_\varepsilon^{\downarrow}(q_1)\\ \phi_i^{\uparrow}(q_2) & \phi_j^{\uparrow}(q_2) & \phi_\varepsilon^{\downarrow}(q_2)\\ \phi_i^{\uparrow}(q_3) & \phi_j^{\uparrow}(q_3) & \phi_\varepsilon^{\downarrow}(q_3)\end{vmatrix}\right). \tag{2.143}$$

In this case we find $a_j = 1, b_j = -1, a_i = 1$ and $b_i = \frac{1}{2}$.

2.3.9.3 Third limiting case

The third limiting case involves two electrons occupying orbital i and two electrons occupying orbital j in the initial state. In the final state, one electron from orbital j escapes to the continuum. The wavefunction is given by

$$\Phi(q_1,q_2,q_3) = \frac{1}{\sqrt{2}}\left(\frac{1}{\sqrt{4!}}\begin{vmatrix}\phi_i^{\uparrow}(q_1) & \phi_i^{\downarrow}(q_1) & \phi_j^{\uparrow}(q_1) & \phi_\varepsilon^{\downarrow}(q_1)\\ \phi_i^{\uparrow}(q_2) & \phi_i^{\downarrow}(q_2) & \phi_j^{\uparrow}(q_2) & \phi_\varepsilon^{\downarrow}(q_2)\\ \phi_i^{\uparrow}(q_3) & \phi_i^{\downarrow}(q_3) & \phi_j^{\uparrow}(q_3) & \phi_\varepsilon^{\downarrow}(q_3)\\ \phi_i^{\uparrow}(q_4) & \phi_i^{\downarrow}(q_4) & \phi_j^{\uparrow}(q_4) & \phi_\varepsilon^{\downarrow}(q_4)\end{vmatrix} - \frac{1}{\sqrt{4!}}\begin{vmatrix}\phi_i^{\uparrow}(q_1) & \phi_i^{\downarrow}(q_1) & \phi_j^{\downarrow}(q_1) & \phi_\varepsilon^{\uparrow}(q_1)\\ \phi_i^{\uparrow}(q_2) & \phi_i^{\downarrow}(q_2) & \phi_j^{\downarrow}(q_2) & \phi_\varepsilon^{\uparrow}(q_2)\\ \phi_i^{\uparrow}(q_3) & \phi_i^{\downarrow}(q_3) & \phi_j^{\downarrow}(q_3) & \phi_\varepsilon^{\uparrow}(q_3)\\ \phi_i^{\uparrow}(q_4) & \phi_i^{\downarrow}(q_4) & \phi_j^{\downarrow}(q_4) & \phi_\varepsilon^{\uparrow}(q_4)\end{vmatrix}\right). \tag{2.144}$$

One can find that $a_i = 2, b_i = 1$ and $a_j = 1, b_j = -1$. Note that, by proceeding as in the first limiting case, we find that

$$2J_i\phi_\varepsilon - K_i\phi_\varepsilon + J_j\phi_\varepsilon + K_j\phi_\varepsilon = \varepsilon^{ee}\phi_\varepsilon. \tag{2.145}$$

This is equivalent to the sum of the first limiting case and the following single Slater determinant, consisting of a fully-occupied orbital i and a continuum electron in the

final state

$$\Phi(q_1,q_2,q_3) = \frac{1}{\sqrt{3!}} \begin{vmatrix} \phi_i^{\uparrow}(q_1) & \phi_i^{\downarrow}(q_1) & \phi_\varepsilon^{\uparrow}(q_1) \\ \phi_i^{\uparrow}(q_2) & \phi_i^{\downarrow}(q_2) & \phi_\varepsilon^{\uparrow}(q_2) \\ \phi_i^{\uparrow}(q_3) & \phi_i^{\downarrow}(q_3) & \phi_\varepsilon^{\uparrow}(q_3) \end{vmatrix}. \tag{2.146}$$

Indeed, for the Slater determinant above, we find $a_i = 2$ and $b_i = 1$.

2.3.9.4 Fourth limiting case

The final limiting case examines the case where the spin symmetry is between orbitals which are not the continuum electron, namely the partially-filled orbitals i and j. The wavefunction is given by

$$\begin{aligned} \Phi(q_1,q_2,q_3) = \frac{1}{\sqrt{2}} \Bigg(& \frac{1}{\sqrt{3!}} \begin{vmatrix} \phi_i^{\uparrow}(q_1) & \phi_j^{\downarrow}(q_1) & \phi_\varepsilon^{\uparrow}(q_1) \\ \phi_i^{\uparrow}(q_2) & \phi_j^{\downarrow}(q_2) & \phi_\varepsilon^{\uparrow}(q_2) \\ \phi_i^{\uparrow}(q_3) & \phi_j^{\downarrow}(q_3) & \phi_\varepsilon^{\uparrow}(q_3) \end{vmatrix} \\ & \pm \frac{1}{\sqrt{3!}} \begin{vmatrix} \phi_i^{\downarrow}(q_1) & \phi_j^{\uparrow}(q_1) & \phi_\varepsilon^{\uparrow}(q_1) \\ \phi_i^{\downarrow}(q_2) & \phi_j^{\uparrow}(q_2) & \phi_\varepsilon^{\uparrow}(q_2) \\ \phi_i^{\downarrow}(q_3) & \phi_j^{\uparrow}(q_3) & \phi_\varepsilon^{\uparrow}(q_3) \end{vmatrix} \Bigg), \end{aligned} \tag{2.147}$$

where the $+$ corresponds to triplet-spin symmetry between orbitals i and j and $-$ corresponds to singlet-spin symmetry. In both cases, one can show that $a_i = a_j = 1$ and $b_i = b_j = \frac{1}{2}$.

2.4 Transitions

2.4.1 Fermi's golden rule

Fermi's golden rule is a formula that describes the transition rate (the probability of a transition per unit time) from an initial energy eigenstate of a quantum system to a final group of energy eigenstates. Suppose that the system begins in an eigenstate $|i\rangle$ with an unperturbed Hamiltonian H. Then we apply a perturbing Hamiltonian H' to the system. In this instance, we assume H' is time-independent. Then Fermi's golden rule states that the transition rate from the initial energy eigenstate $|i\rangle$ to a

final state $|f\rangle$ due to this perturbation is given by [77]

$$\Gamma_{i\to f} = 2\pi \left|\langle f|H'|i\rangle\right|^2. \tag{2.148}$$

Fermi's golden rule is applicable to both atomic and molecular systems.

2.4.2 Photoionization

Photoionization is the physical process in which an ion is formed from the interaction of a photon with an atom or molecule. An electron absorbs the energy of the photon and escapes to the continuum. The probability of photoionization occurring is related to the photoionization cross section. The molecular photoionization cross section of an electron transitioning from a bound molecular orbital ϕ_i to a final continuum orbital ϕ_ε is given by [77]

$$\sigma_{i\to\varepsilon} = \frac{4}{3}\alpha\pi^2\omega N_i \sum_{M=-1,0,1} \left|D^M_{i\varepsilon}\right|^2 \tag{2.149}$$

where α is the fine structure constant, N_i is the occupation number of the initial orbital i, ω is the energy of the photon and $M = -1,0,1$ is the polarization of the photon. In the length gauge, the dipole operator is

$$d^L_M = \mathbf{r}\cdot\hat{n} = \sqrt{\frac{4\pi}{3}} r Y_{1M}(\theta,\phi), \tag{2.150}$$

where $\hat{n}$ is the unit vector of the polarization of the field. In the single centre expansion form, the dipole matrix element then takes the following form

$$\begin{aligned} D^M_{i\varepsilon} &= \langle\phi_\varepsilon| d^L_M |\phi_i\rangle \\ &= \int \phi^*_\varepsilon(\mathbf{r}) \sqrt{\frac{4\pi}{3}} r Y_{1M}(\theta,\phi)\phi_i(\mathbf{r}) d\mathbf{r} \\ &= \sqrt{\frac{4\pi}{3}} \sum_{lm,l'm'} \int_0^\infty dr P^*_{\varepsilon,l'm'}(r) r P_{i,lm}(r) \int d\Omega Y^*_{l'm'}(\theta,\phi) Y_{lm}(\theta,\phi) Y_{1M}(\theta,\phi). \end{aligned} \tag{2.151}$$

Using spherical harmonic integral identities, this is equal to

$$D_{i\varepsilon}^{M} = \sum_{lm,l'm'} (-1)^{m'} \sqrt{(2l+1)(2l'+1)} \times \begin{pmatrix} l' & l & 1 \\ 0 & 0 & 0 \end{pmatrix} \begin{pmatrix} l' & l & 1 \\ -m' & m & M \end{pmatrix} \int_0^\infty dr P^*_{\varepsilon,l'm'}(r) r P_{i,lm}(r). \tag{2.152}$$

From the Wigner-3j symbols we can see how we obtain the l and m numbers for the continuum orbital. The second Wigner-3j symbol gives $-m' + m + M = 0$. From the first Wigner-3j symbol we find that $l' + l + 1$ has to be even. In addition, for homonuclear diatomic molecules the orbitals have even or odd parity. Given the above, for homonuclear diatomic molecules an electron by single-photon ionization can transition from a bound to a continuum state with opposite parity.

Using the limiting cases from Section 2.3.9, we can determine the direct and exchange coefficients for a photoionization transition. Note that here, we only consider photoionization transitions from closed-shell molecules and their ions. Thus, the spin states between orbitals are not considered here. Depending on the initial occupancy of the orbital which ionization occurs from, the coefficients are as follows.

Case A: Orbital from which ionization occurs initially has two electrons. Using the first limiting case (singlet), for the orbital from which ionization occurs we have

$$a_i = 1, b_i = -1. \tag{2.153}$$

For the orbitals not involved in the photoionization transition:

- Occupancy of the orbital is zero, then $a_i = b_i = 0$ (no electrons present).
- Occupancy of the orbital is one, then $a_i = 1, b_i = \frac{1}{2}$ (second limiting case).
- Occupancy of the orbital is two, then $a_i = 2, b_i = 1$ (third limiting case).

Case B: Orbital from which ionization occurs initially has one electron. Since the orbital from which ionization occurs will not be occupied in the final state, we

have

$$a_i = b_i = 0. \tag{2.154}$$

For the orbitals not involved in the photoionization transition:

- Occupancy of the orbital is zero, then $a_i = b_i = 0$ (no electrons present).
- Occupancy of the orbital is one, then $a_i = 1, b_i = 1$ (triplet first limiting case).
- Occupancy of the orbital is two, then $a_i = 2, b_i = 1$ (third limiting case).

As mentioned as above, here we have only covered the cases when photoionization occurs in closed-shell molecules. Open-shell molecules present a more challenging problem due to the singlet/triplet spin state that arises between the open-shell orbital and the orbital from which ionization occurs. In Chapter 4, we will discuss how to obtain these direct and exchange coefficients for open-shell molecules.

2.4.3 Auger-Meitner decay

Auger-Meitner decay is a physical process in which a core or inner valence orbital hole is filled by a valence electron while another valence electron is released to the continuum. Fig. 2.1 provides an example of an Auger-Meitner decay. These Auger-Meitner transitions occur after a photoionization transition leaves a vacancy in a core or inner valence orbital.

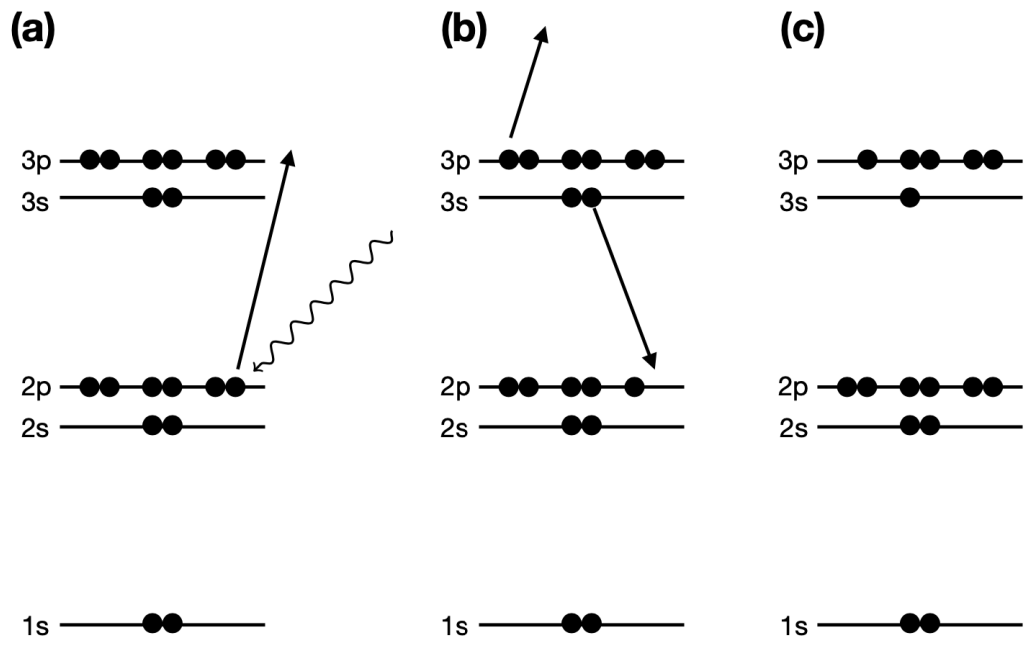

Figure 2.1: Diagram of an Auger-Meitner decay. (a) Photoionization occurs from a core electron, creating an ion with a core hole. (b) A valence electron drops to fill this core hole vacancy. The energy released is transferred to another valence electron (either from the same or different valence orbital), which is then ejected from the atom or molecule to the continuum. (c) The final state of the atom or molecule has a fully occupied core and two missing valence electrons.

By Fermi's Golden Rule in Eq. (2.148), the Auger-Meitner rate to transition from a specific initial state Φ_{init} to a specific final state Φ_{fin} is

$$\Gamma_{init\to fin} = 2\pi|\mathcal{M}|^2 = 2\pi\left|\left\langle\Phi_{fin}\right| H_I \left|\Phi_{init}\right\rangle\right|^2. \tag{2.155}$$

Then the total Auger-Meitner rate is

$$\Gamma = \overline{\sum} 2\pi N_h N_{ab}|\mathcal{M}|^2 = \overline{\sum} 2\pi N_h N_{ab}\left|\left\langle\Phi_{fin}\right| H_I \left|\Phi_{init}\right\rangle\right|^2, \tag{2.156}$$

where N_h is the number of holes in the specified core orbital, $\overline{\sum}$ sums over all final states and averages over all initial states, and N_{ab} will be defined later. The electronic Hamiltonian of the system in the second quantisation formalism [78] is

$$H_I = \sum_{ij} c_i^\dagger c_j \left\langle i\right| h \left|j\right\rangle + \frac{1}{2}\sum_{ijkl} c_i^\dagger c_j^\dagger c_l c_k \left\langle ij\right| \frac{1}{r_{12}} \left|kl\right\rangle, \tag{2.157}$$

where h is sum of the one-electron operators in H_I, $c_i^\dagger$ is a creation operator on electron i and c_j is an annihilation operator on electron j. The summations correspond to both bound and continuum electrons. The creation and annihilation operators follow the following anti-commutator rules

$$\begin{aligned} \{c_i^\dagger, c_j\} &= c_i^\dagger c_j + c_j c_i^\dagger = \delta_{i,j} \\ \{c_i, c_j\} &= 0 \\ \{c_i^\dagger, c_j^\dagger\} &= 0. \end{aligned} \tag{2.158}$$

Hence, we have that

$$\begin{aligned} \left\langle \Phi_{fin} \right| H_I \left| \Phi_{init} \right\rangle = &\sum_{ij} \left\langle \Phi_{fin} \right| c_i^\dagger c_j \left| \Phi_{init} \right\rangle \left\langle i \right| h \left| j \right\rangle \\ &+ \frac{1}{2} \sum_{ijkl} \left\langle \Phi_{fin} \right| c_i^\dagger c_j^\dagger c_l c_k \left| \Phi_{init} \right\rangle \left\langle ij \right| \frac{1}{r_{12}} \left| kl \right\rangle . \end{aligned} \tag{2.159}$$

The first term in Eq. (2.159) is zero, due to the electron configurations required for the initial and final states of an Auger-Meitner process.

$$\left\langle \Phi_{fin} \right| H_I \left| \Phi_{init} \right\rangle_{Auger} = \frac{1}{2} \sum_{ijkl} \left\langle \Phi_{fin} \right| c_i^\dagger c_j^\dagger c_l c_k \left| \Phi_{init} \right\rangle \left\langle ij \right| \frac{1}{r_{12}} \left| kl \right\rangle . \tag{2.160}$$

Let us denote the state

$$\left\langle \tilde{\Phi}_{fin} \right| = \left\langle \Phi_{fin} \right| c_\zeta^\dagger, \tag{2.161}$$

where c_ζ is an annihilation operator on the continuum electron, ζ. Then,

$$\begin{aligned}
\left\langle \tilde{\Phi}_{fin} \right| c_\zeta c_i^\dagger c_j^\dagger c_l c_k \left| \Phi_{init} \right\rangle &= \left\langle \tilde{\Phi}_{fin} \right| c_\zeta c_i^\dagger c_j^\dagger c_l c_k \left| \Phi_{init} \right\rangle + \left\langle \tilde{\Phi}_{fin} \right| c_i^\dagger c_\zeta c_j^\dagger c_l c_k \left| \Phi_{init} \right\rangle \\
&\quad - \left\langle \tilde{\Phi}_{fin} \right| c_i^\dagger c_\zeta c_j^\dagger c_l c_k \left| \Phi_{init} \right\rangle \\
&= \left\langle \tilde{\Phi}_{fin} \right| \{c_\zeta, c_i^\dagger\} c_j^\dagger c_l c_k \left| \Phi_{init} \right\rangle - \left\langle \tilde{\Phi}_{fin} \right| c_i^\dagger c_\zeta c_j^\dagger c_l c_k \left| \Phi_{init} \right\rangle \\
&= \delta_{\zeta,i} \left\langle \tilde{\Phi}_{fin} \right| c_j^\dagger c_l c_k \left| \Phi_{init} \right\rangle - \left\langle \tilde{\Phi}_{fin} \right| c_i^\dagger c_\zeta c_j^\dagger c_l c_k \left| \Phi_{init} \right\rangle \\
&= \delta_{\zeta,i} \left\langle \tilde{\Phi}_{fin} \right| c_j^\dagger c_l c_k \left| \Phi_{init} \right\rangle - \left\langle \tilde{\Phi}_{fin} \right| c_i^\dagger c_\zeta c_j^\dagger c_l c_k \left| \Phi_{init} \right\rangle \\
&\quad + \left\langle \tilde{\Phi}_{fin} \right| c_i^\dagger c_j^\dagger c_\zeta c_l c_k \left| \Phi_{init} \right\rangle - \left\langle \tilde{\Phi}_{fin} \right| c_i^\dagger c_j^\dagger c_\zeta c_l c_k \left| \Phi_{init} \right\rangle \\
&= \delta_{\zeta,i} \left\langle \tilde{\Phi}_{fin} \right| c_j^\dagger c_l c_k \left| \Phi_{init} \right\rangle - \left\langle \tilde{\Phi}_{fin} \right| c_i^\dagger \{c_j^\dagger, c_\zeta\} c_l c_k \left| \Phi_{init} \right\rangle \\
&\quad + \left\langle \tilde{\Phi}_{fin} \right| c_i^\dagger c_j^\dagger c_\zeta c_l c_k \left| \Phi_{init} \right\rangle .
\end{aligned} \tag{2.162}$$

Using the following anti-commutator relations of the creation/annihilation operators

$$\left\langle \tilde{\Phi}_{fin} \right| c_i^\dagger c_j^\dagger c_\zeta c_l c_k \left| \Phi_{init} \right\rangle = \left\langle \tilde{\Phi}_{fin} \right| c_i^\dagger c_j^\dagger c_l c_k c_\zeta \left| \Phi_{init} \right\rangle , \tag{2.163}$$

we have that

$$\begin{aligned}
\left\langle \tilde{\Phi}_{fin} \right| c_\zeta c_i^\dagger c_j^\dagger c_l c_k \left| \Phi_{init} \right\rangle &= \delta_{\zeta,i} \left\langle \tilde{\Phi}_{fin} \right| c_j^\dagger c_l c_k \left| \Phi_{init} \right\rangle - \delta_{j,\zeta} \left\langle \tilde{\Phi}_{fin} \right| c_i^\dagger c_l c_k \left| \Phi_{init} \right\rangle \\
&\quad + \left\langle \tilde{\Phi}_{fin} \right| c_i^\dagger c_j^\dagger c_l c_k c_\zeta \left| \Phi_{init} \right\rangle ,
\end{aligned} \tag{2.164}$$

where the last term is zero since there is no continuum electron for the operator to annihilate when the system is in the initial state. Hence,

$$\begin{aligned}
\left\langle \Phi_{fin} \right| H_I \left| \Phi_{init} \right\rangle_{Auger} &= \frac{1}{2} \sum_{ijkl} (\delta_{\zeta,i} \left\langle \tilde{\Phi}_{fin} \right| c_j^\dagger c_l c_k \left| \Phi_{init} \right\rangle \\
&\quad - \delta_{j,\zeta} \left\langle \tilde{\Phi}_{fin} \right| c_i^\dagger c_l c_k \left| \Phi_{init} \right\rangle) \left\langle ij \right| \frac{1}{r_{12}} \left| kl \right\rangle \\
&= \frac{1}{2} \sum_{ijk} \left\langle \tilde{\Phi}_{fin} \right| c_i^\dagger c_k c_j \left| \Phi_{init} \right\rangle (\left\langle \zeta i \right| \frac{1}{r_{12}} \left| jk \right\rangle - \left\langle i\zeta \right| \frac{1}{r_{12}} \left| jk \right\rangle).
\end{aligned} \tag{2.165}$$

We can rewrite $\left|\tilde{\Phi}_{fin}\right\rangle$ in terms of the initial state

$$\begin{aligned} \left|\tilde{\Phi}_{fin}\right\rangle &= c_s^\dagger c_a c_b \left|\Phi_{init}\right\rangle \\ \Longrightarrow \left\langle\tilde{\Phi}_{fin}\right| &= \left\langle\Phi_{init}\right| c_b^\dagger c_a^\dagger c_s, \end{aligned} \tag{2.166}$$

where a and b are the valence electrons, and s is the electron which fills the core hole. So

$$\begin{aligned} \left\langle\Phi_{fin}\right| H_I \left|\Phi_{init}\right\rangle_{Auger} = \frac{1}{2}\sum_{ijk} &\left\langle\Phi_{init}\right| c_b^\dagger c_a^\dagger c_s c_i^\dagger c_k c_j \left|\Phi_{init}\right\rangle \\ &\times \left(\left\langle\zeta i\right| \frac{1}{r_{12}} \left|jk\right\rangle - \left\langle i\zeta\right| \frac{1}{r_{12}} \left|jk\right\rangle\right). \end{aligned} \tag{2.167}$$

The operators $c_a^\dagger$ or $c_b^\dagger$ acting on $\left|\Phi_{init}\right\rangle$ will be zero by the Pauli-Exclusion Principle (since electrons a and b are contained in the initial state). Also, c_s acting on $\left|\Phi_{init}\right\rangle$ will be zero, as no electron in state s in this initial state for the operator to annihilate

(i.e. in the initial state there is a hole in the core orbital). So

$$
\begin{aligned}
\langle\Phi_{init}|\, c_b^\dagger c_a^\dagger c_s c_i^\dagger c_k c_j \,|\Phi_{init}\rangle &= \langle\Phi_{init}|\, c_b^\dagger c_a^\dagger c_s c_i^\dagger c_k c_j \,|\Phi_{init}\rangle + \langle\Phi_{init}|\, c_b^\dagger c_a^\dagger c_i^\dagger c_s c_k c_j \,|\Phi_{init}\rangle \\
&\quad - \langle\Phi_{init}|\, c_b^\dagger c_a^\dagger c_i^\dagger c_s c_k c_j \,|\Phi_{init}\rangle \\
&= \langle\Phi_{init}|\, c_b^\dagger c_a^\dagger \{c_s, c_i^\dagger\} c_k c_j \,|\Phi_{init}\rangle - \langle\Phi_{init}|\, c_b^\dagger c_a^\dagger c_i^\dagger c_s c_k c_j \,|\Phi_{init}\rangle \\
&= \delta_{s,i} \langle\Phi_{init}|\, c_b^\dagger c_a^\dagger c_k c_j \,|\Phi_{init}\rangle - \underbrace{\langle\Phi_{init}|\, c_b^\dagger c_a^\dagger c_i^\dagger c_s c_k c_j \,|\Phi_{init}\rangle}_{=0} \\
&= \delta_{s,i} \langle\Phi_{init}|\, c_b^\dagger c_a^\dagger c_k c_j \,|\Phi_{init}\rangle \\
&= \delta_{s,i} (\langle\Phi_{init}|\, c_b^\dagger c_a^\dagger c_k c_j \,|\Phi_{init}\rangle + \delta_{s,i} \langle\Phi_{init}|\, c_b^\dagger c_k c_a^\dagger c_j \,|\Phi_{init}\rangle \\
&\quad - \delta_{s,i} \langle\Phi_{init}|\, c_b^\dagger c_k c_a^\dagger c_j \,|\Phi_{init}\rangle) \\
&= \delta_{s,i} (\langle\Phi_{init}|\, c_b^\dagger \{c_a^\dagger, c_k\} c_j \,|\Phi_{init}\rangle - \delta_{s,i} \langle\Phi_{init}|\, c_b^\dagger c_k c_a^\dagger c_j \,|\Phi_{init}\rangle) \\
&= \delta_{s,i}\delta_{a,k} \langle\Phi_{init}|\, c_b^\dagger c_j \,|\Phi_{init}\rangle - \delta_{s,i} \langle\Phi_{init}|\, c_b^\dagger c_k c_a^\dagger c_j \,|\Phi_{init}\rangle \\
&= \delta_{s,i}\delta_{a,k} (\langle\Phi_{init}|\, c_b^\dagger c_j \,|\Phi_{init}\rangle + \langle\Phi_{init}|\, c_j c_b^\dagger \,|\Phi_{init}\rangle \\
&\quad - \langle\Phi_{init}|\, c_j c_b^\dagger \,|\Phi_{init}\rangle) \\
&\quad - \delta_{s,i} (\langle\Phi_{init}|\, c_b^\dagger c_k c_a^\dagger c_j \,|\Phi_{init}\rangle + \langle\Phi_{init}|\, c_b^\dagger c_k c_j c_a^\dagger \,|\Phi_{init}\rangle \\
&\quad - \langle\Phi_{init}|\, c_b^\dagger c_k c_j c_a^\dagger \,|\Phi_{init}\rangle) \\
&= \delta_{s,i}\delta_{a,k} (\langle\Phi_{init}|\, \{c_b^\dagger, c_j\} \,|\Phi_{init}\rangle - \langle\Phi_{init}|\, c_j c_b^\dagger \,|\Phi_{init}\rangle) \\
&\quad - \delta_{s,i} (\langle\Phi_{init}|\, c_b^\dagger c_k \{c_a^\dagger, c_j\} \,|\Phi_{init}\rangle + \langle\Phi_{init}|\, c_b^\dagger c_k c_j c_a^\dagger \,|\Phi_{init}\rangle) \\
&= \delta_{s,i}\delta_{a,k}\delta_{b,j} \langle\Phi_{init}|\Phi_{init}\rangle - \underbrace{\delta_{s,i}\delta_{a,k} \langle\Phi_{init}|\, c_j c_b^\dagger \,|\Phi_{init}\rangle}_{=0} \\
&\quad - \delta_{s,i}\delta_{a,j} \langle\Phi_{init}|\, c_b^\dagger c_k \,|\Phi_{init}\rangle + \delta_{s,i} \underbrace{\langle\Phi_{init}|\, c_b^\dagger c_k c_j c_a^\dagger \,|\Phi_{init}\rangle}_{=0} \\
&= \delta_{s,i}\delta_{a,k}\delta_{b,j} \langle\Phi_{init}|\Phi_{init}\rangle - \delta_{s,i}\delta_{a,j} (\langle\Phi_{init}|\, c_b^\dagger c_k \,|\Phi_{init}\rangle \\
&\quad + \langle\Phi_{init}|\, c_k c_b^\dagger \,|\Phi_{init}\rangle - \langle\Phi_{init}|\, c_k c_b^\dagger \,|\Phi_{init}\rangle) \\
&= \delta_{s,i}\delta_{a,k}\delta_{b,j} \langle\Phi_{init}|\Phi_{init}\rangle \\
&\quad - \delta_{s,i}\delta_{a,j} (\langle\Phi_{init}|\, \{c_b^\dagger, c_k\} \,|\Phi_{init}\rangle + \underbrace{\langle\Phi_{init}|\, c_k c_b^\dagger \,|\Phi_{init}\rangle}_{=0}) \\
&= \delta_{s,i}\delta_{a,k}\delta_{b,j} \underbrace{\langle\Phi_{init}|\Phi_{init}\rangle}_{=1} - \delta_{s,i}\delta_{a,j}\delta_{b,k} \underbrace{\langle\Phi_{init}|\Phi_{init}\rangle}_{=1} \\
&= \delta_{s,i}\delta_{a,k}\delta_{b,j} - \delta_{s,i}\delta_{a,j}\delta_{b,k}.
\end{aligned}
\tag{2.168}
$$

Hence,

$$\begin{aligned}
\left\langle \Phi_{fin} \right| H_I \left| \Phi_{init} \right\rangle_{Auger} &= \frac{1}{2}\sum_{ijk}(\delta_{s,i}\delta_{a,k}\delta_{b,j} - \delta_{s,i}\delta_{a,j}\delta_{b,k}) \\
&\times (\langle \zeta i| \frac{1}{r_{12}} |jk\rangle - \langle i\zeta| \frac{1}{r_{12}} |jk\rangle) \\
&= \frac{1}{2}(\langle \zeta s| \frac{1}{r_{12}} |ba\rangle - \langle \zeta s| \frac{1}{r_{12}} |ab\rangle \\
&- \langle s\zeta| \frac{1}{r_{12}} |ba\rangle + \langle s\zeta| \frac{1}{r_{12}} |ab\rangle) \\
&= \frac{1}{2}(\langle \zeta s| \frac{1}{r_{12}} |ba\rangle - \langle \zeta s| \frac{1}{r_{12}} |ab\rangle \\
&- \langle \zeta s| \frac{1}{r_{12}} |ab\rangle + \langle \zeta s| \frac{1}{r_{12}} |ba\rangle) \\
&= \langle \zeta s| \frac{1}{r_{12}} |ba\rangle - \langle \zeta s| \frac{1}{r_{12}} |ab\rangle .
\end{aligned} \tag{2.169}$$

The first term is the direct term, and the second term is the exchange term. Let us consider these individually. We can write the direct term in terms of double integral

$$\langle \zeta s| \frac{1}{r_{12}} |ba\rangle = \delta_{\mu_\zeta \mu_b}\delta_{\mu_s \mu_a} \int d^3\mathbf{r}_1 \int d^3\mathbf{r}_2 \phi^*_\zeta(\mathbf{r}_1)\phi_b(\mathbf{r}_1)\frac{1}{r_{12}}\phi^*_s(\mathbf{r}_2)\phi_a(\mathbf{r}_2), \tag{2.170}$$

where e.g. μ_b is the projection of the spin of electron b. Since the $\frac{1}{r_{12}}$ operator only acts on space, the Kronecker deltas $\delta_{\mu_\zeta \mu_b}$ and $\delta_{\mu_s \mu_a}$ ensure that the spin of the system is conserved. The continuum electron must have the same spin as one of the valence electrons, and the core electron should have the same spin as the other valence electron. Using the SCE and the multipole expansion [68]

$$\frac{1}{r_{12}} = \sum_{kq} \frac{4\pi}{2k+1} \frac{r^k_<}{r^{k+1}_>} Y^*_{kq}(\theta_1, \phi_1) Y_{kq}(\theta_2, \phi_2), \tag{2.171}$$

we have

$$\begin{aligned}\langle \zeta s|\frac{1}{r_{12}}|ba\rangle = &\sum_{\substack{kql_\zeta l_s l_b l_a\\ m_a m_b m_s m_\zeta}} \delta_{\mu_\zeta\mu_b}\delta_{\mu_s\mu_a}\\ &\times\int d^3\mathbf{r}_1\int d^3\mathbf{r}_2\frac{P^*_{l_\zeta m_\zeta}(r_1)Y^*_{l_\zeta m_\zeta}(\theta_1,\phi_1)P_{l_b m_b}(r_1)Y_{l_b m_b}(\theta_1,\phi_1)}{r_1^2}\\ &\times\frac{4\pi}{2k+1}\frac{r_<^k}{r_>^{k+1}}Y^*_{kq}(\theta_1,\phi_1)Y_{kq}(\theta_2,\phi_2)\\ &\times\frac{P^*_{l_s m_s}(r_2)Y^*_{l_s m_s}(\theta_2,\phi_2)P_{l_a m_a}(r_2)Y_{l_a m_a}(\theta_2,\phi_2)}{r_2^2}.\end{aligned} \tag{2.172}$$

Now using that $Y^*_{lm}=(-1)^m Y_{l-m}$ and the relation between spherical harmonics and Wigner-3j symbols [68]

$$\begin{aligned}\int d\Omega Y^*_{LM}(\theta,\phi)Y_{kq}(\theta,\phi)Y_{l'm'}(\theta,\phi) = (-1)^M\sqrt{\frac{(2L+1)(2k+1)(2l'+1)}{4\pi}}\\ \times\begin{pmatrix}L & k & l'\\ 0 & 0 & 0\end{pmatrix}\begin{pmatrix}L & k & l'\\ -M & q & m'\end{pmatrix},\end{aligned} \tag{2.173}$$

we have

$$\begin{aligned}\langle \zeta s|\frac{1}{r_{12}}|ba\rangle = &\,\delta_{\mu_\zeta\mu_b}\delta_{\mu_s\mu_a}\\ &\times\sum_{\substack{kql_\zeta l_s l_b l_a\\ m_a m_b m_s m_\zeta}}\int dr_1\int dr_2 P^*_{l_\zeta m_\zeta}(r_1)P^*_{l_s m_s}(r_2)\frac{r_<^k}{r_>^{k+1}}P_{l_a m_a}(r_2)P_{l_b m_b}(r_1)\\ &\times(-1)^{m_s}\sqrt{(2l_s+1)(2l_a+1)}\begin{pmatrix}l_s & k & l_a\\ 0 & 0 & 0\end{pmatrix}\begin{pmatrix}l_s & k & l_a\\ -m_s & q & m_a\end{pmatrix}\\ &\times(-1)^{q+m_\zeta}\sqrt{(2l_\zeta+1)(2l_b+1)}\begin{pmatrix}k & l_\zeta & l_b\\ 0 & 0 & 0\end{pmatrix}\begin{pmatrix}k & l_\zeta & l_b\\ -q & -m_\zeta & m_b\end{pmatrix}.\end{aligned} \tag{2.174}$$

Similarly the exchange term can be written as

$$\begin{aligned}\langle \zeta s| \frac{1}{r_{12}} |ab\rangle &= \delta_{\mu_\zeta \mu_a} \delta_{\mu_s \mu_b} \\ &\times \int d^3\mathbf{r}_1 \int d^3\mathbf{r}_2 \frac{P^*_{l_\zeta m_\zeta}(r_1) Y^*_{l_\zeta m_\zeta}(\theta_1,\phi_1) P_{l_a m_a}(r_1) Y_{l_a m_a}(\theta_1,\phi_1)}{r_1^2} \\ &\times \frac{4\pi}{2k+1} \frac{r_<^k}{r_>^{k+1}} Y^*_{kq}(\theta_1,\phi_1) Y_{kq}(\theta_2,\phi_2) \\ &\times \frac{P^*_{l_s m_s}(r_2) Y^*_{l_s m_s}(\theta_2,\phi_2) P_{l_b m_b}(r_2) Y_{l_b m_b}(\theta_2,\phi_2)}{r_2^2}.\end{aligned} \tag{2.175}$$

Using the same relations as for the Direct term we find

$$\begin{aligned}\langle \zeta s| \frac{1}{r_{12}} |ab\rangle &= \delta_{\mu_\zeta \mu_a} \delta_{\mu_s \mu_b} \\ &\times \sum_{\substack{kql_\zeta l_s l_b l_a \\ m_a m_b m_s m_\zeta}} \int dr_1 \int dr_2 P^*_{l_\zeta m_\zeta}(r_1) P^*_{l_s m_s}(r_2) \frac{r_<^k}{r_>^{k+1}} P_{l_a m_a}(r_1) P_{l_b m_b}(r_2) \\ &\times (-1)^{m_s} \sqrt{(2l_s+1)(2l_b+1)} \begin{pmatrix} l_s & k & l_b \\ 0 & 0 & 0 \end{pmatrix} \begin{pmatrix} l_s & k & l_b \\ -m_s & q & m_b \end{pmatrix} \\ &\times (-1)^{q+m_\zeta} \sqrt{(2l_\zeta+1)(2l_a+1)} \begin{pmatrix} k & l_\zeta & l_a \\ 0 & 0 & 0 \end{pmatrix} \begin{pmatrix} k & l_\zeta & l_a \\ -q & -m_\zeta & m_a \end{pmatrix}.\end{aligned} \tag{2.176}$$

Combining the direct and exchange terms gives

$$
\begin{aligned}
&\langle \zeta s| \frac{1}{r_{12}} |ba\rangle - \langle \zeta s| \frac{1}{r_{12}} |ab\rangle \\
&= \delta_{\mu_\zeta \mu_b} \delta_{\mu_s \mu_a} \sum_{\substack{kql_\zeta l_s l_b l_a \\ m_a m_b m_s m_\zeta}} \int dr_1 \int dr_2 P^*_{l_\zeta m_\zeta}(r_1) P^*_{l_s m_s}(r_2) \frac{r_<^k}{r_>^{k+1}} P_{l_a m_a}(r_2) P_{l_b m_b}(r_1) \\
&\times (-1)^{m_s} \sqrt{(2l_s+1)(2l_a+1)} \begin{pmatrix} l_s & k & l_a \\ 0 & 0 & 0 \end{pmatrix} \begin{pmatrix} l_s & k & l_a \\ -m_s & q & m_a \end{pmatrix} \\
&\times (-1)^{q+m_\zeta} \sqrt{(2l_\zeta+1)(2l_b+1)} \begin{pmatrix} k & l_\zeta & l_b \\ 0 & 0 & 0 \end{pmatrix} \begin{pmatrix} k & l_\zeta & l_b \\ -q & -m_\zeta & m_b \end{pmatrix} \\
&- \delta_{\mu_\zeta \mu_a} \delta_{\mu_s \mu_b} \sum_{\substack{kql_\zeta l_s l_b l_a \\ m_a m_b m_s m_\zeta}} \int dr_1 \int dr_2 P^*_{l_\zeta m_\zeta}(r_1) P^*_{l_s m_s}(r_2) \frac{r_<^k}{r_>^{k+1}} P_{l_a m_a}(r_2) P_{l_b m_b}(r_1) \\
&\times (-1)^{m_s} \sqrt{(2l_s+1)(2l_b+1)} \begin{pmatrix} l_s & k & l_b \\ 0 & 0 & 0 \end{pmatrix} \begin{pmatrix} l_s & k & l_b \\ -m_s & q & m_b \end{pmatrix} \\
&\times (-1)^{q+m_\zeta} \sqrt{(2l_\zeta+1)(2l_a+1)} \begin{pmatrix} k & l_\zeta & l_a \\ 0 & 0 & 0 \end{pmatrix} \begin{pmatrix} k & l_\zeta & l_a \\ -q & -m_\zeta & m_a \end{pmatrix}.
\end{aligned}
\tag{2.177}
$$

Note that similarly to photoionization, the Wigner-3j symbols in this expression explain how we obtain the l and m numbers of the continuum orbital. From the second and fourth Wigner-3j symbols, we find that $m_\zeta = m_a + m_b - m_s$. For homonuclear molecules, we can determine the parity of the continuum electron using the first and third Wigner-3j symbols.

The formula for the matrix element in Eq. (2.177) only corresponds to an Auger-Meitner process for two electrons in specific orbitals, with specific spin, filling a hole in a particular orbital with particular spin and releasing an electron of specific spin. In order to find the total Auger-Meitner rate, independent of the spin of the electrons, we sum over the final states and average over the initial states. The summation over the final states is due to the possible pathways from a single initial state, the average over the initial state is because that state is not explicitly defined. In this case, the initial state has a core hole in a specific orbital with either up or down spin.

We average over these two possibilities. We also sum over the different combinations of spin for the two valence holes in the final state. This gives an expression for the total Auger-Meitner transition rate as

$$\Gamma_{a,b\to s} = \sum_{\mu_a\mu_b\mu_s\mu_\zeta} \pi N_h N_{ab} \sum_\zeta \left| \langle \zeta s | \frac{1}{r_{12}} |ba\rangle - \langle \zeta s | \frac{1}{r_{12}} |ab\rangle \right|^2, \tag{2.178}$$

where the $\mu_a\mu_b\mu_s\mu_\zeta$ summation is over the individual spin projections of each orbital involved in the transition. The summation over ζ denotes a summation over the LM channels of the continuum wavefunction. The weighting factor, N_{ab}, is given by

$$N_{ab} = \begin{cases} \frac{N_a N_b}{2\times 2} \text{ for valence electrons in different orbitals} \\ \\ \frac{N_a(N_a-1)}{2} \text{ for valence electrons in the same orbital} \end{cases}, \tag{2.179}$$

and N_a, N_b are the occupancy of the valence orbitals in the initial state. If instead of summing over the individual spin projections we wish to sum over the total spin, S, and its projection, M_S, we can perform the following transformation

$$\begin{aligned} |ba\mu_a\mu_b|12\rangle &= \sum_{S,M_S} |baSMS|12\rangle \langle baSMS|12|ba\mu_a\mu_b|12\rangle \\ &= \sum_{S,M_S} (SM_S|\mu_a\mu_b) |baSMS|12\rangle , \end{aligned} \tag{2.180}$$

where $(SM_S|\mu_a\mu_b)$ are Clebsch–Gordan coefficients. Using symmetry properties of the Clebsch–Gordan coefficients (see Appendix B), for the exchange term we have

$$|baSMS|21\rangle = (-1)^{S-\frac{1}{2}-\frac{1}{2}} |baSMS|12\rangle . \tag{2.181}$$

Using Eqns. (2.180) and (2.181), as well as the orthogonality of the Cleb-

sch–Gordan coefficients (see Appendix B), Eq. (2.178) can be rewritten as

$$\Gamma_{a,b\to s} = \sum_{SM_S} \pi N_h N_{ab} \sum_{\zeta} \left| D + (-1)^S E \right|^2, \tag{2.182}$$

where D, E are the direct and exchange terms $\langle \zeta s | \frac{1}{r_{12}} | ba \rangle$ and $\langle \zeta s | \frac{1}{r_{12}} | ab \rangle$, respectively, without the Kronecker-delta functions in Eq. (2.177). The advantage of using the SM_S scheme is that we can obtain the contribution from the singlet and triplet states separately. For singlet states $S = 0$ and for triplet states $S = 1$.

Using the limiting cases from Section 2.3.9, we can determine the direct and exchange coefficients for an Auger-Meitner decay. Note that in all cases it is impossible for the core orbital to have 2 electrons initially or 0 electrons in the final state by definition of a Auger-Meitner process. Similarly, it is also impossible for the valence orbital(s) to have 2 electrons in the final state. Furthermore, clearly it is the case that the occupancy of orbitals not involved in the Auger-Meitner process will be equal in the initial and final states.

Case A: Both valence electrons are from the same orbital. Since the valence electrons are in the same orbital in the initial state, they form a singlet state. In the final state, the valence orbital is not occupied. Hence, we have

$$a_i = b_i = 0. \tag{2.183}$$

For the core orbital which is filled by one of the valence electrons in the final state:

- Occupancy of core orbital is initially zero and finally one, then $a_i = 1, b_i = -1$ (singlet first limiting case).
- Occupancy of core orbital is initially one and finally two, then $a_i = 2, b_i = 1$ (third limiting case).

For orbitals not involved in the Auger-Meitner process:

- Occupancy of orbital is zero, then $a_i = b_i = 0$ (no electrons present).
- Occupancy of orbital is one, then $a_i = 1, b_i = \frac{1}{2}$ (second limiting case).

- Occupancy of orbital is two, then $a_i = 2, b_i = 1$ (third limiting case).

Case B: Valence electrons in different orbitals. For the cases below, we denote i_2 as the orbital where ionization occurs, and i_1 as the orbital which fills the core orbital.

Case B1: Both valence orbitals initially have two electrons. Using the first (singlet) and second limiting cases for orbitals i_2 and i_1, respectively, we have

$$a_{i_2} = 1, b_{i_2} = -1 \quad a_{i_1} = 1, b_{i_1} = \frac{1}{2}. \tag{2.184}$$

For the core orbital which is filled by one of the valence electrons in orbital i_1 in the final state:

- Occupancy of the core orbital is initially zero and finally one, then $a_i = 1, b_i = \frac{1}{2}$ (second limiting case).
- Occupancy of the core orbital is initially one and finally two, then $a_i = 2, b_i = 1$ (third limiting case).

For orbitals not involved in the Auger-Meitner process:

- Occupancy of the orbital is zero, then $a_i = b_i = 0$ (no electrons present).
- Occupancy of the orbital is one, then $a_i = 1, b_i = \frac{1}{2}$ (second limiting case).
- Occupancy of the orbital is two, then $a_i = 2, b_i = 1$ (third limiting case).

Case B2: Orbital i_2 initially has two electrons, orbital i_1 has one electron initially. Using the first (singlet) limiting case for orbital i_2 and the fact that orbital i_1 will have no electrons in the final state, we have

$$a_{i_2} = 1, b_{i_2} = -1, \quad a_{i_1} = b_{i_1} = 0. \tag{2.185}$$

For the core orbital which is filled by the valence electron in orbital i_1 in the final state:

- Occupancy of the core orbital is initially zero and finally one, then $a_i = 1, b_i = \frac{1}{2}$ (second limiting case).
- Occupancy of the core orbital is initially one and finally two, then $a_i = 2, b_i = 1$ (third limiting case).

For orbitals not involved in the Auger-Meitner process:

- Occupancy of the orbital is zero, then $a_i = b_i = 0$ (no electrons present).
- Occupancy of the orbital is one, then $a_i = 1, b_i = \frac{1}{2}$ (second limiting case).
- Occupancy of the orbital is two, then $a_i = 2, b_i = 1$ (third limiting case).

Case B3: Orbital i_2 initially has one electron, orbital i_1 has two electrons initially. Orbital i_2 will have no electrons in the final state. For orbital i_1, we use the fourth limiting case. We find that

$$a_{i_2} = b_{i_2} = 0, \quad a_{i_1} = 1, b_{i_1} = \frac{1}{2}. \tag{2.186}$$

For the core orbital which is filled by one of the valence electrons in orbital i_1 in the final state:

- Occupancy of the core orbital is initially zero and finally one, then $a_i = 1, b_i = \frac{1}{2}$ (fourth limiting case).
- Occupancy of the core orbital is initially one and finally two, then $a_i = 2, b_i = 1$ (third limiting case).

For orbitals not involved in the Auger-Meitner process:

- Occupancy of the orbital is zero, then $a_i = b_i = 0$ (no electrons present).
- Occupancy of the orbital is one, then $a_i = 1, b_i = -1$ for a singlet state with the continuum orbital (singlet first limiting case), $b_i = 1$ for a triplet state with the continuum orbital (triplet first limiting case).
- Occupancy of the orbital is two, then $a_i = 2, b_i = 1$ (third limiting case).

Case B4: Both valence orbitals initially have one electron. Since both valence orbitals will have no electrons in the final state, we have

$$a_{i_2} = b_{i_2} = 0, \quad a_{i_1} = b_{i_1} = 0. \tag{2.187}$$

For the core orbital which is filled by the valence electrons in orbital i_1 in the final state:

- Occupancy of the core orbital is initially zero and finally one, then $a_i = 1, b_i = -1$ for a singlet state with the continuum orbital (singlet first limiting case), $b_i = 1$ for a triplet state with the continuum orbital (triplet first limiting case).
- Occupancy of the core orbital is initially one and finally two, then $a_i = 2, b_i = 1$ (third limiting case).

For orbitals not involved in the Auger-Meitner process:

- Occupancy of the orbital is zero, then $a_i = b_i = 0$ (no electrons present).
- Occupancy of the orbital is one, then $a_i = 1, b_i = -1$ for a singlet state with the continuum orbital (singlet first limiting case), $b_i = 1$ for a triplet state with the continuum orbital (triplet first limiting case).
- Occupancy of the orbital is two, then $a_i = 2, b_i = 1$ (third limiting case).

2.5 Molecular symmetry

Molecular orbitals possess various forms of symmetry which determine their properties. For each of type of symmetry there is an associated symmetry operation. A point group is a group of symmetry operations with the binary operation of applying the successive operations to the molecule. The elements of a point group are called irreducible representations. Homonuclear and heteronuclear diatomic molecules are part of the $D_{\infty h}$ and $C_{\infty v}$ point groups, respectively. Both of these point groups have an infinite rotational symmetry around the internuclear axis. The $D_{\infty h}$ point group contains an infinite number of two-fold rotational symmetries perpendicular to the

internuclear axis and a single reflective symmetry perpendicular to the internuclear axis. The $C_{\infty v}$ point group contains an infinite number of reflective symmetries parallel to the internuclear axis. The point group of the molecule puts a restriction on the values of l and m that are required in the SCE. These restrictions are shown in Tables 2.1 and 2.2 for $D_{\infty h}$ and $C_{\infty v}$, respectively.

l	$\lvert m\rvert = 0$	$\lvert m\rvert = 1$	$\lvert m\rvert = 2$	$\lvert m\rvert = 3$	$\lvert m\rvert = 4$
0	σ_g				
1	σ_u	π_u			
2	σ_g	π_g	δ_g		
3	σ_u	π_u	δ_u	ϕ_u	
4	σ_g	π_g	δ_g	ϕ_g	γ_g

Table 2.1: Molecular orbitals in $D_{\infty h}$ in terms of the l and m quantum numbers.

l	$\lvert m\rvert = 0$	$\lvert m\rvert = 1$	$\lvert m\rvert = 2$	$\lvert m\rvert = 3$	$\lvert m\rvert = 4$
0	σ				
1	σ	π			
2	σ	π	δ		
3	σ	π	δ	ϕ	
4	σ	π	δ	ϕ	γ

Table 2.2: Molecular orbitals in $C_{\infty v}$ in terms of the l and m quantum numbers.

Quantum-chemistry packages, such as MOLPRO, which we use to calculate the bound orbital wavefunctions do not support infinite point groups and perform calculations in lower symmetry point groups. MOLPRO utilises the D_{2h} point group for homonuclear diatomic molecules and the C_{2v} point group for heteronuclear diatomic molecules. In Tables 2.3 and 2.4, we give the correspondence between infinite and finite point groups for homonuclear and heteronuclear molecules, respectively. In some cases, a molecular orbital in the infinite point group is made up of two degenerate irreducible representations in the finite group. For example, the π_u orbital in the $D_{\infty h}$ point group is made up of two degenerate D_{2h} irreducible representations, namely B_{2u} and B_{3u}. These two irreducible representations correspond to the two degenerate orbitals that make up a π_u orbital.

$D_{\infty h}$		D_{2h}
σ_g	$\rightarrow$	A_g
σ_u	$\rightarrow$	B_{1u}
π_g	$\rightarrow$	$B_{3g}+B_{2g}$
π_u	$\rightarrow$	$B_{3u}+B_{2u}$
δ_g	$\rightarrow$	$B_{1g}+A_g$
δ_u	$\rightarrow$	$B_{1u}+A_u$
ϕ_g	$\rightarrow$	$B_{3g}+B_{2g}$
ϕ_u	$\rightarrow$	$B_{3u}+B_{2u}$
γ_g	$\rightarrow$	$B_{1g}+A_g$

Table 2.3: Molecular orbitals in the $D_{\infty h}$ point group in terms of the elements of the D_{2h} point group.

$C_{\infty v}$		C_{2v}
σ	$\rightarrow$	A_1
π	$\rightarrow$	B_1+B_2
δ	$\rightarrow$	A_1+A_2
ϕ	$\rightarrow$	B_1+B_2
γ	$\rightarrow$	A_1+A_2

Table 2.4: Molecular orbitals in the $C_{\infty v}$ point group in terms of the elements of the C_{2v} point group.

In Tables 2.5 and 2.6, we give the values of l and m for each element of the D_{2h} and C_{2v} point group, respectively, up to $l=4$.

l									
					$m=0$				
0					A_g				
				$m=-1$	$m=0$	$m=1$			
1				B_{2u}	B_{1u}	B_{3u}			
			$m=-2$	$m=-1$	$m=0$	$m=1$	$m=2$		
2			B_{1g}	B_{2g}	A_g	B_{3g}	A_g		
		$m=-3$	$m=-2$	$m=-1$	$m=0$	$m=1$	$m=2$	$m=3$	
3		B_{2u}	A_u	B_{2u}	B_{1u}	B_{3u}	B_{1u}	B_{3u}	
	$m=-4$	$m=-3$	$m=-2$	$m=-1$	$m=0$	$m=1$	$m=2$	$m=3$	$m=4$
4	A_g	B_{2g}	B_{1g}	B_{2g}	A_g	B_{3g}	A_g	B_{3g}	A_g

Table 2.5: Elements of the D_{2h} point group in terms of the l and m quantum numbers.

l									
					$m=0$				
0					A_1				
				$m=-1$	$m=0$	$m=1$			
1				B_2	A_1	B_1			
			$m=-2$	$m=-1$	$m=0$	$m=1$	$m=2$		
2			A_2	B_2	A_1	B_1	A_1		
		$m=-3$	$m=-2$	$m=-1$	$m=0$	$m=1$	$m=2$	$m=3$	
3		B_2	A_2	B_2	A_1	B_1	A_1	B_1	
	$m=-4$	$m=-3$	$m=-2$	$m=-1$	$m=0$	$m=1$	$m=2$	$m=3$	$m=4$
4	A_2	B_2	A_2	B_2	A_1	B_1	A_1	B_1	A_1

Table 2.6: Elements of the C_{2v} point group in terms of the l and m quantum numbers.

Chapter 3

Mapping the direction of electron ionization to phase delay between VUV and IR laser pulses

3.1 Introduction

In this chapter, we theoretically demonstrate that control of electron currents is possible. As in the attosecond streak camera [30], we achieve control by varying the phase delay between a linearly-polarized VUV pulse and a circularly-polarized IR pulse.

We show control of electron motion in the context of the N_2 molecule. Our approach involves, first, releasing the electron at low velocity above the ionization threshold of an atom or molecule using a VUV pulse. The VUV pulse with duration significantly smaller than the IR pulse serves to define the space and time origin of the electron. We consider transitions from an inner or outer valence electron of N_2. Then, the newly released electron is accelerated by a circularly-polarized IR radiation to speeds that are proportional to the field strength and inversely proportional to frequency. We achieve high-electron velocities by choosing the IR pulse to have a long wavelength, $\lambda = 2.3$ μm, and intensity of up to 5×10^{13} W/cm^2.

Since this current study is theoretical and we are thus not constrained by laboratory restrictions, we study N_2 molecules aligned along the linear polarization

of the VUV pulse. We demonstrate a one-to-one mapping between the direction of electron escape and the phase delay between the IR and VUV pulses, achieving excellent control of electron motion.

To show control of electron dynamics, we develop a hybrid quantum-classical approach. The dipole matrix element to transition from an initial bound state of the N_2 molecule to the continuum is obtained using very accurate quantum mechanical techniques. The latter involve computing continuum molecular states. We obtain these states by solving a system of HF equations in the SCE [29]. Also, we derive in detail and implement in our formulation the dependence of the dipole matrix element on the angles that determine the direction of electron ionization due to the VUV pulse.

Following release of the electron in the IR pulse, we neglect the Coulomb potential and in the context of the SFA evolve classical trajectories, while fully accounting for quantum interference. The development of the classical aspect of this hybrid approach is based on previous work in classical techniques describing ionization in strongly driven systems [79].

3.2 Methods

In what follows, we adopt two coordinate systems, namely the molecular-fixed frame (MF frame) and the laboratory frame (LAB frame), which we can convert between in theoretical calculations. The z-axis of the MF frame is along the principal axis of the molecule. The z-axis of the LAB frame is along the polarisation direction of the laser . Both the MF frame and the LAB frame have their origins at the centre of mass of the molecule. We transform the angular dependence of the wavefunction from the LAB to the MF frame using the convention adapted from [80] by [81] and [73]

$$Y_{l_1,m_1}(\hat{r}) = \sum_{m_2} Y_{l_1,m_2}(\hat{r}')\mathcal{D}^{l_1}_{m_2,m_1}(\hat{R}), \tag{3.1}$$

where $\mathcal{D}^{l_1}_{m_2 m_1}(\hat{R})$ is a Wigner rotation matrix [80], the $Y_{l_1 m_1}, Y_{l_1 m_2}$ are spherical harmonics, l_1 is the angular momentum quantum numbers and m_1, m_2 are the magnetic

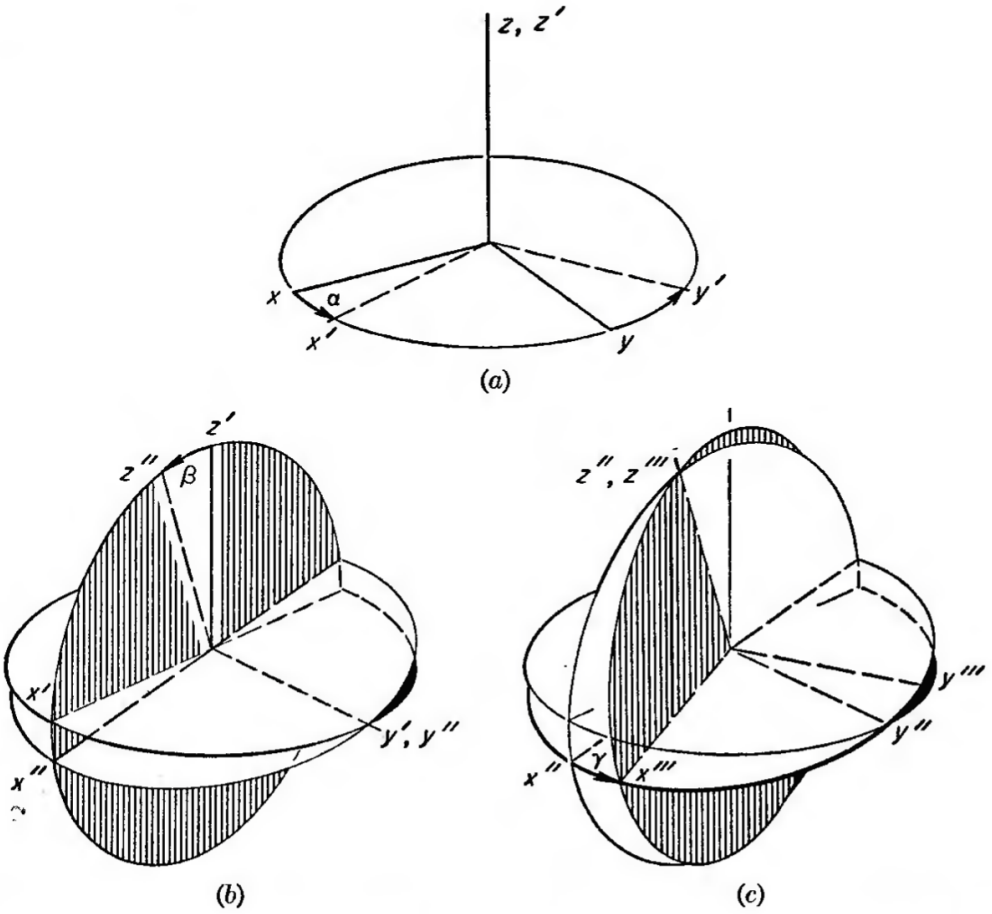

Figure 3.1: The following diagram is taken from Ref. [80]. The Euler angles $\hat{R} = (\alpha, \beta, \gamma)$ define the transition from the molecular frame to the LAB frame. (a) A rotation through an angle α about the z axis (b) a rotation through an angle β about the new y axis, y′ (c) a rotation through an angle γ about the new z axis, z″.

quantum numbers. Note that the unprimed $\vec{r}$ vector denotes the position of the electron in the MF frame, while the primed one denotes the LAB frame. The Euler angles $\hat{R} = (\alpha, \beta, \gamma)$ define the transition from the LAB frame to the molecular frame. For the Euler angles, we use the convention adapted by Rose [80] as in Fig. 3.1. Namely, to transition from the LAB to the molecular frame, we perform a rotation through an angle α about the z axis, then a rotation through an angle β about the new y axis (the y axis after the first rotation) and finally a rotation through an angle γ about the new z axis (the z axis after the second rotation).

Wigner-D functions are the matrix elements of the rotation operator $\mathcal{R} =$

$e^{-i\alpha J_z}e^{-i\beta J_y}e^{-i\gamma J_z}$, i.e.

$$\begin{aligned}\mathcal{D}^{l}_{m',m}(\hat{R}) &= \mathcal{D}^{l}_{m',m}(\alpha,\beta,\gamma) \\ &= \left\langle lm' \right| \mathcal{R}(\alpha,\beta,\gamma) \left| lm \right\rangle \\ &= e^{-im'\alpha} d^{l}_{m',m}(\beta) e^{-im\gamma},\end{aligned} \tag{3.2}$$

where

$$\begin{aligned}d^{l}_{m',m}(\beta) &= [(l+m')!(l-m')!(l+m)!(l-m)!]^{\frac{1}{2}} \\ &\times \sum_{s=\max(0,m-m')}^{\min(l+m,l-m')} \left[\frac{(-1)^{m'-m+s}(\cos\frac{\beta}{2})^{2l+m-m'-2s}}{(l+m-s)!s!} \right. \\ &\times \left. \frac{(\sin\frac{\beta}{2})^{m'-m+2s}}{(m'-m+s)!(l-m'-s)!} \right].\end{aligned} \tag{3.3}$$

Details concerning the efficient computation of the function $d^{l}_{m',m}$ are given in Ref. [82], which we also adopt in this work. From (3.1) it follows that one converts from the MF to the LAB frame as follows

$$Y_{l_1,m_1}(\hat{r}') = \sum_{m_2} Y_{l_1,m_2}(\hat{r}) \mathcal{D}^{l_1 *}_{m_1,m_2}(\hat{R}). \tag{3.4}$$

The momentum eigenstate of the electron ejected in the continuum with momentum k after absorbing one photon from the XUV laser pulse that is normalized in energy is given as follows [83], [73], [84]

$$\left| \vec{k} \right\rangle = \sum_{l_1,m_1} i^{l_1} e^{-i\sigma_{l_1}} Y^{*}_{l_1,m_1}(\hat{k}) \psi_{l_1,m_1}(\vec{r};k), \tag{3.5}$$

where the $\vec{k}$ eigenstate is defined in the MF frame and $\psi_{l_1 m_1}(\vec{r};k)$ is an energy eigenstate normalised in energy, with energy $\varepsilon = \frac{k^2}{2}$. Moreover, $\sigma_l = \sigma_l(k) = \arg\Gamma(l+1-\frac{iZ}{k})$ is the Coulomb phase shift, where Z is the net charge on the molecular ion after the ejection of one electron. Then we obtain the momentum eigenstate

in the LAB frame after substituting (3.1) into (3.5) as follows

$$\left|\vec{k}'\right\rangle = \sum_{l_1,m_1,m_2} i^{l_1} e^{-i\sigma_{l_1}} Y^*_{l_1,m_2}(\hat{k}') \mathcal{D}^{l_1*}_{m_2,m_1}(\hat{R}) \psi_{l_1,m_1}(\vec{r};k). \tag{3.6}$$

3.2.1 Dipole Matrix element

To calculate photoionization cross sections, we require the dipole matrix elements multiplied with their conjugate for each polarization of the beam. The electric-dipole matrix element describes the transition of an electron from an initial state $\psi_i(\vec{r})$ to a final state $\vec{k}'$ due to a single photoabsorbtion from an XUV pulse is given by

$$D_M = D_M(\vec{k}') = \left\langle \vec{k}' \middle| \vec{r}' \cdot \hat{n}' \middle| \psi_i \right\rangle, \tag{3.7}$$

where

$$\vec{r}' \cdot \hat{n}' = \sqrt{\frac{4\pi}{3}} r' Y_{1,M}(\hat{r}'), \tag{3.8}$$

with $\hat{n}'$ being the polarization unit vector of the electric field, and M taking the values of 0 for linear polarization and ± 1 for right/left circular polarization in the LAB frame. Substituting Eq. (3.1) into Eq. (3.8) gives

$$\vec{r}' \cdot \hat{n}' = \sqrt{\frac{4\pi}{3}} r \sum_m Y_{1,m}(\hat{r}) \mathcal{D}^{1*}_{M,m}(\hat{R}), \tag{3.9}$$

where $m = -1, 0, 1$. Next, substituing Eq. (3.9) and Eq. (3.6) into Eq. (3.7) we find

$$D_M = \sum_{l_1,m_1,m_2,m} e^{i\sigma_{l_1}} (-i)^{l_1} \mathcal{D}^{l_1}_{m_2,m_1}(\hat{R}) \mathcal{D}^{1*}_{M,m}(\hat{R}) Y_{l_1,m_2}(\hat{k}') D_{l_1,m_1,m,i}, \tag{3.10}$$

where

$$D_{l_1,m_1,m,i} = \iiint d\vec{r} \psi^*_{l_1,m_1}(\vec{r};k) \sqrt{\frac{4\pi}{3}} r Y_{1,m}(\hat{r}) \psi_i(\vec{r}). \tag{3.11}$$

Eq. (3.10) is the most general form of the dipole matrix element for an electron to be ejected with a $\vec{k}'$ vector in the LAB frame after absorbing a single photon from the initial state ψ_i. In what follows, we give the general expression for $D_M D^*_M$ and show that averaging this over all molecular orientations, $\hat{R}$, and integrating over all

continuum-electron directions, $\hat{k}'$, yields a value proportional to the total photoionization cross section, see Eq. (2.149). Multiplying Eq. (3.10) with its conjugate, we have

$$\begin{aligned} D_M D_M^* = & \sum_{\substack{l_1 m_1 m_2 \\ l_2 m_1' m_2' \\ m m'}} e^{i(\sigma_{l_1} - \sigma_{l_2})} (-i)^{l_1} i^{l_2} \\ & \times \mathcal{D}^{l_1}_{m_2 m_1}(\hat{R}) \mathcal{D}^{l_2 *}_{m_2' m_1'}(\hat{R}) \mathcal{D}^{1 *}_{M m}(\hat{R}) \mathcal{D}^{1}_{M m'}(\hat{R}) \\ & \times D_{l_1 m_1 m} D^*_{l_2 m_1' m'} Y^*_{l_2 m_2'}(\hat{k}') Y_{l_1 m_2}(\hat{k}') \end{aligned} \tag{3.12}$$

where

$$\begin{aligned} D_{l_1 m_1 m} &= D_{l_1 m_1 m}(k) = \left\langle \psi_{l_1 m_1}(\vec{r};k) \right| \sqrt{\frac{4\pi}{3}} r Y_{1m}(\hat{r}) \left| \psi_i(\vec{r}) \right\rangle \\ D^*_{l_2 m_1' m'} &= D^*_{l_2 m_1' m'}(k) = \left\langle \psi_i(\vec{r}) \right| \sqrt{\frac{4\pi}{3}} r Y^*_{1m'}(\hat{r}) \left| \psi_{l_2 m_1'}(\vec{r};k) \right\rangle \end{aligned} \tag{3.13}$$

We will use the following relations of the Wigner rotation matrices [85], spherical harmonics and Wigner-3j symbols

$$\mathcal{D}^{\dagger}(\alpha,\beta,\gamma)^j_{pq} = \mathcal{D}^{j*}_{pq}(\alpha,\beta,\gamma) = [\mathcal{D}^{-1}(\alpha,\beta,\gamma)]^j_{pq} = \mathcal{D}^j_{pq}(-\gamma,-\beta,-\alpha) \tag{3.14}$$

$$\begin{aligned} \sum_{p=-j}^{j} \mathcal{D}^j_{pq}(\alpha,\beta,\gamma) \mathcal{D}^{j*}_{pr}(\alpha,\beta,\gamma) &= \delta_{qr} \\ \sum_{q=-j}^{j} \mathcal{D}^{j*}_{pq}(\alpha,\beta,\gamma) \mathcal{D}^j_{rq}(\alpha,\beta,\gamma) &= \delta_{pr} \end{aligned} \tag{3.15}$$

$$\mathcal{D}^{j*}_{pq} = (-1)^{p-q} \mathcal{D}^j_{-p-q} \tag{3.16}$$

$$\begin{aligned} \mathcal{D}^{j_1}_{p_1 q_1}(\hat{R}) \mathcal{D}^{j_2}_{p_2 q_2}(\hat{R}) = & (-1)^{-P-Q} \sum_{JPQ} (2J+1) \\ & \times \begin{pmatrix} j_1 & j_2 & J \\ p_1 & p_2 & -P \end{pmatrix} \begin{pmatrix} j_1 & j_2 & J \\ q_1 & q_2 & -Q \end{pmatrix} \mathcal{D}^J_{PQ}(\hat{R}), \end{aligned} \tag{3.17}$$

$$\int d\hat{R} \mathcal{D}^{L_1 *}_{M_L^1 M_L^2} \mathcal{D}^J_{M_J^1 M_J^2} = \frac{8\pi^2}{2L_1+1} \delta_{L_1 J} \delta_{M_L^1 M_J^1} \delta_{M_L^2 M_J^2} \tag{3.18}$$

$$
\begin{aligned}
Y_{l_1 m_2}(\hat{k}')Y^*_{l_1 m_2'}(\hat{k}') &= (-1)^{m_2'} Y_{l_1 m_2}(\hat{k}')Y_{l_1 -m_2'}(\hat{k}') \\
&= (-1)^{m_2'}\sqrt{\frac{(2l_1+1)(2l_2+1)}{4\pi}}\sum_{LM_L}(-1)^{M_L}\sqrt{2L+1} \\
&\times \begin{pmatrix} l_1 & l_2 & L \\ m_2 & -m_2' & -M_L \end{pmatrix}\begin{pmatrix} l_1 & l_2 & L \\ 0 & 0 & 0 \end{pmatrix} Y_{L0}(\hat{k}')
\end{aligned} \tag{3.19}
$$

$$
\sum_{m_1 m_2}(2j+1)\begin{pmatrix} j_1 & j_2 & j \\ m_1 & m_2 & m \end{pmatrix}\begin{pmatrix} j_1 & j_2 & j' \\ m_1 & m_2 & m' \end{pmatrix} = \delta_{jj'}\delta_{mm'} \tag{3.20}
$$

$$
\begin{pmatrix} j_1 & j_2 & j \\ m_1 & m_2 & m \end{pmatrix} = (-1)^{j_1+j_2+j}\begin{pmatrix} j_1 & j_2 & j \\ -m_1 & -m_2 & -m \end{pmatrix} \tag{3.21}
$$

$$
Y_{l0} = \sqrt{\frac{2l+1}{4\pi}}P_l^0(\cos\theta). \tag{3.22}
$$

Let us consider the four Wigner rotation matrices in Eq. (3.12). We can simplify them as follows

$$
\begin{aligned}
\mathcal{D}^{l_1}_{m_2 m_1}(\hat{R})\mathcal{D}^{l_2 *}_{m_2' m_1'}(\hat{R}) &= \mathcal{D}^{l_1}_{m_2 m_1}(\hat{R})(-1)^{m_2'-m_1'}\mathcal{D}^{l_2}_{-m_2'-m_1'}(\hat{R}) \\
&= (-1)^{m_2'-m_1'}(-1)^{-M_L^1-M_L^2}\sum_{L_1 M_L^1 M_L^2}(2L_1+1) \\
&\times \begin{pmatrix} l_1 & l_2 & L_1 \\ m_2 & -m_2' & -M_L^1 \end{pmatrix}\begin{pmatrix} l_1 & l_2 & L_1 \\ m_1 & -m_1' & -M_L^2 \end{pmatrix}\mathcal{D}^{L_1}_{M_L^1 M_L^2}(\hat{R}),
\end{aligned} \tag{3.23}
$$

and

$$
\begin{aligned}
\mathcal{D}^{1*}_{Mm}(\hat{R})\mathcal{D}^{1}_{Mm'}(\hat{R}) &= (-1)^{M-m}\mathcal{D}^{1}_{-M-m}(\hat{R})\mathcal{D}^{1}_{Mm'}(\hat{R}) \\
&= (-1)^{M-m}(-1)^{-M_J^1-M_J^2}\sum_{JM_J^1 M_J^2}(2J+1) \\
&\times \begin{pmatrix} 1 & 1 & J \\ -M & M & -M_J^1 \end{pmatrix}\begin{pmatrix} 1 & 1 & J \\ -m & m' & -M_J^2 \end{pmatrix}\mathcal{D}^{J}_{M_J^1 M_J^2}(\hat{R}).
\end{aligned} \tag{3.24}
$$

Then, using Eqns. (3.23) and (3.24), as well as the properties of the Wigner-3j symbols, Eq. (3.12) becomes

$$
\begin{aligned}
D_M D_M^* = & \sum_{\substack{l_1 m_1 m_2 \\ l_2 m_1' m_2' \\ m m'}} e^{i(\sigma_{l_1}-\sigma_{l_2})}(-i)^{l_1} i^{l_2} D_{l_1 m_1 m} D^*_{l_2 m_1' m'} \\
& \times \sum_{\substack{L_1 J \\ M_L^1 M_L^2 \\ M_J^1 M_J^2}} (2L_1+1)(2J+1)(-1)^{-m_1'}(-1)^{-M_L^1-M_L^2}(-1)^{M-m}(-1)^{-M_J^1-M_J^2} \\
& \times \begin{pmatrix} l_1 & l_2 & L_1 \\ m_2 & -m_2' & -M_L^1 \end{pmatrix} \begin{pmatrix} l_1 & l_2 & L_1 \\ m_1 & -m_1' & -M_L^2 \end{pmatrix} \\
& \times \begin{pmatrix} 1 & 1 & J \\ -M & M & -M_J^1 \end{pmatrix} \begin{pmatrix} 1 & 1 & J \\ -m & m' & -M_J^2 \end{pmatrix} \\
& \times \sum_{L M_L} \frac{\sqrt{2l_1+1}\sqrt{2l_2+1}\sqrt{2L+1}}{\sqrt{4\pi}} \begin{pmatrix} l_1 & l_2 & L \\ m_2 & -m_2' & -M_L \end{pmatrix} \begin{pmatrix} l_1 & l_2 & L \\ 0 & 0 & 0 \end{pmatrix} \\
& \times (-1)^{M_L} Y_{L0}(\hat{k}') \mathcal{D}^L_{M_L^1 M_L^2}(\hat{R}) \mathcal{D}^J_{M_J^1 M_J^2}(\hat{R}).
\end{aligned}
\tag{3.25}
$$

Next, we use the following property of Wigner-3j symbols [68]

$$
\sum_{m_2 m_2'} \begin{pmatrix} l_1 & l_2 & L_1 \\ m_2 & -m_2' & -M_L^1 \end{pmatrix} \begin{pmatrix} l_1 & l_2 & L \\ m_2 & -m_2' & -M_L \end{pmatrix} (2L+1) = \delta_{L_1 L} \delta_{-M_L^1 - M_L}. \tag{3.26}
$$

Then, we obtain

$$
\begin{aligned}
D_M D_M^* = & \sum_{\substack{l_1 m_1 \\ l_2 m_1' \\ m m'}} e^{i(\sigma_{l_1}-\sigma_{l_2})}(-i)^{l_1} i^{l_2} D_{l_1 m_1 m} D^*_{l_2 m_1' m'} \\
& \times \sum_{\substack{LJ \\ M_L M_L^2 \\ M_J^1 M_J^2}} \sqrt{2L+1}(2J+1)(-1)^{-m_1'}(-1)^{-M_L^2}(-1)^{M-m}(-1)^{-M_J^1-M_J^2} \\
& \times \begin{pmatrix} l_1 & l_2 & L \\ m_1 & -m_1' & -M_L^2 \end{pmatrix} \begin{pmatrix} 1 & 1 & J \\ -M & M & -M_J^1 \end{pmatrix} \\
& \times \begin{pmatrix} 1 & 1 & J \\ -m & m' & -M_J^2 \end{pmatrix} \begin{pmatrix} l_1 & l_2 & L \\ 0 & 0 & 0 \end{pmatrix} \\
& \times \frac{\sqrt{2l_1+1}\sqrt{2l_2+1}}{\sqrt{4\pi}} Y_{L0}(\hat{k}') \mathcal{D}^L_{M_L M_L^2}(\hat{R}) \mathcal{D}^J_{M_J^1 M_J^2}(\hat{R}).
\end{aligned}
\tag{3.27}
$$

But $M_L^2 = m_1 - m_1'$, $M_J^1 = 0$ and $M_J^2 = m' - m$ by properties of Wigner-3j symbols. Hence, we have

$$
\begin{aligned}
D_M D_M^* = & \sum_{\substack{l_1 m_1 \\ l_2 m_1' \\ m m'}} e^{i(\sigma_{l_1}-\sigma_{l_2})}(-i)^{l_1} i^{l_2} D_{l_1 m_1 m} D^*_{l_2 m_1' m'} (-1)^{M}(-1)^{-m_1-m'} \\
& \times \sum_{\substack{LJ \\ M_L}} \sqrt{(2L+1)}(2J+1) \begin{pmatrix} l_1 & l_2 & L \\ m_1 & -m_1' & m_1'-m_1 \end{pmatrix} \begin{pmatrix} 1 & 1 & J \\ -M & M & 0 \end{pmatrix} \\
& \times \begin{pmatrix} 1 & 1 & J \\ -m & m' & m-m' \end{pmatrix} \begin{pmatrix} l_1 & l_2 & L \\ 0 & 0 & 0 \end{pmatrix} \\
& \frac{\sqrt{2l_1+1}\sqrt{2l_2+1}}{\sqrt{4\pi}} Y_{L0}(\hat{k}') \mathcal{D}^L_{M_L, m_1-m_1'}(\hat{R}) \mathcal{D}^J_{0, m'-m}(\hat{R}).
\end{aligned}
\tag{3.28}
$$

The doubly-differential cross section for a molecular orientation $\hat{R}$ and continuum-electron angle $\hat{k}$ is then given by [86]

$$
\frac{d^2\sigma_{i\to\varepsilon}}{d\hat{R}d\hat{k}} = 4\pi^2 \alpha \omega N_i D_M D_M^*, \tag{3.29}
$$

where α is the fine structure constant, N_i is the occupation number of the initial molecular orbital i and ω is the photon energy. Integrating the Wigner rotation matrices in Eq. (3.28) over $\hat{R}$, we have

$$\begin{aligned}\int d\hat{R}\mathcal{D}^{L}_{M_L,m_1-m_1'}(\hat{R})\mathcal{D}^{J}_{0,m'-m}(\hat{R}) &= (-1)^{M_L-(m_1-m_1')}\int d\hat{R}\mathcal{D}^{L*}_{-M_L,m_1'-m_1}(\hat{R})\mathcal{D}^{J}_{0,m'-m}(\hat{R}) \\ &= (-1)^{M_L-(m_1-m_1')}8\pi^2\frac{1}{2L+1}\delta_{0M_L}\delta_{m_1-m_1',m'-m}\delta_{LJ}.\end{aligned} \tag{3.30}$$

Since $\int d\hat{R} = 8\pi^2$, when we average over all molecular orientations this $8\pi^2$ coefficient above will cancel. Hence, using Eq. (3.30) we obtain

$$\begin{aligned}\frac{1}{8\pi^2}\int d\hat{R}D_M D^*_M = \sum_{\substack{l_1 m_1 \\ l_2 m_1' \\ m m' \\ L}} & e^{i(\sigma_{l_1}-\sigma_{l_2})} i^{l_1+l_2}(-1)^{l_1+m_1'-m'} D_{l_1 m_1 m} D^*_{l_2 m_1' m'}(-1)^M \\ & \times \begin{pmatrix} 1 & 1 & L \\ -m & m' & m-m' \end{pmatrix}\begin{pmatrix} l_1 & l_2 & L \\ 0 & 0 & 0 \end{pmatrix} \\ & \times \begin{pmatrix} l_1 & l_2 & L \\ m_1 & -m_1' & m'-m \end{pmatrix}\begin{pmatrix} 1 & 1 & L \\ -M & M & 0 \end{pmatrix} \\ & \times \frac{\sqrt{2l_1+1}\sqrt{2l_2+1}\sqrt{2L+1}}{\sqrt{4\pi}} Y_{L0}(\hat{k}').\end{aligned} \tag{3.31}$$

In order to find the total cross section, we integrate over all possible angles of ejection of the continuum electron. Using the following property of spherical harmonics

$$\int d\hat{k}' Y_{L0} = 2\sqrt{\pi}\int d\hat{k}' Y_{L0}(\hat{k}')Y_{00}(\hat{k}') = \sqrt{4\pi}\delta_{L0}, \tag{3.32}$$

we obtain the following

$$\int d\hat{k}' \frac{1}{8\pi^2} \int d\hat{R} D_M D_M^* = \sum_{\substack{l_1 m_1 \\ l_2 m_1' \\ m m' \\ L}} e^{i(\sigma_{l_1} - \sigma_{l_2})} i^{l_1 + l_2} (-1)^{l_1 + m_1' - m'} D_{l_1 m_1 m} D^*_{l_2 m_1' m'} (-1)^M$$
$$\times \begin{pmatrix} 1 & 1 & L \\ -m & m' & m - m' \end{pmatrix} \begin{pmatrix} l_1 & l_2 & L \\ 0 & 0 & 0 \end{pmatrix}$$
$$\times \begin{pmatrix} l_1 & l_2 & L \\ m_1 & -m_1' & m' - m \end{pmatrix} \begin{pmatrix} 1 & 1 & L \\ -M & M & 0 \end{pmatrix}$$
$$\times \sqrt{2l_1 + 1} \sqrt{2l_2 + 1} \sqrt{2L + 1} \delta_{L0}. \tag{3.33}$$

For $L = 0$, we have the following values and properties of the Wigner-3j symbols

- $|l_1 - l_2| \leq 0 \implies l_1 = l_2$.
- $i^{l_1 + l_2} = (-1)^{l_1}$
- $m - m' = 0 \implies m' = m$.
- $m_1' = m_1$.
- $\begin{pmatrix} 1 & 1 & 0 \\ -m & m & 0 \end{pmatrix} = \frac{(-1)^{1+m}}{\sqrt{3}}$
- $\begin{pmatrix} l_1 & l_2 & 0 \\ 0 & 0 & 0 \end{pmatrix} = \begin{pmatrix} l_1 & l_1 & 0 \\ 0 & 0 & 0 \end{pmatrix} = \frac{(-1)^{l_1}}{\sqrt{(2l_1+1)}}$
- $\begin{pmatrix} l_1 & l_2 & 0 \\ m_1 & -m_1 & 0 \end{pmatrix} = \begin{pmatrix} l_1 & l_1 & 0 \\ m_1 & -m_1 & 0 \end{pmatrix} = \frac{(-1)^{l_1 - m_1}}{\sqrt{(2l_1+1)}}$
- $\begin{pmatrix} 1 & 1 & 0 \\ -M & M & 0 \end{pmatrix} = \frac{(-1)^{1+M}}{\sqrt{3}}$

Substituting in these expressions we have

$$\int d\hat{k}' \frac{1}{8\pi^2} \int d\hat{R} D_M D_M^* = \frac{1}{3} \sum_{l_1 m_1 m} D_{l_1 m_1 m} D^*_{l_1 m_1 m}. \tag{3.34}$$

As expected, Eq. (3.34) is proportional to the total photoionization cross section given by

$$\sigma_{i\to\varepsilon} = \frac{4}{3}\alpha\pi^2\omega N_i \sum_{m=-1,0,1}\sum_{l_1 m_1} D_{l_1 m_1 m} D^*_{l_1 m_1 m}. \tag{3.35}$$

For diatomic molecules, Eq. (3.10) simplifies since the magnetic quantum number is a good number. That is, after integrating the angles in Eq. (3.11), one finds that $m_1 = m + m_i$, where m_i is the magnetic quantum number of the bound orbital where photoionization takes place and m is the polarization of the photon in the MF frame. Then Eq. (3.10) takes the following form

$$D_M = \sum_{l_1,m_2,m} e^{i\sigma_{l_1}}(-i)^{l_1}\mathcal{D}^{l_1}_{m_2,m+m_i}(\hat{R})\mathcal{D}^{1*}_{M,m}(\hat{R})Y_{l_1,m_2}(\hat{k}')D_{l_1,m+m_i,m,i}. \tag{3.36}$$

Moreover, when the symmetry axis of the diatomic molecule is parallel to the LAB frame, $\mathcal{D}^{l_1}_{m_2,m+m_i}(\hat{0}) = \delta_{m_2,m+m_i}$ and $\mathcal{D}^{1*}_{M,m}(\hat{0}) = \delta_{M,m}$, where $\hat{0} = (0,0,0)$, resulting in $M = m$ and $m_1 = m_2 = M + m_i$. As a result, the dipole matrix element is given by

$$D_M = \sum_{l_1} e^{i\sigma_{l_1}}(-i)^{l_1} Y_{l_1,M+m_i}(\hat{k}')D_{l_1,M+m_i,M,i}. \tag{3.37}$$

3.2.2 Strong field streaking

To resolve dynamics on ultrashort time scales, we use a combination of an attosecond vaccum ultra-violet (VUV) pulse and a femtosecond infrared (IR) pulse (e.g. in our case we used two full width at half maximums of 0.5 fs and 100 fs, respectively). The final momentum of the photoelectrons emitted by the XUV pulse is shifted as a function of the delay time between the XUV and IR pulses. This delay time can be controlled experimentally. In the velocity gauge, the vector potential of the IR pulse has the form

$$\mathbf{A}^{\mathrm{IR}}(t) = -\frac{E_0^{\mathrm{IR}}}{\omega_{\mathrm{IR}}}\exp\left[-2\log\left(\frac{t}{\tau_{\mathrm{IR}}}\right)^2\right]\begin{pmatrix}\varepsilon\sin(\omega_{\mathrm{IR}}(t+\Delta t))\\ 0\\ \cos(\omega_{\mathrm{IR}}(t+\Delta t))\end{pmatrix}, \tag{3.38}$$

where E_0^{IR} is the amplitude of the field, ω_{IR} the circular frequency, τ_{IR} the full width at half maximum (FWHM) and ε the ellipticity. Note in this case the IR pulse is a circular field, so $\varepsilon = 1$. In addition, Δt is the time delay between the VUV and IR pulses. In what follows, we refer to $\omega_{\mathrm{IR}}\Delta t$ as the phase delay ϕ. As we can see the vector potential of the IR field begins at $t = 0$ at the maximum in the z-direction. We use the strong-field approximation (SFA), meaning we ignore the Coulomb potential during the propagation of the laser field. So the canonical momentum due to the presence of the IR field is a conserved quantity.

$$\vec{k}'(t_{ion}) - \mathbf{A}^{\mathrm{IR}}(t_{ion}) = \vec{k}'(t) - \mathbf{A}^{\mathrm{IR}}(t) = \vec{p}_f. \tag{3.39}$$

We use the same convention as [87] and [88], where t_{ion} is the time at which photoionization occurs and $\vec{p}_f$ is the detected momentum (i.e. the final momentum). Then by the SFA, the amplitude to transition from the wave number $\vec{k}'$ to the final momentum $\vec{p}_f$ due to an IR pulse is given by

$$a(\vec{p}_f) = \int_{t_i}^{t_f} dt_{ion} E^{\mathrm{V}}(t_{ion}) D_M(\vec{p}_f + \mathbf{A}^{\mathrm{IR}}(t_{ion})) e^{-iS}, \tag{3.40}$$

where $E^{\mathrm{V}}(t)$ is the electric field of the VUV pulse and the classical action

$$\begin{aligned} S &= -I_p t_{ion} + \int_{t_{ion}}^{t_f} dt' \frac{(\vec{p}_f + \mathbf{A}^{\mathrm{IR}}(t'))^2}{2} \\ &= \underbrace{\frac{\vec{p}_f \cdot \vec{p}_f}{2} t_f}_{diverges} - \frac{\vec{p}_f \cdot \vec{p}_f}{2} t_{ion} - I_p t_{ion} + \int_{t_{ion}}^{t_f} \frac{\vec{A}(t) \cdot (\vec{A}(t) + 2\vec{p}_f)}{2} dt, \end{aligned} \tag{3.41}$$

where I_p is the ionization energy of the orbital i. We can ignore the divergent term since we will select events that have the same final energy. This means that the contribution of this term to the phase i.e. $\exp\left(-i\frac{\vec{p}_f \cdot \vec{p}_f}{2} t_f\right)$, will be the same for all the events in that particular energy bin. The VUV pulse has an electric field of the form

$$\mathbf{E}^{\mathrm{V}}(t) = E_0^{\mathrm{V}} \exp\left[-2\log(2)\left(\frac{t}{\tau_{\mathrm{V}}}\right)^2 \right] \hat{z}, \tag{3.42}$$

where E_0^{V} is the amplitude of the field, and τ_{V} the FWHM.

Next, we describe how to compute $a(\vec{p}_f)$ in Eq. (3.40) for each photon energy of the VUV pulse. First, we create a two-dimensional grid over the polar angle $\theta_{\rm V}$ and azimuthal angle $\phi_{\rm V}$ that define the direction of ejection of the escaping electron with momentum $\vec{k}'$ due to the VUV pulse. For each point of the two-dimensional grid, we compute fully quantum mechanically $D_M(\vec{k}')$, as described in section 3.2.1. Then, we describe classically the propagation in the IR pulse of the electron ejected with momentum $\vec{k}'(t_{\rm ion})$. Specifically, we choose the ionization time $t_{\rm ion}$ using importance sampling [89] in the time interval $[-2.5\tau_{\rm V}, 2.5\tau_{\rm V}]$. For the probability distribution, we use the amplitude of the VUV pulse $E_0^{\rm V}$. For each classical trajectory, we propagate the electron in the IR laser field from time $t_{\rm ion}$ to time t_f. We generate, for each $\theta_{\rm V}$ grid point, 2×10^7 classical trajectories.

In addition, we account for the interference of trajectories corresponding to electrons ejected with different momenta $\vec{k}'$ at different ionization times $t_{\rm ion}$ that finally escape with the same momentum $\vec{p}_f$. To do so, we create a three-dimensional grid over the cylindrical coordinates p_{fr}, θ, p_{fy} of the final momentum that the electron acquires due to both the VUV and IR pulses. We note that p_{fr} is the magnitude of the projection of p_f on the plane of the IR pulse, i.e. $p_{fr} = \sqrt{{p_{fx}}^2 + {p_{fz}}^2}$. Also, θ is the angle of p_{fr} with the z axis, which is also the axis of polarization of the VUV pulse. We obtain the amplitude $\mathcal{A}(\vec{p}_f)$ for each grid point corresponding to an electron momentum $\vec{p}_f$ by adding coherently the amplitudes a_i for all trajectories i with the same $\vec{p}_f$ as follows

$$\left|\mathcal{A}(\vec{p}_f)\right|^2 = \left|\sum_i a_i(\vec{p}_f)\right|^2. \tag{3.43}$$

Finally, we obtain the probability for an electron to be ejected on the plane x–z plane of the IR pulse with momentum (p_{fr}, θ) by integrating $\left|\mathcal{A}(\vec{p}_f)\right|^2$ over the p_{fy} component

$$\left|\mathcal{A}(p_{fr}, \theta)\right|^2 = \int dp_{fy} \left|\mathcal{A}(\vec{p}_f)\right|^2. \tag{3.44}$$

3.3 Calculation details

The electronic configuration of N_2 is ($1\sigma_g^2$, $1\sigma_u^2$, $2\sigma_g^2$, $2\sigma_u^2$, $3\sigma_g^2$, $1\pi_{ux}^2$, $1\pi_{uy}^2$). We consider single photon absorption by the VUV pulse and subsequent ionization of an electron initially occupying the $2\sigma_g$, $3\sigma_g$ or $1\pi_u$ bound orbital. The $1\pi_{ux}$ and $1\pi_{uy}$ orbitals are energy degenerate and have opposite m quantum number. For the computations performed in this work, the initial state ψ_i is given by one of these three orbitals. We compute the bound states using the HF method with the quantum-chemistry package MOLPRO [69]. We implement HF by employing the correlation-consistent polarized triple-zeta basis set (cc-pVTZ) [90]. We find the equilibrium distance to be equal to 2.08 Å and the ionization energies of the $2\sigma_g$, $3\sigma_g$ and $1\pi_u$ orbitals to be equal to 37.7 eV, 16.0 eV and 15.3 eV, respectively, close to the experimental values reported in [91].

In the SCE of the bound states ψ_i, see Eq. (2.26), it suffices to truncate the expansion over the l_i quantum number up to $l_{\max} = 30$. For the computation of the continuum orbitals ψ_{l_1,m_1}, in the single center expansion we truncate the l_1 quantum number up to $l_{\max} = 19$.

We take the amplitude and duration of the electric field of the VUV pulse to be equal to $E_0^{\mathrm{V}} = 8.68 \times 10^9$ V/m (the intensity of the VUV pulse is equal to 10^{13} W/cm^2) and $\tau_{\mathrm{V}} = 0.5$ fs, respectively. In Fig. 3.2, we plot the electric field of the VUV pulse. We consider two amplitudes of the IR pulse corresponding to intensity of either 5×10^{12} W/cm^2 or 5×10^{13} W/cm^2, to roughly identify the strength of the IR pulse required to achieve control.

The ionization probability due to the VUV pulse is proportional to the photon flux multiplied by the photoionization cross section. The photon flux is given by

$$J(t) = 1.554 \times 10^{-16} \frac{E_0^{\mathrm{V}}[\mathrm{W/cm^2}]}{\omega_{\mathrm{V}}[\mathrm{Hartree}]} \exp\left[-4\log(2)(\frac{t}{\tau_{\mathrm{V}}})^2\right], \qquad (3.45)$$

where ω_V is the photon energy of the VUV pulse. We compare this ionization rate to the rate of ionization via tunnelling due to the IR pulse. To do this, we use the

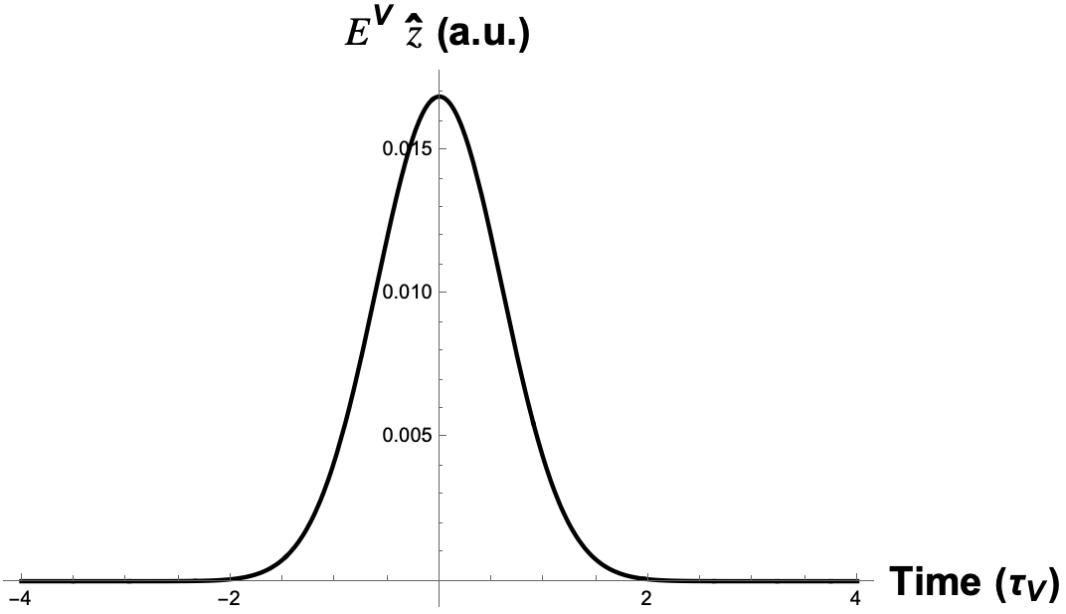

Figure 3.2: The electric field of the XUV pulse along the z axis as a function of the FWHM of the XUV pulse, $\tau_{\rm V}$.

Ammosov-Delone- Krainov (ADK) formula for tunnel-ionization, given by [92–94]

$$\Gamma_{\rm ADK} = \left(\frac{1}{\left|\mathbf{E}^{\rm IR}(t_0)\right|}\right)^{2\sqrt{\frac{Z^2}{2I_p}}-1} \exp\left[-\frac{2(2I_p)^{\frac{3}{2}}}{3\left|\mathbf{E}^{\rm IR}(t_0)\right|}\right], \tag{3.46}$$

where I_p is the ionization energy and $\left|\mathbf{E}^{\rm IR}(t_0)\right|$ is the field strength of the IR laser pulse at the time of tunnel-ionization. We find that for the outermost valence orbital of N_2, $1\pi_u$, with an ionization energy of 15 eV, the ionization rate for the VUV pulse with an intensity of 10^{13} W/cm^2 and photon energy equal to 16 eV is significantly larger than the ADK tunnel-ionization rate for an IR pulse with an intensity upper limit of 5×10^{13} W/cm^2. Hence, for the laser pulses that we utilize in this work, we can safely ignore tunnelling by the IR pulse.

In our studies, the duration of the IR pulse is $\tau_{\rm IR} = 100$ fs and its frequency is equal to $\omega_{\rm IR} = 0.020$ a.u. (2300 nm). In Fig. 3.3, we plot the vector potential of the IR pulse for 5×10^{12} W/cm^2. In the two-dimensional grid of the angles of ejection of the electron due to the VUV pulse in the LAB frame, the polar angle $\theta_{\rm V}$ ranges from 0° to 180° in steps of 1°, while the azimuthal angle ranges $\phi_{\rm V}$ from 0° to 360° in steps of 10°. For the three-dimensional grid of the final electron momentum in

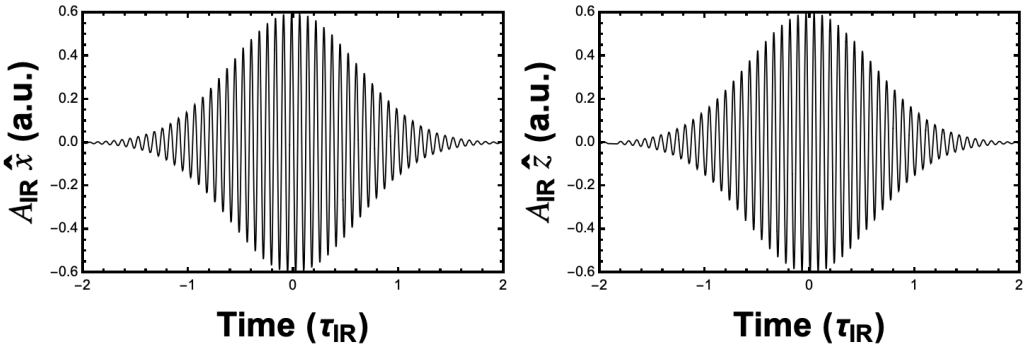

Figure 3.3: The vector potential of the IR pulse along the x and z axes, respectively, as a function of the FWHM of the IR pulse, τ_{IR}.

cylindrical coordinates, p_{fy} and p_{fr} vary from -5 a.u. to 5 a.u. and 0 a.u. to 5 a.u., respectively, in steps of 0.01 a.u., while the angle θ varies from 0° to 360° in steps of 1°.

We demonstrate that the phase delay between the linearly-polarized VUV pulse and the circularly-polarized IR pulse determines the direction of the ionizing electron. We show that best control is achieved when, at the time t_{ion} that the electron is released by the VUV pulse, it has very small energy. That is, the photon energy of the VUV pulse has to be just above the ionization threshold for the IR pulse to steer the electron most effectively.

To illustrate this, we plot the probability $g(\theta)$ for an electron to escape to the continuum on the x–z plane of the IR pulse with an angle θ. The latter angle is measured with respect to the z axis in the LAB frame. Integrating $\left|\mathcal{A}(p_{fr},\theta)\right|^2$ in Eq. (3.44) over p_{fr}, we find g(θ) as follows

$$g(\theta) = \int dp_{f_r} p_{f_r} \left|\mathcal{A}(\vec{p}_f,\theta)\right|^2. \tag{3.47}$$

In our results, we fully account for the energy range of the VUV pulse. That is, the Fourier transform of the VUV pulse with a full-width half maximum equal to 0.5 fs extends over energies roughly $\pm$ 4 eV from the central photon energy. Hence, when considering a VUV pulse with central photon energy equal to, for instance, 23 eV we also consider photon energies in the interval [19, 27] eV in steps of 1 eV. That is, for each of these energies we obtain the amplitudes $a_i(\vec{p}_f)$ which we then

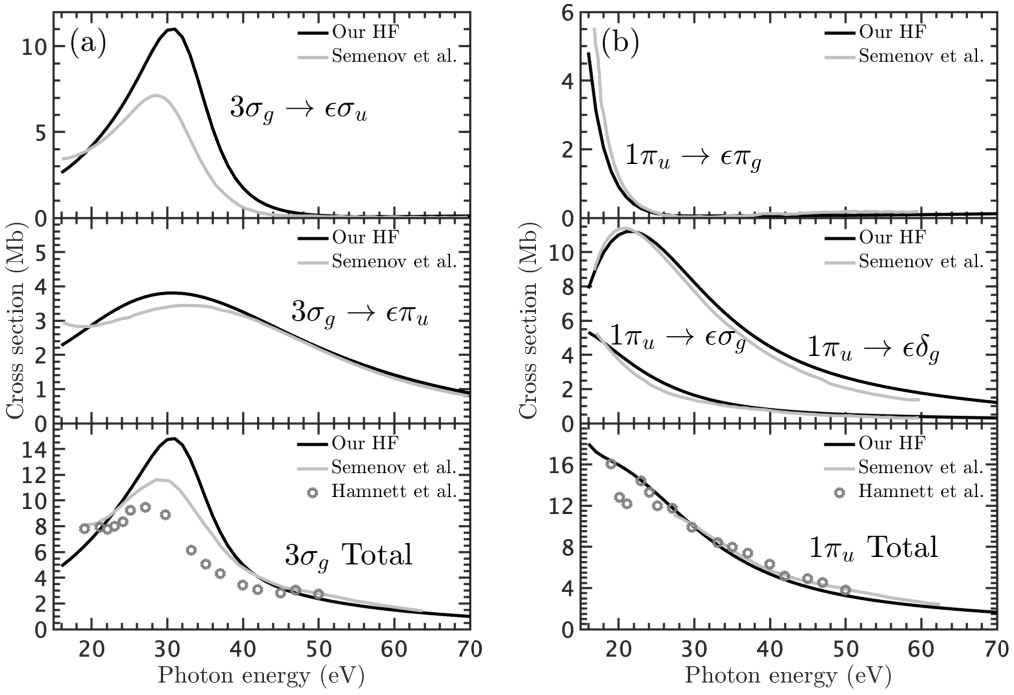

Figure 3.4: Photoionization cross sections for N_2 that we obtain (solid black line) compared with the theoretical results of Semenov et al. [46] (gray solid line) as well as with the experimental results of Hamnett et al. [95] (dark grey circles). The single-photon ionization occurs from (a) the $3\sigma_g$ orbital (b) the $1\pi_u$ orbital.

weight by the value of the Fourier transform at the respective energy. We then add coherently the amplitudes thus obtained to compute $\left|\mathcal{A}(p_{fr},\theta)\right|^2$ in Eq. (3.44).

3.4 Results

In Fig. 3.4, we compare the total photoionization cross sections from the $3\sigma_g$ and $1\pi_u$ orbitals obtained in this work using Eq. (2.149) with the experimental results of Ref.[95], as well as with the theoretical results of Ref. [46].

For ionization from the $1\pi_u$ orbital, we find excellent agreement in the cross sections we obtain (Fig. 3.4(b)) with both the theoretical and experimental work. For ionization from the 3σ orbital, the cross sections we obtain (Fig. 3.4(a)) exhibit a shape resonance [96] at roughly 32 eV, which is a few eV higher than the resonances obtained in the theoretical work of Semenov et al. [46] and experimental work of Hamnett et al. [95]. We also find a difference of approximately 2-4 eV in the peak of our shape resonance compared with the theoretical and experimental

work. Besides this offset in the location and magnitude of the shape resonance, the overall shape of the cross section with respect to the photon energy is in very good agreement with the cross section obtained by Semenov et al. [46] and Hamnett et al. [95].

In Fig. 3.5, we plot the probability distribution $g(\theta)$ when an electron ionizes to the continuum from $3\sigma_g$, an outer valence orbital, with an angle θ with respect to the z axis on the x–z plane. Since we consider linear polarization of the VUV pulse which is aligned with the molecular axis, the relevant transition is $3\sigma_g \rightarrow \varepsilon\sigma_u$. The z axis is both the symmetry axis of the diatomic molecule and the polarization axis of the VUV pulse. The circular IR pulse is polarized on the x–z plane. We take the IR pulse to have an intensity of 5×10^{13} W/cm^2. We consider a 17 eV VUV photon energy, which is 1 eV above the ionization threshold of the $3\sigma_g$ orbital (Fig. 3.5(a)), and a higher photon energy of 24 eV (Fig. 3.5(b)).

In Fig. 3.5, we vary the phase delay ϕ between the VUV and IR pulses from 0° to 315° in steps of 45°. For each phase delay ϕ, we find the angle θ that corresponds to the maximum of $g(\theta)$, i.e. the most probable angle of electron escape on the x–z plane, $\theta_{\max}$. For each ϕ, we expect that $\theta_{\max} = \phi$; we find this to be true when the electron due to the VUV pulse is released at t_{ion} in the IR pulse with very small excess energy, that is $k'(t_{\text{ion}}) = \sqrt{2(\hbar\omega - I_p)}$ is very small. This is seen in Fig. 3.5 where $g(\theta)$ is narrow and centered around $\theta = \theta_{\max} = \phi$ when the excess energy is 1 eV (17 eV photon energy), while $g(\theta)$ is wide and in most cases doubly-peaked for 8 eV excess energy (24 eV photon energy). This finding means that we achieve a one-to-one mapping between the angle of ionization of the electron and the phase delay between the two laser pulses. This holds true for small electron energies at the time the electron is released in the IR pulse.

Hence, we clearly demonstrate control of electron motion for VUV energies around 20 eV. This is important because these energies are within the range of high-harmonics generated from solids where one can harness the surface structure that can be added to solids to focus the VUV light down to the 100 nm scale [97].

In Fig. 3.5, we find that when the electron due to the VUV pulse is released

at t_{ion} in the IR pulse with higher excess energy, there is a double peak structure in g(θ), mostly for $\phi = 90°, 270°$. For instance for $\phi = 90°$, the momentum that the electron gains from the IR pulse is equal to $-\vec{A}_{\text{IR}}(t_{\text{ion}})$ and points along the x axis. In addition, the electron is released due to the VUV pulse at time t_{ion} in the IR pulse along the $+z$ and $-z$ axis with the same probability, since N_2 is a homonuclear molecule. As a result, the final angle of electron escape is smaller than 90° for electrons released along the $+z$ axis and greater than 90° for electrons released along the $-z$ axis.

Similar results are obtained for ionization to the continuum of an electron from $1\pi_u$, another outer valence orbital, see Fig. 3.6. In this case, we achieve excellent control of the angle of electron escape both for 18 eV photon energy (2.7 eV excess energy) but also for a higher photon energy of 23 eV (7.7 eV excess energy). We note that 23 eV photons are feasible for solid state high-harmonic generation. In what follows, we explain the reason for achieving for higher excess energies better control for the $1\pi_u$ orbital compared to the $2\sigma_g$ and $3\sigma_g$ orbitals. We find that the most probable angles of release due only to the VUV pulse are 45° and 135° for the $1\pi_u$ orbital, while they are 0° and 180° for the $2\sigma_g$ and $3\sigma_g$ orbitals. We refer to the $\vec{k}'$ vectors corresponding to these two angles as $\vec{k}'_1$ and $\vec{k}'_2$. To account for the IR pulse, we add to $\vec{k}'_1$ and $\vec{k}'_2$ the $-\vec{A}_{\text{IR}}$ vector. This addition is illustrated in Fig. 3.7(a) for the $2\sigma_g$ and $3\sigma_g$ orbitals and Fig. 3.7(b) for the $1\pi_u$ orbital. Comparing Fig. 3.7(a) with Fig. 3.7(b), it is clear that the angle between the two resultant vectors $\vec{p}_{f,1}$, $\vec{p}_{f,2}$, which is given by $\theta_2 - \theta_1$, is smaller for the $1\pi_u$ orbital than for the $2\sigma_g$ and $3\sigma_g$ orbitals. This is the reason that the double peak structure is significantly less pronounced for the $1\pi_u$ orbital compared to the $2\sigma_g$ and $3\sigma_g$ orbitals for higher excess energies. Indeed, this can be seen by comparing Fig. 3.6(b) with Fig. 3.5(b) for $\phi = 90°$ and $\phi = 270°$.

We further illustrate the one-to-one mapping between the most probable angle of ejection of the electron, θ_{max}, and the phase delay between the VUV and IR pulses by plotting θ_{max} as a function of ϕ in Fig. 3.8. We do so for a transition from the $3\sigma_g$ and $1\pi_u$ orbitals when the VUV photon energy is close to the ionization

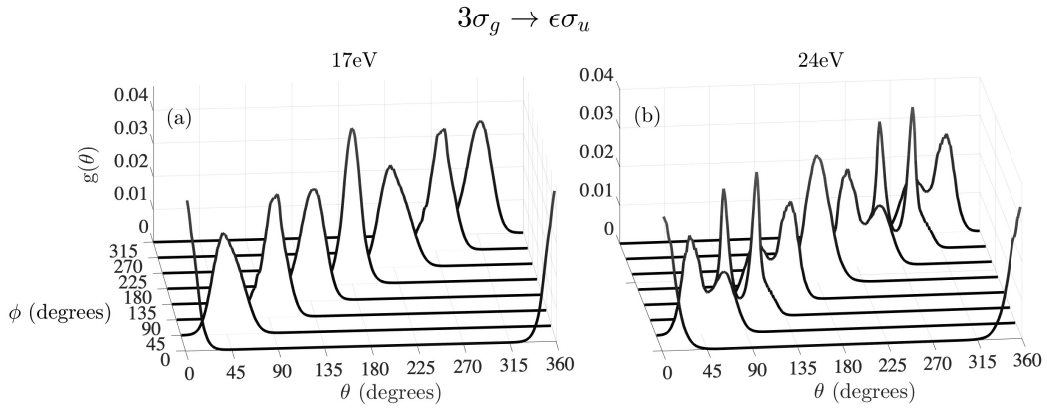

Figure 3.5: Probability $g(\theta)$ for an electron ionizing from the $3\sigma_g$ orbital due to a linearly-polarized VUV pulse and accelerated by a circularly-polarized IR pulse to ionize with an angle θ with respect to the z axis on the x–z plane. The IR pulse is polarized on the x–z plane. The VUV pulse is linearly-polarized along the molecular axis (z axis). We waterfall plot the probability $g(\theta)$ for different phase delays ϕ between the VUV and IR pulses. The VUV photon energy is 17 eV (a) and 24 eV (b). The intensity of the IR pulse is 5×10^{13} W/cm^2.

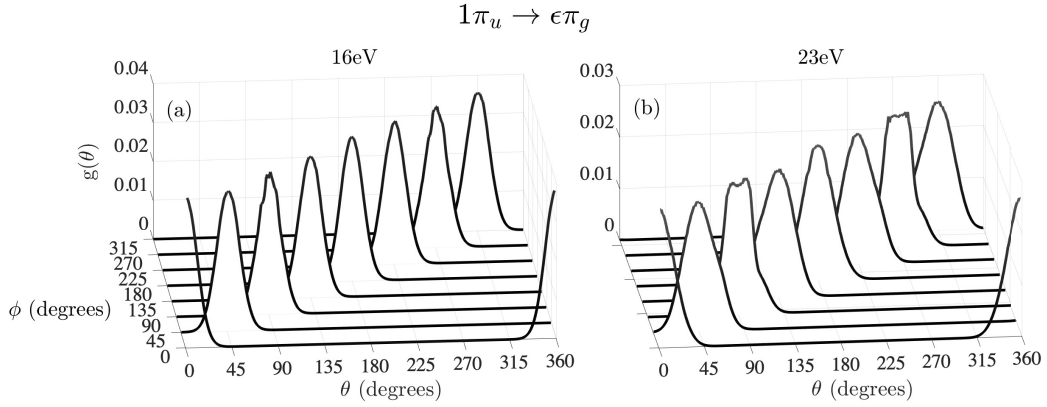

Figure 3.6: Same as Fig. 3.5 but for an electron ionizing from the $1\pi_u$ orbital. The VUV photon energy is 18 eV (a) and 23 eV (b).

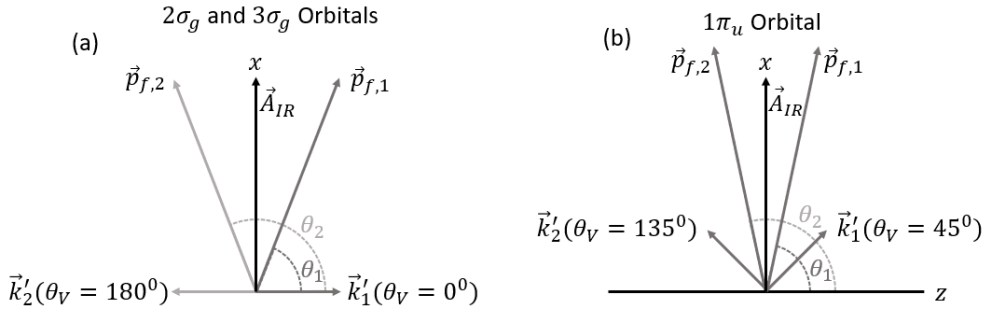

Figure 3.7: Schematic diagram for the resultant final momentum $\vec{p}_f$. The vectors $\vec{k}'_1$ and $\vec{k}'_2$ are the momentum vectors due to the VUV pulse corresponding to the two most probable angles of release due to VUV pulse at time t_{ion}. The resultant vectors $\vec{p}_{f,1}$ and $\vec{p}_{f,2}$ are obtained by $\vec{k}'_1 - \vec{A}_{\text{IR}}$ and $\vec{k}'_2 - \vec{A}_{\text{IR}}$, respectively. The angles θ_1 and θ_2 are the polar angles on the x–z plane of the vectors $\vec{p}_{f,1}$ and $\vec{p}_{f,2}$. The diagram on the left corresponds to the $2\sigma_g$ and $3\sigma_g$ orbitals and on the right to the $1\pi_u$ orbital.

threshold, 17 eV and 18 eV, respectively. The values of θ_{max} for all ϕs lie on the grey line in Fig. 3.8 that corresponds to $\theta_{\text{max}} = \phi$. For each ϕ, we also compute the standard deviation of the probability distribution $g(\theta)$ and find it to be very small, see Fig. 3.8. The small spread of the angles θ around ϕ, for each ϕ, implies excellent control of electron motion.

As we have already noted, the Coulomb potential is fully accounted for the interaction of the N_2 molecule with the VUV pulse. We neglect the Coulomb potential only during the propagation inside the IR pulse of the electron released at time t_{ion}. We expect that this approximation will not affect our finding of the one-to-one mapping between the phase delay ϕ and the most probable angle of electron escape θ_{max}. Fully accounting for the Coulomb potential at all stages will most probably result in a broader distribution $g(\theta)$ that still has a peak around $\theta_{\text{max}} = \phi$. Moreover, the details of the double peak structure of $g(\theta)$ observed for higher photon energies, see Fig. 3.5(b) for $\phi = 90^\circ$ and $\phi = 270^\circ$, depend on the system that is interacting with the VUV and IR pulses. For instance, a more asymmetric double peak structure of $g(\theta)$ is expected for a heteronuclear diatomic molecule. The reason is that the probability for the electron to be released due to the VUV pulse is different when the electron escapes along one centre versus the other one. Finally, we note that in this work we assume that the diatomic molecule is perfectly aligned

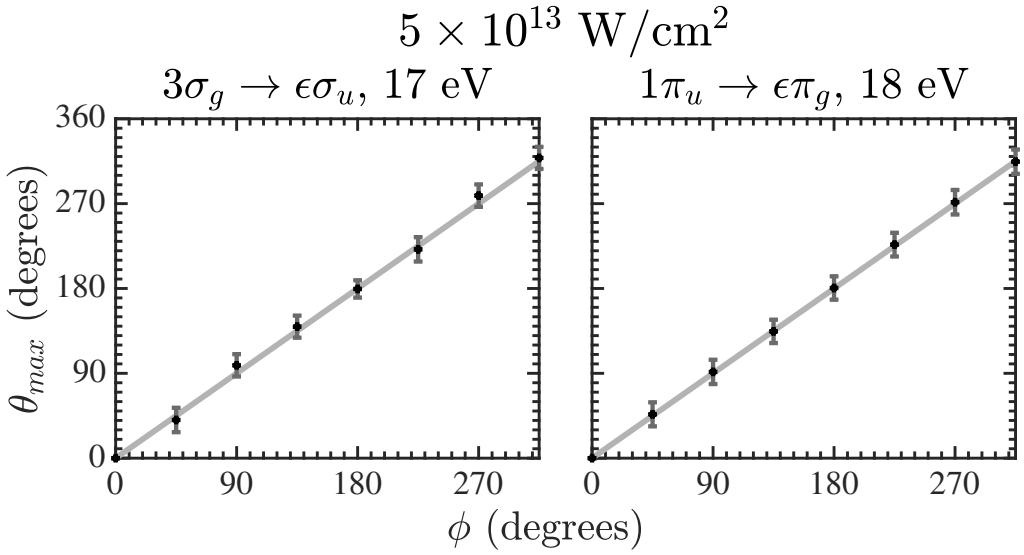

Figure 3.8: $\theta_{\max}$ as a function of the delay ϕ between the VUV and IR pulses, for an electron ionizing from the $3\sigma_g$ and $1\pi_u$ orbital with VUV photon energy equal to 17 eV and 18 eV, respectively. The intensity of the IR pulse is 5×10^{13} W/cm^2. The vertical bars denote the standard deviation of the probability distribution g(θ).

with the VUV laser pulse. In an experiment, the molecule will be aligned along the VUV pulse with a certain distribution. Accounting for such a distribution is expected to only slightly change the results presented in this work and to cause a small increase of the width of the distribution of g(θ) as a function of θ for different phase delays. This is the reason we do not include a distribution of alignments in the current work.

In Fig. 3.9, we demonstrate that, as expected, control of the angle of ionization of the electron depends on the strength of the IR pulse. We take the intensity of the IR pulse to be equal to 5×10^{12} W/cm^2, which is an order of magnitude smaller than the intensity of the IR pulse considered in Fig. 3.5 and Fig. 3.6. We find that for the weaker IR pulse, the distribution g(θ) is wide and not centered around $\theta = \phi$ even for VUV photon energies close to the ionization threshold, 18 eV and 17 eV for the transitions from the $1\pi_u$ and $3\sigma_g$ orbital, respectively. The lack of control is clearly seen by the doubly peaked structure of $g(\theta)$ for most ϕ for both transitions.

We now show that control of the angle of electron ionization is also achieved for electrons ionizing due to the VUV pulse from the $2\sigma_g$ inner valence orbital.

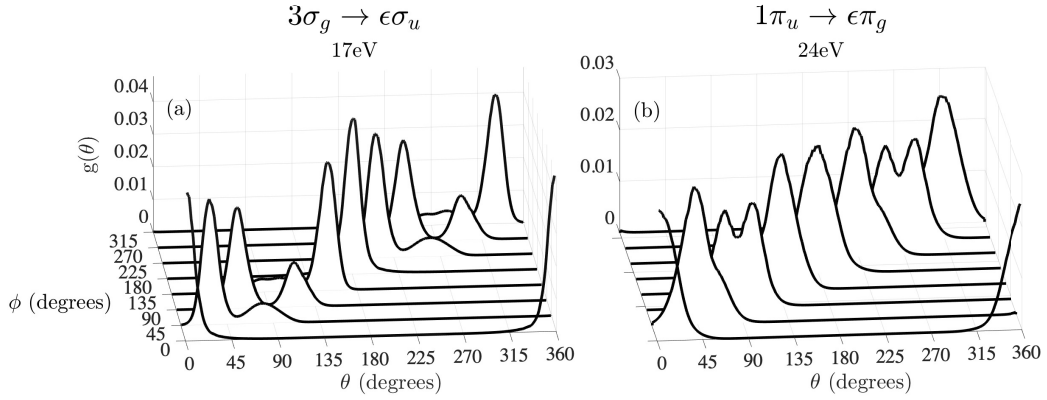

Figure 3.9: Same as in Fig. 3.5 and Fig. 3.6 but for an intensity of the IR pulse equal to 5×10^{12} W/cm^2.

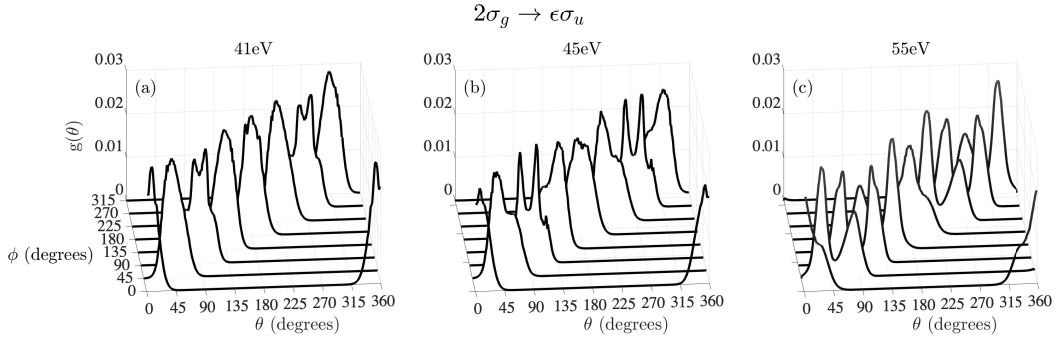

Figure 3.10: Same as in Fig. 3.5 but for an electron ionizing from the $2\sigma_g$ orbital. The waterfall plots (a), (b) and (c) correspond to VUV photon energies of 41 eV, 45 eV and 55 eV respectively.

This is demonstrated in Fig. 3.10(a) for photon energy of the VUV pulse equal to 41 eV, which corresponds to the electron having an excess energy of 3.3 eV when it is released into the IR pulse. However, for photon energies 45 eV and 55 eV, as for the 3σ orbital at 24 eV VUV photon energy, we find that the distribution $g(\theta)$ is wide and doubly-peaked for most values of the phase delay ϕ, see Fig. 3.10(b) and Fig. 3.10(c). Hence, control is not achieved for these higher excess energies.

Next, we investigate the velocities reached by the electron that is released due to the VUV pulse and is accelerated by the circular IR pulse. In Fig. 3.11, we plot the distribution of momenta $g(p_{f_r})$ the electron escapes with on the x–z plane, which is the plane of polarization of the IR pulse. We do so for an electron ionizing from the $3\sigma_g$ orbital for a 17 eV photon energy of the VUV pulse. The distribution of

the magnitude of the projection of the final electron momentum on the x–z plane is given by

$$g(p_{f_r}) = \int d\theta p_{f_r} \left| \mathcal{A}(\vec{p}_f, \theta) \right|^2. \tag{3.48}$$

The maximum momentum an electron gains from the IR field is $E_0^{\rm IR}/\omega$, which is equal to roughly 1.9 a.u. for the higher IR intensity considered in this work. The momentum of the electron at the time of release $t_{\rm ion}$ is $k' = 0.27$ a.u. Hence, when the phase delay ϕ between the two pulses is zero, an electron released due to the VUV pulse along the $+z$ axis at time $t_{\rm ion}$ will finally ionize with a momentum equal to 0.27+1.9=+2.17 a.u. due to both the VUV and IR pulses. An electron released due to the VUV pulse along the $-z$ axis at time $t_{\rm ion}$ will finally escape with a momentum equal to -0.27+1.9=1.63 a.u. due to both the VUV and IR pulses. This explains the doubly-peaked distribution of electron momenta in Fig. 3.11, when $\phi = 0$ and for most ϕs. The height of both peaks is roughly equal, since N_2 is a homonuclear molecule and the electron has the same probability to be released along the $+z$ and $-z$ axis at time $t_{\rm ion}$. Moreover, when $\phi = 90^\circ$, $-\vec{A}_{\rm IR}(t_{\rm ion})$ points along the x axis and hence the resultant electron momentum distribution due to the VUV and IR pulses is centered around $\vec{A}_{\rm IR}(t_{\rm ion}) = E_0^{\rm IR}/\omega_{\rm IR} = 1.9$ a.u. Thus, we find that the ionizing electron is steered to a specific direction by the phase delay of the VUV and IR pulses but it also accelerates to high velocities which are roughly equal to 2×10^6 m/s. If we take an even smaller photon energy of the VUV pulse, the electron momentum distribution (not shown) will be centered around $E_0^{\rm IR}/\omega_{\rm IR}$ for most ϕs.

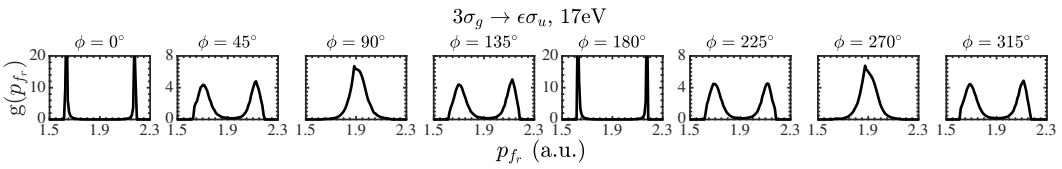

Figure 3.11: Probability for an electron being released from the $3\sigma_g$ orbital due to a linearly-polarized VUV pulse and being accelerated by a circularly-polarized IR pulse to a final momentum whose projection on the x–z plane has magnitude $p_{fr} = \sqrt{{p_{fx}}^2 + {p_{fz}}^2}$. The VUV photon energy is 17eV and the intensity of the IR pulse is 5×10^{13} W/cm^2.

3.5 Magnetic field due to a ring current

Finally, we give a rough estimate for the magnetic field resulting from a ring current generated by a linear VUV pulse of intensity 10^{13} W/cm^2 and pulse duration of 0.5 fs as well as a circular IR field of intensity 5×10^{13} W/cm^2. The number of photons produced from a laser pulse can be calculated using the following

$$N_{\text{photons}} = \frac{IAt}{\omega}, \tag{3.49}$$

where I, t, ω are the intensity, pulse duration and photon energy of the laser pulse, respectively, and A is the cross-sectional area of the beam. For a VUV pulse focused down to roughly 100 nm with 20 eV photon energy the number of photons provided in an area of 100^2 nm^2 is roughly 2×10^5. Then, the ionized atoms and thus the number of electrons, $N_{\text{electrons}}$, released by the VUV pulse in the IR pulse is roughly 2×10^5. We showed that an electron released by a VUV pulse in an IR pulse accelerates by the IR field to speeds $v \approx 2\times10^6$ m/s. The current, J, produced by these electrons can be calculated using

$$J = \frac{eN_{\text{electrons}}v}{r}, \tag{3.50}$$

where e is the charge of an electron and r is the length of the conductor. Then, a current of roughly $J = 0.5$ A can be created around a ring of length roughly equal to $r = 100$ nm. The magnetic field resulting by the ring current is equal to

$$B = \frac{\mu_0 J}{2\pi r}, \tag{3.51}$$

which in this case is roughly equal to 1 Tesla. Hence, our concept can be implemented to produce large magnetic fields confined below 100 nm.

3.6 Conclusions

In conclusion, we have demonstrated a one-to-one mapping between the direction of ionization of an electron and the phase delay between a linearly-polarized VUV

pulse and a circular IR laser field. An ultra-short VUV pulse focused down to 100 nm or less releases the electron in the circular IR pulse with temporal and spatial resolution. Following release, the electron is then accelerated to high velocities by the IR pulse.

We have demonstrated this concept in the context of the N_2 molecule. However, future experiments can employ equally well atoms such as Helium, Argon or Neon. Selection of an atom for experiments should be partly based on the maximum IR intensity that can be considered without tunnel ionization of a valence electron. High IR intensities result in high electron speeds and thus large electron currents. For instance, the first ionization energy of Helium is higher than the first ionization energy of N_2. Hence, for Helium, intensities of the IR pulse higher than 5×10^{13} W/cm^2 can be considered, while still keeping the rate of ionization of the valence electron via tunnelling very small. For experiments, selection of an atom should also be based on transitions from a valence or inner valence shell with a VUV pulse of around 20 eV photon energy having large cross sections.

The theoretical concept of control of electron motion developed here can be implemented to create high magnetic fields. In the near future, it should be possible to generate focused VUV pulses with a corkscrew-like intensity profile [35] that in conjunction with a circular IR pulse can direct electrons around a ring and create magnetic fields. However, the concept of controlling the direction of electron ionization with a VUV and IR pulse we theoretically develop here is general and not restricted to creating ring currents. For instance, it can also be applicable to processes in physical chemistry, an area where coherent control emerged as a tool to steer a system into a particular final state [98]. For instance, controlling the direction of ionization of an electron released from an inner valence or core orbital can influence from which atomic center a valence electron is removed to fill in the hole created by the VUV pulse in a process known as interatomic Coulombic decay [99].

Chapter 4

Streaking single-electron ionization in open-shell molecules driven by X-ray pulses

4.1 Introduction

In this chapter, we study single-electron ionization due to single-photon absorption from the open-shell molecule NO when driven by a linearly-polarized X-ray pulse. In addition, we streak the electron dynamics with a circularly-polarized IR pulse. While previous studies have considered streaking ionization from valence orbitals of NO [100], here we address streaking of single-electron ionization from the core orbitals 1σ and 2σ. To achieve this, first, we obtain the dipole matrix element for an electron to ionize following single-photon absorption by an X-ray laser pulse, as in section 3.2.1. To compute the dipole matrix element, we compute the continuum molecular wavefunctions for open-shell molecules in the Hartree-Fock (HF) framework. We do so while fully accounting for the singlet or triplet symmetry of the final molecular ion. As in 3.2.2, we employ the strong-field approximation [87, 88] to account for the effect of an IR laser pulse on the dynamics of an electron transitioning from a bound molecular state to the continuum due to an X-ray pulse.

Using a high intensity IR pulse we demonstrate control of electron ionization triggered by an X-ray pulse in Section 4.4.0.3. That is, we show that there is a

one-to-one mapping of the angle of electron escape to the phase delay between the X-ray and IR pulses. We note that a high (low) intensity IR pulse refers to an IR pulse with ponderomotive energy that is larger (smaller) than the electron energy following ionization from just the X-ray pulse. Finally, in Section 4.4.0.4, we use a low intensity IR pulse to streak electron ionization by an X-ray pulse. To do so, we obtain doubly differential final electron momenta distributions. We find that several features of these distributions arise from angular patterns of electron ionization solely due to the presence of the X-ray pulse. Such final electron momenta distributions are relevant to the computation of time delays [12, 14].

4.2 Open-shell molecules

The electronic configuration of Nitric Oxide, NO, is ($1\sigma^2$, $2\sigma^2$, $3\sigma^2$, $4\sigma^2$, $1\pi_x^2$, $1\pi_y^2$, $5\sigma^2$, $2\pi^1$) . The 1σ orbital is localized on the O atom, and the 2σ orbital is localized on the N atom. The partially filled 2π orbital in NO leads to singlet and triplet states when we ionize from an orbital other than the 2π. In our calculations, the difference between the singlet and triplet cases is the ionization potentials we calculate and the HF direct/exchange coefficients that we use, see Ref. [49]. These coefficients are derived from the final state wave functions. The total wavefunction, Ψ, of NO when there is a singlet state between the 2π orbital and i, the orbital where photoionization occurs from, can be shown to be the following linear combination of Slater determinants [49]

$$\begin{aligned}\Psi(\vec{r}_1,\vec{r}_2,\ldots,\vec{r}_N) = \frac{1}{\sqrt{2}}\Bigg[&\left|\{\psi_j\}_{j\neq i,2\pi}\psi_i^{\uparrow}\psi_{2\pi}^{\downarrow}\psi_{\varepsilon}^{\uparrow}\right| \\ &-\left|\{\psi_j\}_{j\neq i,2\pi}\psi_i^{\downarrow}\psi_{2\pi}^{\uparrow}\psi_{\varepsilon}^{\uparrow}\right|\Bigg],\end{aligned} \tag{4.1}$$

where $\vec{r}_1,\vec{r}_2,\ldots,\vec{r}_N$ are the positions of the electrons and $\{\psi_j\}_{j\neq i,2\pi}$ are the wavefunctions of the electrons that are not initially in the orbitals i and 2π. The arrow notation represents the two possible spin states ($s=\pm\frac{1}{2}$). To verify that this is indeed a singlet state, we apply the spin projection operator $\hat{S}_z$ and the total spin operator $\hat{S}^2$ to the wavefunction Ψ. Since the initial state has only one open shell,

the total spin and spin projection are $\frac{1}{2}$. Since the Hamiltonian does not depend on spin, the wavefunction must conserve spin. That is, the total spin and spin projection in the initial and final states should be equal. Hence, in both the singlet and triplet states, the operators $\hat{S}_z$ and $\hat{S}^2$ should yield $\frac{1}{2}$ and $\frac{3}{4}$, respectively. As in Ref. [101], it can be shown that application of the $\hat{S}_z$ operator to a Slater determinant Φ is equal to

$$\begin{aligned} \hat{S}_z\Phi &= M_S\Phi \\ M_S &= \frac{1}{2}(n_\alpha - n_\beta), \end{aligned} \tag{4.2}$$

where n_α, n_β are the number of columns with spin up and spin down, respectively. Similarly, application of the operator $\hat{S}^2$ can be shown to be equal to

$$\hat{S}^2\Phi = \left\{ \sum_P \hat{P}_{\alpha\beta} + \frac{1}{4}[(n_\alpha - n_\beta)^2 + 2n_\alpha + 2n_\beta] \right\}\Phi, \tag{4.3}$$

where $\hat{P}_{\alpha\beta}$ is an operator interchanging opposite α and β spins in Φ and the summation over P corresponds to all possible interchanges of spin. For instance,

$$\begin{aligned} \sum_P \hat{P}_{\alpha\beta}\left|\psi_1^\uparrow\psi_2^\downarrow\psi_3^\uparrow\psi_4^\downarrow\right| = &\left|\psi_1^\downarrow\psi_2^\uparrow\psi_3^\uparrow\psi_4^\downarrow\right| + \left|\psi_1^\uparrow\psi_2^\uparrow\psi_3^\downarrow\psi_4^\downarrow\right| \\ &+ \left|\psi_1^\downarrow\psi_2^\downarrow\psi_3^\uparrow\psi_4^\uparrow\right| + \left|\psi_1^\uparrow\psi_2^\downarrow\psi_3^\downarrow\psi_4^\uparrow\right|. \end{aligned} \tag{4.4}$$

Since the orbitals $j \neq i, 2\pi$ are closed, this means that for $\{\psi_j\}_{j\neq i,2\pi}$ in the Slater determinants the number of columns with up spin equals the number of columns with down spin. Hence, it is sufficient to apply the operator $\hat{S}_z$ only to the three-particle system between the orbitals i, 2π and ε. The eigenvalue for the $\hat{S}_z$ on the singlet state Ψ is then given by

$$\begin{aligned} \hat{S}_z\Psi &= \frac{1}{\sqrt{2}}(\hat{S}_z\left|\psi_i^\uparrow\psi_{2\pi}^\downarrow\psi_\varepsilon^\uparrow\right| - \hat{S}_z\left|\psi_i^\downarrow\psi_{2\pi}^\uparrow\psi_\varepsilon^\uparrow\right|) \\ &= \frac{1}{\sqrt{2}}(\frac{1}{2}(2-1)\left|\psi_i^\uparrow\psi_{2\pi}^\downarrow\psi_\varepsilon^\uparrow\right| - \frac{1}{2}(2-1)\left|\psi_i^\downarrow\psi_{2\pi}^\uparrow\psi_\varepsilon^\uparrow\right|) \\ &= \frac{1}{2}\Psi. \end{aligned} \tag{4.5}$$

This is consistent with the total spin of the 2π and i orbitals being 0 and the spin of the continuum electron being $+\frac{1}{2}$. Next, we find eigenvalue of the $\hat{S}^2$ operator when applied to the Ψ singlet state. In order to do this, we utilise two properties of determinants. Namely, a determinant with two identical columns is equal to zero and swapping two adjacent columns in a determinant inverts the sign. Then, since the orbitals $j \neq i, 2\pi$ are closed, interchanging any of the columns $\{\psi_j\}_{j\neq i,2\pi}$ in the Slater determinant will either be equal to zero or cancel with the $\frac{1}{4}[(n_\alpha - n_\beta)^2 + 2n_\alpha + 2n_\beta]\Phi$ term. In other words, the only non-zero terms in the Slater determinants will be those which interchange spins between the i, 2π and ε states. Hence, it is sufficient to apply the operator $\hat{S}^2$ only to the three-particle system between the orbitals i, 2π and ε. The eigenvalue for the $\hat{S}^2$ on the singlet state Ψ is then given by

$$\begin{aligned}
\hat{S}^2\Psi &= \frac{1}{\sqrt{2}}(\hat{S}^2\left|\psi_i^\uparrow \psi_{2\pi}^\downarrow \psi_\varepsilon^\uparrow\right| - \hat{S}^2\left|\psi_i^\downarrow \psi_{2\pi}^\uparrow \psi_\varepsilon^\uparrow\right|) \\
&= \frac{1}{\sqrt{2}}\Bigg[\left|\psi_i^\downarrow \psi_{2\pi}^\uparrow \psi_\varepsilon^\uparrow\right| + \left|\psi_i^\uparrow \psi_{2\pi}^\uparrow \psi_\varepsilon^\downarrow\right| \\
&+ \frac{1}{4}((2-1)^2+4+2)\left|\psi_i^\uparrow \psi_{2\pi}^\downarrow \psi_\varepsilon^\uparrow\right|\Bigg] \\
&- \frac{1}{\sqrt{2}}\Bigg[\left|\psi_i^\uparrow \psi_{2\pi}^\downarrow \psi_\varepsilon^\uparrow\right| + \left|\psi_i^\uparrow \psi_{2\pi}^\uparrow \psi_\varepsilon^\downarrow\right| \\
&+ \frac{1}{4}((2-1)^2+4+2)\left|\psi_i^\downarrow \psi_{2\pi}^\uparrow \psi_\varepsilon^\uparrow\right|\Bigg] \\
&= \frac{3}{4}\Psi.
\end{aligned} \tag{4.6}$$

This is consistent with the i and 2π orbitals having total spin equal to 0 and the continuum electron having total spin $+\frac{1}{2}$. In order to find the a_i and b_i coefficients for the i and 2π orbitals in the singlet state, it is sufficient to consider the following

combination of Slater determinants

$$\begin{aligned}\Psi(q_1,q_2,q_3) = \frac{1}{\sqrt{2}}\Bigg(&\frac{1}{\sqrt{3!}}\begin{vmatrix}\psi_i^{\uparrow}(q_1) & \psi_{2\pi}^{\downarrow}(q_1) & \psi_{\varepsilon}^{\uparrow}(q_1)\\ \psi_i^{\uparrow}(q_2) & \psi_{2\pi}^{\downarrow}(q_2) & \psi_{\varepsilon}^{\uparrow}(q_2)\\ \psi_i^{\uparrow}(q_3) & \psi_{2\pi}^{\downarrow}(q_3) & \psi_{\varepsilon}^{\uparrow}(q_3)\end{vmatrix}\\ &-\frac{1}{\sqrt{3!}}\begin{vmatrix}\psi_i^{\downarrow}(q_1) & \psi_{2\pi}^{\uparrow}(q_1) & \psi_{\varepsilon}^{\uparrow}(q_1)\\ \psi_i^{\downarrow}(q_2) & \psi_{2\pi}^{\uparrow}(q_2) & \psi_{\varepsilon}^{\uparrow}(q_2)\\ \psi_i^{\downarrow}(q_3) & \psi_{2\pi}^{\uparrow}(q_3) & \psi_{\varepsilon}^{\uparrow}(q_3)\end{vmatrix}\Bigg).\end{aligned} \tag{4.7}$$

Using the method outlined in Section 2.3.9, we find the direct coefficients to be $a_i = 1$ and $a_{2\pi} = 1$. The exchange coefficients are found to be $b_i = \frac{1}{2}$ and $b_{2\pi} = \frac{1}{2}$. Then, using the third limiting case in Section 2.3.9, we find $a_j = 2$ and $b_j = 1$ for $j \neq i, 2\pi$. The final state wave function leading to a triplet state can be shown to be

$$\begin{aligned}\Psi = \frac{1}{\sqrt{6}}\Big[&2\left|\{\psi_j\}_{j\neq i,2\pi}\psi_i^{\uparrow}\psi_{2\pi}^{\uparrow}\psi_{\varepsilon}^{\downarrow}\right|\\ &-\left|\{\psi_j\}_{j\neq i,2\pi}\psi_i^{\downarrow}\psi_{2\pi}^{\uparrow}\psi_{\varepsilon}^{\uparrow}\right|\\ &-\left|\{\psi_j\}_{j\neq i,2\pi}\psi_i^{\uparrow}\psi_{2\pi}^{\downarrow}\psi_{\varepsilon}^{\uparrow}\right|\Big].\end{aligned} \tag{4.8}$$

Similarly to the singlet state, the eigenvalue for the $\hat{S}_z$ on the triplet state Ψ is given by

$$\begin{aligned}\hat{S}_z\Psi &= \frac{1}{\sqrt{6}}(2\left|\psi_i^{\uparrow}\psi_{2\pi}^{\uparrow}\psi_{\varepsilon}^{\downarrow}\right| - \left|\psi_i^{\downarrow}\psi_{2\pi}^{\uparrow}\psi_{\varepsilon}^{\uparrow}\right| - \left|\psi_i^{\uparrow}\psi_{2\pi}^{\downarrow}\psi_{\varepsilon}^{\uparrow}\right|)\\ &= \frac{1}{\sqrt{6}}(2\times\frac{1}{2}(2-1)\left|\psi_i^{\uparrow}\psi_{2\pi}^{\uparrow}\psi_{\varepsilon}^{\downarrow}\right| - \frac{1}{2}(2-1)\left|\psi_i^{\downarrow}\psi_{2\pi}^{\uparrow}\psi_{\varepsilon}^{\uparrow}\right|\\ &\quad -\frac{1}{2}(2-1)\left|\psi_i^{\uparrow}\psi_{2\pi}^{\downarrow}\psi_{\varepsilon}^{\uparrow}\right|)\\ &= \frac{1}{2}\Psi,\end{aligned} \tag{4.9}$$

and the eigenvalue for the $\hat{S}^2$ on the triplet state Ψ is given by

$$\begin{aligned}
\hat{S}^2\Psi &= \frac{1}{\sqrt{6}}(2\left|\psi_i^{\uparrow}\psi_{2\pi}^{\uparrow}\psi_{\varepsilon}^{\downarrow}\right| - \left|\psi_i^{\downarrow}\psi_{2\pi}^{\uparrow}\psi_{\varepsilon}^{\uparrow}\right| - \left|\psi_i^{\uparrow}\psi_{2\pi}^{\downarrow}\psi_{\varepsilon}^{\uparrow}\right|) \\
&= \frac{1}{\sqrt{6}}\left[2\left|\psi_i^{\downarrow}\psi_{2\pi}^{\uparrow}\psi_{\varepsilon}^{\uparrow}\right| + 2\left|\psi_i^{\uparrow}\psi_{2\pi}^{\downarrow}\psi_{\varepsilon}^{\uparrow}\right| + \frac{2}{4}[(2-1)^2+4+2]\left|\psi_i^{\uparrow}\psi_{2\pi}^{\uparrow}\psi_{\varepsilon}^{\downarrow}\right|\right. \\
&- \left|\psi_i^{\uparrow}\psi_{2\pi}^{\downarrow}\psi_{\varepsilon}^{\uparrow}\right| - \left|\psi_i^{\uparrow}\psi_{2\pi}^{\uparrow}\psi_{\varepsilon}^{\downarrow}\right| - \frac{1}{4}[(2-1)^2+4+2]\left|\psi_i^{\downarrow}\psi_{2\pi}^{\uparrow}\psi_{\varepsilon}^{\uparrow}\right| \\
&\left.- \left|\psi_i^{\downarrow}\psi_{2\pi}^{\uparrow}\psi_{\varepsilon}^{\uparrow}\right| - \left|\psi_i^{\uparrow}\psi_{2\pi}^{\uparrow}\psi_{\varepsilon}^{\downarrow}\right| - \frac{1}{4}[(2-1)^2+4+2]\left|\psi_i^{\uparrow}\psi_{2\pi}^{\downarrow}\psi_{\varepsilon}^{\uparrow}\right|\right] \\
&= \frac{1}{\sqrt{6}}\left[(\frac{14}{4}-1-1)\left|\psi_i^{\uparrow}\psi_{2\pi}^{\uparrow}\psi_{\varepsilon}^{\downarrow}\right| + (2-\frac{7}{4}-1)\left|\psi_i^{\downarrow}\psi_{2\pi}^{\uparrow}\psi_{\varepsilon}^{\uparrow}\right|\right. \\
&\left.+ (2-\frac{7}{4}-1)\left|\psi_i^{\uparrow}\psi_{2\pi}^{\downarrow}\psi_{\varepsilon}^{\uparrow}\right|\right] \\
&= \frac{3}{4}\Psi,
\end{aligned} \tag{4.10}$$

as expected. In order to find the a_i and b_i coefficients for the i and 2π orbitals in the triplet state, it is sufficient to consider the following wavefunction

$$\begin{aligned}
\Psi(q_1,q_2,q_3) = \frac{1}{\sqrt{6}}\left(\frac{2}{\sqrt{3!}}\begin{vmatrix}\psi_i^{\uparrow}(q_1) & \psi_{2\pi}^{\uparrow}(q_1) & \psi_{\varepsilon}^{\downarrow}(q_1)\\ \psi_i^{\uparrow}(q_2) & \psi_{2\pi}^{\uparrow}(q_2) & \psi_{\varepsilon}^{\downarrow}(q_2)\\ \psi_i^{\uparrow}(q_3) & \psi_{2\pi}^{\uparrow}(q_3) & \psi_{\varepsilon}^{\downarrow}(q_3)\end{vmatrix}\right. \\
\left. - \frac{1}{\sqrt{3!}}\begin{vmatrix}\psi_i^{\downarrow}(q_1) & \psi_{2\pi}^{\uparrow}(q_1) & \psi_{\varepsilon}^{\uparrow}(q_1)\\ \psi_i^{\downarrow}(q_2) & \psi_{2\pi}^{\uparrow}(q_2) & \psi_{\varepsilon}^{\uparrow}(q_2)\\ \psi_i^{\downarrow}(q_3) & \psi_{2\pi}^{\uparrow}(q_3) & \psi_{\varepsilon}^{\uparrow}(q_3)\end{vmatrix} - \frac{1}{\sqrt{3!}}\begin{vmatrix}\psi_i^{\uparrow}(q_1) & \psi_{2\pi}^{\downarrow}(q_1) & \psi_{\varepsilon}^{\downarrow}(q_1)\\ \psi_i^{\uparrow}(q_2) & \psi_{2\pi}^{\downarrow}(q_2) & \psi_{\varepsilon}^{\downarrow}(q_2)\\ \psi_i^{\uparrow}(q_3) & \psi_{2\pi}^{\downarrow}(q_3) & \psi_{\varepsilon}^{\downarrow}(q_3)\end{vmatrix}\right).
\end{aligned} \tag{4.11}$$

Using the same method as for the singlet case, we find that $a_i = 1, b_i = -\frac{1}{2}, a_{2\pi} = 1$ and $b_{2\pi} = -\frac{1}{2}$. Again, using the third limiting case in Section 2.3.9, we find $a_j = 2$ and $b_j = 1$ for $j \neq i, 2\pi$.

4.3 Calculation details

First, we compute the ionization energies of the 1σ, 2σ and 4σ orbitals. We do so using the CASSCF method [62] in the framework of the quantum-chemistry package MOLPRO [69]. In MOLPRO, we employ the augmented Dunning correlation

consistent quadruple valence basis set (aug-cc-pVQZ) [90]. We find the equilibrium distance of the ground state of NO to be equal to 1.1508 Å, in agreement with Ref. [102]. In Table 4.1, we compare the ionization energies we obtain with experimental results [10, 103]. Table 4.1 shows that our results agree very well with experimental ones, particularly for the 1σ and 2σ orbitals.

Orbital	This work (eV)	Experiment (eV)
$1\sigma\ ^1\Pi$	543.5	543.8 [10]
$1\sigma\ ^3\Pi$	543.1	543.3 [10]
$2\sigma\ ^1\Pi$	411.6	411.8 [10]
$2\sigma\ ^3\Pi$	410.2	410.3 [10]
$4\sigma\ ^1\Pi$	23.0	21.8 [103]
$4\sigma\ ^3\Pi$	21.2	21.7 [103]

Table 4.1: Ionization energies of the 1σ, 2σ and 4σ orbitals for NO.

We consider single-photon absorption due to the X-ray pulse from the core orbitals 1σ and 2σ, which are localized on the oxygen and nitrogen sides respectively. We also obtain the single-photon ionization cross section for the valence orbital 4σ. For the calculation of the photoionization cross section from the 4σ orbital, we use the bound orbitals of the ground state of NO. However, for ionization from the 1σ and 2σ orbitals, we use the bound orbitals of the excited state of NO^+ with a core hole in the 1σ or 2σ orbitals, i.e. the final state of the photoionization transition. The reason is that for ionization from the 1σ or 2σ orbitals the hole state is highly localized. This causes the electron density of the remaining electrons to adjust to this new potential. For ionization from the 4σ orbital, the hole is delocalized, so the effect of orbital relaxation is less noticeable, see Ref. [10, 54, 104].

We compute the bound states using the HF method with the aug-cc-pVQZ basis set. Moreover, we find that in the SCE, see Eq. (2.26), it suffices to truncate the expansion over the l quantum numbers up to $l_{max} = 30$ for the bound wavefunctions and $l_{max} = 19$ for the continuum wavefunctions. This truncation ensures convergence of the single-photon ionization cross sections. Also, we note that in the computation of the dipole matrix element in Eq. (3.36) for the 1σ, 2σ and 4σ states, we use $m_i = 0$.

4.4 Results

4.4.0.1 Photoionization cross sections

In Fig. 4.1, we compare the total photoionization cross sections from the 2σ and 4σ orbitals obtained in this work using Eq. (2.149) with the experimental results of Refs. [105, 106], as well as with the theoretical results of Refs. [54, 107].

For ionization from the 2σ orbital, the cross sections we obtain for the singlet and triplet states (Fig. 4.1(a)) exhibit a shape resonance [96] at roughly 417 eV and 418 eV respectively, which are a few eV higher than the resonances obtained in the theoretical work of Lin et al. [54]. We find that besides this offset in the location of the shape resonance, the overall shape of the cross section for the singlet state with respect to the photon energy is in very good agreement with the cross section obtained by Lin et al. [54]. However, the maximum cross section we obtain for the triplet state is roughly two times higher than the one obtained by Lin et al. [54]. For large photon energies, the results we obtain for the singlet and triplet states agree with Lin et al. [54] as well as with the experimental results [105]. The total cross section of the singlet plus the triplet states of NO^+ obtained in this work is found to be in close agreement with the theoretical result of Wallace et al. [107]. We note that the theoretical technique we use to obtain the cross sections is more accurate than the method employed by Wallace et al. [107] but less accurate than the one used by Lin et al. [54]. Specifically, the work of Wallace et al. [107] employs the multiple scattering method (MSM), where the cross section of the singlet and triplet states differ only by the spin-statistical ratio of $1:3$. Lin et al. [54] compute the continuum wavefunctions separately for the singlet and triplet states using the multichannel Schwinger configuration interaction (MCSCI) method. In our work, we compute the continuum wavefunctions in the HF framework using different coefficients b_i for the singlet and triplet states, as discussed in Section 4.2. Finally, we multiply by the spin-statistical ratio $1:3$ the cross sections of the singlet and triplet states of NO^+. In Fig. 4.1(b), we compare our results for the photoionization cross section from the 4σ orbital for the triplet state of NO^+ with the theoretical result of Wallace et al. [107] and with the experimental result of Brion et al. [106]. We find that all

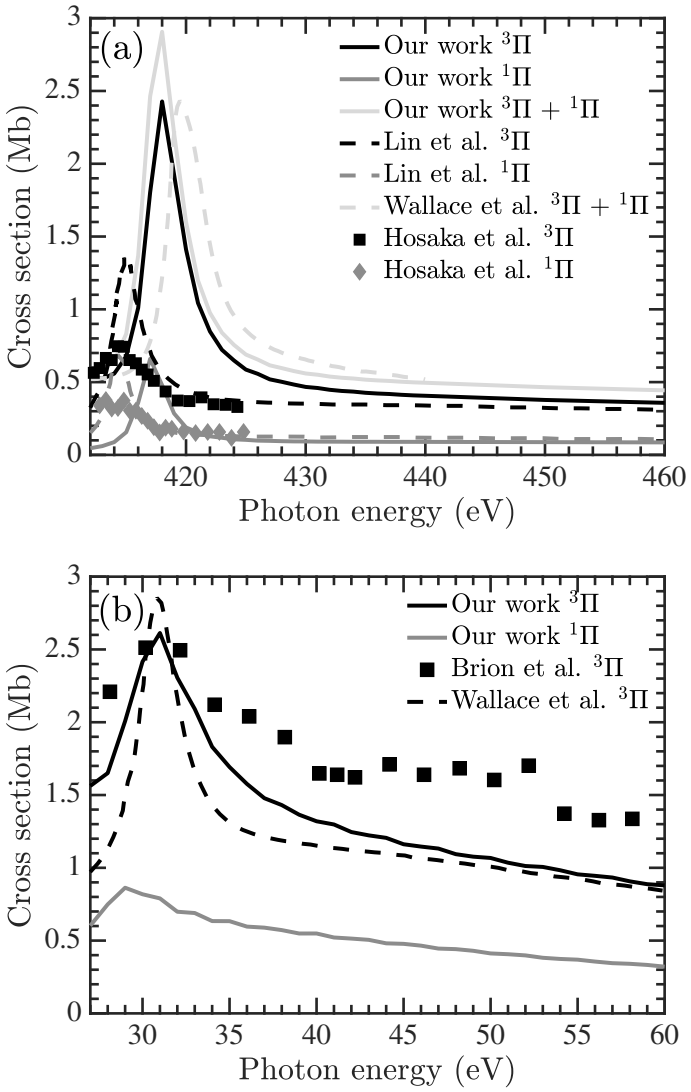

Figure 4.1: Photoionization cross sections for NO (a) from the 2σ orbital (b) from the 4σ orbital. In 1(a), we compare the results we obtain for the singlet state of NO^+ (solid dark grey line) and for the triplet state of NO^+ (solid black line) with the theoretical results of Lin et al. [54] for the singlet (dashed dark grey line) and triplet (dashed black line) of NO^+, as well as with the experimental results of Hosaka et al. [105] (dark grey diamonds and black squares). The total cross section we obtain for the singlet plus the triplet state of NO^+ (solid light grey line) is compared with the theoretical results of Wallace et al. [107] (dashed light grey line). In 1(b), we compare the results we obtain for the triplet state of NO^+ (solid black line) with the theoretical results of Wallace et al. [107] (dashed black line), as well as with the experimental results of Brion et al. [106] (black squares). We also show the results we obtain for the singlet state of NO^+ (solid dark grey line).

results exhibit a shape resonance at roughly 31eV and have similar values for high photon energies. However, the cross section we obtain for the triplet state of NO^+ has a better agreement with the experiment [106] compared to the cross section obtained by Wallace et al. [107].

4.4.0.2 Photoionization by the X-ray pulse

In what follows, we obtain the differential cross section for an electron to ionize by single-photon absorption from the O side, 1σ orbital, or the N side, 2σ orbital, only due to the X-ray laser field. In Fig. 4.2, we plot the absolute value square of $D_M(\vec{k}')$ in Eq. (3.36), which is proportional to the differential cross section. Since we consider a linearly-polarized X-ray pulse, the polarization of the photon in the LAB frame M is equal to 0. We do so for two different photon energies, one close to threshold, i.e. 546 eV for the 1σ and 413 eV for the 2σ orbital and for a photon energy significantly higher than the ionization threshold, i.e. 623 eV for the 1σ and 490 eV for the 2σ orbital. As expected, we find that for the high photon energies the electron has significantly higher probability to ionize towards the side where the electron originally ionizes from. That is, for ionization from the 1σ orbital the electron mostly escapes towards the O side for a photon energy of 623 eV. For ionization from the 2σ, the electron mostly ionizes along the N side for a photon energy of 490 eV. However, for lower photon energies the electron has significant probability to ionize towards the other side as well, see Figs. 4.2(a) and 4.2(c).

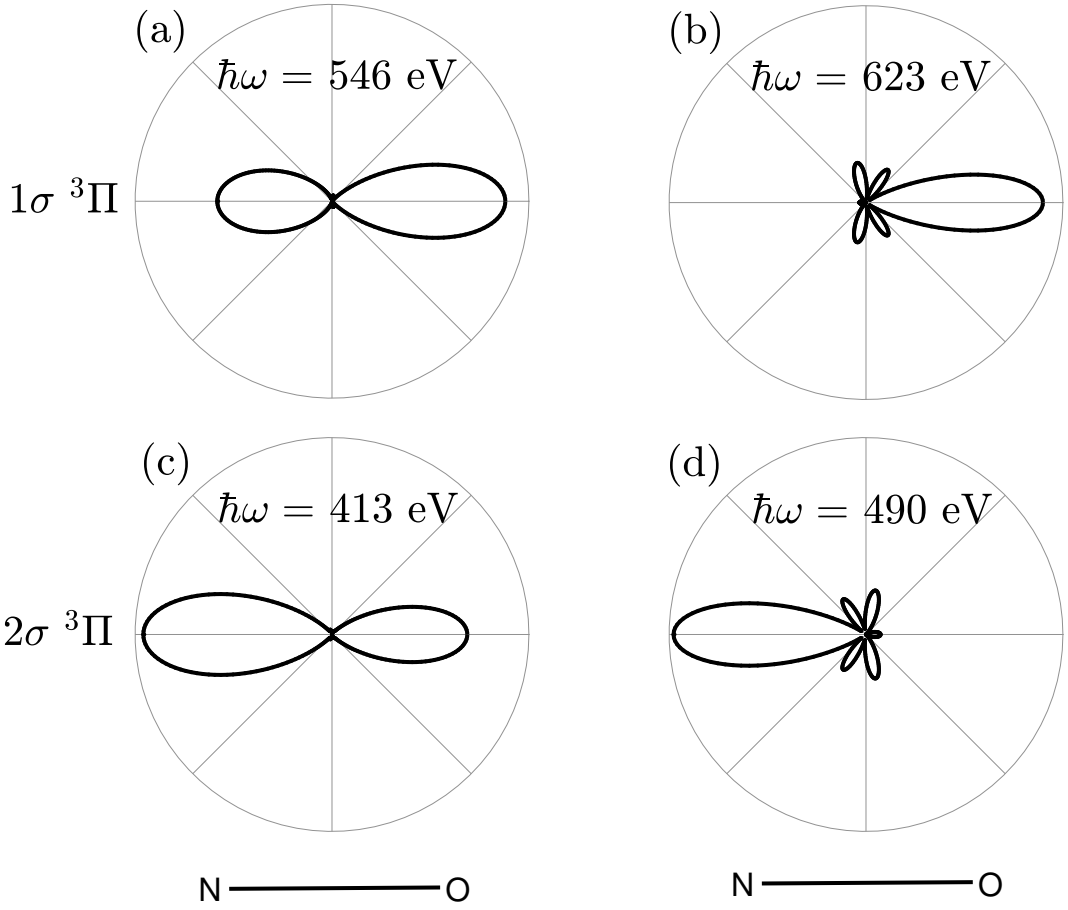

Figure 4.2: Differential cross section for an electron to ionize at a certain angle θ_X from ((a)-(b)) the 1σ orbital and ((c)-(d)) the 2σ orbital for the triplet state of NO^+.

4.4.0.3 Control of electron ionization triggered by an X-ray pulse

Coherent control is an important tool with wide applications in quantum optics and metrology [36–38], attosecond metrology [39, 40], optoelectronics [41] and laser cooling [42, 43]. Recent studies [32–35], succeeded in steering the direction of electron current by controlling the quantum interference of excitation or ionization pathways resulting from a mid-IR ω pulse and its second harmonic 2ω [32]. Control of the interference between the two-photon (ω) and single-photon (2ω) pathways and finally of the direction of electron motion was achieved using as a tool the phase delay of the two pulses [32].

In this optical technique, the dimensions over which the electron current is generated are limited to roughly one wavelength of the infrared light that is used to accelerate the electrons [108], i.e. to a few μm. Using coherent control of one and

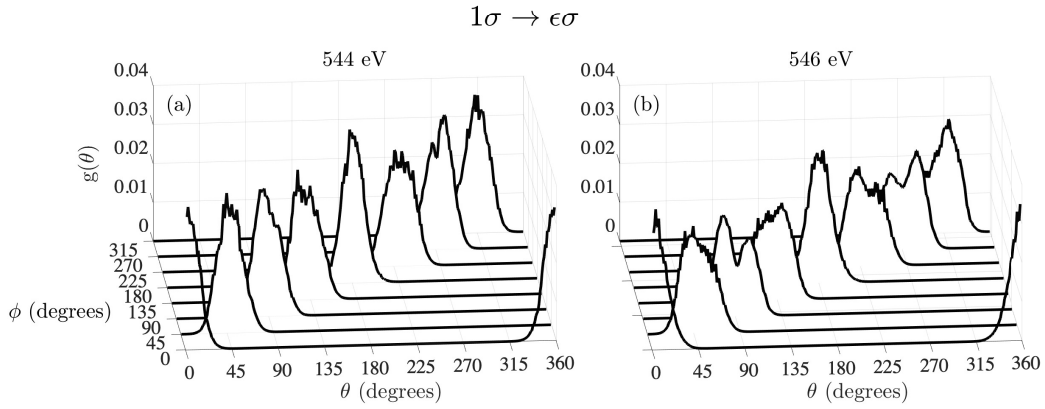

Figure 4.3: For the triplet state of NO^+, we waterfall plot the probability $g(\theta)$ as a function of the angle θ of electron escape for different phase delays ϕ between the X-ray and IR pulses. The electron ionizes from the 1σ orbital of NO and the intensity of the circularly-polarized IR pulse is 5×10^{13} W/cm^2. The photon energy of the X-ray pulse is (a) 544 eV and (b) 546 eV.

two photon processes to reduce to the nm scale the dimensions over which current is produced requires optically generating ω and 2ω vacuum ultraviolet (VUV) light beams. This is currently impractical.

In what follows, we theoretically demonstrate that control of electron currents generated at roughly a few nm is possible. We demonstrate control by varying the phase delay between a linearly-polarized X-ray pulse and a circularly-polarized IR pulse, while keeping the orientation of the NO molecule fixed and parallel to the linear polarization of the X-ray pulse. Specifically, for high intensities of the IR pulse we find a one-to-one correspondence between the final angle of electron escape and the phase delay between the X-ray and IR pulses. This has been shown in Chapter 3 in the context of N_2.

We obtain the probability for an electron to escape to the continuum on the x–z plane of the IR pulse with an angle θ. This angle is measured with respect to the z axis in the LAB frame. In this section, the NO molecule lies along the z axis. To obtain the probability for an electron to ionize on the x–z plane with momentum (p_{fr},θ), we integrate $\left|\mathcal{A}(\vec{p}_f)\right|^2$ from Eq. (3.44) over the p_{f_y} component

$$\left|\mathcal{A}(p_{fr},\theta)\right|^2 = \int dp_{fy}\left|\mathcal{A}(\vec{p}_f)\right|^2. \tag{4.12}$$

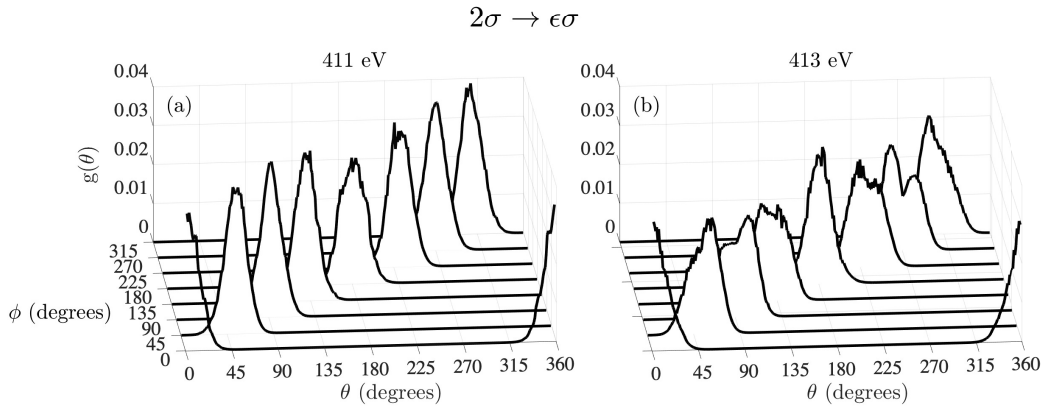

Figure 4.4: Same as Fig. 4.3, but for an electron ionizing from the 2σ orbital of NO. The X-ray photon energy is (a) 411 eV and (b) 413 eV.

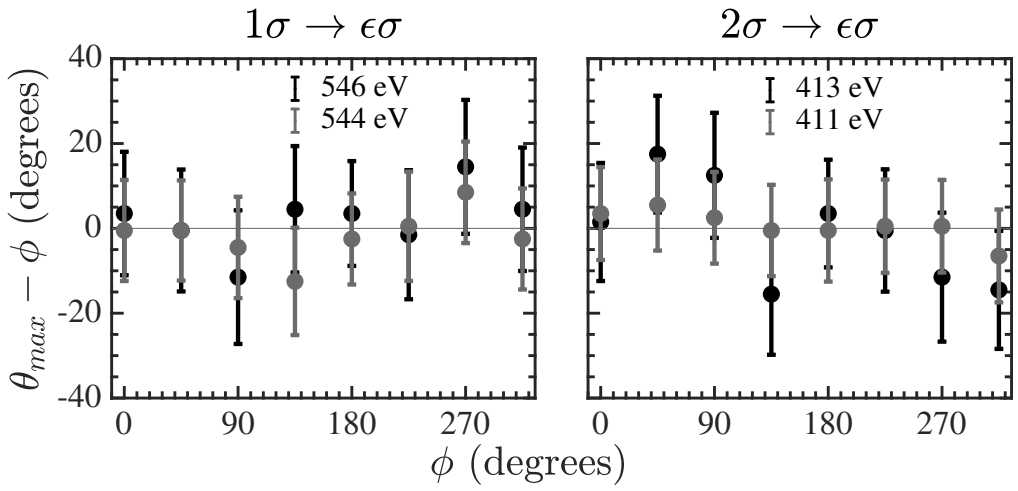

Figure 4.5: The most probable angle of ejection $\theta_{\max}$ (black dots) as a function of the delay ϕ between the X-ray and IR pulses, for an electron ionizing from the 1σ and 2σ orbitals. The intensity of the IR pulse is 5×10^{13} W/cm^2. The vertical grey bars denote the standard deviation of the probability distribution g(θ).

Then, integrating $\left|\mathcal{A}(p_{fr},\theta)\right|^2$ in Eq. (4.12) over p_{fr}, we find that g(θ), the probability for an electron to ionize with angle θ on the x–z plane, is given as follows

$$g(\theta) = \int dp_{f_r} p_{f_r} \left|\mathcal{A}(p_{fr},\theta)\right|^2. \tag{4.13}$$

In Figs. 4.3 and 4.4, we plot the probability $g(\theta)$ for a high intensity of the circularly-polarized IR pulse, equal to 5×10^{13} W/cm^2. Here, the molecular axis of the NO molecule is parallel to the X-ray pulse. We use the same expression to describe the vector potential of the IR pulse as in Eq. (3.38) with $\phi = 0$, and the same expression for the electric field of the X-ray pulse as for the electric field of the VUV pulse in Eq. (3.42). We consider a photon energy of the IR pulse ω_{IR} equal to 2300 nm, while the FWHM is $\tau_{IR} = 100$ fs. We take the amplitude and duration of the electric field of the X-ray pulse to be such that the intensity of the X-ray pulse is 10^{13} W/cm^2 and $\tau_{\rm X} = 0.5$ fs. We consider ionization from the 1σ (O side) and 2σ (N side) orbitals for the triplet state of NO^+. In our results, we fully account for the energy range of the X-ray pulse. That is, the Fourier transform of the X-ray pulse, since the full-width half maximum is equal to 0.5 fs, extends over energies roughly $\pm$ 4 eV from the central photon energy.

In Figs. 4.3(a) and 4.4(a), for photon energies of the X-ray pulse close to the ionization threshold, such as 544 eV (0.9 eV excess energy) for the 1σ orbital and 411 eV (0.8 eV excess energy) for the 2σ orbital, we show that we achieve control of the final angle of electron escape. That is, we achieve control when the electron due to the X-ray pulse is released at $t_{\rm ion}$ in the IR pulse with very small momentum $k'(t_{\rm ion}) = \sqrt{2(\hbar\omega - I_p)}$ compared to the momentum the electron gains from the IR pulse (0.6 a.u.). For the 544 eV and 411 eV photon energies considered here the excess momentum of the ionized electron is 0.26 a.u and 0.24 a.u., respectively. Indeed, Figs. 4.3(a) and 4.4(a) show that for each ϕ the distribution $g(\theta)$ is narrow and centered around the angle $\theta_{\rm max}$ of θ that corresponds to the maximum $g(\theta)$, that is, $\theta_{\rm max} = \phi$. This means that there is a one-to-one mapping between the phase delay ϕ and the most probable angle of electron escape $\theta_{\rm max}$.

However, as we increase the photon energy of the X-ray pulse and hence the

excess energy of the electron released due to the X-ray pulse at t_{ion} in the IR pulse, Figs. 4.3(b) (2.9 eV excess energy) and 4.4(b) (2.8 eV excess energy) show that the distributions of $g(\theta)$ become more wide. Hence, for higher photon energies, we do not control the final angle of electron escape as well as for smaller photon energies. Quite interestingly, for high photon energies the distributions of $g(\theta)$ preserve features of the angular patterns of ionization in the presence of just the X-ray pulse. This is clearly seen for $\phi = 90^\circ, 270^\circ$ for a transition from the 1σ orbital when the X-ray energy is 543 eV (Fig. 4.3(b)) as well as for a transition from the 2σ orbital when the photon energy is 413 eV (Fig. 4.4(b)). Indeed, in Fig. 4.3(b), for $\phi = 90^\circ, 270^\circ$, we find that $g(\theta)$ has a double peak structure. The momentum gain of the ionizing electron from the IR pulse points along the +*x* axis for $\phi = 90^\circ$, while it points along the -*x* axis for $\phi = 270^\circ$. Hence, the higher probability of an electron to be ejected along the O side just in the presence of the X-ray pulse, see Fig. 4.2(a), gives rise to the higher valued peak at $\theta < 90^\circ$ for $\phi = 90^\circ$ and at $\theta > 90^\circ$ for $\phi = 270^\circ$. For the transition from the 2σ orbital in Fig. 4.4(b), we observe a reversed pattern of the higher value peak of $g(\theta)$. This is due to an electron having a higher probability to be ejected along the N side just in the presence of the X-ray pulse, see Fig. 4.2(c).

In addition, we better illustrate in Fig. 4.5 the one-to-one mapping between θ_{max} and the phase delay ϕ between the X-ray and IR pulses by plotting $\theta_{\text{max}} - \phi$ as a function of ϕ. We do so for the transitions from the 1σ and 2σ orbitals for the same photon energies of the X-ray pulses as the ones considered in Figs. 4.3 and 4.4. For smaller photon energies of the X-ray pulse, we find that for each ϕ the values of $\theta_{\text{max}} - \phi$ are close to zero, i.e. they lie close to the black horizontal line at zero in Fig. 4.5. Furthermore, for each ϕ, the standard deviation of θ with respect to the probability distribution $g(\theta)$ is smaller for the lower photon energies. This is seen by the shorter (smaller range in degrees) error bars for the smaller photon energies (grey bars) compared to the longer error bars for the larger photon energies (black bars). The difference between smaller and larger photon energies is especially evident for the transition from the 2σ orbital, since a 2 eV increase in

the photon energy of the X-ray pulse is relatively larger for the 2σ orbital that has a lower threshold energy. The small spread of the angles θ around θ_{max}, for each ϕ, means we achieve excellent control of electron motion.

On a final note, in the framework of the SFA considered in this work after the electron is released in the IR pulse due to the X-ray pulse, it is evident that the electron motion is completely determined by the IR pulse if the electron is released in the IR pulse with zero excess energy. In this case the final momentum of the electron is completely determined by the vector potential at the time of ionization which forms an angle ϕ with the z axis and thus the final angle of electron ejection θ is equal to ϕ. In this section we have demonstrated that we achieve control of electron motion with the IR pulse for a range of photon energies of the X-ray pulse above the threshold energy for a given transition.

4.4.0.4 Streaking of electron ionization by an IR pulse

In the following, we obtain doubly differential final electron momenta distributions for low intensities of the circularly-polarized IR pulse. We show that many of the features of these doubly differential electron distributions correspond to angular patterns of electron ionization just in the presence of the X-ray pulse.

We plot the final electron momenta distributions on the x–z plane of the IR pulse for an electron ionizing from the 1σ (Fig. 4.6) and the 2σ (Fig. 4.7) orbitals for the triplet state of NO^+. To obtain the probability for an electron to escape with final momentum components p_{fx} and p_{fz} regardless of the component p_{fy}, we perform the following integration

$$\left|\mathcal{A}(p_{fx},p_{fz})\right|^2 = \int dp_{fy}\left|\mathcal{A}(\vec{p}_f)\right|^2. \tag{4.14}$$

In Figs. 4.6 and 4.7, we plot $\left|\mathcal{A}(p_{fx},p_{fz})\right|^2$, that is the doubly differential probability for an electron to ionize on the x–z plane with final momenta (p_{fx},p_{fz}), for a low intensity of the circularly-polarized IR pulse equal to 5×10^{12} W/cm^2. The photon energy and FWHM of the IR pulse are $\omega_{IR} = 2300$ nm and $\tau_{IR} = 100$ fs. The amplitude and duration of the electric field of the X-ray pulse are such that the

intensity of the X-ray pulse is equal to 10^{13} W/cm^2 and $\tau_X = 0.5$ fs. Here, unlike section IIID, there is no phase delay between the X-ray and IR pulse, i.e. $\phi = 0$. We obtain these momenta distributions when the NO molecule is on the x–z plane for various orientations θ_{mol} with respect to the z axis. The angle θ_{mol} corresponds to the angle β in Euler angles notation, see Section 3.2. We vary the angle θ_{mol} from 0 to π in steps of $\frac{\pi}{4}$.

We take the photon energies of the X-ray pulse to be equal to 561 eV for the 1σ orbital (Fig. 4.6) and 428 eV for the 2σ orbital (Fig. 4.7), which is roughly 18 eV above their respective ionization thresholds. Hence, at the time t_{ion}, the electron ionizes due to the X-ray pulse with momentum roughly equal to 1.15 a.u. Since the X-ray pulse is taken to have a short duration, the times of ionization that we sample are close to the center of the IR pulse. Hence from Eq. (3.38), the momentum gain of the ionizing electron from the IR pulse is equal to $-A_{IR}(t_{\text{ion}}) = -A_{IR}(\approx 0) = \frac{E_0^{IR}}{\omega_{IR}} = 0.60$ a.u. From Eq. (3.39), we thus find that the maximum and minimum final momentum of the electron is 1.75 a.u. and -0.55 a.u., respectively. Indeed, these maximum and minimum values of the momentum are seen in the right columns of Figs. 4.6 and 4.7 for $p_{f_x} \approx 0$.

Next, we show that the momenta distributions obtained from the X-ray+IR pulses in the right columns of Figs. 4.6 and 4.7 exhibit features consistent with the angular pattern of ionization solely due to the X-ray pulse. We show this by pairing each color plot of $\left|\mathcal{A}(p_{fx}, p_{fz})\right|^2$ (right column of Figs. 4.6 and 4.7) with the respective polar plot of $\left|D_0(\vec{k}')\right|^2$ (left column of Figs. 4.6 and 4.7). We note that in the polar plots, we plot the projection of $\left|D_0(\vec{k}')\right|^2$ on the x-z plane, i.e. we integrate over the angle ϕ_X, in order to better compare with the color plots of $\left|\mathcal{A}(p_{fx}, p_{fz})\right|^2$. Starting with the molecular orientation $\theta_{mol} = 0$, we observe that the high probability lobe towards the O side in Fig. 4.6(b1) corresponds to the high probability lobe in Fig. 4.6(a1). The smaller lobes in Fig. 4.6(a1) that are located at angles different to 0° and 180°, are shifted compared to Fig. 4.6(b1) due to the momentum gain along the z axis from the IR pulse. This is true for all angles θ_{mol} considered in Figs. 4.6 and 4.7. For the molecular orientations

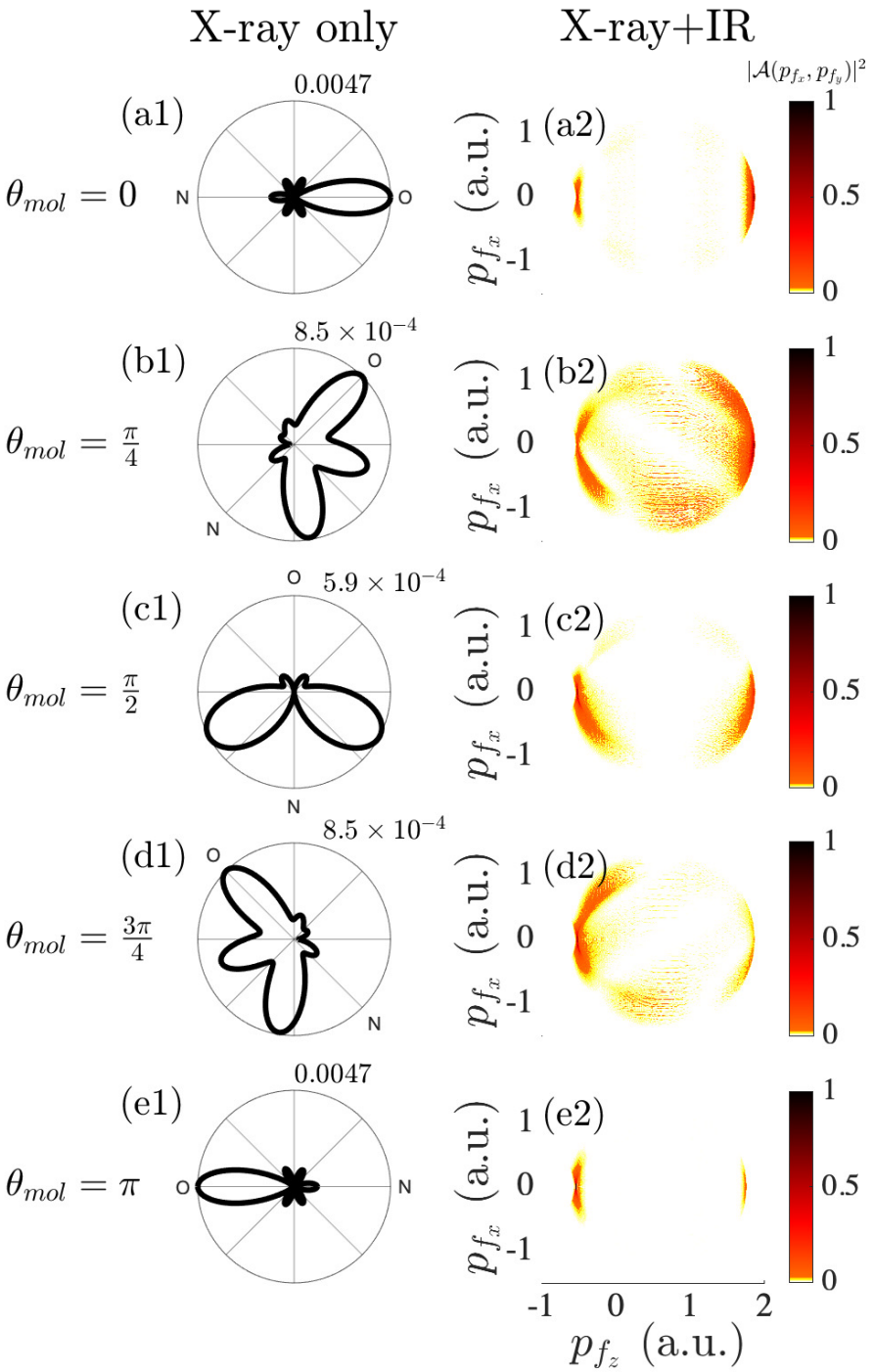

Figure 4.6: For the triplet state of NO^+ for ionization from the 1σ orbital and a photon energy of the X-ray pulse equal to 561 eV, on the left column, we polar plot $\left|D_0(\vec{k'})\right|^2$ and project on the x-z plane, i.e. we integrate over all angles ϕ_X. On the right column, we plot the doubly differential probability $\left|\mathcal{A}(p_{fx}, p_{fz})\right|^2$ for an electron to escape on the plane of the circularly-polarized IR pulse, which is the x-z plane. The color plots are divided by their respective maximum differential probability to give the same relative scale for all color plots. The intensity of the circularly-polarized IR pulse is equal to 5×10^{12} W/cm^2. The phase delay between the X-ray and IR pulses, ϕ, is equal to 0°. The right and left column plots are obtained for the NO molecule being on the x–z plane with an angle θ_{mol}, measured with respect to the z axis, ranging from 0 to π in steps of $\frac{\pi}{4}$.

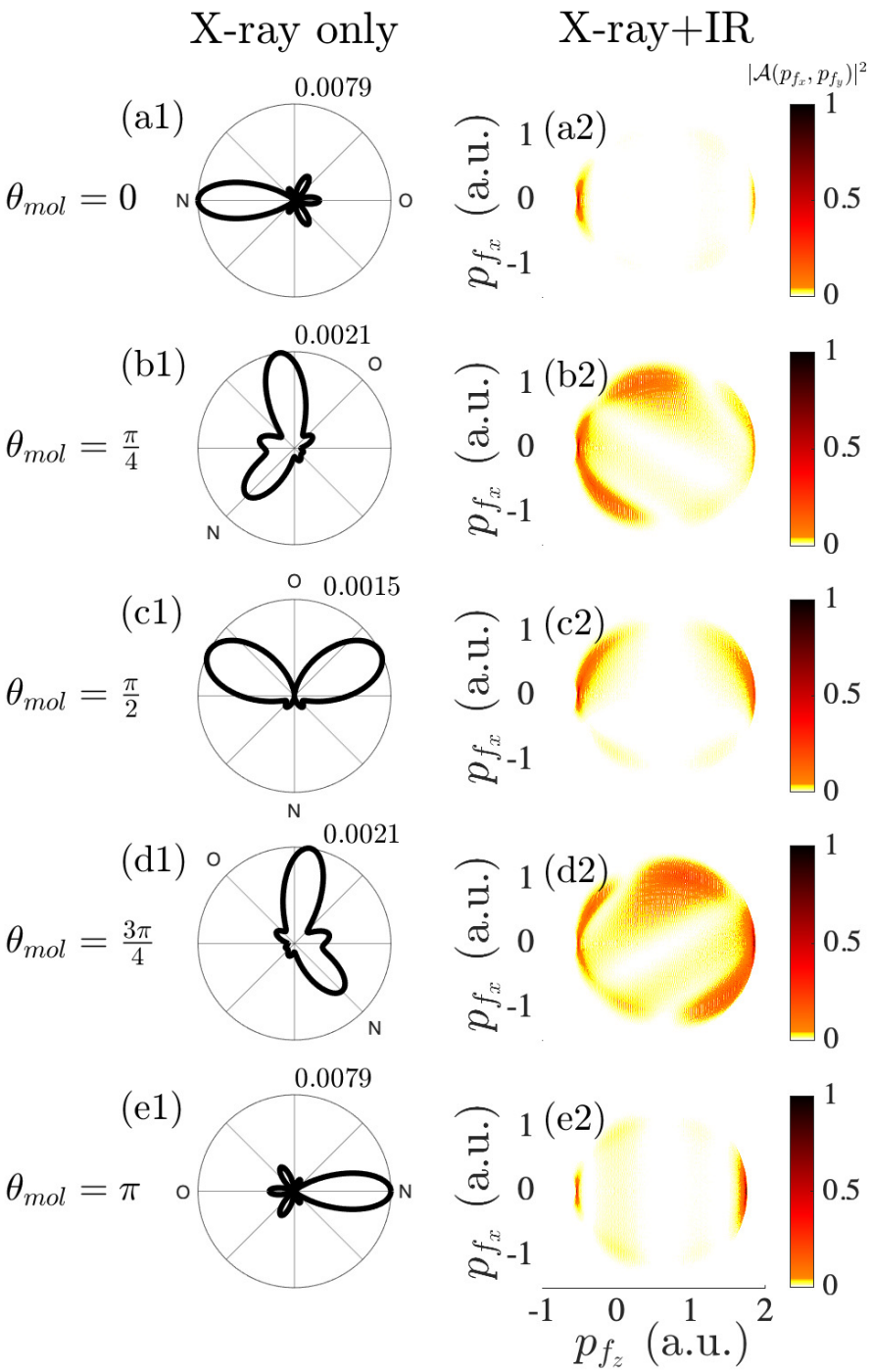

Figure 4.7: Same as Fig. 4.6, but for ionization from the 2σ orbital with a photon energy of the X-ray pulse equal to 428 eV.

$\theta_{mol} = 0, \frac{\pi}{4}, \frac{3\pi}{4}, \pi$, we see that a significant probability in the color plots of Figs. 4.6 and 4.7 corresponds to a large probability for the electron to ionize along the O side for ionization from the 1σ orbital and along the N side for ionization from the 2σ orbital, see the corresponding large lobes in the polar plots. However, this is not the case for $\theta_{mol} = \frac{\pi}{2}$. In Figs. 4.6(b3) and 4.7(b3), we see that when the molecule is perpendicular to the X-ray pulse the electron does not escape along the molecular axis. In this latter case, the electron escapes with larger probability at angles roughly equal to 120° with respect to the O (N) side for ionization from the 1σ (2σ) orbital. These smaller probability lobes are present for all angles θ_{mol}.

Overall, comparing the doubly differential plots of $\left|\mathcal{A}(p_{fx}, p_{fz})\right|^2$ with the polar plots of $\left|D_0(\vec{k}')\right|^2$ we find that, for small intensities of the IR pulse, most features in the former plots correspond to angular patterns of ionization in the presence of just the X-ray pulse. This is the reason why doubly differential plots of an electron to ionize with momenta (p_{fx}, p_{fz}) are used to extract photoionization time delays [12].

Finally, we note again that the Coulomb potential is fully accounted for the interaction of the NO molecule with the X-ray pulse. We neglect the Coulomb potential only during the propagation inside the IR pulse of the electron released at time t_{ion}. We expect that this approximation will not affect our findings concerning control and streaking of the electron motion. Fully accounting for the Coulomb potential at all stages will most probably result in broader distributions $g(\theta)$, for the high intensity IR case, and doubly differential probability $\left|\mathcal{A}(p_{fx}, p_{fz})\right|^2$ for the low intensity IR case.

4.5 Conclusions

In conclusion, we have shown how to obtain continuum molecular wavefunctions for open-shell molecules in the Hartree-Fock framework. We have obtained these wavefunctions when the total spin symmetry of the open-shell orbital and the orbital where the electron ionizes from is singlet or triplet. Using these continuum wavefunctions, we have obtained dipole matrix elements for ionization of an electron

due to a linearly-polarized X-ray pulse.

Following ionization from the X-ray pulse, we have investigated the effects on final electron escape when we streak with a circularly-polarized infrared pulse. These effects depend on the intensity of the streaking infrared pulse. For a high intensity, we have shown that we control the angle of an electron escaping to the continuum. This control is achieved by varying the phase delay between the ionizing X-ray pulse and the infrared pulse. When the photon energy of the X-ray pulse is very close to the ionization threshold, a one-to-one mapping between the phase delay and the final angle of electron escape is achieved. For a low intensity, we have shown that the momentum distributions on the plane of the infrared pulse roughly image the angular electron escape patterns resulting by the X-ray pulse. The information obtained from the latter momentum distributions is of use to computing photoionization time delays.

Chapter 5

Formation of singly ionized oxygen atoms from O_2 driven by XUV pulses: a toolkit for the break-up of FEL-driven diatomics

5.1 Introduction

In this chapter, we formulate a hybrid quantum-classical theoretical model to address the interaction of molecules with intense laser pulses while accounting for the nuclear dynamics of the molecule. We will use this model to simulate the interaction between O_2 and an XUV pulse.

Molecular oxygen, O_2, is of great interest due to its significance in biology and atmospheric chemistry. Specifically, oxygen is the key component in both the metabolic processes of all living organisms and the ozone layer which shields us from the Sun's ultraviolet radiation [109–112]. There has already been a number of studies on singly and doubly ionized O_2, for instance see Refs. [113–115].

Our hybrid quantum-classical model allows us to identify the ionization sequences that lead to the formation of the two O^+ fragments. Namely, for photon energies from 20 eV to 42 eV, up to two sequential single-photon ionization processes can take place starting from the ground state of O_2. The electronic configu-

ration of the ground state of O_2 ($X^3\Sigma_g^-$) is given by ($1\sigma_g^2$, $1\sigma_u^2$, $2\sigma_g^2$, $2\sigma_u^2$, $3\sigma_g^2$, $1\pi_{ux}^2$, $1\pi_{uy}^2$, $1\pi_{gx}^1$, $1\pi_{gy}^1$), with the two open π_g orbitals resulting in a triplet spin state. These single-photon ionization processes include the removal of valence or inner-valence electrons from the ground state and singly excited states of O_2. The different ionization sequences result from the different O_2^+ states the molecule transitions to after the removal of the first electron as well as the different O_2^{2+} states the molecule transitions to after the escape of the second electron. For each sequence, we also identify the times and the inter-nuclear distance when ionization takes place. This detailed analysis allows us to relate specific features of the KER spectra for the O^+ + O^+ dissociation pathway with certain ionization sequences. We also investigate the dependence of the KER features and their connection to ionization sequences on pulse duration and intensity.

The hybrid model we develop in this work consists of employing state-of-the-art quantum-mechanical computations for describing electron escape to the continuum. At the same time, we allow the nuclei to move using classical equations of motion. However, in these classical equations of motion the force between the nuclei is provided by employing accurate quantum-mechanically obtained potential-energy curves (PECs). Specifically, in order to calculate the necessary ionization cross sections for our theoretical calculations, we utilise state-of-the-art ab-initio quantum-mechanical techniques [3]. Namely, we compute the continuum wavefunction of the escaping electron using molecular orbital wavefunctions obtained in the HF framework [29]. Most other studies do not provide such accurate molecular wavefunctions and instead use approximations that employ linear combination of atomic orbitals. Also, to provide the force in the classical equations that account for the motion of the nuclei, we obtain accurate PECs of the various states of O_2 and singly and doubly ionized O_2 by using advanced quantum-mechanical techniques in the framework of the quantum-chemistry package MOLPRO [67, 69, 116]. Computing PECs of these various states is not an easy task due to the open-shell configuration of O_2, especially in the cases where an electron is removed from an inner-valence orbital.

In Section 5.2, we discuss our theoretical methods for describing the interaction of a diatomic molecule, in this work O_2, with an XUV pulse. Then, in Section 5.3, we discuss our results for the KER of the two O^+ fragments. In particular, we consider both a low- and high-intensity XUV pulse in the photon-energy range from 20 eV to 42 eV. We identify the key features of the KER distributions, as well as the ionization sequences that lead to the obtained spectra.

5.2 Theoretical method

In what follows, we formulate a hybrid quantum-classical model to describe the interaction of a diatomic molecule, in this work O_2, with an XUV pulse. This model adapts the Born-Oppenheimer approximation [60] in order to separate the nuclear from the electronic motion in the driven molecule. We model the ionization of electrons quantum mechanically, as described in Section 2. We account for the motion of the nuclei and compute the velocities of the atomic fragments using the classical equations of motion of the two-body system, see Section 5.2.1. In Section 5.2.2, we describe how we use the Velocity-Verlet algorithm to calculate the internuclear distance and momentum at each time step. The force in these classical equations is computed via the PECs of up to doubly ionized Oxygen, which are obtained using advanced quantum-chemistry techniques, see Section 5.2.3. In Section 5.2.6, we describe how we sample the initial conditions for the nuclei using the Wigner distribution for the Morse oscillator. Both electron escape and nuclear motion are incorporated in a Monte-Carlo simulation described in Section 5.2.7. In Section 5.2.4, we outline the criteria we use to identify the time in the Monte-Carlo simulation when the molecule dissociates transitioning to two atomic fragments interacting with an XUV pulse.

5.2.1 Two-body equations for nuclear motion

In classical mechanics the Lagrangian of a two-body system with potential energy $U(\boldsymbol{r})$ is given by

$$L = \frac{1}{2}m_1\dot{\boldsymbol{x}}_1^2 + \frac{1}{2}m_2\dot{\boldsymbol{x}}_2^2 - U(\boldsymbol{r}), \tag{5.1}$$

where m_1, m_2 and $\dot{\boldsymbol{x}}_1, \dot{\boldsymbol{x}}_2$ are the masses and velocities of the two bodies, respectively. In our case, the two bodies are the nuclei of the diatomic molecule. The potential is a function of the difference between the position vectors of the nuclei, namely the difference vector $\boldsymbol{r} = \boldsymbol{x}_1 - \mathbf{x}_2$. The internuclear distance of the molecule is $r = |\boldsymbol{r}|$. The center of mass, $\boldsymbol{R}$, of the molecule is defined as

$$\begin{aligned} \boldsymbol{R} &= \frac{m_1}{m_1+m_2}\boldsymbol{x}_1 + \frac{m_2}{m_1+m_2}\boldsymbol{x}_2 \\ &= \frac{\mu}{m_2}\boldsymbol{x}_1 + \frac{\mu}{m_1}\boldsymbol{x}_2, \end{aligned} \tag{5.2}$$

where $\mu = \frac{m_1 m_2}{m_1+m_2}$ is the reduced mass of the molecule. The Lagrangian in Eq. (5.1) can be rewritten in terms of the center of mass velocity, $\dot{\boldsymbol{R}}$, and the relative velocity between the nuclei, $\dot{\mathbf{r}}$ as follows [117]

$$L = \frac{1}{2}(m_1+m_2)\dot{\boldsymbol{R}}^2 + \frac{1}{2}\mu\dot{\boldsymbol{r}}^2 - U(\mathbf{r}). \tag{5.3}$$

By Newton's second and third law, the force between the nuclei is given by

$$F = -\frac{dU}{dr}. \tag{5.4}$$

The position and velocities of the nuclei can be expressed in terms of $\boldsymbol{r}$ and the reduced mass as follows

$$\begin{aligned} \boldsymbol{x}_1 = \frac{\mu}{m_1}\boldsymbol{r} &\implies \dot{\boldsymbol{x}}_1 = \frac{\mu}{m_1}\dot{\boldsymbol{r}} \\ \boldsymbol{x}_2 = -\frac{\mu}{m_2}\boldsymbol{r} &\implies \dot{\boldsymbol{x}}_2 = -\frac{\mu}{m_2}\dot{\boldsymbol{r}}. \end{aligned} \tag{5.5}$$

5.2.2 Algorithm for propagating the nuclei in time

Next, we explain how we obtain the velocities of the nuclei $\dot{\boldsymbol{x}}_1$ and $\dot{\boldsymbol{x}}_2$. Eq. (5.5) shows that to obtain the final velocities, we need to track the internuclear distance, r, and the relative velocity, $\boldsymbol{v} = \dot{\boldsymbol{r}}$, as a function of time. To do so, we employ the Velocity-Verlet algorithm [118]. This algorithm calculates recursively the internu-

clear distance and the magnitude of the relative velocity at each time step as follows

$$\begin{aligned} r_{n+1} &= r_n + v_n \Delta t + \frac{1}{2\mu} F_n (\Delta t)^2 \\ v_{n+1} &= v_n + \frac{1}{2\mu} (F_{n+1} + F_n)(\Delta t), \end{aligned} \tag{5.6}$$

where Δt is the time step of the propagation and F_n is the force at each time step given by

$$\begin{aligned} F_n &= -\frac{dU(r_n)}{dr} \\ F_{n+1} &= -\frac{dU(r_{n+1})}{dr}, \end{aligned} \tag{5.7}$$

where $U(r_n)$ is the potential energy at the end of the n^{th} time step, while $U(r_{n+1})$ is the potential energy at the end of the $(n+1)^{th}$ time step. To obtain the potential $U(r)$, we compute the PECs of the singly and doubly ionized states of O_2. We describe how to do so in the next section. Hence, obtaining v at each time step allows us, through Eq. (5.5), to compute the magnitudes of the velocities $\dot{x}_1$ and $\dot{x}_2$ of the two atomic fragments.

5.2.3 Computation of potential-energy curves

Next, we describe the computation of the PECs of O_2 up to O_2^{2+} ionic states. We perform these calculations for all singly and doubly ionized states of O_2 that are energetically accessible by absorption of a single photon with energy varying from 20 eV to 42 eV. This range of photon energies suffices to ionize electrons from all outer-valence orbitals and the inner-valence orbital $2\sigma_g$. As a result, we can access and thus compute the PECs of eighteen states which are comprised of the ground state of O_2, five O_2^+ and twelve O_2^{2+} states.

First, we employ the HF method in MOLPRO to obtain, as a function of distance, the bound orbitals of O_2 in its ground state. We use these orbitals as input in the subsequent computation of the PECs employing the CASSCF method [62, 63]. In the current work, in a similar fashion to the one followed in Ref. [67] for the N_2 molecule, we consider 12 active orbitals. These orbitals include the nine occu-

pied ones in the ground state of O_2, which are given by $1\sigma_g$, $1\sigma_u$, $2\sigma_g$, $2\sigma_u$, $3\sigma_g$, $1\pi_{ux}$, $1\pi_{uy}$, $1\pi_{gx}$, $1\pi_{gy}$ and the three virtual orbitals $3\sigma_u$, $4\sigma_g$ and $4\sigma_u$. Lastly, to obtain even more accurate PECs, using as input the bound orbitals obtained with the CASSCF method, we next employ the MRCI method [64–66]. In our current computations, while the CASSCF method includes all possible excitations among only the 12 active orbitals, the MRCI method allows single and double excitations from all active orbitals to all orbitals. The MRCI method produces more accurate PECs compared to CASSCF by improving the description of the electron-electron repulsion [67, 119].

To compute the PECs, we employ the augmented Dunning correlation consistent quadruple valence basis set (aug-cc-pVQZ) [90]. For the states of singly and doubly ionized O_2 where at least one electron is missing from the inner valence orbitals $2\sigma_g$, there are several other states with the same symmetry and lower energy besides the desired state. This leads to variational collapse [120], where MOLPRO computes the lowest-energy state with the same symmetry as the desired state. We address this issue during the calculations of the PECs with the CASSCF and MRCI methods by employing the state-averaging technique in MOLPRO. This technique ensures that MOLPRO computes a sufficient number of states with the same symmetry as a function of the internuclear distance. We identify the desired state by selecting the state that has the desired electronic configuration at the equilibrium distance of the ground state of the O_2 molecule. We find the equilibrium distance to be equal to $r_e = 1.205$ Å = 2.28 a.u., in agreement with Refs. [121, 122]. As in Ref. [67], to obtain the PECs of all states with electrons missing from outer-valence orbitals, we optimize all orbitals at the same time. We obtain the PECs for sixteen states using the MRCI states, while for the states $O_2^+(^4\Sigma_g^-)$ and $O_2^{2+}(^3\Sigma_g^-)$, we could not achieve convergence using the MRCI method and hence obtained the PECs using the CASSCF method.

In Fig. 5.1, we compare the PECs we obtained using the method outlined above (black solid lines) with the theoretical PECs obtained in Refs. [52, 123, 124] (gray-dashed lines). The PECs obtained from the literature also utilise the MRCI

method. In Refs. [52, 123, 124], the PECs for $O_2^+(^4\Sigma_g^-)$, $O_2^{2+}(^5\Pi_g)$ and both of the $O_2^{2+}(^3\Sigma_g^-)$ states are not obtained, hence the lack of comparison in Fig. 5.1, with our PECs for these states. To produce smooth PECs, we compute the potential energy of the states at internuclear distances in steps of 0.05 Å = 0.094 a.u. Fig. 5.1 shows that we find an excellent agreement for our computations of the PECs with the ones obtained in Refs. [52, 123, 124].

In the first row of Fig. 5.1, we plot the PECs of the neutral ground state and the singly ionized states of O_2. These states possess a potential well and do not exhibit any repulsive behaviour, with the exception of the $O_2^+(^4\Sigma_g^-)$ state. In the second and third rows of Fig. 5.1, we plot the PECs of the doubly ionized states of O_2. Due to the increased electrostatic repulsion between the ions, all of the O_2^{2+} states exhibit repulsive behaviour. Note that only the $O_2^{2+}(X^1\Sigma_g^+)$, $O_2^{2+}(B^3\Pi_g)$ and $O_2^{2+}(W^3\Delta_u)$ states possess a potential well. However, the potential well of the $O_2^{2+}(W^3\Delta_u)$ state in particular is very shallow. To further verify the accuracy of the PECs we obtain in this work, we compare the atomic fragments resulting from the dissociation of each molecular state with the atomic fragments obtained in the literature [52, 125]. Next, we describe how to determine these atomic fragments.

5.2.4 Dissociation of molecular states

To describe the interaction of O_2 with an XUV pulse, we use the Monte-Carlo technique described in Section 5.2.7. If dissociation does take place, we need to specify the time during propagation when the diatomic molecule dissociates to two atomic fragments. We take this time to be when the energy of each molecular state, i.e. the PEC, converges to 99% of each asymptotic value, known as the dissociation energy. From this time onwards, we perform Monte-Carlo simulations for the interaction of each of the two individual atomic fragments with the pulse. We calculate the dissociation energy for each molecular state by computing the potential energy at an internuclear distance equal to 10^4 Å.

Once we compute the dissociation energy of each molecular state of O_2 up to O_2^{2+}, we identify the atomic fragments resulting from the dissociation of each of these states. To do so, for each molecular state, we take all possible combinations

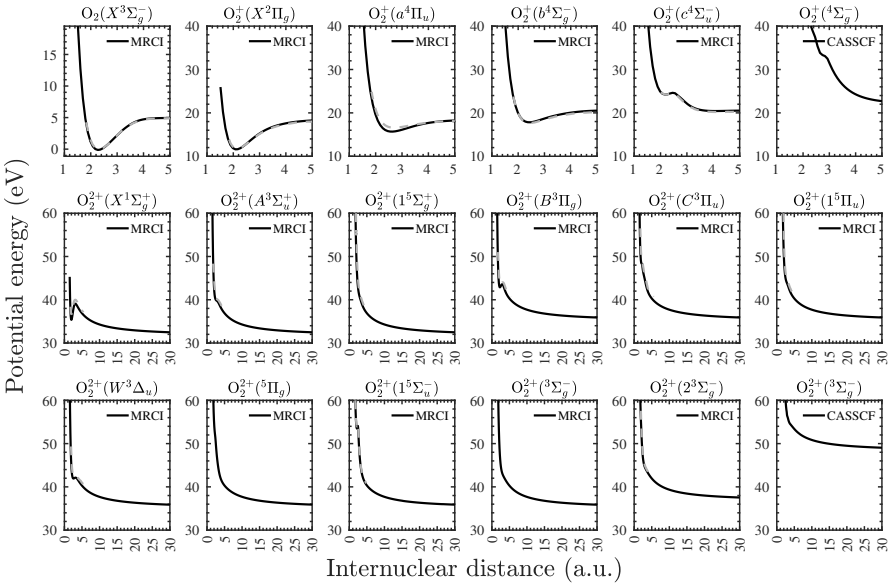

Figure 5.1: Potential-energy curves of O_2, O_2^+ and O_2^{2+} obtained using the techniques outlined in Section 5.2.3 (black-solid line), compared with the PECs obtained in Refs. [52, 123, 124] (gray-dashed lines).

of atomic fragments that sum to the same net charge as the molecular state under consideration. For all these combinations, we compute the sum of the energies of the atomic fragments and identify the one that matches the dissociation energy of the molecule.

In Table 5.1, we list all the O and O^+ atomic states, as well as their electronic configurations, that appear in the literature [52, 125] as the atomic fragments for the energetically accessible states of O_2, O_2^+ and O_2^{2+} in the current work. The atomic states in Table 5.1 are given using spectroscopic notation, i.e. in the form ^{2S+1}L, where S is the total spin of the system and L is the total orbital angular momentum of the system, found by summing up the projections of the angular momentum of each orbital. The spin multiplicity and total orbital angular momentum of the atomic states in Table 5.1 follow from Hund's rules [126]. Namely, Hund's first rule tells us that the term with maximum spin multiplicity has the lowest energy. Hence, this is why the spin multiplicities for the O(^{3}P) and O(^{4}S) states are 3 and 4, respectively. Furthermore, Hund's second rules states that the term with the largest total orbital angular momentum is lowest in energy. This is why, for example, the ground state

Atomic state	Configuration (1s, 2s, $2p_x$, $2p_y$, $2p_z$)
$O(^3P)$	22211
$O(^1D)$	22202
$O^+(^4S)$	22111
$O^+(^2D)$	22201
$O^+(^2P)$	22210

Table 5.1: Atomic states of O and O^+ which were found to be the atomic fragments of the molecular states considered in this work.

of atomic oxygen is a P state and not, for instance, the S state with configuration 22112.

In Table 5.2, we provide the dissociation energies of the energetically accessible molecular states in the current work, which we compare with dissociation energies from the literature [52, 125], and find them to be in very good agreement. For the sixteen states for which we were able to calculate their PECs using the MRCI method, we find a 1-2% difference in the dissociation energies with respect to the literature. For the PECs where we were able to utilize only the CASSCF method, we find larger deviations of 7% and 19%. This is due to the difference in the techniques used. Moreover, in Table 5.2 we list the atomic fragments each molecular state dissociates to, according to Refs. [52, 125]. Using the sum of the energies of the atomic fragments, which we computed with the MRCI method, we have verified that these are indeed the final atomic fragments for each molecular state.

5.2.5 Algorithm for propagating atomic fragments

In this work, we only consider up to O_2^{2+} ionic states. Using the criterion that we use for dissociation, outlined in Section 5.2.4, we find that in the photon energy range 20 eV to 42 eV, the largest internuclear distance at which one of the accessible O_2^+ states converges to 99 % of its dissociation energy is 5.2 a.u. For internuclear distances larger than this, we transition from molecules to atoms and utilise atomic transition rates. Hence, we only require molecular transition rates up to an internuclear distance of 5.2 a.u. The advantage of using the dissociation criterion outlined in Section 5.2.4 is that after this internuclear distance, the rate of change of the PECs is very small. In other words, the interaction potential between the atoms is

Molecular state	Atomic fragments	Sum of energies of atomic fragments	
		Our work (eV)	Other work (eV)
$O_2(X^3\Sigma_g^-)$	$O(^3P)$+$O(^3P)$	5.0	5.0 [52]
$O_2^+(X^2\Pi_g)$	$O^+(^4S)$+$O(^3P)$	18.5	18.8 [52]
$O_2^+(a^4\Pi_u)$	$O^+(^4S)$+$O(^3P)$	18.5	18.8 [52]
$O_2^+(b^4\Sigma_g^-)$	$O^+(^4S)$+$O(^1D)$	20.5	20.7 [52]
$O_2^+(c^4\Sigma_u^-)$	$O^+(^4S)$+$O(^1D)$	20.5	20.7 [52]
$O_2^+(^4\Sigma_g^-)$	$O^+(^2P)$+$O(^3P)$	22.3*	23.8 [125]
$O_2^{2+}(X^1\Sigma_g^+)$	$O^+(^4S)$+$O^+(^4S)$	31.6	32.4 [52]
$O_2^{2+}(A^3\Sigma_u^+)$	$O^+(^4S)$+$O^+(^4S)$	31.6	32.4 [52]
$O_2^{2+}(1^5\Sigma_g^+)$	$O^+(^4S)$+$O^+(^4S)$	31.6	32.4 [52]
$O_2^{2+}(B^3\Pi_g)$	$O^+(^4S)$+$O^+(^2D)$	35.0	35.7 [52]
$O_2^{2+}(C^3\Pi_u)$	$O^+(^4S)$+$O^+(^2D)$	35.0	35.7 [52]
$O_2^{2+}(1^5\Pi_u)$	$O^+(^4S)$+$O^+(^2D)$	35.0	35.7 [52]
$O_2^{2+}(W^3\Delta_u)$	$O^+(^4S)$+$O^+(^2D)$	35.0	35.7 [52]
$O_2^{2+}(^5\Pi_g)$	$O^+(^4S)$+$O^+(^2D)$	35.0	35.7 [52]
$O_2^{2+}(1^5\Sigma_u^-)$	$O^+(^4S)$+$O^+(^2D)$	35.0	35.7 [52]
$O_2^{2+}(^3\Sigma_g^-)$	$O^+(^4S)$+$O^+(^2D)$	35.0	35.7 [52]
$O_2^{2+}(2^3\Sigma_g^-)$	$O^+(^4S)$+$O^+(^2P)$	36.6	37.3 [52]
$O_2^{2+}(^3\Sigma_g^-)$	$O^+(^2D)$+$O^+(^2D)$	48.1*	39.0 [52]

Table 5.2: Atomic fragments resulting from the dissociation of O_2, O_2^+ and O_2^{2+}. We also provide the dissociation energy relevant to these atomic fragments, and compare with dissociation energies from Refs. [52, 125], denoted as other work. The * denotes states calculated using only the CASSCF method due to lack of convergence of the MRCI method, as mentioned in Section 5.2.3.

negligible. Hence, we take the final velocities of the atomic fragments at the end of the propagation to be equal to the velocities of the atomic fragments when the internuclear distance reaches 5.2 a.u.

However, when considering interactions with higher photon energies, we will access higher ionic states. The criterion for the PECs of higher ionic states to converge to 99 % of their dissociation energies is satisfied at very large, and increasing with charge, internuclear distances. For example, we find that internuclear distances for O_2^{2+} states are larger than 95 a.u. when they satisfy the above mentioned criterion. This implies that we would have to compute molecular photoionization cross sections and Auger-Meitner rates up to 95 a.u., which is computationally intense. Hence, for larger photon energies we find the final velocities of the atomic fragments in a different way. For this method, instead of feeding into the Monte Carlo

simulation the internuclear distance that satisfies the above mentioned convergence criterion for each molecular state, we consider the same internuclear distance for all molecular states where we transition from molecular to atomic interactions with the laser pulse. This internuclear distance will be chosen as the one where the PECs converge to a purely Coulomb repulsion interaction between the resulting atomic fragments. This method significantly reduces the number of molecular transition rates we would have to compute. However, it also means that we have to account for the repulsion of the atomic fragments, which results in different final velocities for the atomic fragments compared to the ones they have at the time when we transition from a molecule to atoms in the Monte Carlo simulations. To do so, we continue to propagate in time the nuclear dynamics as follows:

1. First, from the time when we transition from molecules to atoms until the end of the Monte Carlo simulation, we record all transitions that occur and the time at which they occur for each one of the atoms. In this way, we obtain the charge of each of the atoms as a function of time.

2. We combine the arrays of transition times of both atoms together and arrange these times in ascending order. Then, for each of these times, we find the product of the charges of the atoms at that time. Using this information, we apply the Velocity-Verlet algorithm. We use Δt as a time step and update it to the time difference between the next transition time in the ordered array and the current time if this time step is smaller than Δt.

5.2.6 Sampling the initial conditions of the nuclei

In the Monte-Carlo technique, at time step $n = 0$, we need to specify the initial internuclear distance, r_0, and relative momentum of the nuclei, $p_0 = \mu v_0$. To avoid importance sampling of both r_0 and p_0 at the same time, which requires the use of a 2-dimensional distribution, we use an approximation and sample r_0 and p_0 as follows. First, for the internuclear distance, we employ importance sampling [89] with the distribution given by the square of the Morse wavefunction [127] for the ground state of neutral O_2. The Morse potential is widely recognised as a good

approximation for potentials of diatomic molecules [128]. The Morse potential is given by

$$U_M(r) = D_e[(1 - e^{-\beta|r-r_e|})^2 - 1], \tag{5.8}$$

where D_e is the dissociation energy of the ground state of O_2, which is equal to 5 eV. The coefficient β is related to the frequency of vibration of the nuclei, ω_e, by the following expression

$$\omega_e = \beta\sqrt{\frac{2D_e}{\mu}}, \tag{5.9}$$

where μ is the reduced mass of the molecule. Using NIST, we assign ω_e to be equal to 1580.16 cm^{-1} [129]. Using Eq. (5.9) and the values we obtain for D_e, μ and ω_e, we compute β and find it to be equal to 1.27. The Morse wavefunction of the ground state of neutral O_2 [127] is given by

$$\begin{aligned} \psi_{j,0}(r) &= N_{j,0} e^{-\xi/2} \xi^j L_0^{2j}(\xi) \\ N_{j,0} &= \frac{\beta j}{\Gamma(2j+1)} \\ \xi &= (2j+1)e^{-\beta|r-r_e|}, \end{aligned} \tag{5.10}$$

where L_0^{2j} is an associated Laguerre polynomial [130] and Γ is the Gamma function. The quantum number j is related to the dissociation energy through

$$D_e = \frac{\beta^2}{2\mu}(j+\frac{1}{2})^2. \tag{5.11}$$

Given D_e, μ and β, we solve for j. Next, after obtaining with importance sampling r_0, we use this r_0 as input to the Wigner function of the ground state of neutral O_2, which is given by

$$W(\psi_{j,0}|r,p) = \frac{2}{\pi\Gamma(2j)}\xi^{2j}K_{-2ip/\beta}(\xi), \tag{5.12}$$

where $K_{-2ip/\beta}(\xi)$ is the modified Bessel function of the third kind [130]. We sample the initial relative momentum p_0 by employing importance sampling with the Wigner function in Eq. (5.12) at $r = r_0$. In Fig. 5.2, we plot the distributions of the

Morse wavefunction squared, $\left|\psi_{j,0}(r)\right|^2$, and the Wigner function, $W(\psi_{j,0}|r,p)$, for the ground state of O_2. For any given r_0, the cut of the Wigner function at r_0 is a function of p_0 centred around 0 a.u., i.e. centred around the nuclei being at rest.

5.2.7 Monte-Carlo technique

In what follows, we outline the steps involved in the Monte-Carlo technique that describes the interaction between the O_2 molecule and the XUV pulse.

For each event in the Monte-Carlo simulation, we start in the ground state of O_2 with an internuclear distance and relative momentum resulting from the sampling described in Section 5.2.6. We choose the default time step to be $\Delta t = 0.01$ fs, as we found convergence in our results at this granularity. For a given photon energy, at the start of a time step, we identify all the electronic transitions that are energetically accessible for a given photon energy from the molecular or atomic state α at this time to a state i at the end of this time step. In order to determine which transition occurs in this time step, we calculate the transition rates for each single-photon ionization and Auger-Meitner process. The transition rates are given by

$$\begin{aligned} \omega_{\alpha i}(t) &= \sigma_{\alpha i} J(t) \quad \text{Photoionization} \\ \omega_{\alpha i}(t) &= \Gamma_{\alpha i} \qquad \text{Auger-Meitner decay}, \end{aligned} \tag{5.13}$$

where $\omega_{\alpha i}$ is the transition rate from the initial state α to the final state i, $\sigma_{\alpha i}$ is the photoionization cross section for this transition, given by Eq. (2.149) and $\Gamma_{\alpha i}$ is the Auger-Meitner rate, given by Eq. (2.178). The photon flux, J, at time t is given by

$$J(t) = \frac{I}{\omega} \exp\left(-4\log 2\left(\frac{t}{\tau}\right)^2\right), \tag{5.14}$$

where I, ω, τ are the max intensity, photon energy and FWHM of the laser pulse, respectively. Note that we calculate these rates both for the molecular ions and for the atomic fragments that result from dissociation of the molecule due to the interaction with the XUV pulse. The molecular transition rates depend on the internuclear distance. The population of the molecular and atomic states follow an exponential

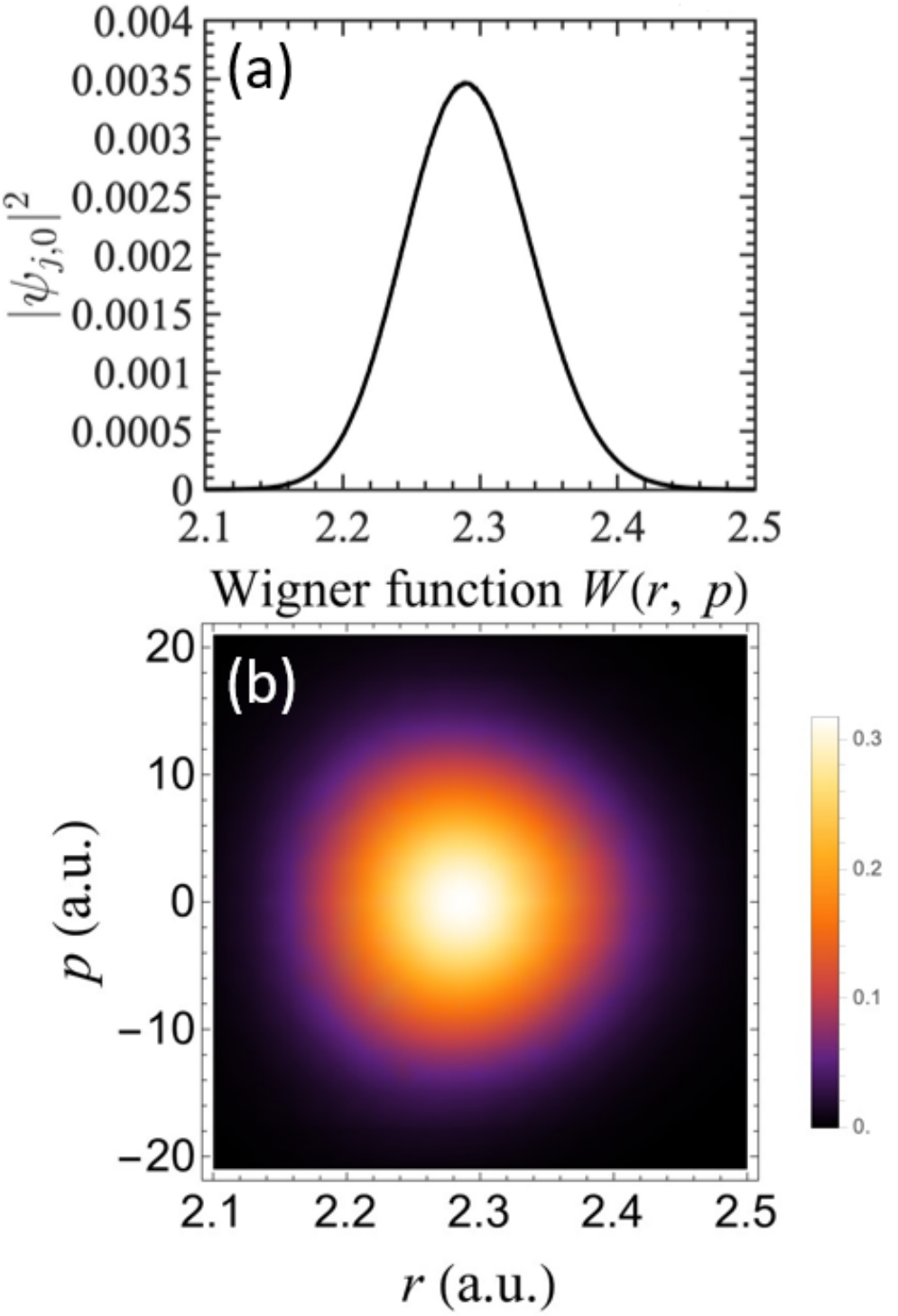

Figure 5.2: Distributions used in importance sampling. Top: distribution of the internuclear distance using the square of the Morse wavefunction for the ground state of O_2. Bottom: distribution of the internuclear distance and the relative momenta using the Wigner function for the ground state of O_2. For each r_0 obtained using the distribution in Fig. 5.2(a), we sample p_0 using the distribution that is given by a cut of the Wigner function at r_0 in Fig. 5.2(b).

decay law [27], i.e.

$$P = P_0 e^{-\omega_{\alpha i} t}, \tag{5.15}$$

where P, P_0 are the populations of molecular and atomic states at times t and at the start of a given time step, respectively. Hence, selecting a random value of P such that $\frac{P}{P_0} \leq 1$, the corresponding time for this transition for a given time step is given by

$$t_{\alpha i}(t) = -\frac{\log \frac{P}{P_0}}{\omega_{\alpha i}}. \tag{5.16}$$

At the start of each time step, we compute the times $t_{\alpha i}$ for all transitions from the state α to energetically allowed states i. We identify the smallest time $t_{\alpha i}$, which corresponds to the most probable transition at a given time step. If this time is greater than the default time step of 0.01 fs, no electronic transition takes place and the time increases by the default time step of 0.01 fs. If $t_{\alpha i}$ is smaller than the default time step, then the time increases by $t_{\alpha i}$ and the transition to state i takes place.

For a given time step, we propagate the nuclei, as described in Section 5.2.2, using as the potential $U(r_n)$ and $U(r_{n+1})$, the potential of the state α at the distances corresponding to the start and the end of this time step, respectively. If a transition occurs, this time step is $t_{\alpha i}$, otherwise it is the default one, equal to 0.01 fs.

Finally, at each time step we check if dissociation occurs at the corresponding internuclear distance using the criteria outlined in Section 5.2.4. If dissociation does occur, from this time on in the Monte-Carlo simulation, we account for the interactions of the resulting atomic fragments with the XUV pulse.

5.3 Results

In what follows, we present and discuss our results for the KER distributions of the atomic fragments in the $O^+ + O^+$ dissociation pathway of O_2 interacting with an XUV pulse. Here, the photon energy of the laser pulse ranges between 20 eV and 42 eV in increments of 1 eV. In this photon energy range, we find that Auger-Meitner transitions are very rare and the transitions that occur are predominantly single-photon ionization processes. At each photon energy, we propagate in time 5×10^6

Monte-Carlo events. Concerning the XUV pulse, we consider laser intensities of 5×10^{12} W/cm^2 and 5×10^{14} W/cm^2 and full-width-at-half-maximum (FWHM) pulse durations of 50 fs and 100 fs. For each Monte-Carlo event, we propagate in time starting 500 fs before the peak of the laser pulse and ending 1000 fs afterwards. We have checked that our results converge when using these initial and final limits in the time propagation. At the end of the time propagation, we collect the events leading to the formation of the $O^+ + O^+$ pathway. For each of these events, we record the sequence of single-photon ionization processes. That is, we record the initial and final states involved in a photoionization transition, as well as the times and internuclear distances at which this transition occurs. We also record the final velocities of the two O^+ fragments and calculate the sum of the kinetic energies of the atomic fragments to compare with the experimental results.

First, in Section 5.3.1 we discuss the probability out of all Monte-Carlo events to obtain the $O^+ + O^+$ pathway as a function of photon energy. Then, in Section 5.3.2, we plot the KER distribution of the two O^+ fragments for all $O^+ + O^+$ events as a function of photon energy. We compare our theoretical results to the experimental KER distribution and identify the main ionization sequences that lead to the formation of the $O^+ + O^+$ pathway. In Section 5.3.3, we plot the KER distribution for a higher intensity of the laser pulse in order to understand the effect of intensity on the kinetic-energy spectra of the O^+ fragments. Finally, in Section 5.3.4, we plot the distribution of internuclear distances at which single-photon ionization occurs. We use this distribution, as well as the various sequences of ionization processes, in order to explain the main features of the KER distribution.

Note that in our theoretical calculations, we do not include excited states of O_2^+ and O_2^{2+}. For the photon energies we consider in this work, it is energetically allowed to transition from the ground state of O_2 to excited states of O_2^+ and also to transition from O_2^+ states to excited states of O_2^{2+}. However, such transitions involve the calculation of matrix elements where in the final state there is a simultaneous one-electron excitation and one-electron ionization. For instance, to transition to the excited state $O_2^+(f^4\Pi_g)$ from the ground state of O_2 would involve

the ionization of an electron from a π_u orbital and the excitation of another electron from a π_u to a π_g orbital. Hence, the accurate computation of such matrix elements is only possible when electron-electron correlation is included in the description of the wavefunctions. This is not accounted for in our current formulation, where we utilise Hartree-Fock wavefunctions. Moreover, the reason that it is a reasonable approximation to not include these excited states is that from the O_2^+ excited states, one could transition to non-excited states of O_2^{2+} by single-photon absorption. However, in our calculations, we do get these same non-excited states of O_2^{2+} by transitions from non-excited states of O_2^+. Finally, the O_2^{2+} excited states, accessible by the photon energies in this calculation, tunnel to non-excited states of O_2^{2+} due to coupling effects between states. These final non-excited states of O_2^{2+} we do access in our calculation, resulting in similar KER spectra as in the experiment.

5.3.1 Probability of the $O^+ + O^+$ dissociation pathway for different pulse durations

In Fig. 5.3, we plot, out of all Monte-Carlo events, the probability of the O_2, O_2^+ and O_2^{2+}, i.e. of the non-dissociating pathways, as well as of the $O^+ + O^+$ dissociation pathway as a function of photon energy. We use a laser-pulse intensity of 5×10^{12} W/cm^2 and FWHM durations of 50 fs and 100 fs. We find that it is more probable to obtain the $O^+ + O^+$ pathway for a FWHM of 100 fs versus a 50 fs one. This is expected, since for a longer laser pulse there is more of a chance to absorb photons. This is also consistent with the probability of O_2^{2+} being higher, while the probability for O_2 is lower for 100 fs. We also find that for both pulse durations, the probability of the $O^+ + O^+$ pathway is very small for small photon energies, it peaks at roughly 30 eV photon energy and then decreases with increasing photon energy. For small photon energies, the probability of the $O^+ + O^+$ pathway is small, even though the probability of O_2^+ formation is large, since no transition is allowed from O_2^+ to O_2^{2+}. For larger photon energies, the probability of the $O^+ + O^+$ pathway decreases since the single-photon ionization cross sections for transitioning from O_2 to O_2^+ states decrease or remain constant for these photon energies. This is shown in Fig. 5.4, where for photon energies above 30 eV for transitions to the O_2^+ states

$X^2\Pi_g$ and $a^4\Pi_u$ the cross sections decrease, while they remain flat for transitions to the states $b^4\Sigma_g^-$ and $c^4\Sigma_u^-$.

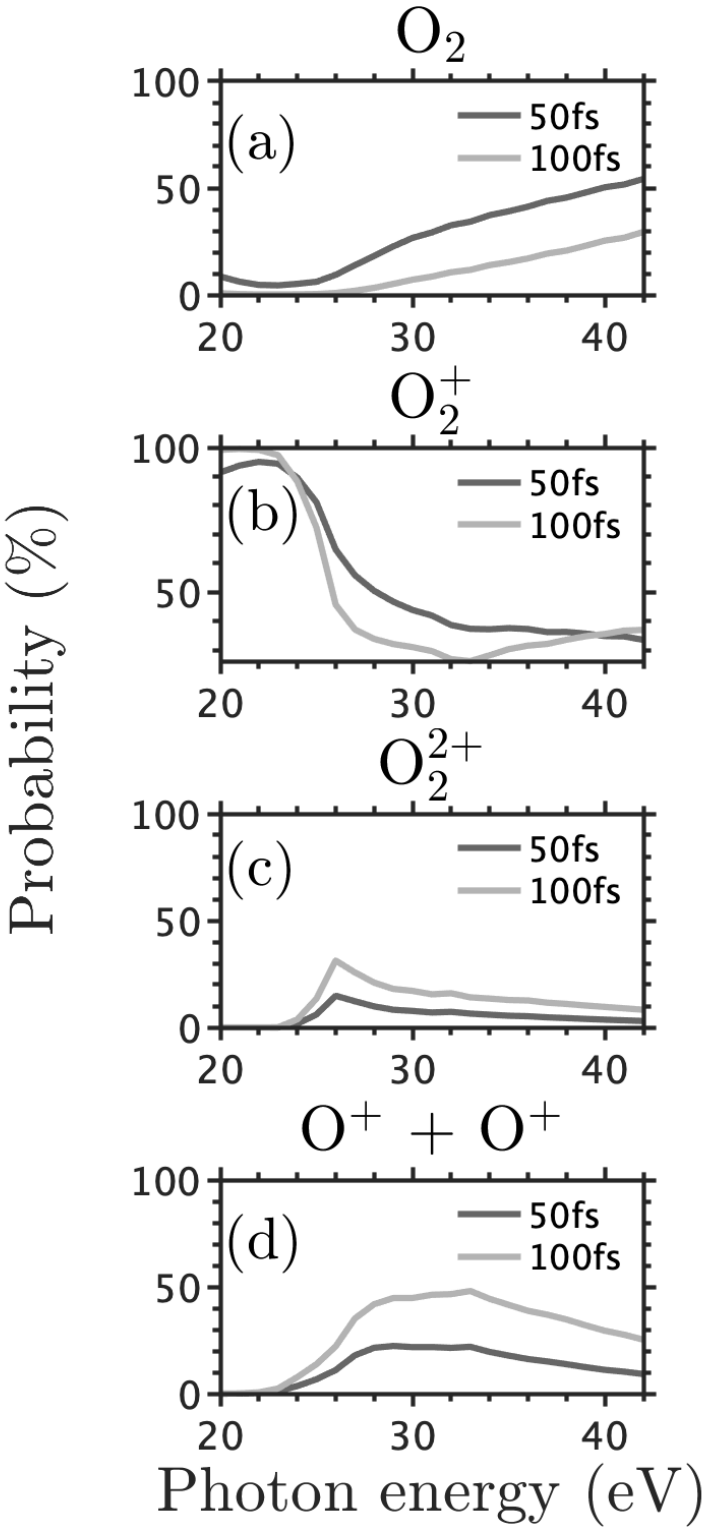

Figure 5.3: Probability, out of all Monte-Carlo events, of the (a) O_2, (b) O_2^+, (c) O_2^{2+} pathways and of the (d) O^+ + O^+ dissociation pathway as a function of photon energy. The intensity of the laser pulse is 5×10^{12} W/cm^2 and the FWHM are 50 fs and 100 fs.

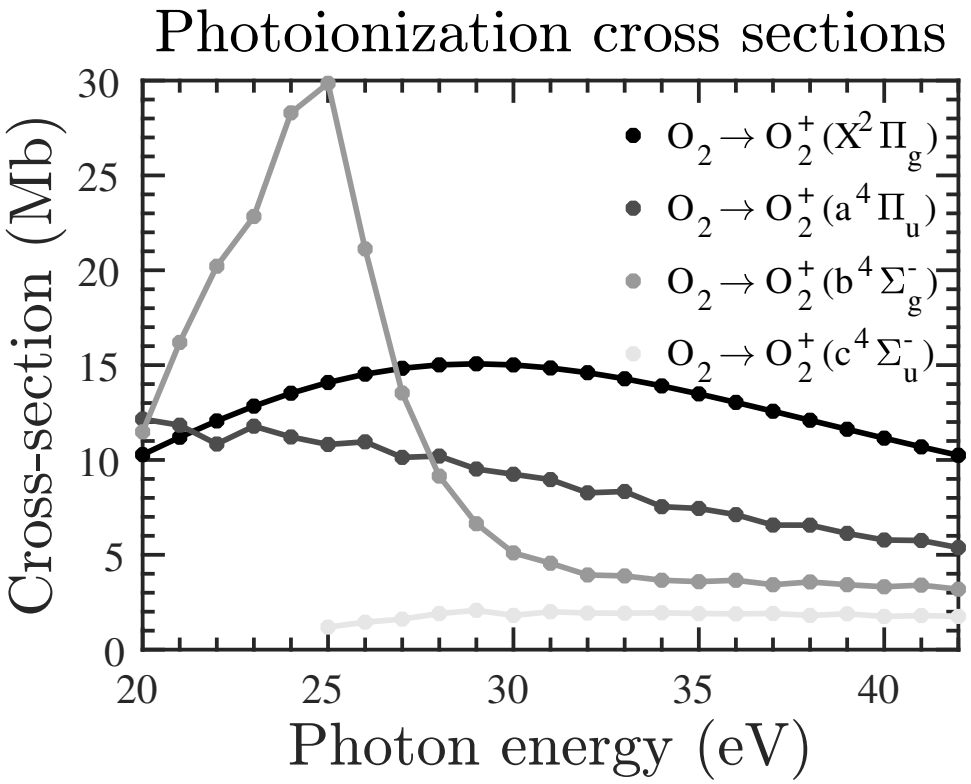

Figure 5.4: Photoionization cross sections to transition from O_2 to O_2^+ at the equilibrium distance of O_2, $r_e = 2.28$ a.u., as a function of photon energy.

5.3.2 KER distribution and the main ionization sequences

In Fig. 5.5(a), we plot the sum of the kinetic energies of the atomic fragments of the O^+ + O^+ dissociation pathway as a function of the photon energy. At each photon energy, the KER distribution is normalized to 1, i.e. we divide by all O^+ + O^+ events at this photon energy. For our simulations, we use a weak laser-pulse intensity of 5×10^{12} W/cm^2 and a FWHM of 100 fs in order to closely resemble the parameters of the laser pulses used in the experiment. We compare our theoretical results for the KER distribution, shown in Fig. 5.5(a), with the experimental ones shown in Fig. 5.5(b). We find that our theoretical results reproduce well most of the features in the experimental KER distribution. That is, the KER distribution peaks at 5 eV for 20 eV photon energy, increases with increasing photon energy, reaching 8 eV at 25 eV photon energy. From 25 eV photon energy onwards, we observe numerous peaks in the kinetic-energy spectra, ranging from 7 eV to 13 eV. These peaks in the spectra remain mostly constant from 25 eV until 42 eV photon

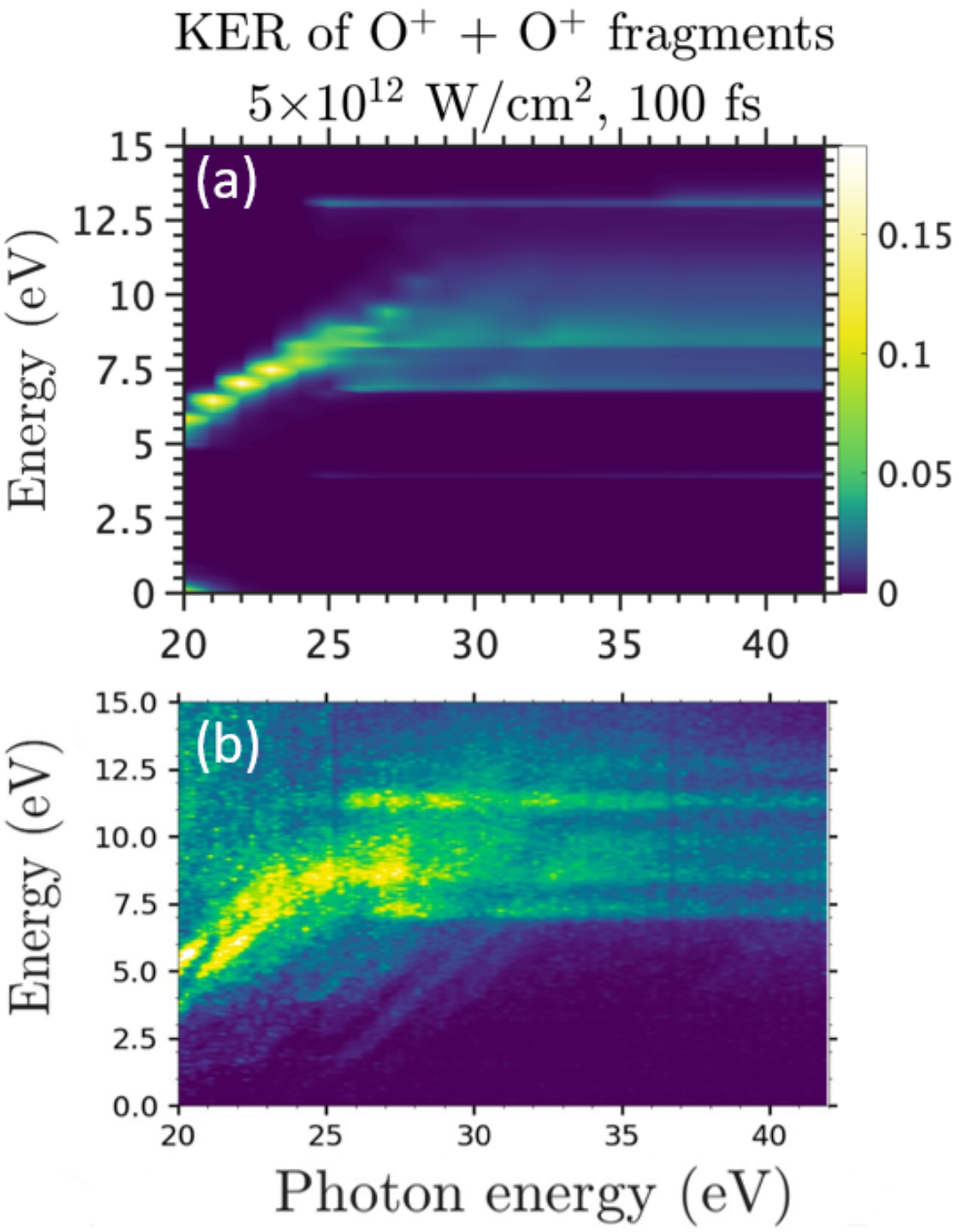

Figure 5.5: Kinetic-energy-release spectra of the $O^+ + O^+$ pathway as a function of photon energy. (a) Theoretical results obtained in the current work using a laser-pulse intensity equal to 5×10^{12} W/cm^2 and FWHM of 100 fs. (b) Experimental results, for more information on the set-up see Refs. [113, 114].

energy, giving rise to the straight lines that we see in Fig. 5.5(a) and Fig. 5.5(b). However, our theoretical results do not reproduce the experimental KER peak at approximately 11 eV. It is possible that this is due to the exclusion of the excited states in our calculations.

To explain the features of the KER distribution of the $O^+ + O^+$ pathway, in Table 5.3, we identify the main ionization sequences leading to the formation of two O^+ fragments. Each ionization sequence involves a single-photon ionization leading to a transition from the ground state of O_2, i.e. the $O_2(X^3\Sigma_g^-)$ state, to a O_2^+ state and a subsequent single-photon ionization leading to a transition from an O_2^+ state to an O_2^{2+} state. The difference between these sequences are the O_2^+ and O_2^{2+} states involved in the photoionization transitions. After transitioning to an O_2^{2+} state, as described in Section 5.2.4, this state dissociates to two O^+ fragments, shown in Table 5.2. As shown in Fig. 5.1, the PECs of all the O_2^{2+} states involved in the ionization sequences 1 through 8 in Table 5.3 are repulsive due to the Coulomb potential of the atomic ions. As a result, during time propagation the internuclear distance increases rapidly leading to the formation of two O^+ fragments. For additional clarity, in Fig. 5.6, we schematically depict the two single-photon ionization transitions involved for the ionization sequences 1,2,3.

As mentioned earlier, we do not include excited states of O_2^{2+}, such as the $1^1\Pi_g$, $1^1\Delta_u$, $1^1\Sigma_u^-$ and $B^3\Sigma_u^-$ states. However, these states are coupled to non-excited states of O_2^{2+}, namely the $C^3\Pi_u$, $1^5\Sigma_g^+$ and $1^5\Pi_u$ states, all three of which are the final O_2^{2+} states for some of the eight ionization sequences in Table 5.3. This is the reason the theoretical KER distribution in Fig. 5.5(a) still reproduces the features that appear in the experimental distribution in Fig. 5.5(b).

5.3.3 KER dependence on intensity of the laser pulse

In what follows, we investigate how the KER distribution of the $O^+ + O^+$ pathway changes with the laser-pulse intensity. In Fig. 5.7, we plot the KER distribution for a laser-pulse intensity of 5×10^{14} W/cm^2, while in Fig. 5.5(a) the laser-pulse intensity is smaller and equal to 5×10^{12} W/cm^2. Comparing the KER distribution in Fig. 5.7 with Fig. 5.5(a), we find that the KER distribution for each photon energy from 20

	Ionization Sequence
1	$O_2 \rightarrow O_2^+(a^4\Pi_u) \rightarrow O_2^{2+}(1^5\Sigma_g^+)$
2	$O_2 \rightarrow O_2^+(a^4\Pi_u) \rightarrow O_2^{2+}(A^3\Sigma_u^+)$
3	$O_2 \rightarrow O_2^+(c^4\Sigma_u^-) \rightarrow O_2^{2+}(C^3\Pi_u)$
4	$O_2 \rightarrow O_2^+(a^4\Pi_u) \rightarrow O_2^{2+}(W^3\Delta_u)$
5	$O_2 \rightarrow O_2^+(b^4\Sigma_g^-) \rightarrow O_2^{2+}(1^5\Pi_u)$
6	$O_2 \rightarrow O_2^+(a^4\Pi_u) \rightarrow O_2^{2+}(1^5\Pi_u)$
7	$O_2 \rightarrow O_2^+(X^2\Pi_g) \rightarrow O_2^{2+}(W^3\Delta_u)$
8	$O_2 \rightarrow O_2^+(X^2\Pi_g) \rightarrow O_2^{2+}(A^3\Sigma_u^+)$

Table 5.3: Main ionization sequences leading to the formation of the $O^+ + O^+$ dissociation pathway. These eight ionization sequences account for almost all $O^+ + O^+$ events.

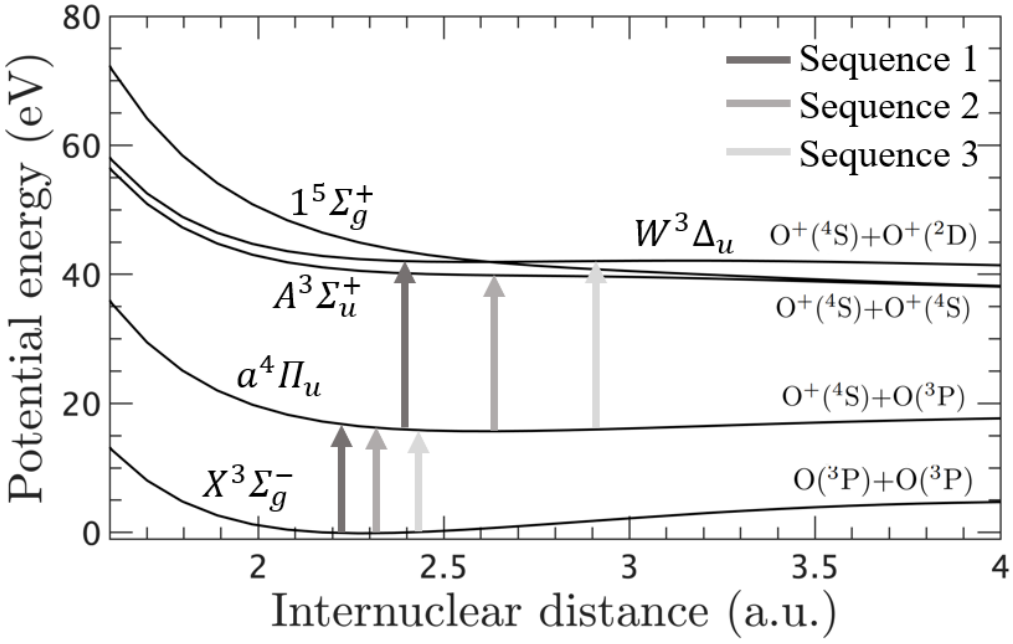

Figure 5.6: Schematic depiction of the two single-photon ionization transitions, first, from the ground state to an O_2^+ state and, then, from the O_2^+ state to an O_2^{2+} state for ionization sequences 1,2,3.

eV to 25 eV is broader for the lower intensity. From 25 eV photon energy onwards, the KER distributions are similar in Fig. 5.7 and Fig. 5.5(a). To explain the wider KER distributions for small photon energies for the lower intensity, in Fig. 5.8, we plot the probabilities of each of the eight ionization sequences as a function of photon energy. We find that for photon energies roughly up to 25 eV, only sequences 1 and 2 contribute to the $O^+ + O^+$ pathway. For the higher intensity, sequence 2

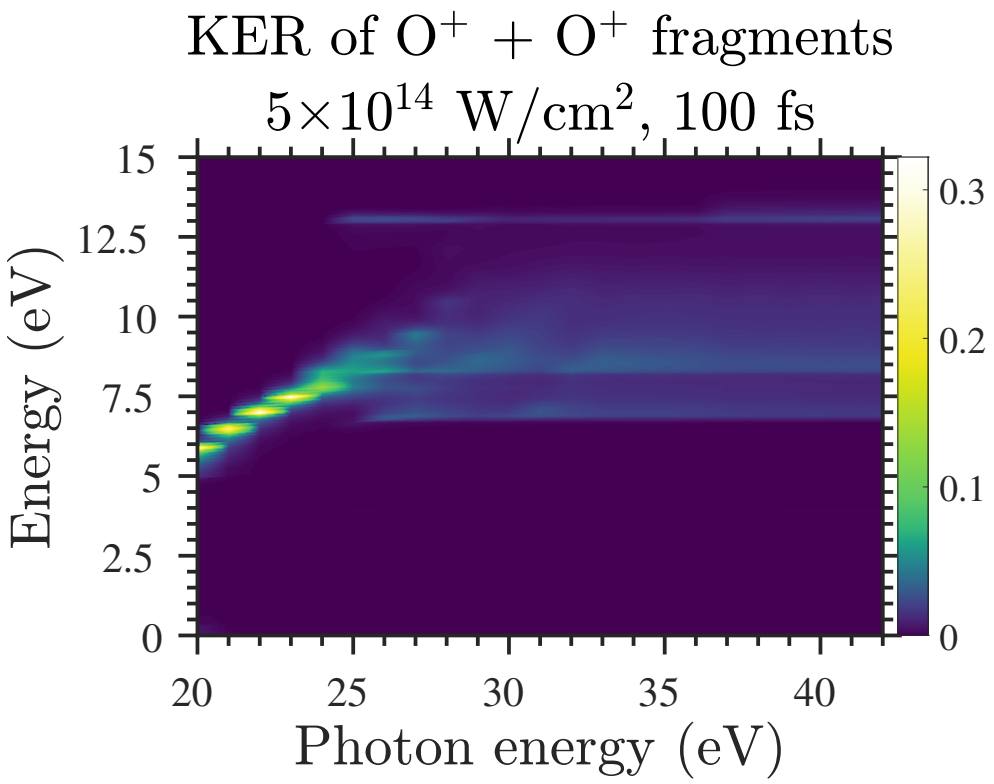

Figure 5.7: Same as Fig. 5.5(a) with a laser intensity of 5×10^{14} W/cm^2.

contributes more, while for the lower intensity both sequences contribute roughly equally. The contribution of one versus two ionization sequences is consistent with a narrower KER distribution for the higher intensity. For 25 eV photon energy onwards, we find that almost all ionization sequences contribute roughly the same for both intensities, resulting in similar KER distributions for these photon energies for both intensities.

5.3.4 Main features of the KER distribution

In this section, we associate the main features of the KER distribution as a function of photon energy with the ionization sequences. Plotting the KER distribution of each sequence individually (not shown), we are able to assign features from the overall KER distribution to specific sequences. This correspondence is shown in Fig. 5.9, for the KER distribution of the $O^+ + O^+$ pathway for the laser-pulse intensity of 5×10^{12} W/cm^2 and FWHM of 100 fs. For photon energies from 20 eV to 25 eV, the centre of the KER distributions changes almost linearly from 5 eV to 9 eV.

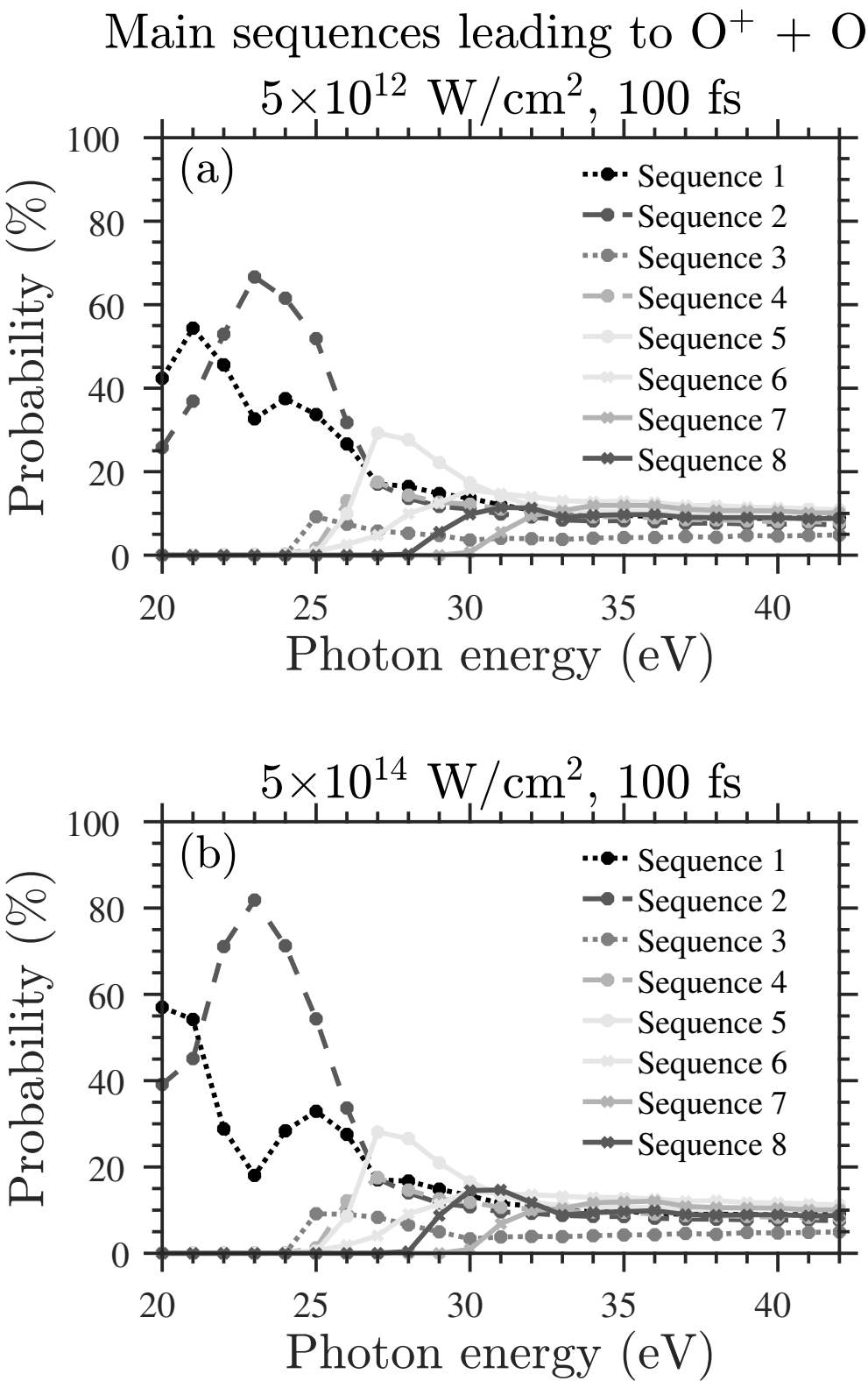

Figure 5.8: Probability, computed out of all $O^+ + O^+$ events, of each of the 8 main ionization sequences leading to the formation of the $O^+ + O^+$ pathway, as a function of the photon energy. The FWHM of the laser pulse is 100 fs and the laser intensity is (a) 5×10^{12} W/cm^2 (b) 5×10^{14} W/cm^2.

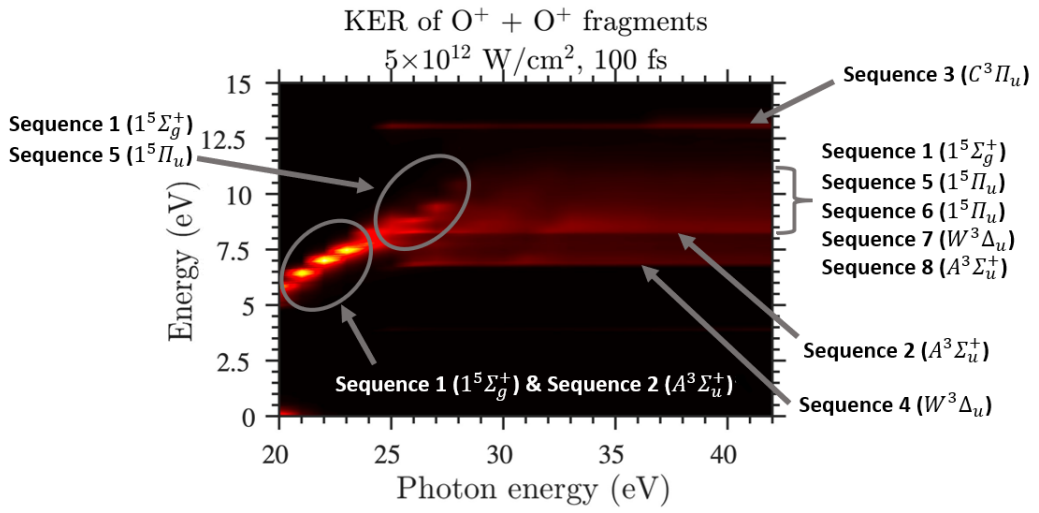

Figure 5.9: Annotated kinetic-energy release spectra of the atomic fragments in the $O^+ + O^+$ dissociation pathway, associating different ionization sequences to different features. The laser-pulse intensity is equal to 5×10^{12} W/cm^2 and the FWHM is equal to 100 fs.

This is due to the ionization sequences 1 and 2, as we have previously mentioned in Section 5.3.3. Another aspect of the KER distributions is an almost linear increase from 9 eV to 11 eV between 25 eV and 28 eV photon energy. We find that this KER feature is due to the ionization sequences 1 and 5. Also, for photon energies higher than 25 eV, we see a series of constant lines in the kinetic-energy spectra. The line corresponding to the highest kinetic energy of 13 eV is due to sequence 3, while the line corresponding to the lowest kinetic energy of 7 eV is due to sequence 4. The sequences 1, 5, 6, 7 and 8 equally contribute to the broad spectra between 8 eV and 11 eV kinetic energy.

To explain the features of Fig. 5.9, in Fig. 5.10, we plot the distributions of the internuclear distances when each of the two single-photon ionization transitions occur for ionization sequence 1. The reason we focus on this sequence is that we obtain similar results for all eight sequences. In Fig. 5.10, for the first ionization process, we see that the distribution of internuclear distances is narrower for small compared to larger photon energies. The reason is that as we increase the photon energy the first ionization step from the ground O_2 state to the single ionized O_2^+ state is energetically accessible at more internuclear distances. In addition, we find

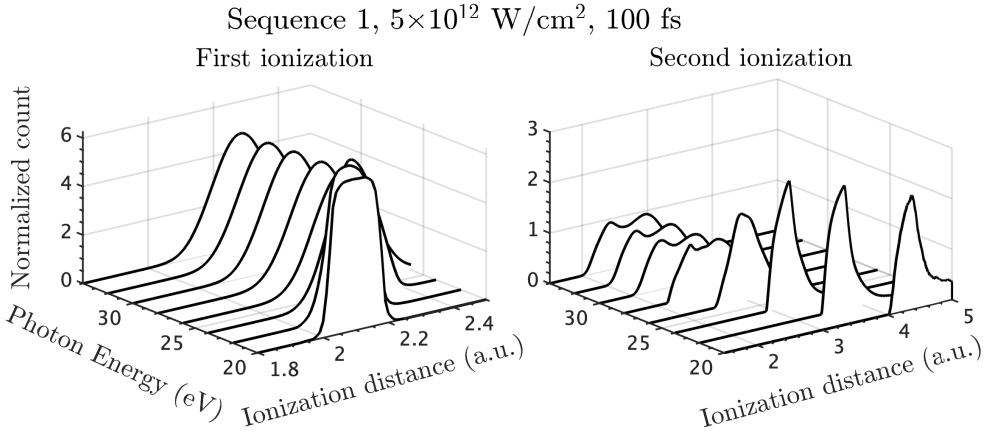

Figure 5.10: For ionization sequence 1, distributions of internuclear distances when the first single-photon ionization (left column) and second single-photon ionization (right column) take place.

that for all photon energies, the distribution of internuclear distances are centred around the equilibrium distance of O_2, which is $r_e = 2.28$ a.u. For the second ionization transition, we find that the distribution of internuclear distances is narrower for small photon energies compared to photon energies above 25 eV. Also, the second ionization transition takes place at large internuclear distances, around 4.5 a.u., for 20 eV photon energy, decreasing to roughly 3 a.u. at 26 eV photon energy. For photon energies above 26 eV, the distribution of internuclear distances doesn't change and is centred around small internuclear distances of roughly 2.5 a.u. The reason is that for small photon energies, a transition from an O_2^+ state to an O_2^{2+} state is only allowed for larger distances, note from Fig. 5.1 the energy difference between the PECs of $O_2^+(a^4\Pi_u)$ and $O_2^{2+}(1^5\Sigma_g^+)$ involved in sequence 1.

For photon energies between 20 eV and 25 eV, the decrease of the internuclear distance in the second ionization step is consistent with the linear increase in the centre of the KER distribution in Fig. 5.9. Indeed, in Fig. 5.1, we see that at larger internuclear distances the PEC of the $O_2^{2+}(1^5\Sigma_g^+)$ state involved in sequence 1 is shallower and hence the derivative of the PEC, which is the repulsive force, is smaller leading to a smaller velocity gain of the two O^+ fragments at dissociation. Also, the spectral lines remaining constant for photon energies higher than 25 eV is consistent with the width of the distribution of internuclear distances being

the same for higher photon energies in Fig. 5.10. The value of the sum of the final kinetic energies of the O^+ atomic fragments, and hence the kinetic energy each spectral line corresponds to, depends on the slope of the PECs of the O_2^{2+} states at the internuclear distance when the second ionization transition takes place.

5.4 Conclusions

We have presented a hybrid quantum-classical technique to account for both the electronic structure and electron escape as well as the nuclear dynamics of a diatomic molecule during its interaction with an XUV laser pulse. In our technique, we treat quantum mechanically the electronic structure and ionization as well as the single-photon ionization and Auger-Meitner processes. In addition, we compute, with accurate quantum-chemistry methods, the potential-energy curves for molecular ion states of O_2 up to O_2^{2+}. We then use these potential-energy curves to compute the force between the two nuclei and classically account for the final velocities of the atomic fragments. Both the quantum and classical aspects of our techniques are incorporated in a stochastic Monte-Carlo calculation that accounts for the interaction of an O_2 molecule with an XUV pulse. The accuracy of our technique is demonstrated by comparing the sum of the kinetic energies of the two O^+ atomic fragments in the $O^+ + O^+$ pathway as a function of photon energy with experimental results. We find very good agreement with experiment. Moreover, we are able to associate the main features of the kinetic-energy release distribution as a function of photon energy for the $O^+ + O^+$ pathway to the main ionization sequences leading to this pathway. Our technique is general and can be applied to any diatomic molecule.

Chapter 6

Conclusions

In this dissertation, we explored the interactions of molecules with intense laser pulses in the ultraviolet and X-ray range. In order to study the phenomena that occur during single-photon ionization and Auger-Meitner decay, we computed continuum wavefunctions in the Hartree-Fock framework. When performing our calculations, we used parameters for the laser pulses such that we were able to compare our results with experiment and other theoretical work, thus allowing us to verify our methods.

First, we theoretically modelled angular streaking using a combination of a linearly-polarized UV or X-ray laser pulse and a circularly-polarized IR pulse. We developed a hybrid quantum-classical method to achieve this. In the first step, we computed the dipole matrix element to transition from an initial bound state to a continuum state due to a UV or X-ray laser pulse. To do this, we obtain the continuum wavefunction quantum-mechanically by solving a system of Hartree-Fock equations. Following ionization, we then solved classically for the trajectory of the continuum electron when it is exposed to an IR pulse using the strong field approximation. We applied this hybrid technique to the diatomic molecules N_2 and NO.

For N_2, we were able to demonstrate a one-to-one mapping between the direction of ionization of an electron and the phase delay between a linearly-polarized vacuum ultraviolet pulse and a circularly-polarized IR laser field. We were able to display this control of the ionizing electron for ionization from three orbitals of N_2,

namely $2\sigma_g$, $3\sigma_g$ and $1\pi_u$ using photon energies of 41 eV, 17 eV and 16 eV, respectively. We found that we achieved a greater degree of control when the photon energy was smaller and the intensity of the IR pulse was higher. We also verified the accuracy of our continuum wavefunctions by comparing our photoionization cross sections with the literature. Finally, from these findings we showed that production of large magnetic fields, roughly equal to 1 Tesla, is possible using a VUV pulse below 100 nm.

Using NO as a case study, we were able to demonstrate our methods for computing continuum wavefunctions and model angular streaking for open-shell molecules. We utilised an X-ray pulse with photon energies sufficient to ionize the core orbitals of NO, namely 1σ and 2σ. We considered both singlet and triplet spin spin symmetries. Again we verified the accuracy of our continuum wavefunctions by comparing our photoionization cross sections with the literature. We showed that control of electron current was also possible in open-shell molecules, and furthermore for electrons ionized from core orbitals. Similarly to N_2, we found using a high intensity IR pulse resulting in better control of the ionizing electron. We also investigated the effects on final electron escape when we streak with an IR pulse by comparing the doubly differential probabilities for an electron to escape on the plane of the IR pulse with the angular distributions of the ionizing electron due solely to the X-ray pulse. We found that using a low intensity IR pulse allows us to preserve the angular escape patterns resulting from the X-ray pulse.

Finally, we developed techniques to simulate the interaction between diatomic molecules and intense laser pulses, incorporating both the quantum and classical aspects of molecular dynamics. Specifically, we computed transition rates for photoionization and Auger-Meitner decay using our quantum mechanical methods, while modelling nuclear dynamics with classical techniques. These components were integrated within a stochastic Monte-Carlo framework, enabling us to track the molecular dissociation into atomic fragments and follow the dynamics of these fragments throughout the simulation. Applying these methods to the interaction between O_2 and an XUV pulse, we observed excellent agreement between our sim-

ulated final velocities of the dissociated atomic fragments and experimental results.

We note that we have only considered sequential ionization processes in this work where only a single electron escapes to the continuum. Furthermore, in this thesis we have only considered interactions involving diatomic molecules. However, in future work our models could be used for polyatomic molecules consisting of more than two atoms.

Appendix A

Laplace multipole expansion

The law of cosines states

$$c^2 = a^2 + b^2 - 2ab\cos\gamma, \tag{A.1}$$

where a, b, c are sides of a triangle and γ is the angle between a and b. Then

$$\begin{aligned} \left|\mathbf{r} - \mathbf{r}'\right| &= r^2 + (r')^2 - 2rr'\cos\gamma \\ \implies \frac{1}{|\mathbf{r} - \mathbf{r}'|} &= \frac{1}{r\sqrt{1 + h^2 - 2h\cos\gamma}}, \end{aligned} \tag{A.2}$$

where $h = \frac{r'}{r}$. The Legendre polynomials can be defined as the coefficients in the expansion of the function

$$\frac{1}{\sqrt{1 - 2xt + t^2}} = \sum_{n=0}^{\infty} P_n(t) t^n. \tag{A.3}$$

Hence in our case we have

$$\frac{1}{|\mathbf{r} - \mathbf{r}'|} = \frac{1}{r} \sum_{l=0}^{\infty} h^l P_l(\cos\gamma). \tag{A.4}$$

The spherical harmonic addition theorem states

$$P_l(\cos\gamma) = \frac{4\pi}{2l+1} \sum_{m=-l}^{l} (-1)^m Y_l^{-m}(\theta, \phi) Y_l^m(\theta', \phi'). \tag{A.5}$$

Hence, we have

$$\begin{aligned}\frac{1}{|\mathbf{r}-\mathbf{r}'|} &= \frac{1}{r}\sum_{l=0}^{\infty}\frac{4\pi}{2l+1}h^l\sum_{m=-l}^{l}(-1)^m Y_l^{-m}(\theta,\phi)Y_l^m(\theta',\phi') \\ &= \sum_{lm}\frac{4\pi}{2l+1}\frac{r_<^l}{r_>^{l+1}}Y_{lm}(\theta,\phi)Y_{lm}^*(\theta',\phi'),\end{aligned} \tag{A.6}$$

where $r_< = \min(r,r')$ and $r_> = \max(r,r')$ and we have used the fact that $Y_l^{m*}(\theta,\phi) = (-1)^m Y_l^{-m}(\theta,\phi)$. This is known as the Laplace multipole expansion.

Appendix B

Clebsh-Gordan and Wigner-3j symbols

B.1 Clebsh-Gordan Coefficients

Suppose $\mathbf{J}_1, \mathbf{J}_2$ are commutable angular momentum operators. For example, they could be the angular momentum operators for two different particles or the respective orbital and spin angular momentum operators for a single particle. Let $\psi_{j_1 m_1}$ be the simultaneous eigenfunctions of $\mathbf{J}_1^2$ and J_{1z}, and similarly $\psi_{j_2 m_2}$ for $\mathbf{J}_2^2$ and J_{2z}. Then the simultaneous eigenfunctions of $\mathbf{J}_1^2$, J_{1z}, $\mathbf{J}_2^2$ and J_{2z} satisfy

$$\psi_{j_1 m_1, j_2 m_2} = \psi_{j_1 m_1} \times \psi_{j_2 m_2}. \tag{B.1}$$

There are $(2j_1+1)(2j_2+1)$ of such functions. The eigenfunctions of $\mathbf{J} = \mathbf{J}_1 + \mathbf{J}_2$ satisfy

$$\begin{aligned} \mathbf{J}^2 \Phi^{jm}_{j_1,j_2} &= j(j+1)\hbar^2 \Phi^{jm}_{j_1,j_2} \\ J_z \Phi^{jm}_{j_1,j_2} &= m\hbar \Phi^{jm}_{j_1,j_2}, \end{aligned} \tag{B.2}$$

for $-j \le m \le j$ and $j = |j_1 - j_2|, |j_1 - j_2| + 1, \ldots, j_1 + j_2$. Then we have the following relation

$$\Phi^{jm}_{j_1,j_2} = \sum_{m_1,m_2} \langle j_1 j_2 m_1 m_2 | jm \rangle \, \psi_{j_1 m_1, j_2 m_2}. \tag{B.3}$$

The $\langle j_1 j_2 m_1 m_2 | jm \rangle$ are known as the **Clebsh-Gordan coefficients**. They satisfy the following orthonormality relations

$$\begin{aligned} \sum_{m_1,m_2} \langle j_1 j_2 m_1 m_2 | jm \rangle \left\langle j_1 j_2 m_1 m_2 \middle| j'm' \right\rangle &= \delta_{jj'}\delta_{mm'} \\ \sum_{m_1,m_2} \langle j_1 j_2 m_1 m_2 | jm \rangle \left\langle j_1 j_2 m_1' m_2' \middle| jm \right\rangle &= \delta_{m_1 m_1'}\delta_{m_2 m_2'}, \end{aligned} \tag{B.4}$$

and the following symmetry properties

$$\begin{aligned} \langle j_1 j_2 m_1 m_2 | jm \rangle &= (-1)^{j_1+j_2-j} \langle j_2 j_1 m_2 m_1 | jm \rangle \\ &= (-1)^{j_1+j_2-j} \langle j_1 j_2 -m_1 -m_2 | j -m \rangle . \end{aligned} \tag{B.5}$$

It can be shown that the product of spherical harmonic functions can be written as

$$\begin{aligned} Y_{l_1}^{m_1}(\theta,\phi) Y_{l_2}^{m_2}(\theta,\phi) = \sum_{l=|l_1-l_2|}^{l_1+l_2} \sum_{m=-l}^{l} \sqrt{\frac{(2l_1+1)(2l_2+1)}{4\pi(2l+1)}} \\ \times \langle l_1 l_2 00 | l0 \rangle \langle l_1 l_2 m_1 m_2 | lm \rangle Y_l^m(\theta,\phi). \end{aligned} \tag{B.6}$$

Using this, the orthonormality of spherical harmonic functions and the fact that $Y_l^{-m}(\theta,\phi) = (-1)^m Y_l^{*m}(\theta,\phi)$, we have the following identity

$$\begin{aligned} \int Y_{l_1}^{m_1}(\theta,\phi) Y_{l_2}^{m_2}(\theta,\phi) Y_{l_3}^{m_3}(\theta,\phi) d\Omega = (-1)^{m_3} \sqrt{\frac{(2l_1+1)(2l_2+1)}{4\pi(2l_3+1)}} \\ \times \langle l_1 l_2 00 | l_3 0 \rangle \langle l_1 l_2 m_1 m_2 | l_3 -m_3 \rangle Y_l^m(\theta,\phi). \end{aligned} \tag{B.7}$$

B.2 Wigner-3j Symbols

Wigner-3j symbols are an alternative to Clebsh-Gordan coefficients, given by

$$\begin{pmatrix} l_1 & l_2 & l_3 \\ m_1 & m_2 & m_3 \end{pmatrix} = \frac{(-1)^{j_1-j_2-m_3}}{\sqrt{2j_3+1}} \langle j_1 m_1 j_2 m_2 | j_3 -m_3 \rangle . \tag{B.8}$$

A Wigner-3j symbol is zero unless all of the following conditions are satisfied:

$$\begin{aligned} &m_i \in \{-j_i, -j_i+1, \ldots, j_i\} \text{ for } i = 1,2,3 \\ &m_1 + m_2 + m_3 = 0 \\ &|j_1 - j_2| \leq j_3 \leq j_1 + j_2 \\ &j_1 + j_2 + j_3 \text{ is an integer.} \end{aligned} \tag{B.9}$$

By Eq. (B.8), they follow the symmetry properties

$$\begin{aligned} \begin{pmatrix} l_1 & l_2 & l_3 \\ m_1 & m_2 & m_3 \end{pmatrix} &= (-1)^{(l_1+l_2+l_3)} \begin{pmatrix} l_1 & l_2 & l_3 \\ -m_1 & -m_2 & -m_3 \end{pmatrix} \\ \begin{pmatrix} l_1 & l_2 & l_3 \\ m_1 & m_2 & m_3 \end{pmatrix} &= (-1)^{(l_1+l_2+l_3)} \begin{pmatrix} l_1 & l_2 & l_3 \\ m_2 & m_1 & m_3 \end{pmatrix}. \end{aligned} \tag{B.10}$$

We can rewrite the integral of the three spherical harmonic functions in terms of Wigner-3j symbols [68]

$$\begin{aligned} \int Y_{l_1}^{m_1}(\theta,\phi) Y_{l_2}^{m_2}(\theta,\phi) Y_{l_2}^{m_3}(\theta,\phi) d\Omega = &\sqrt{\frac{(2l_1+1)(2l_2+1)(2l_3+1)}{4\pi}} \\ &\times \begin{pmatrix} l_1 & l_2 & l_3 \\ 0 & 0 & 0 \end{pmatrix} \begin{pmatrix} l_1 & l_2 & l_3 \\ m_1 & m_2 & m_3 \end{pmatrix}. \end{aligned} \tag{B.11}$$

Bibliography

[1] T. Driver, M. Mountney, J. Wang, L. Ortmann, A. Al-Haddad, N. Berrah, C. Bostedt, E. G. Champenois, L. F. DiMauro, J. Duris, D. Garratt, J. M. Glownia, Z. Guo, D. Haxton, E. Isele, I. Ivanov, J. Ji, A. Kamalov, S. Li, M.-F. Lin, J. P. Marangos, R. Obaid, J. T. O'Neal, P. Rosenberger, N. H. Shivaram, A. L. Wang, P. Walter, T. J. A. Wolf, H. J. Wörner, Z. Zhang, P. H. Bucksbaum, M. F. Kling, A. S. Landsman, R. R. Lucchese, A. Emmanouilidou, A. Marinelli, and J. P. Cryan, Nature **632**, 762 (2024).

[2] M. Mountney, G. P. Katsoulis, S. H. Møller, K. Jana, P. B. Corkum, and A. Emmanouilidou, Phys. Rev. A **106**, 043106 (2022).

[3] M. E. Mountney, T. C. Driver, A. Marinelli, M. F. Kling, J. P. Cryan, and A. Emmanouilidou, Phys. Rev. A **107**, 063111 (2023).

[4] M. Mountney, Z. Wang, G. P. Katsoulis, S. Meister, R. Moshammer, T. Pfeifer, and A. Emmanouilidou, "Formation of two singly-ionized oxygen atoms during the breakup of O_2 driven by an XUV pulse," (2024), arXiv:2403.20098 [physics.atom-ph] .

[5] C. Pellegrini, Eur. Phys. J. H **37**, 659 (2012).

[6] P. B. Corkum, Phys. Rev. Lett. **71**, 1994 (1993).

[7] M. Drescher, M. Hentschel, R. Kienberger, M. Uiberacker, V. Yakovlev, A. Scrinzi, T. Westerwalbesloh, U. Kleineberg, U. Heinzmann, and F. Krausz, Nature **419**, 803 (2002).

[8] S. Biswas, B. Förg, L. Ortmann, J. Schötz, W. Schweinberger, T. Zimmermann, L. Pi, D. Baykusheva, H. A. Masood., I. Liontos, A. M. Kamal, N. G. Kling, A. F. Alharbi, M. Alharbi, A. M. Azzeer, G. Hartmann, H. J. Wörner, A. S. Landsman, and M. F. Kling, Nat. Phys. **16**, 778 (2020).

[9] A. L. Cavalieri, N. Müller, T. Uphues, V. S. Yakovlev, A. Baltuška, B. Horvath, B. Schmidt, L. Blümel, R. Holzwarth, S. Hendel, M. Drescher, U. Kleineberg, P. M. Echenique, R. Kienberger, F. Krausz, and U. Heinzmann, Nature **449**, 1029 (2007).

[10] W. B. Li, R. Montuoro, J. C. Houver, L. Journel, A. Haouas, M. Simon, R. R. Lucchese, and D. Dowek, Phys. Rev. A **75**, 052718 (2007).

[11] R. Pazourek, S. Nagele, and J. Burgdörfer, Rev. Mod. Phys. **87**, 765 (2015).

[12] M. Schultze, M. Fieß, N. Karpowicz, J. Gagnon, M. Korbman, M. Hofstetter, S. Neppl, A. L. Cavalieri, Y. Komninos, T. Mercouris, C. A. Nicolaides, R. Pazourek, S. Nagele, J. Feist, J. Burgdörfer, A. M. Azzeer, R. Ernstorfer, R. Kienberger, U. Kleineberg, E. Goulielmakis, F. Krausz, and V. S. Yakovlev, Science **328**, 1658 (2010).

[13] P. Hockett, E. Frumker, D. M. Villeneuve, and P. B. Corkum, J. Phys. B. At Mol. Opt. Phys. **49**, 095602 (2016).

[14] L. Gallmann, I. Jordan, H. J. Wörner, L. Castiglioni, M. Hengsberger, J. Osterwalder, C. A. rrell, M. Chergui, E. Liberatore, U. Rothlisberger, and U. Keller, Struct. Dyn. **4**, 061502 (2017).

[15] W. Helml, I. Grguraš, P. N. Juranić, S. Düsterer, T. Mazza, A. R. Maier, N. Hartmann, M. Ilchen, G. Hartmann, L. Patthey, C. Callegari, J. T. Costello., M. Meyer, R. N. Coffee, A. L. Cavalieri, and R. Kienberger, Appl. Sci. **7** (2017), 10.3390/app7090915.

[16] W. Helml, A. R. Maier, W. Schweinberger, I. Grguraš, P. Radcliffe, G. Doumy, C. Roedig, J. Gagnon, M. Messerschmidt, S. Schorb, C. Bostedt,

F. Grüner, L. F. DiMauro, D. Cubaynes, J. D. Bozek, T. Tschentscher, J. T. Costello, M. Meyer, R. Coffee, S. Düsterer, A. L. Cavalieri, and R. Kienberger, Nat. Photon **8**, 950 (2014).

[17] I. Grguraš, A. R. Maier, C. Behrens, T. Mazza, T. J. Kelly, P. Radcliffe, S. Düsterer, A. K. Kazansky, N. M. Kabachnik, T. Tschentscher, J. T. Costello, M. Meyer, M. C. Hoffmann, H. Schlarb, and A. L. Cavalieri, Nat. Photon **6**, 852 (2012).

[18] P. M. Maroju, M. D. Fraia, O. Plekan, M. Bonanomi, B. Merzuk, D. Busto, I. Makos, M. Schmoll, R. Shah, P. R. Ribič, L. Giannessi, G. D. Ninno, C. Spezzani, G. Penco, A. Demidovich, M. Danailov, M. Coreno, M. Zangrando, A. Simoncig, M. Manfredda, R. J. Squibb, R. Feifel, S. Bengtsson, E. R. Simpson, T. Csizmadia, M. Dumergue, S. Kühn, K. Ueda, J. Li, K. J. Schafer, F. Frassetto, L. Poletto, K. C. Prince, J. Mauritsson, C. Callegari, and G. Sansone, Nat. Photonics **17**, 200 (2023).

[19] N. Hartmann, G. Hartmann, R. Heider, M. S. Wagner, M. Ilchen, J. Buck, A. O. Lindahl, C. Benko, J. Grünert, J. Krzywinski, J. Liu, A. A. Lutman, A. Marinelli, T. Maxwell, A. A. Miahnahri, S. P. Moeller, M. Planas, J. Robinson, A. K. Kazansky, N. M. Kabachnik, J. Viefhaus, T. Feurer, R. Kienberger, R. N. Coffee, and W. Helml, Nat. Photon. **12**, 215 (2018).

[20] S. Li, Z. Guo, R. N. Coffee, K. Hegazy, Z. Huang, A. Natan, T. Osipov, D. Ray, A. Marinelli, and J. P. Cryan, Opt. Express **26**, 4531 (2018).

[21] J. Duris, S. Li, T. Driver, E. G. Champenois, J. P. MacArthur, A. A. Lutman, Z. Zhang, P. Rosenberger, J. W. Aldrich, R. Coffee, G. Coslovich, F.-J. Decker, J. M. Glownia, G. Hartmann, W. Helml, A. Kamalov, J. Knurr, J. Krzywinski, M.-F. Lin, J. P. Marangos, M. Nantel, A. Natan, J. T. O'Neal, N. Shivaram, P. Walter, A. L. Wang, J. J. Welch, T. J. A. Wolf, J. Z. Xu, M. F. Kling, P. H. Bucksbaum, A. Zholents, Z. Huang, J. P. Cryan, and A. Marinelli, Nat. Photon **14**, 30 (2020).

[22] S. Li, T. Driver, P. Rosenberger, E. G. Champenois, J. Duris, A. A.-H., V. Averbukh, J. C. T. Barnard, N. Berrah, C. Bostedt, P. H. Bucksbaum, R. N. Coffee, L. F. DiMauro, L. Fang, D. Garratt, A. Gatton, Z. Guo, G. Hartmann, D. Haxton, W. Helml, Z. Huang, A. C. LaForge, A. Kamalov, J. Knurr, M.-F. Lin, A. A. Lutman, J. P. MacArthur, J. P. Marangos, M. Nantel, A. Natan, R. Obaid, J. T. O'Neal, N. H. Shivaram, A. Schori, P. Walter, A. L. Wang, T. J. A. Wolf, Z. Zhang, M. F. Kling, A. Marinelli, and J. P. Cryan, Science **375**, 285 (2022).

[23] D. C. Haynes, M. Wurzer, A. Schletter, A. Al-Haddad, C. Blaga, C. Bostedt, J. Bozek, H. Bromberger, M. Bucher, A. Camper, S. Carron, R. Coffee, J. T. Costello, L. F. DiMauro, Y. Ding, K. Ferguson, I. Grguraš, W. Helml, M. C. Hoffmann, M. Ilchen, S. Jalas, N. M. Kabachnik, A. K. Kazansky, R. Kienberger, A. R. Maier, T. Maxwell, T. Mazza, M. Meyer, H. Park, J. Robinson, C. Roedig, H. Schlarb, R. Singla, F. Tellkamp, P. Walker, K. Zhang, G. Doumy, C. Behrens, and A. L. Cavalieri, Nat. Phys. **17**, 512 (2021).

[24] C. Buth, J. L. M. H. Chen, J. P. Cryan, L. Fang, J. M. Glownia, M. Hoener, R. N. Coffee, and N. Berrah, J. Chem. Phys. **136**, 214310 (2012).

[25] J.-C. Liu, N. Berrah, L. S. Cederbaum, J. P. Cryan, J. M. Glownia, K. J. Schafer, and C. Buth, J. Phys. B: At., Mol. Opt. Phys. **49**, 075602 (2016).

[26] Y. Hao, L. Inhester, K. Hanasaki, S.-K. Son, and R. Santra, Struct. Dyn. **2**, 041707 (2015).

[27] Z. Jurek, S.-K. Son, B. Ziaja, and R. Santra, J. Appl. Crystallogr. **49**, 1048 (2016).

[28] L. Inhester, K. Hanasaki, Y. Hao, S.-K. Son, and R. Santra, Phys. Rev. A **94**, 023422 (2016).

[29] H. I. B. Banks, D. A. Little, J. Tennyson, and A. Emmanouilidou, Phys. Chem. Chem. Phys. **19**, 19794 (2017).

[30] E. Constant, V. D. Taranukhin., A. Stolow, and P. B. Corkum, Phys. Rev. A **56**, 3870 (1997).

[31] I. Tudosa, C. Stamm, A. B. Kashuba, F. King, H. C. Siegmann, J. Stöhr, G. Ju, B. Lu, and D. Weller, Nature **428**, 831 (2004).

[32] E. Dupont, P. B. Corkum, H. C. Liu, M. Buchanan, and Z. R. Wasilewski, Phys. Rev. Lett. **74**, 3596 (1995).

[33] S. Sederberg, F. Kong, F. Hufnagel, C. Zhang, E. Karimi, and P. B. Corkum, Nat. Photonics **14**, 680 (2020).

[34] K. Jana, K. R. Herperger, F. Kong, Y. Mi, C. Zhang, P. B. Corkum, and S. Sederberg, Nat. Photonics **15**, 622 (2021).

[35] S. Sederberg, F. Kong, and P. B. Corkum, Phys. Rev. X **10**, 011063 (2020).

[36] J. J. García-Ripoll, P. Zoller, and J. I. Cirac, Phys. Rev. Lett. **91**, 157901 (2003).

[37] B. Scharfenberger, W. J. Munro, and K. Nemoto, New J. Phys. **16**, 093043 (2014).

[38] J. I.-J. Wang, D. Rodan-Legrain, L. Bretheau, D. L. Campbell, B. Kannan, D. Kim, M. Kjaergaard, P. Krantz, G. O. Samach, F. Yan, J. L. Yoder, K. Watanabe, T. Taniguchi, T. P. Orlando, S. Gustavsson, P. Jarillo-Herrero, and W. D. Oliver, Nat. Nanotechnol. **14**, 120 (2019).

[39] P. Corkum and F. Krausz, Nat. Phys. **3**, 381 (2007).

[40] W. Boutu, S. Haessler, H. Merdji, P. Breger, G. Waters., M. Stankiewicz, L. J. Frasinski, R. Taieb, J. Caillat, A. Maquet, P. Monchicourt, B. Carre, and P. Salieres, Nat. Phys. **4**, 545 (2008).

[41] A. Hache, J. E. Sipe, and H. M. van Driel, IEEE J. Quantum Electron. **34**, 1144 (1998).

[42] M. Viteau, A. Chotia, M. Allegrini, N. Bouloufa, O. Dulieu, D. Comparat, and P. Pillet, Science **321**, 232 (2008).

[43] C.-Y. Lien, C. M. Seck, Y.-W. Lin, J. H. V. Nguyen, D. A. Tabor, and B. C. Odom, Nat. Commun. **5**, 4783 (2014).

[44] P. Eckle, M. Smolarski, P. Schlup, J. Biegert, A. Staudte, M. Schöffler, H. G. Muller, R. Dörner, and U. Keller, Nat. Phys. **4**, 565 (2008).

[45] J. Itatani, F. Quéré, G. L. Yudin, M. M. Ivanov, F. Krausz, and P. B. Corkum, Phys. Rev. Lett. **88**, 173903 (2002).

[46] S. K. Semenov, N. A. Cherepkov, G. H. Fecher, and G. Schönhense, Phys. Rev. A **61**, 032704 (2000).

[47] J. W. Davenport, Phys. Rev. Lett. **36**, 945 (1976).

[48] G. R. Wight, C. E. Brion, and M. J. Van Der Wiel, J. Electron Spectros. Relat. Phenomena **1**, 457 (1972).

[49] M. E. Smith, V. McKoy, and R. R. Lucchese, J. Chem. Phys. **82**, 4147 (1985).

[50] W. Ackermann, G. Asova, V. Ayvazyan, A. Azima, N. Baboi, J. Bähr, V. Balandin, B. Beutner, A. Brandt, A. Bolzmann, R. Brinkmann, O. I. Brovko, M. Castellano, P. Castro, L. Catani, E. Chiadroni, S. Choroba, A. Cianchi, J. T. Costello, D. Cubaynes, J. Dardis, W. Decking, H. Delsim-Hashemi, A. Delserieys, G. Di Pirro, M. Dohlus, S. Düsterer, A. Eckhardt, H. T. Edwards, B. Faatz, J. Feldhaus, K. Flöttmann, J. Frisch, L. Fröhlich, T. Garvey, U. Gensch, C. Gerth, M. Görler, N. Golubeva, H. J. Grabosch, M. Grecki, O. Grimm, K. Hacker, U. Hahn, J. H. Han, K. Honkavaara, T. Hott, M. Hüning, Y. Ivanisenko, E. Jaeschke, W. Jalmuzna, T. Jezynski, R. Kammering, V. Katalev, K. Kavanagh, E. T. Kennedy, S. Khodyachykh, K. Klose, V. Kocharyan, M. Körfer, M. Kollewe, W. Koprek, S. Korepanov, D. Kostin, M. Krassilnikov, G. Kube, M. Kuhlmann, C. L. S. Lewis, L. Lilje, T. Limberg, D. Lipka, F. Löhl, H. Luna, M. Luong, M. Martins,

M. Meyer, P. Michelato, V. Miltchev, W. D. Möller, L. Monaco, W. F. O. Müller, O. Napieralski, O. Napoly, P. Nicolosi, D. Nölle, T. Nuñez, A. Oppelt, C. Pagani, R. Paparella, N. Pchalek, J. Pedregosa-Gutierrez, B. Petersen, B. Petrosyan, G. Petrosyan, L. Petrosyan, J. Pflüger, E. Plönjes, L. Poletto, K. Pozniak, E. Prat, D. Proch, P. Pucyk, P. Radcliffe, H. Redlin, K. Rehlich, M. Richter, M. Roehrs, J. Roensch, R. Romaniuk, M. Ross, J. Rossbach, V. Rybnikov, M. Sachwitz, E. L. Saldin, W. Sandner, H. Schlarb, B. Schmidt, M. Schmitz, P. Schmüser, J. R. Schneider, E. A. Schneidmiller, S. Schnepp, S. Schreiber, M. Seidel, D. Sertore, A. V. Shabunov, C. Simon, S. Simrock, E. Sombrowski, A. A. Sorokin, P. Spanknebel, R. Spesyvtsev, L. Staykov, B. Steffen, F. Stephan, F. Stulle, H. Thom, K. Tiedtke, M. Tischer, S. Toleikis, R. Treusch, D. Trines, I. Tsakov, E. Vogel, T. Weiland, H. Weise, M. Wellhöfer, M. Wendt, I. Will, A. Winter, K. Wittenburg, W. Wurth, P. Yeates, M. V. Yurkov, I. Zagorodnov, and K. Zapfe, Nat. Photon **1**, 336 (2007).

[51] B. Faatz, E. Plönjes, S. Ackermann, A. Agababyan, V. Asgekar, V. Ayvazyan, S. Baark, N. Baboi, V. Balandin, N. von Bargen, Y. Bican, O. Bilani, J. Bödewadt, M. Böhnert, R. Böspflug, S. Bonfigt, H. Bolz, F. Borges, O. Borkenhagen, M. Brachmanski, M. Braune, A. Brinkmann, O. Brovko, T. Bruns, P. Castro, J. Chen, M. K. Czwalinna, H. Damker, W. Decking, M. Degenhardt, A. Delfs, T. Delfs, H. Deng, M. Dressel, H.-T. Duhme, S. Düsterer, H. Eckoldt, A. Eislage, M. Felber, J. Feldhaus, P. Gessler, M. Gibau, N. Golubeva, T. Golz, J. Gonschior, A. Grebentsov, M. Grecki, C. Grün, S. Grunewald, K. Hacker, L. Hänisch, A. Hage, T. Hans, E. Hass, A. Hauberg, O. Hensler, M. Hesse, K. Heuck, A. Hidvegi, M. Holz, K. Honkavaara, H. Höppner, A. Ignatenko, J. Jäger, U. Jastrow, R. Kammering, S. Karstensen, A. Kaukher, H. Kay, B. Keil, K. Klose, V. Kocharyan, M. Köpke, M. Körfer, W. Kook, B. Krause, O. Krebs, S. Kreis, F. Krivan, J. Kuhlmann, M. Kuhlmann, G. Kube, T. Laarmann, C. Lechner, S. Lederer, A. Leuschner, D. Liebertz, J. Liebing, A. Liedtke, L. Lilje, T. Lim-

berg, D. Lipka, B. Liu, B. Lorbeer, K. Ludwig, H. Mahn, G. Marinkovic, C. Martens, F. Marutzky, M. Maslocv, D. Meissner, N. Mildner, V. Miltchev, S. Molnar, D. Mross, F. Müller, R. Neumann, P. Neumann, D. Nölle, F. Obier, M. Pelzer, H.-B. Peters, K. Petersen, A. Petrosyan, G. Petrosyan, L. Petrosyan, V. Petrosyan, A. Petrov, S. Pfeiffer, A. Piotrowski, Z. Pisarov, T. Plath, P. Pototzki, M. J. Prandolini, J. Prenting, G. Priebe, B. Racky, T. Ramm, K. Rehlich, R. Riedel, M. Roggli, M. Röhling, J. Rönsch-Schulenburg, J. Rossbach, V. Rybnikov, J. Schäfer, J. Schaffran, H. Schlarb, G. Schlesselmann, M. Schlösser, P. Schmid, C. Schmidt, F. Schmidt-Föhre, M. Schmitz, E. Schneidmiller, A. Schöps, M. Scholz, S. Schreiber, K. Schütt, U. Schütz, H. Schulte-Schrepping, M. Schulz, A. Shabunov, P. Smirnov, E. Sombrowski, A. Sorokin, B. Sparr, J. Spengler, M. Staack, M. Stadler, C. Stechmann, B. Steffen, N. Stojanovic, V. Sychev, E. Syresin, T. Tanikawa, F. Tavella, N. Tesch, K. Tiedtke, M. Tischer, R. Treusch, S. Tripathi, P. Vagin, P. Vetrov, S. Vilcins, M. Vogt, A. de Zubiaurre Wagner, T. Wamsat, H. Weddig, G. Weichert, H. Weigelt, N. Wentowski, C. Wiebers, T. Wilksen, A. Willner, K. Wittenburg, T. Wohlenberg, J. Wortmann, W. Wurth, M. Yurkov, I. Zagorodnov, and J. Zemella, NJP **18**, 062002 (2016).

[52] M. Magrakvelidze, O. Herrwerth, Y. H. Jiang, A. Rudenko, M. Kurka, L. Foucar, K. U. Kühnel, M. Kübel, N. G. Johnson, C. D. Schröter, S. Düsterer, R. Treusch, M. Lezius, I. Ben-Itzhak, R. Moshammer, J. Ullrich, M. F. Kling, and U. Thumm, Phys. Rev. A **86**, 013415 (2012).

[53] A. Rudenko, Y. H. Jiang, M. Kurka, K. U. Kühnel, L. Foucar, O. Herrwerth, M. Lezius, M. F. Kling, C. D. Schröter, R. Moshammer, and J. Ullrich, J. Phys. B At. Mol. Opt. **43**, 194004 (2010).

[54] P. Lin and R. R. Lucchese, J. Synchrotron Radiat. **8**, 150 (2001).

[55] M. Nisoli and G. Sansone, Prog. Quant. Electron **33**, 17 (2009).

[56] J. L. Miller, Phys. Today **71**, 20 (2018).

[57] L. Cattaneo, J. Vos, R. Y. Bello, A. Palacios, S. Heuser, L. Pedrelli, M. Lucchini, C. Cirelli, F. Martín, and U. Keller, Nat. Phys **14**, 733 (2018).

[58] R. Borrego-Varillas, M. Lucchini, and M. Nisoli, Rep. Prog. Phys. **85**, 066401 (2022).

[59] I. N. Levine, D. H. Busch, and H. Shull, *Quantum chemistry*, Vol. 6 (Pearson Prentice Hall Upper Saddle River, NJ, 2009).

[60] M. Born and R. Oppenheimer, Annalen der Physik **389**, 457 (1927).

[61] B. H. Bransden and C. J. Joachain, *Physics of atoms and molecules* (Pearson Education India, 2003).

[62] H.-J. Werner and P. J. Knowles, J. Chem. Phys. **82**, 5053 (1985).

[63] P. J. Knowles and H.-J. Werner, Chem. Phys. Lett. **115**, 259 (1985).

[64] H.-J. Werner and P. J. Knowles, J. Chem. Phys. **89**, 5803 (1988).

[65] P. J. Knowles and H.-J. Werner, Chem. Phys. Lett. **145**, 514 (1988).

[66] P. J. Knowles and H.-J. Werner, Theor. Chim. Acta **84**, 95 (1992).

[67] D. Bhattacharya, K. R. Shamasundar, and A. Emmanouilidou, J. Phys. Chem. A **125**, 7778 (2021).

[68] G. B. Arfken and J. H. Weber, *Mathematical methods for physicists 6th ed.* (Elsevier, 2005).

[69] H.-J. Werner, P. J. Knowles, G. Knizia, F. R. Manby, and M. Schütz, M. WIRE: Comput. Mol. Sci. **2**, 242 (2012).

[70] L. Inhester, *Auger decay in double core ionized molecules*, Ph.D. thesis, Georg-August-Universität Göttingen (2013).

[71] M. Abramowitz and I. Stegun, *Handbook of Mathematical Functions*, 1st ed. (Dover publications, 1965).

[72] M. J. Seaton, Rep. Prog. Phys. **46**, 167 (1983).

[73] H. Park and R. N. Zare, J. Chem. Phys. **104**, 4554 (1996).

[74] P. V. Demekhin, A. Ehresmann, and V. L. Sukhorukov, J. Chem. Phys. **134**, 024113 (2011).

[75] I. J. Thompson and F. M. Nunes, *Nuclear reactions for astrophysics: principles, calculation and applications of low-energy reactions* (Cambridge University Press, 2009).

[76] J. D. Hoffman and S. Frankel, *Numerical methods for engineers and scientists* (CRC press, 2018).

[77] J. J. Sakurai, *Modern Quantum Physics* (Addison-Wesley, Reading, MA, 1994).

[78] A. Szabo and N. S. Ostlund, *Modern quantum chemistry: introduction to advanced electronic structure theory* (Courier Corporation, 1996).

[79] G. P. Katsoulis, M. B. Peters, A. Staudte, R. Bhardwaj, and A. Emmanouilidou, Phys. Rev. A **103**, 033115 (2021).

[80] M. E. Rose, *Elementary theory of angular momentum* (John Wiley and Sons, New York, 1957).

[81] D. Dill and J. L. Dehmer, J. Chem. Phys. **61**, 692 (1974).

[82] H. Dachsel, J. Chem. Phys. **124**, 144115 (2006).

[83] U. Fano and A. R. P. Rau, *Atomic collisions and spectra* (Elsevier, 2012).

[84] V. L. Jacobs, J. Phys. B: Atom. Mol. Phys. **5**, 2257 (2001).

[85] J. Pagaran, S. Fritzsche, and G. Gaigalas, Comput. Phys. Commun. **174**, 616 (2006).

[86] R. R. Lucchese, G. Raseev, and V. McKoy, Phys. Rev. A **25**, 2572 (1982).

[87] M. Y. Ivanov and O. Smirnova, Lecture Notes, CORINF Network (2012).

[88] A.-T. Le, H. Wei, C. Jin, and C. D. Lin, J. Phys. B: Atom. Mol. Phys. **49**, 053001 (2016).

[89] R. Y. Rubinstein and D. P. Froese, *Simulation and the Monte Carlo Method*, 2nd ed. (John Wiley and Sons, New York, 2007).

[90] T. H. Dunning, J. Chem. Phys. **90**, 1007 (1989).

[91] I. Cacelli, R. Moccia, and A. Rizzo, Phys. Rev. A **57**, 1895 (1998).

[92] L. D. Landau and E. M. Lifshitz, *Quantum mechanics: non-relativistic theory*, Vol. 3 (Elsevier, 2013).

[93] M. V. Ammosov, N. B. Delone, and V. Krainov, SPIE **664**, 138 (1986).

[94] N. B. Delone and V. P. Krainov, J. Opt. Soc. Am. B **8**, 1207 (1991).

[95] A. Hamnett, W. Stoll, and C. E. Brion, J. Electron Spectrosc. Relat. Phenom. **8**, 367 (1976).

[96] M. N. Piancastelli, J. Electron Spectros. Relat. Phenomena **100**, 167 (1999).

[97] A. Korobenko, S. Rashid, C. Heide, A. Y. Naumov, D. A. Reis, P. Berini, P. B. Corkum, and G. Vampa, Opt. Express **29**, 24161 (2021).

[98] M. Shapiro and P. Brumer, *Quantum Control of Molecular Processes*, 2nd ed. (John Wiley & Sons, 2012).

[99] L. S. Cederbaum, J. Zobeley, and F. Tarantelli, Phys. Rev. Lett. **79**, 4778 (1997).

[100] F. Holzmeier, J. Joseph, J. C. Houver, M. Lebech, D. Dowek, and R. R. Lucchese, Nat. Commun. **12** (2021), 10.1038/s41467-021-27360-y.

[101] F. L. Pilar, *Elementary quantum chemistry* (Courier Corporation, 2001).

[102] R. P. Orenha and S. E. Galembeck, J. Chem. Educ. **91**, 1064 (2014).

[103] R. E. Stratmann, R. W. Zurales, and R. R. Lucchese, J. Chem. Phys. **104**, 8989 (1996).

[104] J. Breidbach and L. S. Cederbaum, Phys. Rev. Lett. **94**, 033901 (2005).

[105] K. Hosaka, J. Adachi, M. Takahashi, and A. Yagishita, J. Phys. B. At Mol. Opt. Phys. **36**, 4617 (2003).

[106] C. E. Brion and K. H. Tan, J. Electron Spectros. Relat. Phenomena **23**, 1 (1981).

[107] S. Wallace, D. Dill, and J. L. Dehmer, J. Chem. Phys. **76**, 1217 (1982).

[108] K. Jana, E. Okocha, S. H. Møller, Y. Mi, S. Sederberg, and P. B. Corkum, Nanophotonics **11**, 787 (2022).

[109] K. Schmidt-Rohr, ACS Omega **5**, 2221 (2020).

[110] K. P. Jensen and U. Ryde, J. Biol. Chem. **279**, 14561 (2004).

[111] M. J. Paterson, O. Christiansen, F. Jensen, and P. R. Ogilby, Photochem. Photobiol. **82**, 1136 (2006).

[112] D. H. Parker, Acc. Chem. Res. **33**, 563 (2000).

[113] P. Cörlin, A. Fischer, M. Schönwald, A. Sperl, T. Mizuno, U. Thumm, T. Pfeifer, and R. Moshammer, Phys. Rev. A **91**, 043415 (2015).

[114] G. Schmid, K. Schnorr, S. Augustin, S. Meister, H. Lindenblatt, F. Trost, Y. Liu, M. Braune, R. Treusch, C. D. Schröter, T. Pfeifer, and R. Moshammer, J. Synchrotron Radiat. **26**, 854 (2019).

[115] A. Magunia, M. Rebholz, E. Appi, C. C. Papadopoulou, H. Lindenblatt, F. Trost, S. Meister, T. Ding, M. Straub, G. D. Borisova, J. Lee, R. Jin, A. von der Dellen, C. Kaiser, M. Braune, S. Düsterer, S. Ališauskas, T. Lang, C. Heyl, B. Manschwetus, S. Grunewald, U. Frühling, A. Tajalli, A. B. Wahid, L. Silletti, F. Calegari, P. Mosel, U. Morgner, M. Kovacev,

U. Thumm, I. Hartl, R. Treusch, R. Moshammer, C. Ott, and T. Pfeifer, Sci. Adv. **9**, eadk1482 (2023).

[116] A. Hadjipittas and A. Emmanouilidou, J. Phys. B At. Mol. Opt. **56**, 205102 (2023).

[117] H. Goldstein, *Classical Mechanics* (Addison-Wesley, 1980).

[118] L. Verlet, Phys. Rev. **159**, 98 (1967).

[119] H.-J. Werner and P. J. Knowles, Theor. Chim. Acta **78**, 175 (1990).

[120] N. A. Besley, A. T. B. Gilbert, and P. M. W. Gill, J. Chem. Phys. **130**, 124308 (2009).

[121] L. Bytautas, N. Matsunaga, and K. Ruedenberg, J. Chem. Phys. **132**, 074307 (2010).

[122] R. C. Weast, *CRC Handbook of Chemistry and Physics. MJ Astle and WH Beyer, eds* (CRC Press, Inc, Boca Raton, FL, 1985).

[123] M. Lundqvist, D. Edvardsson, P. Baltzer, M. Larsson, and B. Wannberg, J. Phys. B At. Mol. Opt. **29**, 499 (1996).

[124] M. Larsson, P. Baltzer, S. Svensson, B. Wannberg, N. Martensson, A. N. de Brito, N. Correia, M. P. Keane, M. Carlsson-Gothe, and L. Karlsson, J. Phys. B At. Mol. Opt. **23**, 1175 (1990).

[125] Y. Hikosaka, T. Aoto, R. I. Hall, K. Ito, R. Hirayama, N. Yamamoto, and E. Miyoshi, J. Chem. Phys. **119**, 7693 (2003).

[126] W. Kutzelnigg and J. D. Morgan, Zeitschrift für Physik D Atoms, Molecules and Clusters **36**, 197 (1996).

[127] A. Frank, A. L. Rivera, and K. B. Wolf, Phys. Rev. A **61**, 054102 (2000).

[128] P. M. Morse, Phys. Rev. **34**, 57 (1929).

[129] K. K. Irikura, JPCRD **36**, 389 (2007).

[130] L. J. Slater, M. Abramowitz, and I. A. Stegun, Appl. Math. Ser. **55** (1965).